Nanostructuration of silica particles and design of composite biomaterials

Dounia Dems

To cite this version:

Dounia Dems. Nanostructuration of silica particles and design of composite biomaterials. Material chemistry. Sorbonne Université, 2018. English. NNT : 2018SORUS373 . tel-02865351

Sorbonne Université

Ecole doctorale 397 : Physique et Chimie des Matériaux

Laboratoire de Chimie de la Matière Condensée de Paris

Nanostructuration de particules de silice et élaboration de biomatériaux composites

Par **Dounia Dems**

Pour obtenir le grade de
DOCTEUR

Spécialité : Physique et Chimie des Matériaux

Présentée et soutenue publiquement le 12 Octobre 2018

Devant un jury composé de :

Sébastien Lecommandoux	Professeur - Université de Bordeaux	Rapporteur
Gilles Subra	Professeur - Université de Montpellier	Rapporteur
Christine Ménager	Professeur – Sorbonne Université	Examinatrice
Valérie Jeanne-Rose	Chercheur Associée - L'Oréal R&D	Examinatrice
Nicolas Delsuc	Chargé de recherche – CNRS	Invité
Carole Aimé	Chargée de recherche – CNRS	Encadrante de thèse
Thibaud Coradin	Directeur de recherche – CNRS	Directeur de thèse

Content

Introduction

In the context of the global increase of average life expectancy, a major challenge to be addressed in a near future is to improve healthcare and well-being of aging patients. Regenerative medicine that aims at “replacing, engineering or regenerating human cells, tissues or organs to restore or establish normal function” is currently considered as the most promising therapeutic approach to reach this objective.[1,2]

Tissue engineering approaches, that consist in building new tissues by combining cells and materials, strongly rely on our improved understanding of how the extracellular matrix (ECM) is organized and functions to reach the specifications of the tissues. This matrix not only acts as a structural environment (“scaffold”) to support cells, but also regulates many cellular processes including growth, migration, differentiation, survival, homeostasis, and morphogenesis.[3] Thus if biomaterials could be engineered to mimic as closely as possible the extracellular architecture and bioactivity, they should provide the ideal environment for cells to build a new healthy tissue.[4]

This concept, that is at the heart of my PhD project, is presented in more details in the first chapter of this manuscript. Starting from a general description of the ECM and its principal interactions with cells, we will emphasize that each tissue or organ has its own specific properties. These specificities must be taken into account to design suitable scaffolds, as illustrated for the regeneration of the peripheral nervous system. We will then introduce the field of bionanocomposite materials and expose the principles that drive their engineering, from nanoparticles to the proper composite structures, and the resulting properties. Finally, we will explain why silica-collagen bionanocomposites are particularly interesting biomaterials for tissue engineering.

As a first demonstration of the potentialities of the bionanocomposite approach, we will describe the work performed in collaboration with Pr. Stupp laboratory (Northwestern University, Chicago) during a 8 months internship funded by a Fulbright grant, that used peptide amphiphiles as synthetic alternatives to collagen. Because both the silica nanoparticles (SiNPs) and the peptides could be functionalized with multiple bioactive motifs, this approach has allowed to investigate the impact of the clusterization of bioactive ligands on cell behavior and study possible synergistic interactions between two epitopes.

In order to combine these two key features, clusterization and bifunctionality, we have developed a new strategy to control the display of functional ligands i.e. surface nanostructuration. As described in chapter III, we have designed and synthesized self-assembling alkoxysilanes to induce the formation of functional patches on SiNPs. Although evidences have been gathered of the success of our strategy, we have emphasized that the characterization of nanostructured particle surfaces is highly challenging.

Chapter IV is dedicated to the study of the behavior of PC12 neural type cells seeded on thread-shaped collagen-silica as scaffolds for peripheral nerve regeneration. The surface of the SiNPs was functionalized to interact with cells, collagen or both. Significant variations in cell response were observed depending on particle surface chemistry and concentration that we have tried to relate to the composite scaffold architecture.

Finally, chapter V presents our first steps towards the preparation of collagen-based self-supported membranes by electrospinning that would be interesting for applications in tissue engineering. As a key criterion to optimize the bioactivity of these scaffolds, special attention has been paid to the preservation of the native state of collagen at the different stages of the membrane processing. Encouraging results validated by multiscale characterization techniques were obtained.

As exposed in the Conclusion section, extending the electrospinning technique to bionanocomposite processing constitutes one of the main perspectives of this work, together with further developments of patchy SiNPs and incorporation of additional cell-regulating factors within our scaffolds.

References

(1) Giannoudis, P. V.; Pountos, I. Tissue Regeneration. *Injury* **2005**, *36* (4), S2–S5.

(2) Mao, A. S.; Mooney, D. J. Regenerative Medicine: Current Therapies and Future Directions. *Proc Natl Acad Sci U S A* **2015**, *112* (47), 14452–14459.

(3) Frantz, C.; Stewart, K. M.; Weaver, V. M. The Extracellular Matrix at a Glance. *Journal of Cell Science* **2010**, *123* (24), 4195–4200.

(4) Abbott, R. D.; Kaplan, D. L. Engineering Biomaterials for Enhanced Tissue Regeneration. *Current Stem Cell Reports* **2016**, *2* (2), 140–146.

I. Biomaterials for tissue regeneration

Content

1. The extracellular matrix

1.1. Structure and function

The extracellular matrix (ECM) is the noncellular component present within all tissues and organs. The ECM is composed mostly of water and macromolecules organized in a 3D network (Figure I-1). These macromolecules, mostly proteins and polysaccharides, provide a scaffold into which cells are embedded and also regulate many cellular processes including growth, migration, differentiation, survival, homeostasis, and morphogenesis.[1–3]

The composition and topology of the ECM is tissue-dependent. During tissue development, cells (e.g. epithelial and endothelial cells, fibroblasts, adipocytes) synthesize the constitutive elements of the ECM, that influence its organization and buffering (e.g. water retention) properties. The ECM further evolved *via* biophysical and biochemical modifications induced by cells and the environment. The direct consequence is the variation in the tensile and compressive strength, elasticity and protection abilities. ECM features are indeed varying remarkably from one tissue to another: the same characteristics are not required for lungs versus skin or bones.[1,2,4]

ECM components are interacting with cells *via* biochemical and biomechanical cues (Figure I-1-A). They present chemical signals directly on the macromolecular network or through specialized proteins such as binding growth factors (GF), interacting with cell-surface receptors and triggering signal transduction. This process directly modifies the regulation of the gene transduction and subsequently cell behavior.[1,2,4]

The ECM has a highly heterogeneous and dynamic organization. Components are constantly synthesized, degraded and reshaped by cells. The remodeling is particularly high during development, wound repair or after a disease. It is initiated by a complex interplay between cells, *via* ECM receptors, and action of enzymes such as matrix metalloproteases involving mechanical modulations.[1,2,4]

The three major components of the ECM are proteoglycans (PGs), collagens, and glycoproteins. PGs are the combination between a protein and a glycosaminoglycan (GAG, e.g. long unbranched polysaccharides). They fill the extracellular interstitial space within the tissue, creating a hydrated gel. The diversity of structures translates a multitude of functions: protection, lubrication, biomechanical resistance to pressure, GF reservoir…[1,2,5–7] Collagen and glycoproteins are fibrillary proteins of particular interest in this PhD work.

Figure I-1 : (A) Schematic representation of intersticial ECM adapted from[2]. B) Scanning electron microscopy (SEM) of native ECM in connective tissues, largely composed of collagen fibrils. The hydrogel, composed of proteoglycans and glycosaminoglycans, that normally fills the interstices of this fibrous network has been removed by the processing treatment (reproduced from[8]).

1.2. Collagens

Collagens are the most abundant proteins in the human body (ca. 30% of its protein mass). At this day, 28 collagen types have been described in the literature, with various sequences of polypeptide chains. All collagen molecules consist of three polypeptide chains, called α-chains, and contain at least one domain composed of repeating Gly-X-Y sequences in each of the constituent chains. X and Y positions are frequently occupied by the two amino acids proline and 4-hydroxyproline. Because of the high content of proline, 4-hydroxyproline and glycine, α-chains exhibit a tendency to spontaneously form left-handed helices without any formation of intrachain hydrogen bonds. Those three left-handed helices coiled into a common axis to form a right-handed triple helix. This superstructure is allowed because of the presence of glycine, the smallest amino acid, on every third position that enables the close packing. The triple helix is stabilized by interchain hydrogen bonds, mostly due to 4-hydroxyproline amino acids.[1,2,5,6,9–11]

Some collagens can self-assemble into fibrils, such as the types I, II, III, V and XI. They are mostly present in tissues that need to resist shear, tensile force or pressure. Consequently, they are a structural key element of connective tissues. Other collagens can form a non-fibrillar network (IV, VII, X) principally found in the basal membrane. The most abundant type of collagen is the fibrillar collagen I, present throughout the body, except in cartilage. Moreover, it is the principal collagen in the dermis, fasciae, and tendons and it is massively present in mature scar tissues.

Fibrillar collagen is responsible not only for structural integrity of the ECM but also contributes to cell adhesion, chemotaxis, migration and direct tissue development.[12]

Fibrillar collagen molecules are mostly synthesized by fibroblasts directly in the stroma or from adjacent tissues. The α-chains synthesized in the endoplasmic reticulum self-assemble inside the cell, goes through post translational modifications and are secreted by exocytosis (Figure I-2-A). This initial triple helix is the procollagen bearing propeptides at the N- and C-terminal ends of their polypeptide chains (Figure I-2-B). As monomer, the triple helix is approximately 300 nm in length and 1.5 nm in diameter. Metalloprotease enzymes cleave the terminal procollagen peptides, which triggers the self-assembly of the triple helix into fibrils that further self-assemble into collagen fibers (Figure I-2-C). The self-assembly of triple helices produce “overlap” and “gap” areas creating a typical pattern of fibrillar collagen identified by electron microscopy (Figure I-2-D-E). This structure presents a characteristic 67 nm axial periodicity, independently of the fibrils diameters.

Type I collagen molecules are soluble as triple helix in acidic conditions. Their fibrillation can be induced *in vitro* without any enzyme by modification of physico-chemical parameters such as temperature or pH.[13–17] In our group, a usual technique to trigger collagen fibrillation is to raise the pH, by ammonia vapor or neutralization in aqueous medium.

Figure I-2 : (A-D) Schematic representation of the synthesis and hierarchical structure of collagen *in vivo*, adapted from[18] (E) Electron micrograph of negatively stained reconstituted collagen fibrils, adapted from[19].

1.3. Glycoproteins

Fibronectin and laminin are two key glycoproteins. Fibronectin is the major glycoprotein of connective tissues, while laminin is present is basement membranes.

Fibronectin is composed of two subunits covalently connected by disulfide bonds at their C-termini (Figure I-3-A). Each subunit is a repetition of three modules, Type I, II and III differing by their amino-acid sequence.[1,2,5,20] Fibronectin is also synthesized by cells, mostly fibroblasts, *via* a soluble state: a soluble protein dimer. This precursor self-assembles in solution into an insoluble complex of fibers. Fibronectin is critical for cell attachment and migration.

Laminins constitute a family of about 20 glycoproteins assembled into a cross-linked web.[2,5,6] They are heterodimers formed by three chains (α, β and γ) linked together by disulfide bonds (Figure I-3-B). They are synthesized by a wide variety of cells, depending on the considered tissue (e.g. endothelial cells, skeletal and cardiac muscle cells). Many laminins self-assemble into networks within the ECM. Laminins have a major role in embryonic development and organogenesis. They trigger cell adhesion, migration, and differentiation. They are notably well-known to be crucial for axonal regeneration, Schwann cell differentiation and myelination in the injured peripheral nervous system.

Figure I-3 : Schematic representation of (A) Fibronectin and (B) Laminin, adapted from[21,22].

Collagens, fibronectin and laminins interact with each other, and other molecules such as elastin, to create an insoluble supramolecular network. Some domains are directly interacting with other molecules of the ECM, as indicated in Figure I-3, but they also have the ability to interact with cells *via* transmembrane proteins.

1.4. ECM – Cells interactions

Cells interact with the ECM *via* transmembrane proteins. In animal cells, the principal family of such proteins is the integrin one. Integrins are heterodimer glycoproteins (subunits α and β) that act as a linker between the ECM and the actin cytoskeleton of mammalian cells. When they create weak bonds with macromolecules of the ECM, it activates intracellular signaling pathways that communicate to the cell the characteristics of the ECM. Many different kinds of integrins exist (at least 22 in mammals), which interact specifically with collagen, laminin or fibronectin domains. The affinity is relatively low between integrins and their ligand, which enable to have dynamic bindings. [23,24]

Three amino acid sequences have been found to play a key role in ECM-cell interactions:

(i) the **RGD** motif is a tripeptide sequence (arginine (R), glycine (G) and aspartic acid (D)) that was first discovered on fibronectin, but is also present on laminin (Figure I-3). When integrins specifically bind to RGD on fibronectin, this triggers cytoskeleton reorganization and formation of focal adhesion. Focal adhesions are large structures clustering integrins, but also many other proteins that anchor the cells to the ECM. The formation of focal adhesions concentrates actin stress fibers, which helps maintaining cells shape and adhesion to the matrix. This triggers adhesion-dependent signal transduction inside the cells, allowing either cell adhesion, spreading or motility.[21–24] RGD is also present in some laminins and collagens but it is less accessible because of the molecules conformation.[25]

(ii) the **PHSRN** sequence (proline (P), histidine (H), serine (S), arginine (R) and asparagine (N)) is localized on fibronectin near RGDS (Figure I-3-A). Although it is itself not biologically active, it enhances the cell-adhesive activity of RGD synergistically. RGD is the primary recognition site for $\alpha5\beta1$ integrins, in fibronectin III10 repeat and PHSRN is the synergy site for $\alpha5\beta1$, in fibronectin III9 repeat. The presence of both peptides, in native conformation and spacing, allows $\alpha5\beta1$-mediated adhesion, thus instructing cells to adhere, spread, differentiate, migrate, and, in the case of osteogenic cells, mineralize more efficiently than RGD alone.[26,27]

(iii) In laminins and collagens other amino acid motifs are known to serve as alternative selective binding modules. For example, on laminin, another important peptide sequence **IKVAV** (isoleucine (I)-lysine (K)-valine (V)-alanine (A)-valine (V)) is located on the C-terminal end of laminin. This sequence promotes cell adhesion, neurite outgrowth, collagenase IV activity, angiogenesis, plasminogen activation, cell growth, tumor growth and differentiation of progenitor cells.[28,29]

ECMs being the key element in which cells live and work so as to preserve healthy and functional tissues and organs, it is particularly important to understand how their bio-chemical, structural and physical features, including stiffness, fiber orientation, and ligand presentation trigger specific cellular behaviors. Such an understanding should provide fruitful guidelines for the design of biomimetic scaffolds for tissue engineering.

2. Biomaterials to mimic the ECM

Tissues can be damaged by diseases, injuries or traumas and necessitate treatments to help their repair, replacement or regeneration. The autograft, transplant of an organ from one site to the other within the same patient, is currently the gold standard. However, it presents several disadvantages such as having to suffer another injury for the patient, with possible complications and pain on the site of the organ removal and the possible mismatch of function between the damaged and donor organs. The alternative is the allograft, i.e. the transplantation of an organ from another donor. However, this possibility also has a lot of constraints, such as difficulties of accessing available compatible tissues, risks of rejection by the patient's immune system and the possibility of introducing infection or disease from the donor to the patient. Additionally, immunosuppressive treatments required to decrease organ rejection compromise the immune system, leading to weakening of the patient.[30–33]

The field of tissue engineering is an interesting alternative to those treatments. How to regenerate damaged tissues with a minimum of surgical work? Indeed, the body has intrinsic self-healing abilities. However, extent of repair varies amongst different tissues, the severity of injuries or diseases and the age and state of health of the patient.[34] That is where biomaterials come in, to restore or improve tissue integrity.

2.1. Biomaterials specifications

The definition of biomaterials is not easy to establish because of the diversity of applications and processes. According to the International Union of Pure and Applied Chemistry (IUPAC), it is the material exploited in contact with living tissues, organisms, or microorganisms.[35] It can be, in particular, a matrix providing cells with structural scaffolding, chemical signaling and ideal mechanical properties to regenerate a tissue. Since antiquity, humans have been taking materials (glass, metals or polymers) to replace body parts that have been damaged by disease or injury.[36]

Bioengineering approaches link biological tools and engineering principles. They have the advantages over grafts of having low immunogenicity while avoiding the creation of a second injury. The material provides a direct framework for tissue regeneration with minimum surgery work. This scaffold needs to simulate the environment required for cell growth and consequently has to fit specific requirements.

First of all, the material must be **biocompatible**. It is a complex notion, the organism must accept it and in parallel the material should be functional and beneficial for the organism. In particular, the body's immune reaction should be minimal, without severe inflammatory response that could lead to rejection of the scaffold.

The scaffold should provide **mechanical and structural properties** similar to the initial tissue. Native ECMs have a fibrillar architecture in 3D. Using a hierarchical structuration is important to feature the properties at all scales from the nanometer to millimeter level.[37] The influence of the mechanical properties on cell differentiation is evidenced by mesenchymal stem cells: they differentiate into different cell types, such as neurons, myoblasts and osteoblasts on increasing stiffer substrates.[38] The mechanical properties can be modulated by different approaches depending on the nature of the materials and applications such as using cross-linkers,[39] controlling crystallinity during processing,[40] and using inorganic reinforcing fillers…[41] Additionally, to facilitate its surgical implementation, it should be solid enough to be manipulated without hampering its integrity. An ideal scaffold also needs to combine these interesting mechanical properties with **porosity** to allow vascularization, supply in nutrients, and cell colonization. The size and connectivity of the pores should also be modulated depending on the target tissue.[30,37,42]

Because cells need to adhere to the biomaterial to differentiate, the cell-material interface is of primary importance. The **surface chemistry** of materials is one of the key parameters. Many studies have been conducted by directly using ECM proteins such as collagen, fibronectin or laminin as materials or as coatings.[43] Another option is to incorporate only the bioactive ligand such as RGDS or IKVAV by chemical binding or physical adsorption.[44–52]

Another challenge in engineering an interesting scaffold is to address the display of biochemical signals, in particular when it comes to control their spatial distribution. Indeed, more than the chemical nature of a biological component, its **clustering** is a key signal to rule biological activity and trigger cell behaviors such as adhesion, migration, proliferation, and differentiation.[52–57] A typical example is the formation of focal adhesions during cell adhesion that is triggered only after the formation of an effective integrin cluster.

A combination of optimal size, architecture, and surface properties may lead to biomaterials that allow the formation of a new ECM in the body and create a favorable environment for tissue regeneration to occur. Finally, the biomaterials should be able to

degrade by itself to be replaced by this new ECM. The products of this biodegradation should not be toxic and be cleared from the body without any damage.[30,58]

2.2. Tissue-specific structural properties

To successfully engineer a biomaterial for tissue regeneration, a crucial parameter to take into account is to mimic the specific structure of the native tissue. The biochemical nature of the ECM is the first step, but the architecture of the scaffold is at least as important.

Biomaterials can be synthesized from synthetic or biological materials. Biological materials have intrinsically ideal properties to interact with surrounding native tissues. Many of them have been used as materials for neural tissue engineering, including fibronectin, silk fibroin, chitosan and collagen.[59–61] The molecules of collagen are present in all tissues, but in different density and with specific structures. Table I-1 presents the properties of engineered biomaterials that are required when mimicking different types of tissues .

Alternatively, synthetic polymers are synthesized to mimic the structural characteristics and properties of biological macromolecules. They have tailorable mechanical properties, good biocompatibility, and easy processability. Moreover, it is usually easier to reach a good reproducibility and obtain higher yields and purity than with extracted biomolecules.

They can be covalently linked polymers, such as Poly(Glycolic Acid), Polylactic Acid, Poly(ethylene Glycol).[62–64] However, they lack the biological properties of their natural counterparts. Innovative attempts to design biomimetic molecules that can assemble in an ECM-like manner have been described. For example, a covalent network by sol–gel polymerization of a silylated peptide bearing a sequence derived from the consensus collagen sequence [Pro-Hyp-Gly] was reported.[65] Other collagen-mimicking peptides have been produced and form a supramolecular self-assembly.[66–68] Supramolecular polymers are dynamic and self-assemble hierarchically, similar to the native proteins. The monomeric building blocks are interacting with each other by multiple noncovalent intermolecular interactions such as hydrogen bonding, metal–ligand coordination, $\pi - \pi$ stacking, and hydrophobic interactions. Numerous peptides, not always with collagen-similar sequences, have been synthesized in order to engineer a scaffold for tissue engineering, such as peptide amphiphiles.[44,69–74]

Tissue	*Requirement*	*Structures*
Bones[75–77]	High mechanical properties (tensile strength, bending strength, impact energy, moduli) Young's modulus for compact bones: 17–20 GPa	Interconnected pores structure Collagen fibrils in bundles with coil organization Inorganic component (hydroxyapatite)
Dermis[78–81]	Physical strength and stress absorbing character	Wounded Cord-shape collagen bundles Large size distribution of fibrils diameter
Skeletal Muscles[82,83]	High elastic properties Young's modulus ~100 kPa Increasing energy dissipation at higher sarcomere length Stress relaxation at a constant strain Alignment	Bundles of collagen fibers in tubes surrounding muscles fibers Anisotropic orientation
Blood vessels[84–88]	Compliance 5–15%/100 mmHg (aorta) Resistance to high pressure	With an endothelial linin and luminal surface. Circumferentially, helically, and axially aligned collagen
Tendons[89–92]	Young modulus: 0.5 to 1.9 GPa, ultimate tensile strength: 50 to 120 MPa	Aligned collagen fibers in bundles along the tendon axis revealing a "crimp" feature. Hypothesis of liquid-crystal phases for collagen.
Peripheral nervous system[93–95]	Alignment to guide axons	Anisotropic orientation
Central nervous system[96–98]	Allow cells infiltration and proliferation without comprising the blood barrier.	Substrate needs to fill the void
Corneal Stroma[99,100]	Transparency	Regular spacing Layer structure of collagen reminiscent of plywood Narrow size distribution of fibrils diameter (~ 30 nm)

Table I-1 : Required mechanical and structural properties of tissue-like materials

Altogether a wide variety of molecules, being natural or synthetic, are available or can be designed for the development of tissue engineering scaffolds. However, each targeted tissue has its own intrinsic properties, including its specific pathways of regeneration. Therefore, there is no universal scaffold and, even for the same targeted tissue or organs, requirements can depend on the origin and extent of the damages as well as on the patient age or health state. Thus for each situation, it is first important to precisely define the objectives of the therapeutic device and to set up adapted technical specifications. In the following section, we will focus on peripheral nerve regeneration.

2.3. A concrete example: peripheral nerve regeneration

Our nervous system is mainly composed of two parts: the central nervous system (CNS, brain and spinal cord) and peripheral nerve systems (PNS, nerves). PN tissues are able to regenerate by themselves when the gaps after injuries are smaller than 6 mm. For larger gaps, a graft is usually required, but with the drawbacks detailed above. In addition, in the case of PN, there is the possibility of generating a painful neuroma (*i.e.* tumor of nervous tissue) on the injured zone or on the site of the organ removal.[28-30]

PN are composed of highly ordered and aligned bundles of axons. Consequently, to help the regeneration, bioengineered devices should be longitudinally oriented to provide the physical support to bridge gap and contact guidance for neurite regrowth, while maintaining the biological functionality.[101] The ECM of PNS will be detailed in chapter IV.

PN scaffold materials have been synthesized from many synthetic or biological materials.[102] For example, Neurotube®, made of poly(glycolic acid) (PGA) has been approved by governmental regulation authorities and is currently commercialized. This device allows to get comparable result to autografts in the treatment of lesions with a maximum length of 3 cm and a small diameter, but do not allow a complete functional recovery, especially for more extensive injuries.[103] Interesting results have also been obtained with polyaminodoamines (PAA) *in vivo* on animal models but for a maximum of 5 mm gap injury on PN. This material shows interesting elasticity properties and helps to improve axon size and density.[104] With a rigid material from poly(lactic-co-glycolic acid)(PLGA),[105,106], axons with large diameters were obtained leading to thick myelin sheaths. PN regeneration has also been nicely evidenced *in vitro* with aligned polymer fiber-based constructs, such as poly(acrylonitrile-co-methylacrylate)[107] or polycaprolactone (PCL).[108] With the latter, confocal microscopy images show that the direction of neurite out-growth from the cell body on 5 μm PCL fibers corresponds to the direction of fiber alignment (see arrow, Figure I-4-A1-2).[108] On the contrary, as expected, neurite out-growth was observed in random directions on flat substrates (Figure I-4-A3). However, synthetic materials can induce inflammatory reactions and be rejected by the body.[109]

Figure I-4 : A1) SEM image of 5 μm electrospun PCL fibers, and confocal microscopy images of NG108-15 neuronal cells immunocytochemically-labelled for beta-III tubulin after 4 days culture in serum free medium (A2) on 5 μm PCL fibers and (A3) on flat PCL film (adapted from [108]). (B1) Scheme of an IKVAV-containing peptide amphiphile and its self-assembly into nanofibers. (B2) SEM image of the aligned nanofiber structure, and (B3) fluorescence microscopy image of hippocampal neurons cultured on the aligned scaffold for seven days and stained for b-III-tubulin (green), GFAP (red), and DAPI (blue) revealing extensive aligned neurite growth, adapted from[44,45].

Numerous studies have been using biological materials as an interesting scaffold for PN regeneration.[59–61] We will here focus on the use of type I collagen, the major component of the ECM, and its processing into aligned scaffolds.[104,110] Among the aligned collagen-based scaffolds reported to date, NeuraGen® is a conduit that was the first approved from the Food and Drug Administration (FDA) in 2001. In this biomaterial, the fibrillar structure of collagen is preserved throughout the whole process, giving rise to a biocompatible matrix with mechanical strength similar to the native collagen, defined permeability and controlled rate of resorption.[111,112] As described by Stang and co-workers,[113] and more recently by Pandit and co-workers,[105,114] the wall structure, the thickness of the scaffold, its porosity and alignment, as well as its inner structure and diameter of the fibers are important parameters to consider. The regeneration is enhanced with porous small-diameter grafts and well-aligned fibers.

Importantly, the integration of bioactive molecules within the scaffold has a strong influence on cell attachment, proliferation and differentiation. Concentration gradients of biomolecules, such as neurotrophic factors, have been shown to guide axonal growth.[115] Since then, the incorporation of bioactive molecules within anisotropic scaffolds for tissue engineering has gathered a lot of research interest.[116,117] From a functional point of view, of particular interest for PN regeneration is the development of synthetic nanofiber scaffolds from laminin proteins, one of the previously described ECM components.[28,29] Laminin is continuously synthesized after nerve injury[118] and plays a crucial role in cell migration, differentiation and axonal growth.[29,119] Laminins are key proteins possessing cell-binding domains such as IKVAV peptide that facilitate neurite extension[120] and cell adhesion *in vivo* and *in vitro*.[121] Therefore, scaffolds made of biomacromolecules or synthetic polymer scaffolds have been functionalized with laminin adhesive peptides, guiding cell adhesion and inducing neurite outgrowth.[46–48]

Alternatively, self-assemblies of peptide amphiphiles derived from laminin bioactive motifs have been shown by Stupp and coworkers to rapidly and predictably control cell differentiation.[44] This laminin-derived epitope is a pentapeptide having the IKVAV sequence. Moreover, IKVAV-based aligned peptide assemblies are very efficient scaffolds to guide the growth of oriented neurites and the direction of cell migration (Figure I-4-B).[45] In parallel, the Stupp group described the engineering of biomaterials combining collagen with the epitope-based peptide amphiphile nanofibers.[122] With such a synthetic co-assembled matrix, they show how to support neuronal survival and morphogenesis, while easily adjusting the epitope density and the mechanical properties of the resulting matrix. The design of the biomaterials could be even more sophisticated by creating IKVAV gradients, enhancing axonal guidance.[123]

Another possible strategy to functionalize scaffolds with bioactive epitopes is to conjugate these to exogeneous carriers that are dispersed in the macromolecular network, following a composite approach.

3. Bionanocomposites for tissue regeneration

3.1. What is a bionanocomposite?

Nanocomposites are materials associating at least two distinct phases that differ in composition and form, one of them being at the nanoscale.[124] The purpose of elaborating such materials is to retain their identities and properties while interacting at their interface, and add up new functionalities. Ideally, synergetic effects are created between the two components. From a structural point of view, composites can be constituted of fibers, layers or particles in a matrix. One option is to combine an inorganic component with an organic one, usually inorganic nanoparticles dispersed in a polymer matrix.[124,125] Typically, the continuous phase provides elasticity, embedding the inorganic components. When the polymer part is a biological macromolecule, such as a protein, a polysaccharide or a nucleic acid, the material is called a bionanocomposite. While biopolymers often combine hierarchical structure with biocompatibility, bioactivity and responsiveness, they often lack chemical and physical stability. In parallel, inorganic colloids exhibit many functional properties to design conductive, optical or magnetic devices but most of them exhibit unfavorable interactions with living systems and their processing at the macroscale is a real issue (Table I-2).

Bionanocomposites can be found in nature, such as in sea shell and bones.[126,127] The association of the organic and inorganic phases combines their properties : the resilience, stability, responsiveness, modularity and multifunctionality.[124] These materials are an inspiration to engineer innovative materials.

	Advantages	*Shortcomings*
Inorganic colloids	Functional properties (optical, magnetic, conductive, mechanical and bioactive)	Unfavorable interactions with living systems
	Thermal, chemical, physical stability	Harsh synthesis condition (pH, organic solvent, temperature and pressure)
	Controlled porosity	
	Versatile surface functionalization	
Biopolymers	Renewable resource (limited environmental impact)	Low mechanical strength
	Favorable interactions with living systems	High degradation rate
	Chemical and structural diversity	Preformed polymers
	Hierarchically organized structures	
	Dynamic properties	
	Molecular recognition and bioresponsiveness	

Table I-2 : Interesting benefits and shortcomings of biomacromolecules and inorganic colloids, adapted from [125].

3.2. Nanoparticles

3.2.1. Definition and properties

Nanoparticles and colloids are isolated objects with at last one dimension in the nanoscale. The International Organization for standardization defines nanoparticles as nano-objects with a size in between 1 nm and 100 nm.[128] However, it exists some controversy about this definition and, practically, nanoparticles are usually defined as objects with dimension below 1 µm. It will be the definition employed in the following.

Nanoparticles can be organic or inorganic. Organic materials usually include elements such as carbon, hydrogen, oxygen, nitrogen, sulfur, phosphorus and halides, when all other compounds are considered as inorganic. Though, the barrier is not strongly defined between the two classifications, and for example carbon-only materials are usually classified as inorganic.[129]

Depending on their chemical composition, nanoparticles have interesting properties for a wide range of applications, such as optical, magnetic, antibacterial…[130] This is particularly well-known and used for inorganic particles.

The high ratio between the number of atoms at the surface and the number of atoms in the core of a nanoparticle is at the origin of some of the specific properties of nanoparticles in comparison with the bulk material.[130] This large number of surface atoms create a great number of adsorption/reaction sites that are available to interact with the surrounding environment.[131] Curvature effects may also impact the reactivity of nanosurfaces. Quantum confinement effects are observed when the size of the particle is small enough to restrict for charge carriers inside the particle (electron and hole). It modifies the energies level occupied by electrons, and consequently may affect the electronic and optical properties of the material. Additionally, other modified properties (e.g. magnetic properties) can be exhibited in comparison with the bulk element.[132,133]

3.2.2. Synthesis of inorganic nanoparticles

Nanoparticles can be synthesized by top-down or bottom-up strategies. In the top-down approach, large objects are converted by mechanical forces or irradiation into smaller ones (e.g. by fragmentation, etching or lithography).[134,135] However, the disadvantage of the top-down approach to synthesize nanoparticles is the large distribution and poor morphological control in case of mechanical procedure, or time and energy consuming process for lithography techniques.

The bottom-up strategy is the opposite approach. From small objects (i.e. atoms, ions or molecules) larger structures are built, by keeping a control over the size of the resulting nanoscale object. The synthesis can occur in gas or liquid, and is performed in two steps: (1) a nucleation phase, were the first object form a small and stable assembly; and (2) a growth phase, by adding precursors at the surface of the nuclei or by associating nuclei together. The synthesis stops when there is no longer precursor available or the surface reactivity is no longer high enough for the reaction. This process is ruled by thermodynamic law. The key parameters to control the size and dispersity of the nanoparticles are the concentration, the surface reactivity, the temperature and stirring.[132]

As an example, we shortly introduce the use of the sol-gel process to synthesize metal oxide nanomaterials. This inorganic polymerization from a metal ion M^{z+} or an alcoolate

$M\text{-}(O\text{-}R)_n$ can occur in aqueous solution or in organic solvents and includes in both cases two steps (1) hydroxylation and (2) condensation.[136]

(1) hydroxylation of the precursor to create M-OH bonds or $M\text{-}O^-$ bonds
(2) condensation process leading to the departure of a water molecule:
$M\text{-}OH + M\text{-}OH \rightarrow M\text{-}O\text{-}M + H_2O$
$M\text{-}OH + M\text{-}O\text{-}R \rightarrow M\text{-}O\text{-}M + R\text{-}OH$

Condensed species are linked by oxygen atoms. Reaction parameters (pH, temperature…) need to be adjusted to get nanoparticle *via* this sol-gel process. One typical synthesis method using this sol-gel route is the Stöber process.[137] From tetraethylorthosilicate $Si(OC_2H_5)_4$ (TEOS), silica nanoparticles with tunable size can be obtained in ethanol solution with basic catalysis.[138]

3.2.3. Biofunctionalization of inorganic nanoparticles

Nanoparticles have a wide range of applications in the biomedical field, such as targeted drug delivery, hyperthermia, bioimaging and biosensors.[139,140] Some of these applications need a biofunctionalization of the surface of the nanoparticles. The conjugation of biomolecules at the surface to create hybrid particles allowed to target a receptor at the surface of cells, to improve their colloidal stability or to interact with objects of interest and display information to the cell for example. The large surface-to-volume ratio of nanoparticles enable a large number of molecules to be grafted at the surface. The molecules can be covalently linked at the surface of the particles (peptide linkage, click chemistry…) or be stabilized at the surface by electrostatic interactions.[141–143]

Silica nanoparticle and other hydroxylated surfaces can be functionalized with silicon-based functional reagents. Commercially available alkoxysilanes can be grafted *via* Si–O–Si bonds to the surface in a condensation reaction with the surface silanol groups. Many kinds of groups can be displayed at the surface of the particles such as amines, polyethylene glycol or thiols. They can be further used for the conjugation of biomolecules.[141,144]

Because of the diversity of the chemical nature, the numerous possibilities of functionalization and their intrinsic physical properties, inorganic nanoparticles are ideal building blocks to be incorporated within nanocomposites to enhance their functionality. However, those approaches can be extended to organic particles, especially that interesting progresses have been realized in the last decades.[145]

3.3. From nanoparticle to bionanocomposite

3.3.1. Bionanocomposite engineering

Bionanocomposites can by synthesized following different procedures. The first one is a mechanical mixing between the two phases in solution (Figure I-5-A).[125] The gelation of the resulting material is induced only after mixing the nanoparticles with the biopolymer. The great advantage of this method is that the nanoparticles are already synthesized at the required size with the appropriate functionalization. Additionally, the conditions of nanoparticle synthesis are regularly not ideal to preserve the native state of the biopolymer (e.g. aggressive pH, solvents, temperature…). The main shortcoming of this method is to reach a good dispersion of the nanoparticles in the matrix in solution, with an increasing difficulty when the polymer is viscous, for example at high concentration or because of the interactions with nanoparticles.[146] Inhomogeneity in the nanocomposite is an issue for its characterization and application. The inorganic compounds need to be stable in the biopolymer mixing medium and under the gelation conditions, such as change in the pH (collagen), temperature (gelatin) or addition of crosslinking agents (alginate).

Another approach consists in using the biopolymer as a template to synthesize the inorganic nanoparticles within the matrix (Figure I-5-B).[125,147] The particle precursors (typically ions) are dispersed in the polymer, usually before gelation. By modifying the external conditions, they are converted into inorganic colloids, with limited issues in their dispersion.

Similarly, bifunctional ions can be inserted within the biopolymer matrix and that can act both as inorganic nanoparticle precursors and network cross-linkers (Figure I-5-C).[125] In this case, ions have a key role in hydrogel formation and become afterward precursors for the templated synthesis of inorganic particles.

In the above detailed strategies to elaborate bionanocomposites, the bio/inorganic interface between the biomacromolecule and the particle surface has to be subtly defined and investigated to fit the required molecular and supramolecular features of the composite. Indeed, the presence of inorganic colloids may disturbe the formation of the hydrogel. This will depend on the particle/polymer ratio, the surface chemistry of the particles and the synthesis conditions.

Figure I-5 : Schematic representation of bionanocomposite synthesis by (A) mechanical mixing, (B) *in situ* synthesis of particles and (C) *in situ* synthesis of particles as crosslinkers (adapted from[125]).

3.3.2. Application as a biomaterial

Combining two (or more) elements provide a high modularity in the composition, structure, properties and function of bionanocomposites. This is of particular interest in the biomaterials field. To illustrate the richness of possibilities, two examples will be exposed in the following section.

Ayutsede and coworkers have associated silk fibers with single-walled carbon nanotubes (SWNT) *via* electrospinning process in an attempt to increase the mechanical properties of the fibers.[148] The modulation of the mechanical properties of the SWNT-reinforced nanofibers may have an effect on the transfer of mechanical stimuli to the cells, important for tissue regeneration. Moreover, SWNT have exceptional electrical properties, which can be an interesting new property for materials in tissue regeneration, in particular for nerve regeneration. However, the challenge remains in mixing the two components in solution before the electrospinning process (Figure I-6-A-B). Indeed, SWNTs have a poor solubility in aqueous solution and organic solvent. The dispersion, driven by steric and hydrophobic effects between silk and SWNT, is quite poor. After electrospinning, the conformation of the silk is conserved as shown by FTIR. In addition, Young's modulus was found to be up to 460% in comparison with as-spun fibers but hampering the strength and strain to failure. The initial Young's modulus of the as-spun aligned fibers (calculated from the slope of the initial part of the stress-strain curve) was 337 MPa at a breaking strain of 4.6% (Figure I-6-C). The 0.5 and 2% SWNT reinforced fibers have a lower modulus in comparison with the aligned as-spun fibers, probably because of a poor dispersion and imperfect alignment of the nanotubes. However, the 1% SWNT reinforced fibers increases the initial modulus in the range of 110-460%, which can be due to a more uniform distribution and alignment of SWNT along the nanofibers. This is an interesting example of successful engineering of a bionanocomposite, even if the SWNT-silk interactions have to be better understood and controlled. Identifying the optimal interfacial stress transfer conditions of the composite could allow to fully reach their potential applications.

Figure I-6 : SEM photos of 1% SWNT-reinforced electrospun silk fibers: (A) aligned and (B) randomly distributed. (C) Typical stress-strain curves of aligned SWNT-reinforced and unreinforced fibers (adapted from [148]). (D) SEM photo of chitosan/β-TCP/glass composite scaffolds with the weight ratio 90/5/5. (E) Release profile of gentamicin sulfate released from (1) the pure chitosan scaffold and chitosan/β-TCP/glass composite scaffolds with the weight ratio equal to (2) 90/10/0, (3) 90/5/5, (4) 90/0/10; mean ± S.D. (n = 3). (F) SEM photo of MG63 cells after 5 days of culture on the chitosan/β-TCP/glass composite scaffolds, with the weight ratio equal to 90/5/5 (adapted from [149]).

In the area of hard tissue repair, Zhang and coworkers have developed a chitosan scaffold reinforced by β-tricalcium phosphate (β-TCP) and calcium phosphate glasses (Figure I-6-D).[149] Chitosan is a polysaccharide, found in crustacean shells. The porous matrix of chitosan is interesting for tissue regeneration, especially when mixed with calcium phosphate, a chemical component similar to the mineral phase of natural bones. In a previous work, the authors already reported that β-TCP and calcium phosphate invert glasses were interesting powder fillers to reinforce the chitosan scaffold.[150] In this study, they additionally show that incorporating β-TCP and glass into the chitosan matrix improved the drug delivery function of the material. It effectively reduced the initial burst release of gentamicin-sulfate (GS), an antibiotic used for osteomyelitis, a common bone disease caused by bacterial infection of bone (Figure I-6-E). It is possible according to the FTIR and SEM results that the controlled release of GS is allowed by the strong crosslinking in the composite between amine groups of chitosan and phosphate ions. Moreover, cell culture of MG63 osteoblast-like cells on the composite scaffolds demonstrated growth and migration into the scaffolds (Figure I-6-F). In addition to being a controlled drug carrier material, these materials have suitable properties to be a bone substitute and become a scaffold for bone tissue regeneration.

3.4. Silica nanoparticle – collagen bionanocomposites

3.4.1. Why combining silica and collagen?

Collagen type I is the most abundant component of the ECM. It is an ideal polymer to synthesize biomaterials for tissue regeneration. Collagen can be directly obtained from decellularized native tissue.[151] However, if any cell is still present it can result in complications for the patient. An alternative is to extract collagen, in acidic medium, and trigger fibrillogenesis after purification. Currently an effort to produce large scale recombinant human collagen from yeast, insect cells and plants has been engaged. This allows to prevent batch to batch differences and impurities of extracted collagen. Moreover, it enables to eliminate most concerns about pathogen contamination from animal sources.[152] The formation of fibrils and afterwards fibers is possible for example by neutralizing the collagen with a buffer solution, or increasing the pH under basic vapors.

Collagen is frequently associated with hydroxyapatite for bone regeneration,[153,154] or with silica. Silicon, the most prevalent element on earth can be found in its oxidized form SiO_2 either crystallized (quartz is the most abundant mineral in the earth's crust) or amorphous (in diatoms, sponges, and other organisms).[155] It can be an interesting component to synthesize biomaterials.[156] Silica can improve the stiffness, modify the architecture of collagen network, encapsulate cells and allow controlled drug delivery.

One of the first parameter to check is the cytotoxicity of silica. Its biocompatibility depends on the form under which it is incorporated: gel, film, nanoparticle. Silica is generally considered as weakly cytotoxic, especially as bulk or xerogel. However, even if silica nanoparticles (SiNPs) have been used for years as additives for drugs and food, controversies exist about their safety.[157,158] Studies underlined the strong correlation between SiNP size, charge and porosity on the cytotoxicity, along with the cell type, on the potential toxicity of the SiNPs.[159] In our group, a low cytotoxicity has been evidenced in Normal Human Dermal Fibroblast cells when using bare SiNPs of diameters 60 nm or higher.[160]

Collagen and silica combined within bionanocomposites are interesting scaffolds for tissue engineering.[156] Numerous possibilities exist to combine silica and collagen, modulating the mechanical properties and structural characteristics of the composite, as represented on Figure I-7.

Figure I-7 : Possible combinations of silica and collagen to form a bionanocomposite with their respective characteristics and applications, from[156].

In this process, silica precursors can be added only in a controlled amount to avoid disturbing collagen self-assembly and fibrillation.[161]

3.4.2. Collagen- Silica for tissue engineering

Multiple investigations have been conducted with collagen-silica bionanocomposites for bone, nerve or dermis regeneration.[156,162,163] Two examples have been selected to present the possibilities.

Heinemann and co-workers have reported on the synthesis of a monolithic silica-collagen hybrid xerogels for bone repair.[164] Interestingly, the bovine collagen is used as an organic template for the silicification *in vitro*. The prehydrolysed silica precursor, TEOS, is mixed with a homogenous collagen suspension in acidic medium. After collagen fibrillation in buffer solution at pH 9, the sol-gel reaction occurs, forming silica particles that aggregate in a three-dimensional network. Interaction between negatively-charged silica species and the protonated, positively-charged amine groups of the collagen determine the formation of the hydrogel. By evaporation, a monolithic hybrid xerogel is created with remarkable mechanical properties (SEM, Figure I-8-A). After 14 days of culture, human mesenchymal stem cells of a donor become differentiated into osteoblast-like cells that form a dense layer covering the xerogel surface (Figure I-8-B-C). The hybridation allowed to improve the stability and stiffness of the material, enhancing the adhesion, proliferation and osteogenic differentiation of human mesenchymal stem cells. This xerogel could be an interesting material to provide an alternative of clinical substitution of hard tissue.

Figure I-8 : (A) SEM photos of the silica-collagen hybrid xerogel 1 day after seeding human mesenchymal stem cells. Laser scanning microscopy image of (B) human mesenchymal stem cells seeded on the silica-collagen hybrid xerogel leading to proliferation in dense cell agglomerates after 14 days. (C) The same region shows distinct activity of alkaline phosphatase due to osteogenic differentiation (adapted from[164]).

Alternatively, Jing and coworkers have proposed to combine SiNPs and collagen to create a porous scaffold for peripheral nerve regeneration.[162] Commercial SiNPs (*ca.* 150-190 nm in diameter) were mixed with pre-fibrillated collagen and the resulting composite scaffold was lyophilized. SEM characterization shows that SiNPs were successfully integrated and homogeneously distributed. Their incorporation modifies the characteristics of the scaffold. While the interconnected porous microstructure was preserved, the hydrophilicity, porosity and swelling ratio were found to be significantly decreased, leading to a decrease in the degradation rate of the materials (Figure I-9-A-C,1-2).

The possible application of this scaffold for peripheral nerve regeneration has been tested by Schwann cells culture. Schwann cells were able to penetrate into the scaffold with a homogeneous distribution. The proliferation of cells in the collagen/silica composite scaffolds, measured by the number of cells and the DNA content, increased firstly and then decreased with the concentration increase of incorporated SiNPs (Figure I-9-A-C, 3). The decrease is attributed to the cytotoxicity caused by high amount of SiNPs. These interesting results indicate that silica modulates the structure of the porous collagen patch and could become a potential scaffold material for the peripheral nerve regeneration.

Figure I-9 : Porous (A) pure collagen scaffolds, (B) collagen-SiNP scaffold at 50 µg.mL^{-1} and (C) 100 µg.mL^{-1}. 1,2- SEM images and 3- Optical images of Schwann cells cultured in the scaffolds (adapted from[162]).

In this PhD work, we have focused on the engineering of new biomaterials for regenerative medicine and investigated how we could tune the structural and biochemical properties of such materials to instruct cells. With this purpose, we have designed bionancomposites associating collagen and SiNPs. A synthetic alternative to collagen, peptide amphiphiles, has also been considered, in combination with SiNPs. Fibroblasts and neuron-like PC12 cells were used to evaluate the biological activity of these materials. All along these studies, a constant interest has been devoted to the control of the hierarchical structure of collagen and the surface chemistry of SiNPs using diverse strategies. Our final objective was to provide new tools for tissue engineering.

4. References

(1) Frantz, C.; Stewart, K. M.; Weaver, V. M. The Extracellular Matrix at a Glance. *Journal of Cell Science* **2010**, *123* (24), 4195–4200.

(2) Theocharis, A. D.; Skandalis, S. S.; Gialeli, C.; Karamanos, N. K. Extracellular Matrix Structure. *Advanced Drug Delivery Reviews* **2016**, *97*, 4–27.

(3) Hay, E. D. *Cell Biology of Extracellular Matrix: Second Edition*, Springer Science & Business Media.; 2013.

(4) Daley, W. P.; Peters, S. B.; Larsen, M. Extracellular Matrix Dynamics in Development and Regenerative Medicine. *Journal of Cell Science* **2008**, *121* (3), 255–264.

(5) Yue, B. Biology of the Extracellular Matrix: An Overview. *J Glaucoma* **2014**, S20–S23.

(6) Bosman, F. T.; Stamenkovic, I. Functional Structure and Composition of the Extracellular Matrix. *The Journal of Pathology* **2003**, *200* (4), 423–428.

(7) Järveläinen, H.; Sainio, A.; Koulu, M.; Wight, T. N.; Penttinen, R. Extracellular Matrix Molecules: Potential Targets in Pharmacotherapy. *Pharmacol Rev* **2009**, *61* (2), 198–223.

(8) Nishida, T.; Yasumoto, K.; Otori, T.; Desaki, J. The Network Structure of Corneal Fibroblasts in the Rat as Revealed by Scanning Electron Microscopy. *Invest. Ophthalmol. Vis. Sci.* **1988**, *29* (12), 1887–1890.

(9) Myllyharju, J. Collagens, Modifying Enzymes and Their Mutations in Humans, Flies and Worms. *Trends in Genetics* **2004**, *20* (1), 33–43.

(10) Myllyharju, J.; Kivirikko, K. I. Collagens and Collagen-Related Diseases. *Annals of Medicine* **2001**, *33* (1), 7–21.

(11) Gordon, M. K.; Hahn, R. A. Collagens. *Cell Tissue Res* **2010**, *339* (1), 247–257.

(12) Rozario, T.; DeSimone, D. W. The Extracellular Matrix In Development and Morphogenesis: A Dynamic View. *Dev Biol* **2010**, *341* (1), 126–140.

(13) Gross, J.; Kirk, D. The Heat Precipitation of Collagen from Neutral Salt Solutions: Some Rate-Regulating Factors. *J Biol Chem* **1958**, *233* (2), 355–360.

(14) Jackson, D. S.; Fessler, J. . Isolation and Properties of a Collagen Soluble in Salt Solution at Neutral PH. *Nature* **1955**, *179*, 69–70.

(15) Mosser, G.; Anglo, A.; Helary, C.; Bouligand, Y.; Giraud-Guille, M.-M. Dense Tissue-like Collagen Matrices Formed in Cell-Free Conditions. *Matrix Biology* **2006**, *25* (1), 3–13.

(16) Picaut, L. Synthèse d'un Tendon Artificiel, Université Pierre et Marie Curie: Paris, 2017.

(17) Heino, J. The Collagen Family Members as Cell Adhesion Proteins. *BioEssays* **2007**, *29* (10), 1001–1010.

(18) Yamauchi, M.; Sricholpech, M. Lysine Post-Translational Modifications of Collagen. *Essays In Biochemistry* **2012**, *52*, 113–133.

(19) Williams, B. R.; Gelman, R. A.; Poppke, D. C.; Piez, K. A. Collagen Fibril Formation. Optimal in Vitro Conditions and Preliminary Kinetic Results. *Journal of Biological Chemistry* **1978**, *253* (18), 6578–6585.

(20) Pankov, R. Fibronectin at a Glance. *Journal of Cell Science* **2002**, *115* (20), 3861–3863.

(21) Dalton, P. D. Neural Interactions with Materials. *Frontiers in Bioscience* **2009**, *Volume* (14), 769–795.

(22) Xu, J.; Mosher, D. Fibronectin and Other Adhesive Glycoproteins. In *The Extracellular Matrix: an Overview*; Mecham, R. P., Ed.; Springer Berlin Heidelberg: Berlin, Heidelberg, 2011; pp 41–75.

(23) Lodish, H.; Berk, A.; Zipursky, S. L.; Matsudaira, P.; Baltimore, D.; Darnell, J. *Molecular Cell Biology*, 4th ed.; W. H. Freeman, 2000.

(24) Alberts, B.; Johnson, A.; Lewis, J.; Raff, M.; Roberts, K.; Walter, P. *Molecular Biology of the Cell*, 4th ed.; Garland Science, 2002.

(25) Bellis, S. L. Advantages of RGD Peptides for Directing Cell Association with Biomaterials. *Biomaterials* **2011**, *32* (18), 4205–4210.

(26) Aota, S.-I.; Nomizu, M.; Yamada, K. M. The Short Amino Acid Sequence Pro-His-Ser-Arg-Asn in Human Fibronectin Enhances Cell-Adhesive Function. *Journal of Biological Chemistry* **1994**, *269* (40), 24756–24761.

(27) Ochsenhirt, S.; Kokkoli, E.; Mccarthy, J.; Tirrell, M. Effect of RGD Secondary Structure and the Synergy Site PHSRN on Cell Adhesion, Spreading and Specific Integrin Engagement. *Biomaterials* **2006**, *27* (20), 3863–3874.

(28) Timpl, R.; Rohde, H.; Robey, P. G.; Rennard, S. I.; Foidart, J.-M.; Martin, G. R. Laminin– a Glycoprotein from Basement Membranes. *Journal of Biological Chemistry* **1979**, *254* (19), 9933–9937.

(29) Rutka, J. .; Apodaca, G.; Stern, R.; Rosenblum, M. The Extracellular Matrix of the Central and Peripheral Nervous Systems: Structure and Function. *J Neurosurg* **1988**, *69*, 155–170.

(30) O'Brien, F. J. Biomaterials & Scaffolds for Tissue Engineering. *Materials Today* **2011**, *14* (3), 88–95.

(31) Wu, J.; Chiu, D. T. W. Painful Neuromas: A Review of Treatment Modalities. *Ann. Plas. Surg.* **1999**, *43*, 661–667.

(32) Marinescu, S.-A.; Zărnescu, O.; Mihai, I.-R.; Giuglea, C.; Sinescu, R. D. An Animal Model of Peripheral Nerve Regeneration after the Application of a Collagen-Polyvinyl

Alcohol Scaffold and Mesenchymal Stem Cells. *Rom J Morphol Embryol* **2014**, *55* (3), 891–903.

(33) Mackinnon, S. E.; Hudson, A. R. Clinical Application of Peripheral Nerve Transplantation. *Plast. Reconstr. Surg.* **1992**, *90* (4), 695–699.

(34) Lanza, R.; Langer, R.; Vacanti, J. *Principles of Tissue Engineering - 2nd Edition*; Elsevier; 2000.

(35) Vert, M.; Doi, Y.; Hellwich, K.-H.; Hess, M.; Hodge, P.; Kubisa, P.; Rinaudo, M.; Schué, F. Terminology for Biorelated Polymers and Applications (IUPAC Recommendations 2012). *Pure and Applied Chemistry* **2012**, *84* (2), 377–410.

(36) Huebsch, N.; Mooney, D. J. Inspiration and Application in the Evolution of Biomaterials. *Nature* **2009**, *462* (7272), 426–432.

(37) Hollister, S. J. Porous Scaffold Design for Tissue Engineering. *Nature Materials* **2005**, *4* (7), 518–524.

(38) Engler, A. J.; Sen, S.; Sweeney, H. L.; Discher, D. E. Matrix Elasticity Directs Stem Cell Lineage Specification. *Cell* **2006**, *126* (4), 677–689.

(39) Weadock, K.; Olson, R. M.; Silver, F. H. Evaluation of Collagen Crosslinking Techniques. *Biomaterials, Medical Devices, and Artificial Organs* **1983**, *11* (4), 293–318.

(40) Xiao, S.; Stacklies, W.; Cetinkaya, M.; Markert, B.; Gräter, F. Mechanical Response of Silk Crystalline Units from Force-Distribution Analysis. *Biophysical Journal* **2009**, *96* (10), 3997–4005.

(41) Xu, H. H. K.; Sun, L.; Weir, M. D.; Takagi, S.; Chow, L. C.; Hockey, B. Effects of Incorporating Nanosized Calcium Phosphate Particles on Properties of Whisker-Reinforced Dental Composites. *Journal of Biomedical Materials Research Part B: Applied Biomaterials* **2007**, *81B* (1), 116–125.

(42) Abbott, R. D.; Kaplan, D. L. Engineering Biomaterials for Enhanced Tissue Regeneration. *Current Stem Cell Reports* **2016**, *2* (2), 140–146.

(43) von der Mark, K.; Park, J.; Bauer, S.; Schmuki, P. Nanoscale Engineering of Biomimetic Surfaces: Cues from the Extracellular Matrix. *Cell and Tissue Research* **2010**, *339* (1), 131–153.

(44) Silva, G. A.; Czeisler, C.; Niece, K. L.; Beniash, E.; Harrington, D. A.; Kessler, J. A.; Stupp, S. I. Selective Differentiation of Neural Progenitor Cells by High-Epitope Density Nanofibers. *Science* **2004**, *303* (5662), 1352–1355.

(45) Berns, E. J.; Sur, S.; Pan, L.; Goldberger, J. E.; Suresh, S.; Zhang, S.; Kessler, J. A.; Stupp, S. I. Aligned Neurite Outgrowth and Directed Cell Migration in Self-Assembled Monodomain Gels. *Biomaterials* **2014**, *35* (1), 185–195.

(46) Matsuda, A.; Kobayashi, H.; Itoh, S.; Kataoka, K.; Tanaka, J. Immobilization of Laminin Peptide in Molecularly Aligned Chitosan by Covalent Bonding. *Biomaterials* **2005**, *26* (15), 2273–2279.

(47) Rangappa, N.; Romero, A.; Nelson, K. D.; Eberhart, R. C.; Smith, G. M. Laminin-Coated Poly (L-Lactide) Filaments Induce Robust Neurite Growth While Providing Directional Orientation. *Journal of biomedical materials research* **2000**, *51* (4), 625–634.

(48) Yu, T. T.; Shoichet, M. S. Guided Cell Adhesion and Outgrowth in Peptide-Modified Channels for Neural Tissue Engineering. *Biomaterials* **2005**, *26* (13), 1507–1514.

(49) Gabriel, M.; Nazmi, K.; Dahm, M.; Zentner, A.; Vahl, C.-F.; Strand, D. Covalent RGD Modification of the Inner Pore Surface of Polycaprolactone Scaffolds. *Journal of Biomaterials Science, Polymer Edition* **2012**, *23* (7), 941–953.

(50) Zan, X.; Sitasuwan, P.; Powell, J.; Dreher, T. W.; Wang, Q. Polyvalent Display of RGD Motifs on Turnip Yellow Mosaic Virus for Enhanced Stem Cell Adhesion and Spreading. *Acta Biomaterialia* **2012**, *8* (8), 2978–2985.

(51) Huang, J.; Ding, J. Nanostructured Interfaces with RGD Arrays to Control Cell–matrix Interaction. *Soft Matter* **2010**, *6* (15), 3395–3401.

(52) Maheshwari, G.; Brown, G.; Lauffenburger, D. A.; Wells, A.; Griffith, L. G. Cell Adhesion and Motility Depend on Nanoscale RGD Clustering. *J Cell Sci* **2000**, *113* (10), 1677–1686.

(53) Arnold, M.; Cavalcanti-Adam, E. A.; Glass, R.; Blümmel, J.; Eck, W.; Kantlehner, M.; Kessler, H.; Spatz, J. P. Activation of Integrin Function by Nanopatterned Adhesive Interfaces. *ChemPhysChem* **2004**, *5* (3), 383–388.

(54) Cavalcantiadam, E.; Micoulet, A.; Blummel, J.; Auernheimer, J.; Kessler, H.; Spatz, J. Lateral Spacing of Integrin Ligands Influences Cell Spreading and Focal Adhesion Assembly. *European Journal of Cell Biology* **2006**, *85* (3–4), 219–224.

(55) Banani, S. F.; Lee, H. O.; Hyman, A. A.; Rosen, M. K. Biomolecular Condensates: Organizers of Cellular Biochemistry. *Nature Reviews Molecular Cell Biology* **2017**, *18* (5), 285–298.

(56) Schense, J. C.; Hubbell, J. A. Three-Dimensional Migration of Neurites Is Mediated by Adhesion Site Density and Affinity. *Journal of Biological Chemistry* **2000**, *275* (10), 6813–6818.

(57) Kong, H. J.; Hsiong, S.; Mooney, D. J. Nanoscale Cell Adhesion Ligand Presentation Regulates Nonviral Gene Delivery and Expression. *Nano Letters* **2007**, *7* (1), 161–166.

(58) Babensee, J. E.; Anderson, J. M.; McIntire, L. V.; Mikos, A. G. Host Response to Tissue Engineered Devices. *Advanced Drug Delivery Reviews* **1998**, *33* (1–2), 111–139.

(59) Battiston, B.; Raimondo, S.; Tos, P.; Gaidano, V.; Audisio, C.; Scevola, A.; Perroteau, I.; Geuna, S. Chapter 11 Tissue Engineering of Peripheral Nerves. In *International Review of Neurobiology*; Elsevier, 2009; Vol. 87, pp 227–249.

(60) Ma, P. X. Biomimetic Materials for Tissue Engineering. *Advanced Drug Delivery Reviews* **2008**, *60* (2), 184–198.

(61) Yang, Y.; Ding, F.; Wu, J.; Hu, W.; Liu, W.; Liu, J.; Gu, X. Development and Evaluation of Silk Fibroin-Based Nerve Grafts Used for Peripheral Nerve Regeneration. *Biomaterials* **2007**, *28* (36), 5526–5535.

(62) Maurus, P. B.; Kaeding, C. C. Bioabsorbable Implant Material Review. *Operative Techniques in Sports Medicine* **2004**, *12* (3), 158–160.

(63) Lopes, M. S.; Jardini, A. L.; Filho, R. M. Poly (Lactic Acid) Production for Tissue Engineering Applications. *Procedia Engineering* **2012**, *42*, 1402–1413.

(64) Kutikov, A. B.; Song, J. Biodegradable PEG-Based Amphiphilic Block Copolymers for Tissue Engineering Applications. *ACS Biomaterials Science & Engineering* **2015**, *1* (7), 463–480.

(65) Echalier, C.; Jebors, S.; Laconde, G.; Brunel, L.; Verdié, P.; Causse, L.; Bethry, A.; Legrand, B.; Van Den Berghe, H.; Garric, X.; et al. Sol–gel Synthesis of Collagen-Inspired Peptide Hydrogel. *Materials Today* **2017**, *20* (2), 59–66.

(66) Yamazaki, C. M.; Asada, S.; Kitagawa, K.; Koide, T. Artificial Collagen Gels via Self-Assembly of de Novo Designed Peptides. *Biopolymers* **2008**, *90* (6), 816–823.

(67) Pires, M. M.; Przybyla, D. E.; Chmielewski, J. A Metal-Collagen Peptide Framework for Three-Dimensional Cell Culture. *Angewandte Chemie International Edition* **2009**, *48* (42), 7813–7817.

(68) O'Leary, L. E. R.; Fallas, J. A.; Bakota, E. L.; Kang, M. K.; Hartgerink, J. D. Multi-Hierarchical Self-Assembly of a Collagen Mimetic Peptide from Triple Helix to Nanofibre and Hydrogel. *Nature Chemistry* **2011**, *3* (10), 821–828.

(69) Freeman, R.; Boekhoven, J.; Dickerson, M. B.; Naik, R. R.; Stupp, S. I. Biopolymers and Supramolecular Polymers as Biomaterials for Biomedical Applications. *MRS Bulletin* **2015**, *40* (12), 1089–1101.

(70) Hartgerink, J. D.; Beniash, E.; Stupp, S. I. Peptide-Amphiphile Nanofibers: A Versatile Scaffold for the Preparation of Self-Assembling Materials. *Proceedings of the National Academy of Sciences* **2002**, *99* (8), 5133–5138.

(71) Pashuck, E. T.; Cui, H.; Stupp, S. I. Tuning Supramolecular Rigidity of Peptide Fibers through Molecular Structure. *Journal of the American Chemical Society* **2010**, *132* (17), 6041–6046.

(72) Zhang, S.; Greenfield, M. A.; Mata, A.; Palmer, L. C.; Bitton, R.; Mantei, J. R.; Aparicio, C.; de la Cruz, M. O.; Stupp, S. I. A Self-Assembly Pathway to Aligned Monodomain Gels. *Nature Materials* **2010**, *9* (7), 594–601.

(73) Stephanopoulos, N.; Ortony, J. H.; Stupp, S. I. Self-Assembly for the Synthesis of Functional Biomaterials. *Acta Materialia* **2013**, *61* (3), 912–930.

(74) Gazit, E. Self Assembly of Short Aromatic Peptides into Amyloid Fibrils and Related Nanostructures. *Prion* **2007**, *1* (1), 32–35.

(75) El-Ghannam, A. Bone Reconstruction: From Bioceramics to Tissue Engineering. *Expert Review of Medical Devices* **2005**, *2* (1), 87–101.

(76) Sheikh, Z.; Najeeb, S.; Khurshid, Z.; Verma, V.; Rashid, H.; Glogauer, M. Biodegradable Materials for Bone Repair and Tissue Engineering Applications. *Materials* **2015**, *8* (9), 5744–5794.

(77) Feng, X. Chemical and Biochemical Basis of Cell-Bone Matrix Interaction in Health and Disease. *Current Chemical Biology* **2009**, *3* (2), 189–196.

(78) Ushiki, T. Collagen Fibers, Reticular Fibers and Elastic Fibers. A Comprehensive Understanding from a Morphiligical Viewpoint. *Arch. Histol. Cytol.* **2002**, *65* (2), 109–126.

(79) MacNeil, S. Biomaterials for Tissue Engineering of Skin. *Materials Today* **2008**, *11* (5), 26–35.

(80) Chaudhari, A.; Vig, K.; Baganizi, D.; Sahu, R.; Dixit, S.; Dennis, V.; Singh, S.; Pillai, S. Future Prospects for Scaffolding Methods and Biomaterials in Skin Tissue Engineering: A Review. *International Journal of Molecular Sciences* **1974**, *17* (12), 1–31.

(81) Tidu, A. Synthèse d'une cornée artificielle à base de collagène I, Université Pierre et Marie Curie: Paris, 2016.

(82) Lv, S.; Dudek, D. M.; Cao, Y.; Balamurali, M. M.; Gosline, J.; Li, H. Designed Biomaterials to Mimic the Mechanical Properties of Muscles. *Nature* **2010**, *465* (7294), 69–73.

(83) Qazi, T. H.; Mooney, D. J.; Pumberger, M.; Geißler, S.; Duda, G. N. Biomaterials Based Strategies for Skeletal Muscle Tissue Engineering: Existing Technologies and Future Trends. *Biomaterials* **2015**, *53*, 502–521.

(84) Kumar, V. A.; Brewster, L. P.; Caves, J. M.; Chaikof, E. L. Tissue Engineering of Blood Vessels: Functional Requirements, Progress, and Future Challenges. *Cardiovascular Engineering and Technology* **2011**, *2* (3), 137–148.

(85) Zhang, W. J.; Liu, W.; Cui, L.; Cao, Y. Tissue Engineering of Blood Vessel. *Journal of Cellular and Molecular Medicine* **2007**, *11* (5), 945–957.

(86) Konig, G.; McAllister, T. N.; Dusserre, N.; Garrido, S. A.; Iyican, C.; Marini, A.; Fiorillo, A.; Avila, H.; Wystrychowski, W.; Zagalski, K.; et al. Mechanical Properties of Completely Autologous Human Tissue Engineered Blood Vessels Compared to Human Saphenous Vein and Mammary Artery. *Biomaterials* **2009**, *30* (8), 1542–1550.

(87) Ravi, S.; Chaikof, E. L. Biomaterials for Vascular Tissue Engineering. *Regenerative Medicine* **2010**, *5* (1), 107–120.

(88) Dahl, S. L. M.; Vaughn, M. E.; Niklason, L. E. An Ultrastructural Analysis of Collagen in Tissue Engineered Arteries. *Annals of Biomedical Engineering* **2007**, *35* (10), 1749–1755.

(89) Rieu, C.; Picaut, L.; Mosser, G.; Trichet, L. From Tendon Injury to Collagen-Based Tendon Regeneration: Overview and Recent Advances. *Current Pharmaceutical Design* **2017**, *23* (24), 3483-3506.

(90) Jung, H.-J.; Fisher, M. B.; Woo, S. L.-Y. Role of Biomechanics in the Understanding of Normal, Injured, and Healing Ligaments and Tendons. *BMC Sports Science, Medicine and Rehabilitation* **2009**, *1* (1), 1–17.

(91) Shah, J. S.; Palacios, E.; Palacios, L. Development of Crimp Morphology and Cellular Changes in Chick Tendons. *Developmental Biology* **1982**, *94* (2), 499–504.

(92) Murthy, N. S. Liquid Crystallinity in Collagen Solutions and Magnetic Orientation of Collagen Fibrils. *Biopolymers* **1984**, *23* (7), 1261–1267.

(93) Georgiou, M.; Bunting, S. C. J.; Davies, H. A.; Loughlin, A. J.; Golding, J. P.; Phillips, J. B. Engineered Neural Tissue for Peripheral Nerve Repair. *Biomaterials* **2013**, *34* (30), 7335–7343.

(94) Nectow, A. R.; Marra, K. G.; Kaplan, D. L. Biomaterials for the Development of Peripheral Nerve Guidance Conduits. *Tissue Engineering Part B: Reviews* **2012**, *18* (1), 40–50.

(95) Belanger, K.; Dinis, T. M.; Taourirt, S.; Vidal, G.; Kaplan, D. L.; Egles, C. Recent Strategies in Tissue Engineering for Guided Peripheral Nerve Regeneration. *Macromolecular Bioscience* **2016**, *16* (4), 472–481.

(96) Crompton, K. E.; Goud, J. D.; Bellamkonda, R. V.; Gengenbach, T. R.; Finkelstein, D. I.; Horne, M. K.; Forsythe, J. S. Polylysine-Functionalised Thermoresponsive Chitosan Hydrogel for Neural Tissue Engineering. *Biomaterials* **2007**, *28* (3), 441–449.

(97) *Scaffolding in Tissue Engineering*; Ma, P. X., Ed.; CRC/Taylor & Francis: Boca Raton, Fla., 2006.

(98) Zhang, H.; Uchimura, K.; Kadomatsu, K. Brain Keratan Sulfate and Glial Scar Formation. *Annals of the New York Academy of Sciences* **2006**, *1086* (1), 81–90.

(99) Hassell, J. R.; Birk, D. E. The Molecular Basis of Corneal Transparency. *Experimental Eye Research* **2010**, *91* (3), 326–335.

(100) Tidu, A.; Ghoubay-Benallaoua, D.; Lynch, B.; Haye, B.; Illoul, C.; Allain, J.-M.; Borderie, V. M.; Mosser, G. Development of Human Corneal Epithelium on Organized Fibrillated Transparent Collagen Matrices Synthesized at High Concentration. *Acta Biomaterialia* **2015**, *22*, 50–58.

(101) Bellamkonda, R. Peripheral Nerve Regeneration: An Opinion on Channels, Scaffolds and Anisotropy☆. *Biomaterials* **2006**, 3515–3518.

(102) Aijie, C.; Xuan, L.; Huimin, L.; Yanli, Z.; Yiyuan, K.; Yuqing, L.; Longquan, S. Nanoscaffolds in Promoting Regeneration of the Peripheral Nervous System. *Nanomedicine* **2018**, *13* (9), 1067–1085.

(103) Moore, A. M.; Kasukurthi, R.; Magill, C. K.; Farhadi, H. F.; Borschel, G. H.; Mackinnon, S. E. Limitations of Conduits in Peripheral Nerve Repairs. *HAND* **2009**, *4* (2), 180–186.

(104) Hoogenkamp, H. R.; Bakker, G.-J.; Wolf, L.; Suurs, P.; Dunnewind, B.; Barbut, S.; Friedl, P.; van Kuppevelt, T. H.; Daamen, W. F. Directing Collagen Fibers Using Counter-Rotating Cone Extrusion. *Acta Biomaterialia* **2015**, *12*, 113–121.

(105) Yao, L.; Daly, W.; Newland, B.; Yao, S.; Wang, W.; Chen, B. K. K.; Madigan, N.; Windebank, A.; Pandit, A. Improved Axonal Regeneration of Transected Spinal Cord Mediated by Multichannel Collagen Conduits Functionalized with Neurotrophin-3 Gene. *Gene Therapy* **2013**, *20* (12), 1149–1157.

(106) Nisbet, D. R.; Pattanawong, S.; Ritchie, N. E.; Shen, W.; Finkelstein, D. I.; Horne, M. K.; Forsythe, J. S. Interaction of Embryonic Cortical Neurons on Nanofibrous Scaffolds for Neural Tissue Engineering. *Journal of Neural Engineering* **2007**, *4* (2), 35–41.

(107) Kim, Y.; Haftel, V. K.; Kumar, S.; Bellamkonda, R. V. The Role of Aligned Polymer Fiber-Based Constructs in the Bridging Long Peripheral Nerve Gaps. *Biomaterials* **2008**, *29* (21), 3117–3127.

(108) Daud, M. F. B.; Pawar, K. C.; Claeyssens, F.; Ryan, A. J.; Haycock, J. W. An Aligned 3D Neuronal-Glial Co-Culture Model for Peripheral Nerve Studies. *Biomaterials* **2012**, *33* (25), 5901–5913.

(109) Zhu, W.; O'Brien, C.; O'Brien, J. R.; Zhang, L. G. 3D Nano/Microfabrication Techniques and Nanobiomaterials for Neural Tissue Regeneration. *Nanomedicine* **2014**, *9* (6), 859–875.

(110) Lai, E. S.; Anderson, C. M.; Fuller, G. G. Designing a Tubular Matrix of Oriented Collagen Fibrils for Tissue Engineering. *Acta Biomaterialia* **2011**, *7* (6), 2448–2456.

(111) Kehoe, S.; Zhang, X. F.; Boyd, D. FDA Approved Guidance Conduits and Wraps for Peripheral Nerve Injury: A Review of Materials and Efficacy. *Injury* **2012**, *43* (5), 553–572.

(112) LI, S.-T.; Archibald, S. J.; Krarup, C.; Madison, R. D. Peripheral Nerve Repair with Collagen Conduits. *Clinical Materials* **1995**, *9* (3–4), 195–200.

(113) Stang, F.; Fansa, H.; Wolf, G.; Reppin, M.; Keilhoff, G. Structural Parameters of Collagen Nerve Grafts Influence Peripheral Nerve Regeneration. *Biomaterials* **2005**, *26* (16), 3083–3091.

(114) Abu-Rub, M. T.; Billiar, K. L.; van Es, M. H.; Knight, A.; Rodriguez, B. J.; Zeugolis, D. I.; McMahon, S.; Windebank, A. J.; Pandit, A. Nano-Textured Self-Assembled Aligned Collagen Hydrogels Promote Directional Neurite Guidance and Overcome Inhibition by Myelin Associated Glycoprotein. *Soft Matter* **2011**, *7* (6), 2770–2781.

(115) Cao, X.; Shoichet, M. . Investigating the Synergistic Effect of Combined Neurotrophic Factor Concentration Gradients to Guide Axonal Growth. *Neuroscience* **2003**, *122* (2), 381–389.

(116) Dodla, M. C.; Bellamkonda, R. V. Anisotropic Scaffolds Facilitate Enhanced Neurite Extensionin Vitro. *Journal of Biomedical Materials Research Part A* **2006**, *78A* (2), 213–221.

(117) Labour, M.-N.; Banc, A.; Tourrette, A.; Cunin, F.; Verdier, J.-M.; Devoisselle, J.-M.; Marcilhac, A.; Belamie, E. Thick Collagen-Based 3D Matrices Including Growth Factors to Induce Neurite Outgrowth. *Acta Biomaterialia* **2012**, *8* (9), 3302–3312.

(118) Mcdonald, D.; Cheng, C.; Chen, Y.; Zochodne, D. Early Events of Peripheral Nerve Regeneration. *Neuron Glia Biology* **2005**, *2* (02), 139.

(119) luckenbill-Edds, L. Laminin and the Mechanism of Neuronal Outgrowth Luckenbilledds1997.Pdf. *Brain Research Reviews* **1997**, *23*, 1–27.

(120) Jucker, M.; Kleinman, H. K.; Ingram, D. K. Fetal Rat Septal Cells Adhere to and Extend Processes on Basement Membrane, Laminin, and a Synthetic Peptide from the Laminin A Chain Sequence. *Journal of neuroscience research* **1991**, *28* (4), 507–517.

(121) Graf, J.; Ogle, R. C.; Robey, F. A.; Sasaki, M.; Martin, G. R.; Yamada, Y.; Kleinman, H. K. A Pentapeptide from the Laminin B1 Chain Mediates Cell Adhesion and Binds to 67000 Laminin Receptor. *Biochemistry* **1987**, *26* (22), 6896–6900.

(122) Sur, S.; Pashuck, E. T.; Guler, M. O.; Ito, M.; Stupp, S. I.; Launey, T. A Hybrid Nanofiber Matrix to Control the Survival and Maturation of Brain Neurons. *Biomaterials* **2012**, *33* (2), 545–555.

(123) Adams, D. N.; Kao, E. Y.-C.; Hypolite, C. L.; Distefano, M. D.; Hu, W.-S.; Letourneau, P. C. Growth Cones Turn and Migrate up an Immobilized Gradient of the Laminin IKVAV Peptide. *Journal of Neurobiology* **2005**, *62* (1), 134–147.

(124) Urvoas, A.; Valerio-Lepiniec, M.; Minard, P.; Zollfrank, C. What Are Bionanocomposites? In *Bionanocomposites*; Wiley-Blackwell, 2017; pp 1–7.

(125) Aimé, C.; Coradin, T. Nanocomposites from Biopolymer Hydrogels: Blueprints for White Biotechnology and Green Materials Chemistry. *Journal of Polymer Science Part B: Polymer Physics* **2012**, *50* (10), 669–680.

(126) Vaz, M. F.; Canhão, H.; Fonseca, J. E. *Bone: A Composite Natural Material*, InTech.; Pavla Tesinova, 2011.

(127) Vijaya Ramnath, B.; Jeykrishnan, J.; Ramakrishnan, G.; Barath, B.; Ejoelavendhan, E.; Arun raghav, P. Sea Shells And Natural Fibres Composites: A Review. *Materials Today: Proceedings* **2018**, *5* (1), 1846–1851.

(128) Commission Recommendation of 18 October 2011 on the Definition of NanomaterialText with EEA Relevance. 3.

(129) York, A. P. E. Inorganic Fullerenes, Onions, and Tubes. *J. Chem. Educ.* **2004**, *81* (5), 673–676.

(130) Aimé, C.; Coradin, T. *Bionanocomposites: Integrating Biological Processes for Bio-Inspired Nanotechnologies.*, Wiley-VCH.; Hoboken USA, 2017.

(131) Fahlman, B. D. *Materials Chemistry*; Springer: Dordrecht, 2007.

(132) Aimé, C.; Coradin, T. Inorganic Nanoparticles. In *Bionanocomposites*; Wiley-Blackwell, 2017; pp 129–151.

(133) Willets, K. A.; Van Duyne, R. P. Localized Surface Plasmon Resonance Spectroscopy and Sensing. *Annual Review of Physical Chemistry* **2007**, *58* (1), 267–297.

(134) Biswas, A.; Bayer, I. S.; Biris, A. S.; Wang, T.; Dervishi, E.; Faupel, F. Advances in Top–down and Bottom–up Surface Nanofabrication: Techniques, Applications & Future Prospects. *Advances in Colloid and Interface Science* **2012**, *170* (1–2), 2–27.

(135) Yu, H.-D.; Regulacio, M. D.; Ye, E.; Han, M.-Y. Chemical Routes to Top-down Nanofabrication. *Chemical Society Reviews* **2013**, *42* (14), 6006–6018.

(136) Livage, J.; Sanchez, C.; Henry, M.; Doeuff, S. The Chemistry of the Sol-Gel Process. *Solid State Ionics* **1989**, *32–33*, 633–638.

(137) Stöber, W.; Fink, A.; Bohn, E. Controlled Growth of Monodisperse Silica Spheres in the Micron Size Range. *Journal of Colloid and Interface Science* **1968**, *26* (1), 62–69.

(138) Greasley, S. L.; Page, S. J.; Sirovica, S.; Chen, S.; Martin, R. A.; Riveiro, A.; Hanna, J. V.; Porter, A. E.; Jones, J. R. Controlling Particle Size in the Stöber Process and Incorporation of Calcium. *Journal of Colloid and Interface Science* **2016**, *469*, 213–223.

(139) McNamara, K.; Tofail, S. A. M. Nanoparticles in Biomedical Applications. *Advances in Physics: X* **2017**, *2* (1), 54–88.

(140) Caetano, B. L.; Guibert, C.; Fini, R.; Fresnais, J.; Pulcinelli, S. H.; Ménager, C.; Santilli, C. V. Magnetic Hyperthermia-Induced Drug Release from Ureasil-PEO-γ-Fe $_2$ O $_3$ Nanocomposites. *RSC Advances* **2016**, *6* (68), 63291–63295.

(141) Knežević, N. Ž.; Raehm, L.; Durand, J.-O. Hybrid Particles. In *Bionanocomposites*; Wiley-Blackwell, 2017; pp 153–168.

(142) Fang, C.; Bhattarai, N.; Sun, C.; Zhang, M. Functionalized Nanoparticles with Long-Term Stability in Biological Media. *Small 5* (14), 1637–1641.

(143) Lale, S. V.; R. G., A.; Aravind, A.; Kumar, D. S.; Koul, V. AS1411 Aptamer and Folic Acid Functionalized PH-Responsive ATRP Fabricated PPEGMA–PCL–pPEGMA Polymeric Nanoparticles for Targeted Drug Delivery in Cancer Therapy. *Biomacromolecules* **2014**, *15* (5), 1737–1752.

(144) Banga, R.; Yarwood, J.; Morgan, A. M.; Evans, B.; Kells, J. FTIR and AFM Studies of the Kinetics and Self-Assembly of Alkyltrichlorosilanes and (Perfluoroalkyl)Trichlorosilanes onto Glass and Silicon. *Langmuir* **1995**, *11* (11), 4393–4399.

(145) Bonduelle, C.; Oliveira, H.; Gauche, C.; Huang, J.; Heise, A.; Lecommandoux, S. Multivalent Effect of Glycopolypeptide Based Nanoparticles for Galectin Binding. *Chemical Communications* **2016**, *52* (75), 11251–11254.

(146) Oliveira, F.; Monteiro, S. R.; Barros-Timmons, A.; Lopes-da-Silva, J. A. Weak-Gel Formation in Dispersions of Silica Particles in a Matrix of a Non-Ionic Polysaccharide:

Structure and Rheological Characterization. *Carbohydrate Polymers* **2010**, *82* (4), 1219–1227.

(147) Sotiropoulou, S.; Sierra-Sastre, Y.; Mark, S. S.; Batt, C. A. Biotemplated Nanostructured Materials †. *Chemistry of Materials* **2008**, *20* (3), 821–834.

(148) Ayutsede, J.; Gandhi, M.; Sukigara, S.; Ye, H.; Hsu, C.; Gogotsi, Y.; Ko, F. Carbon Nanotube Reinforced *Bombyx Mori* Silk Nanofibers by the Electrospinning Process. *Biomacromolecules* **2006**, *7* (1), 208–214.

(149) Zhang, Y.; Zhang, M. Calcium Phosphate/Chitosan Composite Scaffolds for Controlledin Vitro Antibiotic Drug Release. *Journal of Biomedical Materials Research* **2002**, *62* (3), 378–386.

(150) Zhang, Y.; Zhang, M. Synthesis and Characterization of Macroporous Chitosan/Calcium Phosphate Composite Scaffolds for Tissue Engineering. *Journal of Biomedical Materials Research* **2001**, *55* (3), 304–312.

(151) Hodde, J. Naturally Occurring Scaffolds for Soft Tissue Repair and Regeneration. *Tissue Engineering* **2002**, *8* (2), 295–308.

(152) Olsen, D.; Yang, C.; Bodo, M.; Chang, R.; Leigh, S.; Baez, J.; Carmichael, D.; Perälä, M.; Hämäläinen, E.-R.; Jarvinen, M.; et al. Recombinant Collagen and Gelatin for Drug Delivery. *Advanced Drug Delivery Reviews* **2003**, *55* (12), 1547–1567.

(153) Rodrigues, C. V. M.; Serricella, P.; Linhares, A. B. R.; Guerdes, R. M.; Borojevic, R.; Rossi, M. A.; Duarte, M. E. L.; Farina, M. Characterization of a Bovine Collagen–hydroxyapatite Composite Scaffold for Bone Tissue Engineering. *Biomaterials* **2003**, *24* (27), 4987–4997.

(154) Wahl, D.; Czernuszka, J. Collagen-Hydroxyapatite Composites for Hard Tissue Repair. *European Cells and Materials* **2006**, *11*, 43–56.

(155) Fernandes, F.; Coradin, T.; Aimé, C. Self-Assembly in Biosilicification and Biotemplated Silica Materials. *Nanomaterials* **2014**, *4* (3), 792–812.

(156) Heinemann, S.; Coradin, T.; Desimone, M. F. Bio-Inspired Silica–collagen Materials: Applications and Perspectives in the Medical Field. *Biomaterials Science* **2013**, *1* (7), 688–702.

(157) Manzano, M.; Colilla, M.; Vallet-Regí, M. Drug Delivery from Ordered Mesoporous Matrices. *Expert Opinion on Drug Delivery* **2009**, *6* (12), 1383–1400.

(158) Vallet-Regí, M.; Balas, F.; Colilla, M.; Manzano, M. Drug Confinement and Delivery in Ceramic Implants. *Drug Metabolism Letters* **2007**, *1*, 37–40.

(159) Quignard, S.; Masse, S.; Coradin, T. *Intracellular Delivery: Fundamentals and Applications, Fundamental Biomedical Technologies, Ed. A. Prokop*; Springer Science; 2011.

(160) Quignard, S.; Hélary, C.; Boissière, M.; Fullana, J.-M.; Lagrée, P.-Y.; Coradin, T. Behaviour of Silica Nanoparticles in Dermis-like Cellularized Collagen Hydrogels. *Biomater. Sci.* **2014**, *2* (4), 484–492.

(161) Eglin, D.; Shafran, K. L.; Livage, J.; Coradin, T.; Perry, C. C. Comparative Study of the Influence of Several Silica Precursors on Collagen Self-Assembly and of Collagen on 'Si' Speciation and Condensation. *J. Mater. Chem.* **2006**, *16* (43), 4220–4230.

(162) Jing, S.; Jiang, D.; Wen, S.; Wang, J.; Yang, C. Preparation and Characterization of Collagen/Silica Composite Scaffolds for Peripheral Nerve Regeneration. *Journal of Porous Materials* **2014**, *21* (5), 699–708.

(163) Foglia, M. L.; Camporotondi, D. E.; Alvarez, G. S.; Heinemann, S.; Hanke, T.; Perez, C. J.; Diaz, L. E.; Desimone, M. F. A New Method for the Preparation of Biocompatible Silica Coated-Collagen Hydrogels. *Journal of Materials Chemistry B* **2013**, *1* (45), 6283–6290.

(164) Heinemann, S.; Heinemann, C.; Ehrlich, H.; Meyer, M.; Baltzer, H.; Worch, H.; Hanke, T. A Novel Biomimetic Hybrid Material Made of Silicified Collagen: Perspectives for Bone Replacement. *Advanced Engineering Materials* **2007**, *9* (12), 1061–1068.

II. Influence of the bio-chemical signal clusterization on cell adhesion in a Peptide Amphiphile - SiNP composite

Content

1. Introduction to Peptide Amphiphiles

Peptide Amphiphiles (PA) are short peptide sequences linked to an aliphatic tail.[1] The first PA ever reported was by Tirrell and co-workers in 1995. It was made of a dialkyl ester tail appended to a peptide sequence from collagen, resulting in the assembly of a monolayer at the air–water interface.[2] The Stupp laboratory reported in 2001 a novel PA structure, whereby an unbranched palmitic acid tail was appended to the N-terminus of a peptide sequence.[3] Driven by the hydrophobic collapse of the alkyl tail, as well as the conical shape of the molecule, these PAs, insoluble in water, self-assembled in aqueous solution into one-dimensional nanofibers (6 nm in diameter and several microns in length).[4]

Typical structure of PA from Stupp and co-workers' library is depicted in Figure II-1. Region 1, the hydrophobic domain, consists of a long alkyl tail. To prevent the PA from forming amorphous precipitates and to control the self-assembly, two domains are incorporated in the molecule sequence: region 2 and 3. Region 2, directly attached to the alkyl tail, consists of a short peptide sequence capable of forming intermolecular hydrogen bonding (or β-sheets).[5] Region 3 contains charged amino acids for enhanced solubility in water and for the design of pH- and salt-responsive nanostructures and networks. Region 4 and 5 are attached to the charged domain to provide the fiber with functionality, such as a cell-binding domain[6] or a catalytically-active domain.[7] On Figure II-1, they are respectively linker and bioactive epitopes RGDS able to interact with cells. In aqueous media, the amphiphilic nature of the molecules allows the specific presentation of hydrophilic peptide signals on the surfaces of the assembled nanofibers under specific solution conditions (pH, ionic strength and temperature).

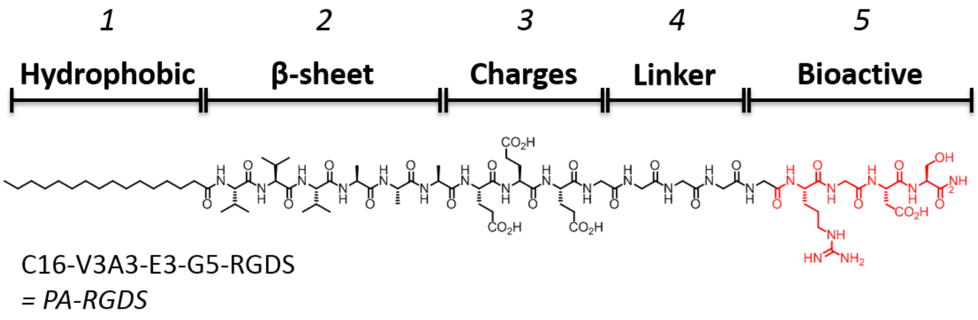

Figure II-1 : Presentation of the Peptide Amphiphile (PA) structure.

This design strategy is directly inspired from biomolecules such as proteins.[8] The amino acid sequence of those domains directly encodes for the organization on several hierarchical levels. For example, on Figure II-2, similarly to collagen (left), the rather simple PA primary structure prescribes the secondary structure based on non-covalent interactions between monomers (right). Monomers can be defined as the basic unit (collagen triple helix, PA) that interact through supramolecular interactions. A third level of organization is achieved by the collagen fibrils in one case, and the one-dimensional nanofibers in the other case. Finally, the superstructure, or quaternary structure, originates from the hierarchical assembly of those fibrillar functional polymers into complex architectures over various length scales. This hierarchical assembly process is directly responsible for numerous properties and functions of protein-based tissues in nature or PA-based bulk materials.

Figure II-2 : Hierarchical self-assembly of (left) biopolymers collagen and (right) supramolecular polymers (PA). On the left, G represents glycine, and X and Y can be any amino acid, including glycine, proline, or hydroxyproline. In the primary structure of the peptide amphiphile on the right, A, K and V represent the amino acids alanine, lysine, and valine, respectively. This figure is adapted from[8].

The highly modular nature of PA molecules has made them well-suited as biomaterials for regenerative medicine. They are easily synthesized and biodegradable. Additionally, the nanofibers that result from PA self-assembly can often be gelled by screening their surface charges, resulting in a material that can be readily injected and form a gel *in situ*.[9] Moreover, the fourth domain, or exposed region, can be a biomimetic epitope (RGDS[10], IKVAV[6], VEGF [11]…). The Stupp laboratory explored a wide range of molecules with different amino acid sequences. In these self-assembled structures, all the PA molecules are close-packed resulting in an extremely high density of peptides, which can induce an effective cellular response.

Because of those advantages and abilities, PAs have been found useful in many areas including neurite outgrowth,[12] cartilage and bone regeneration[13]. By using this biomaterial, we can exactly control the nature and the amount of the bioactive molecules that we are actually exposing to cells. However, despite the possibility to conjugate multiple peptide motifs, the control over their spatial distribution remains limited and the display is statistically homogeneous. Because the positioning and clustering of biomolecules dictates cell behavior, the engineering of biomaterials where the display of bioactive ligands can be controlled is of major interest and represents an exciting challenge.

The work presented hereafter was conducted during an 8-month internship at Northwestern University (Chicago, IL, USA). I have obtained a Fulbright grant to set-up this collaboration between Pr. Stupp's laboratory and our team. The aim of this common project was to combine silica nanoparticles (SiNPs) with self-assembled scaffolds from PAs (SiNP@PA) to design novel composite biomaterials. Because each component can be functionalized with multiple bioactive motifs, this composite approach should offer a unique modularity making SiNP@PA composites highly promising multifunctional biomaterials.

In particular, we used SiNPs to cluster bioactive motifs, allowing for the comparison of two display configurations for a selected biomimetic epitope: homogeneous dispersion within PA fibers (Figure II-3-A) or clusterization on the surface of SiNPs (Figure II-3-B). The selected epitope for this study is RGDS, a four amino acid peptide present in the fibronectin glycoprotein of the ECM. It is a peptide motif known for interacting with a_vb_3 and a_5b_1 integrins and by consequence influencing cell attachment and migration.[14]

Most importantly, we could also use particle surface and PA fibers as platforms to control the display of multiple ligands and study possible synergistic interactions necessary for triggering a given cell behavior. With this purpose, we simultaneously grafted two integrin-binding sequences RGDS and PHSRN, known to work in a distance-dependent manner, on SiNP surface (Figure II-3-C-G).[15,16] We could therefore compare five display configurations: the two peptides homogeneously distributed on PA fibers (Figure II-3-C), one clustered on SiNP and the other dispersed over the PA fibers (Figure II-3-D,E) and finally both clustered, either together or on the same SiNPs (Figure II-3-G), or individually on two populations of SiNPs (Figure II-3-F). This model enabled us to determine the influence of the 3D clustering and of the spacing between epitopes.

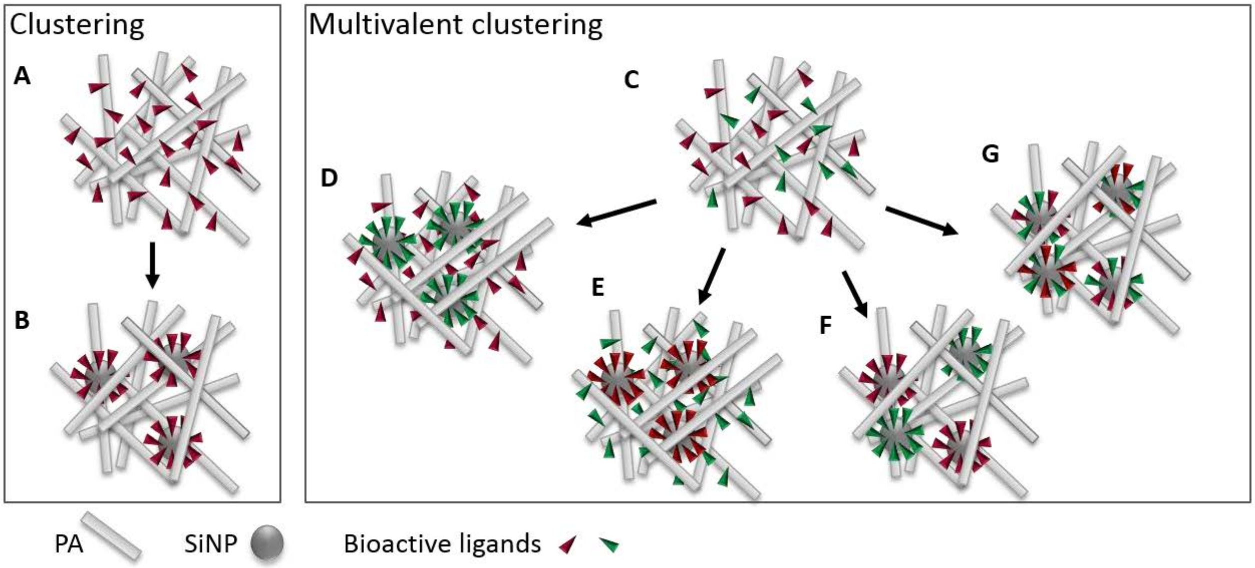

Figure II-3 : Schematic representation of the different composites investigated. (A,B) Effect of the 3D peptide clustering in biomaterials, and of (C-F) the clustering of the two synergistic peptide motifs (RGDS and PHSRN) and effect of ligand inter-distance.

2. Chemical Design

2.1. Peptide Amphiphile synthesis

PA were synthesized by solid phase peptide synthesis, which allowed us to choose and couple each amino acid one by one. We synthesized C16V3A3E3, that stand for a **16 C**arbone aliphatic chain, **3 V**alines, **3 A**lanine, **3** Glutamic acids (**E**). From this PA we synthesized two others PA with a bioactive epitope. RGDS, already mentioned, stood for Arginine (R), **G**lycine, Aspartic Acid (**D)** and **S**erine, and PHSRN for **P**roline, **H**istidine, **S**erine, Arginine (**R**) and Asparagine (**N**). We obtained pure product analyzed by Mass Spectrometry by ElectroSpray Ionization (ESI-MS) on Figure II-4 (1152.l Da for C16V3A3E3, 1853.1 Da for PA-RGDS and 2029.1 Da for PA-PHSRN).

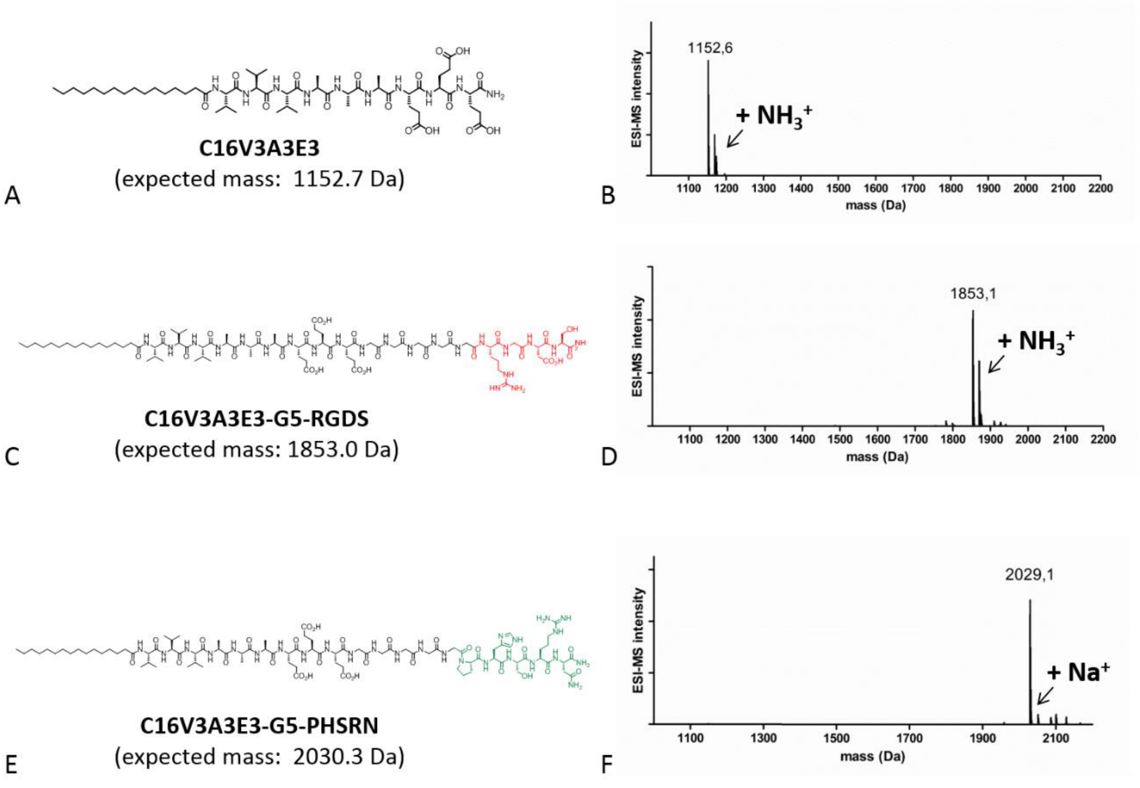

Figure II-4 : Molecular structure of (A) C16V3A3E3, (C) C16V3A3E3-G5-RGDS and (E) C16V3A3E3-G5-PHSRN and their experimental Mass Spectrometry spectra by Electrospray ionization (B-D-F respectively).

The three PAs have the typical structure previously described on Figure II-1. C16V3A3E3 (Figure II-5) is a well-characterized PA in Pr. Stupp Laboratory. When mixed with the bioactive derivative PA-RGDS and PA-PHSRN, we created *bioactive fibers*. The ratio between PA-RGDS or PA-PHSRN and PA has been varied (here from 0.6 to 2.6 mol% of the total peptide) to study the impact of RGDS concentration on cell adhesion. Those C16V3A3E3 PA and the relative co-assemblies form nanofibers gel named here *matrix* when screened by a salt solution.

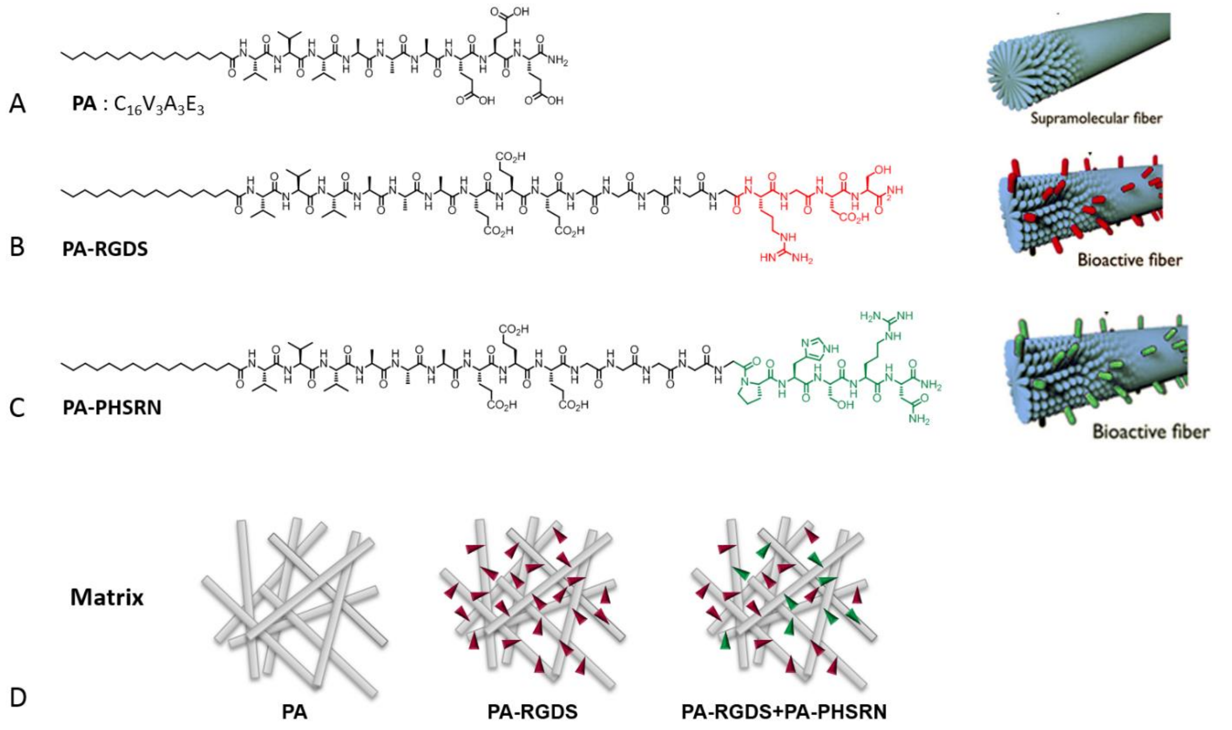

Figure II-5 : Molecular structure of (A) C16V3A3E3 containing the peptide sequence lacking epitope used to co-assemble with epitope-presenting PAs : (B) PA-RGDS and (C) PA-PHSRN with their corresponding schematic representations as unique fiber. (D) Schematic representation of PA matrices with and without epitopes.

We visualized our PA co-assemblies by Transmission Electron Microscopy (TEM) to be sure that they were able to create nanostructures. As shown on Figure II-6-A, PA C16V3A3E3 in H_2O self-assembles into nanofibers. Really similar 1D structures are obtained on Figure II-6-B and C, corresponding respectively to PA-RGDS@PA and PA-PHSRN@PA. Those two co-assemblies were obtained with 2.6 mol% of bioactive peptides and we can see that the presence of the functionalized PA did not influence the nano-structure of the final material. Interestingly, we also obtained the same nanofibers when both PA-RGDS and PA-PHSRN were mixed at 1.3 mol% each (2.6 mol% total peptide). So, having different epitopes did not influence the self-assembly process.

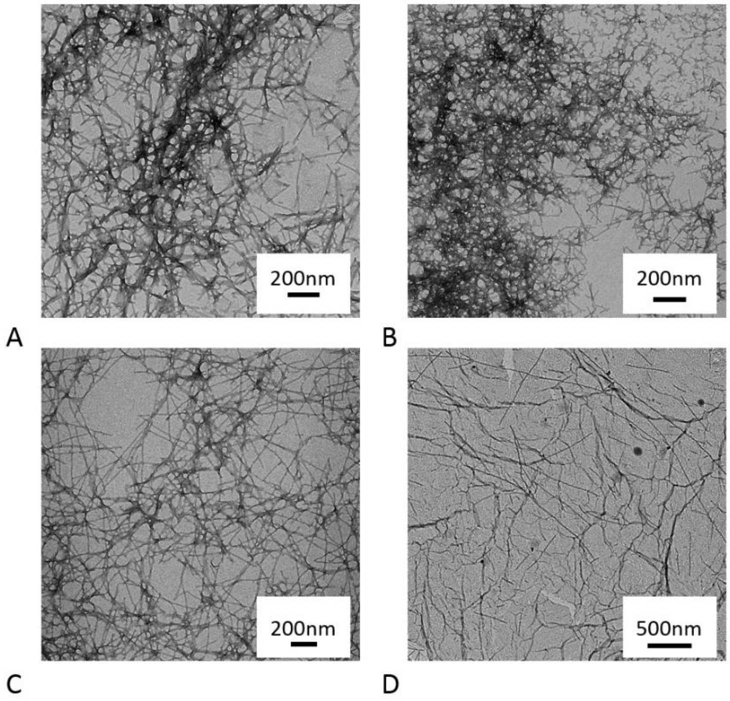

Figure II-6 : TEM images of A) PA C16V3A3E3, B) Co-assembly PA-RGDS@PA at 2.6 mol% peptide, C) Co-assembly PA-PHSRN@PA at 2.6 mol% peptide, D) Co-assembly PA-RGDS + PA-PHSRN@PA at 1.3 mol% each.

In conclusion, the co-assembly strategy allows for the introduction of one or two bioactive epitopes while preserving the structure of the PA gel. Such PA matrix will constitute the first building block of our composite material.

2.2. Silica Nanoparticles

2.2.1. Synthesis and characterization

The second building block of the composite was SiNPs. They were synthesized by the Stöber synthesis,[17] according to the protocol described by Thommassen and co-workers[18] that is suitable to prepare SiNPs with diameters ranging from *ca*. 20 to 3300 nm. Based on previous works in the team,[19] we targeted particle size around *ca*. 200 nm, which was successfully achieved as assessed by TEM (Figure II-7-A) and Dynamic Light Scattering (DLS, Figure II-7-B). The particles were quite monodispersed: 200 ± 28 nm by TEM measurement, 218.6 nm (PDI 0.045) in hydrodynamic diameter measured by DLS.

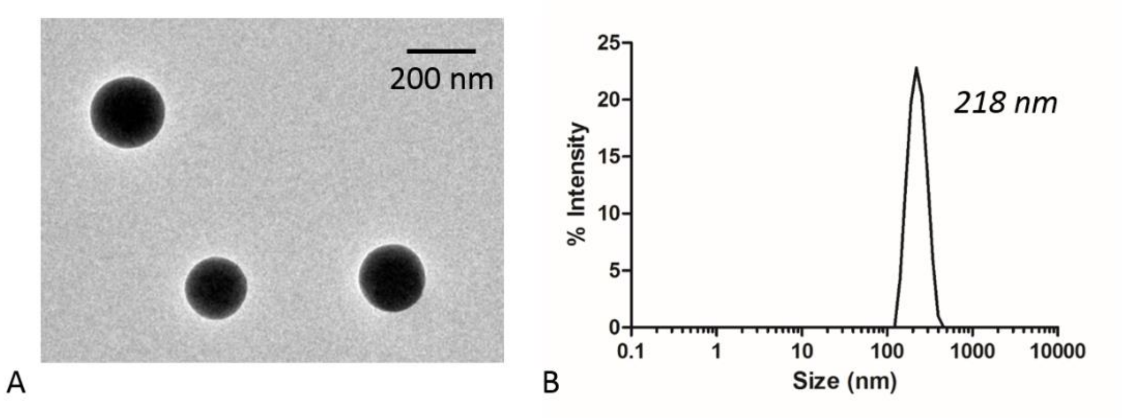

Figure II-7 : Characterization of SiNPs by A) TEM and B) DLS.

2.2.2. Synthesis of the peptide motifs

We synthesized the peptide-azides by solid phase peptide synthesis. On Figure II-8, three peptide-azides were synthesized: RGDS and PHSRN to be able to compare SiNP-peptides directly with PAs, and RGES, similar to RGDS except for the glutamic acid (E) replacing the aspartic acid (D). RGES is well-known in the literature for being non-bioactive but having still the same design than RGDS.[20] It makes it a suitable negative control. To add an azide in the structure of the peptide we used a lysine azide (Kaz). This modified amino acid, common in Solid Phase Peptide Synthesis, is commercially available and can be used to convert the azido group into amine. The linker made of a six-carbon alkyl chain and two glycines enable the bioactive epitope to be kept apart from the SiNP surface, enhancing its accessibility to the cells.

We obtained pure products as checked by ESI-MS on Figure II-8 (813.9 Da. for Kaz-C6-GG-RGDS, 827.9 Da for Kaz-C6-GG-RGES and 889.5 Da for Kaz-C6-GG-PHSRN).

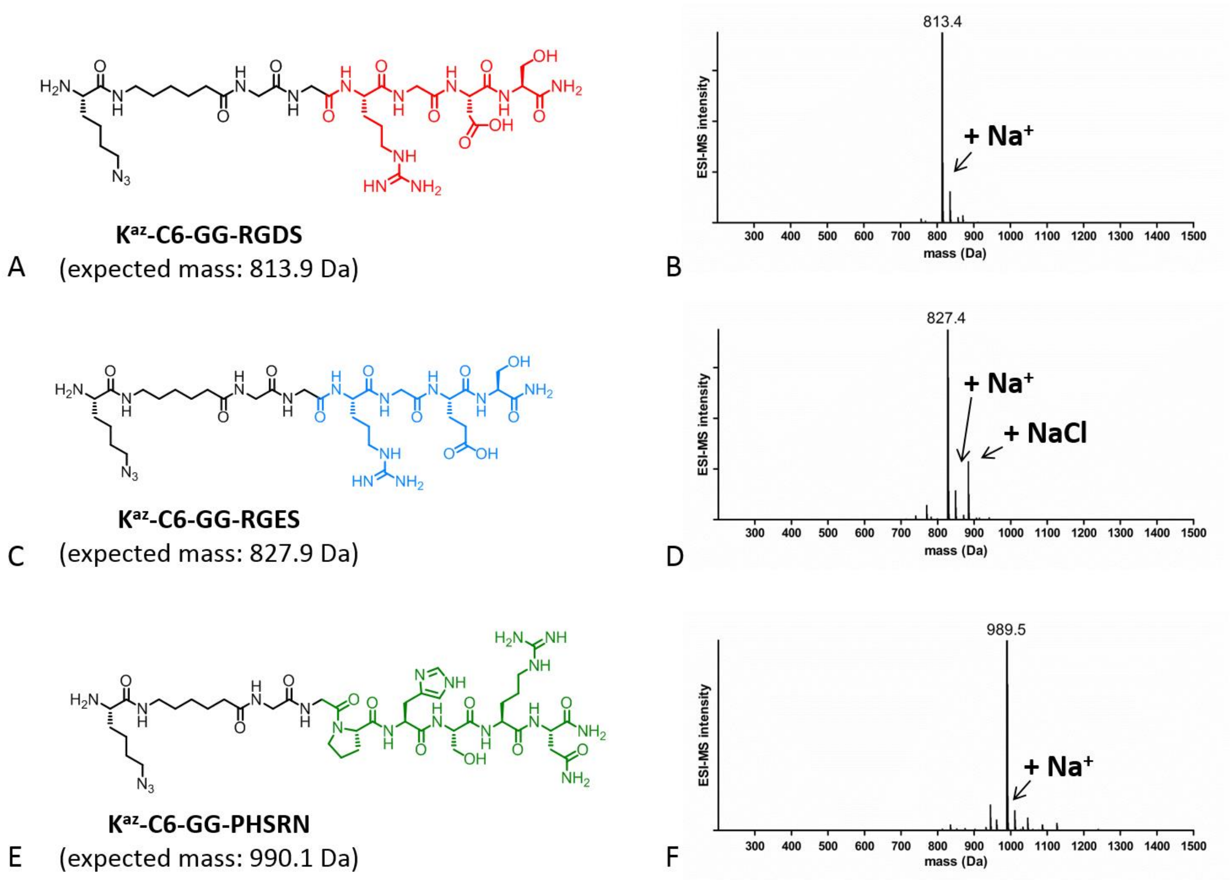

Figure II-8 : Molecular structure of the Peptides (A) Kaz-C6-GG-RGDS, (C) Kaz-C6-GG-RGES and (E) Kaz-C6-GG-PHSRN and their experimental MS spectra (B-D-F respectively).

2.2.3. Functionalization

To functionalize SiNPs with peptides we chose the click chemistry route (Figure II-9-A). Azide groups can be clicked on a Dibenzocyclooctyne-N-hydroxysuccinimidyl ester (DBCO). This highly specific reaction does not require any copper catalyst because of the higher stability of the resulting triazole than the triple bond on the cyclo-octane. We can create mono-functional SiNPs with only one type of peptide, or bi-functional SiNPs by mixing two peptide-azides before the click. On Figure II-9-B we pictured all configurations we could possibly create with our particles: one population of mono-functional SiNPs, or two mixed populations of SiNPs, and finally bi-functional SiNPs.

SiNPs were functionalized by several successive steps shown on Figure II-9-A. We followed the different synthesis steps and the different functionalization states by comparing the zeta potential of SiNPs along our pH scale (Figure II-9-C-D). The first step of functionalization of SiNPs is to display amine groups at the surface of the particles by grafting (3-Aminopropyl)triethoxysilane (APTES). Zeta potential measurements of SiNPs at constant ionic strength are indicative of the density of charge at the SiNP surface. More precisely, at low pH, we can see that the neutral contribution of the silanol groups (in SiNP-OH) is replaced by the positive contribution of the ammonium groups following the sol-gel grafting of APTES.

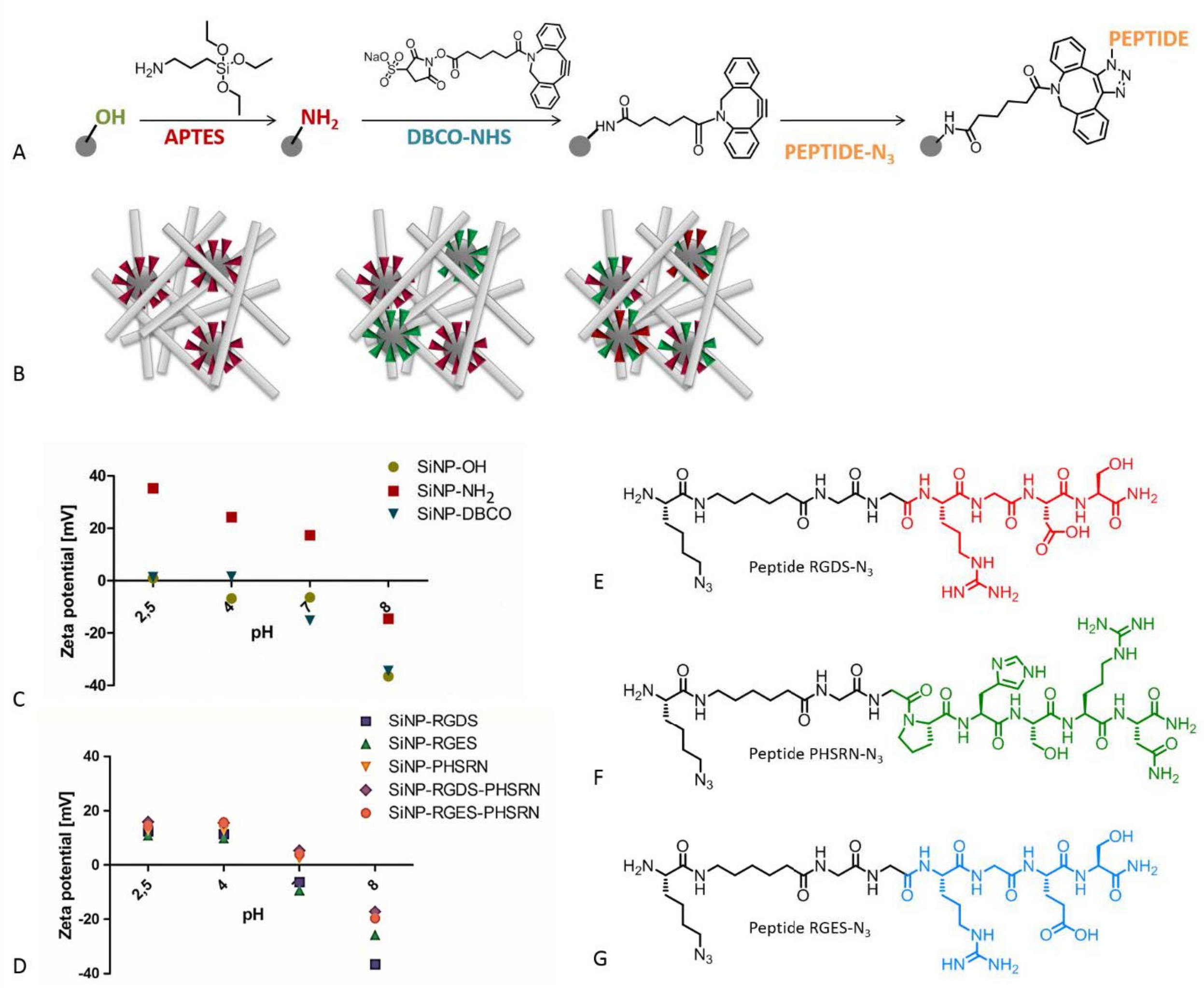

Figure II-9 : (A) Schematic representation of SiNP functionalization steps. (B) Schematic representation of peptide-functionalized SiNPs in a PA matrix. (C) Zeta Potential measurements of SiNPs after preliminary functionalization and (D) peptide functionalization. (E-G) Molecular structure of the RGDS, PHSRN and RGES Peptides.

Those amine groups were the reactive sites on which we covalently linked DBCO by an amide binding. We could confirm the grafting of DBCO by zeta potential measurements (Figure II-9-C). At low pH the positive contribution of the amines disappeared, hidden by DBCO groups.

All the peptides schematized on Figure II-9-E-G were successfully clicked on SiNP-DBCO, alone or as mixtures. On zeta potential measurements, we see an appearance of positive charges at acidic pH for all configurations, as expected from the presence of amine groups from arginine in all peptide compositions. In this region SiNP-DBCO particles were merely neutral, whereas all peptides are expected to be fully protonated. In more basic conditions (pH 8), all PHSRN-bearing particles showed higher (i.e. less negative) values than RGDS- and RGES-only bearing SiNPs, that should correspond to the presence of a deprotonated carboxylic acid in these two amino acid sequences.

To quantify how many groups we were able to click on the SiNP surface, we used a cyanide dye Cy3 with an azide group. We clicked it on DBCO-SiNPs (Figure II-10-A-B) as we clicked the peptides and on SiNP-OH as a control. We measured a fluorescence signal only when SiNP-DBCO were used (Figure II-10-C) which demonstrated the specificity of the reaction. Similarly, we could record an absorption band only for the grafted SiNP-DBCO particles (Figure II-10-D). This absorbance spectrum helped us to quantify the number of Cy3 we effectively grafted on SiNPs by Beer-Lambert Law. We found a density of 0.2 molecules / nm^2 and a concentration of 0.03 mol% ligand/SiNP.

As peptides are grafted to SiNP surface following the same protocol as Cy3, we will assume in the following work that their grafting density is the same as for the dye. This assumption is based on the fact that click chemistry is a robust method with a high yield. Moreover, the peptides and the dye have close molecular weights (805.0 Da for Cy3) so that the possible influence of steric constraints on the grafting efficiency should be quite similar. Indeed, further experiments such as trying to graft Cy3 after surface functionalization with peptides to check for any unreacted DBCO moiety or use of Isothermal Titration Calorimetry to determine the particle/peptide binding process in more details would be necessary to fully conclude on that matter.

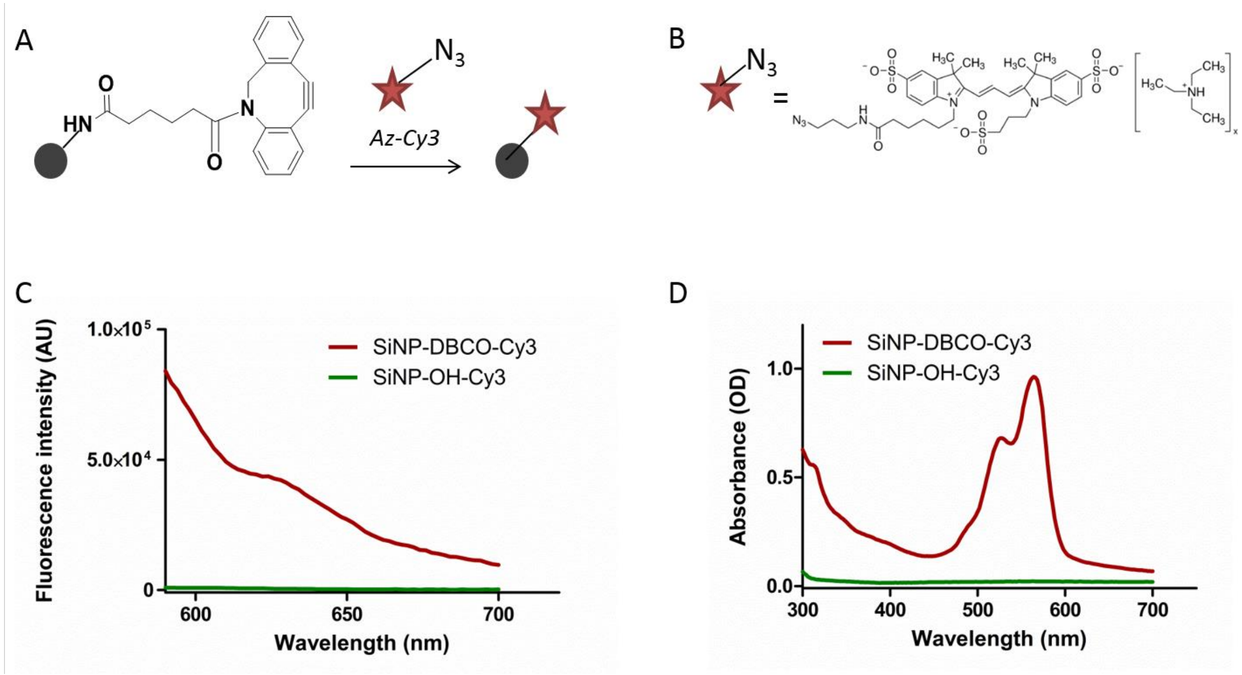

Figure II-10 : (A) Schematic representation of click chemistry between SiNP-DBCO and Cy3-Azide. (B) Molecular structure of Cy3-azide. (C) Fluorescence and (D) absorbance of SiNP-DBCO and SiNP-OH after reaction with Cy3-Azide.

SiNPs, our second building block of this composite material, were successfully synthesized and characterized. They will be used as platform to graft bioactive peptides with a precise quantification.

3. Preparation and characterization of the composite

In a composite approach, SiNPs modified with amine groups can be mixed with the PA at 10 mg.mL^{-1} before gel formation. Different SiNP:PA ratios were tested with various amount of SiNP, from 3 mg.mL^{-1} to 25 mg.mL^{-1} that would correspond to peptide amounts varying from 0.2 to 2.6 mol%. The different co-assemblies all form a gel. TEM and SEM show that SiNPs are very well-dispersed within the nanofiber network of the PA matrix (Figure II-11-A,B,D,E). This indicates that the presence of SiNPs do not disturb the self-assembly of the PA.

The localization of SiNPs within the PA matrix could further be visualized by the conjugation of azide-cyanine 3 dye to SiNPs (Figure II-11-C,F). We added the DAPI dye, which binds to the PA to visualize also the organic part of the composite. Observations by confocal microscopy confirmed the good dispersion of SiNPs in the volume of the 3D gel.

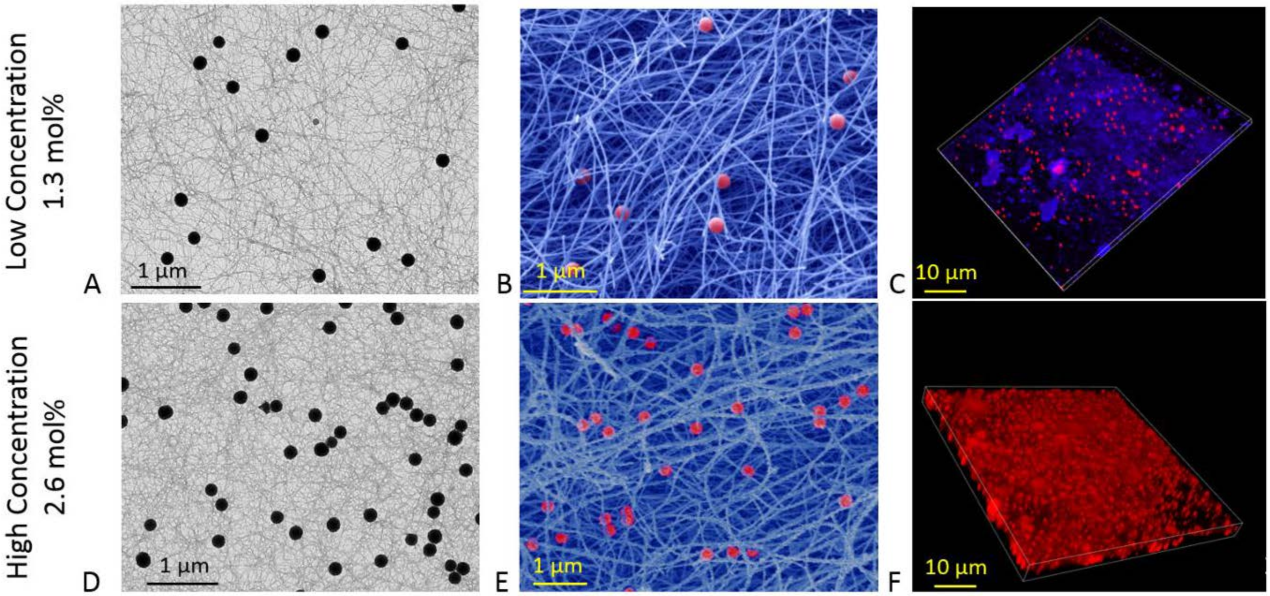

Figure II-11 : (A-C) TEM, SEM (colored image), and confocal images of 1.3 mol% SiNP@PA co-assembly. (D-F) TEM, SEM (colored image) and confocal images of 2,6 mol% SiNP@PA co-assembly (red fluorescence: Cy3 = SiNPs ; blue fluorescence: DAPI = PA).

Finally, the rheological properties of the composites were assessed. When comparing the starting PA system with those incorporating SiNPs at 2.6 mol% peptide equivalent, no significant difference could be measured in the loss and storage moduli indicating that the presence of SiNPs does not significantly affect the mechanical properties of the gel (Figure II-12). Those results were replicated and reproducible showing that composites at 2.6 mol% peptide equivalent were in the same range of G' and G'' values than PA alone. This is really important because we need to be sure that cell behavior would not be influenced by any modification of the mechanical properties.

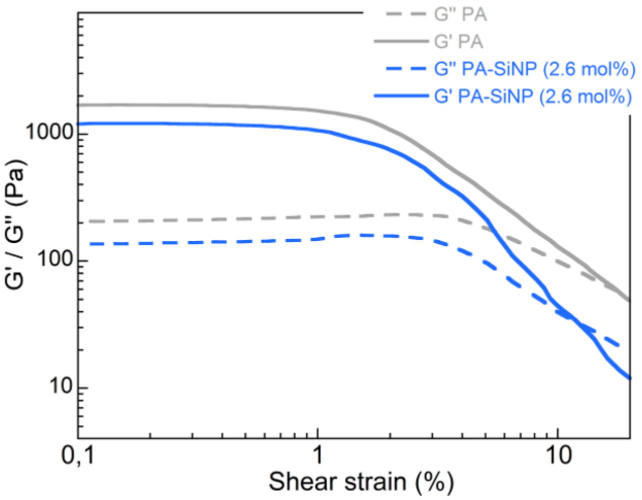

Figure II-12 : Rheology measurements of the PA alone and of the co-assembly at 2.6 mol% SiNP@PA.

To perform cell experiments, we prepared thin layers of the composite materials on glass slides. The PA solution with or without embedded SiNPs was deposited on the slide pre-coated with poly-D-Lysine and gelation was induced by adding $CaCl_2$. On Figure II-13, we show the corresponding images obtained by Scanning Electron Microscopy (SEM). PA only exhibits a rough surface of fibers (Figure II-13-A). On Figure II-13-B and C we can observe that for both 1.3 mol% and 2.6 mol% concentrations, SiNPs are well-dispersed inside the fibrous network. These films will be used as seeding surfaces to study the influence of peptide concentrations and organization on cell behavior.

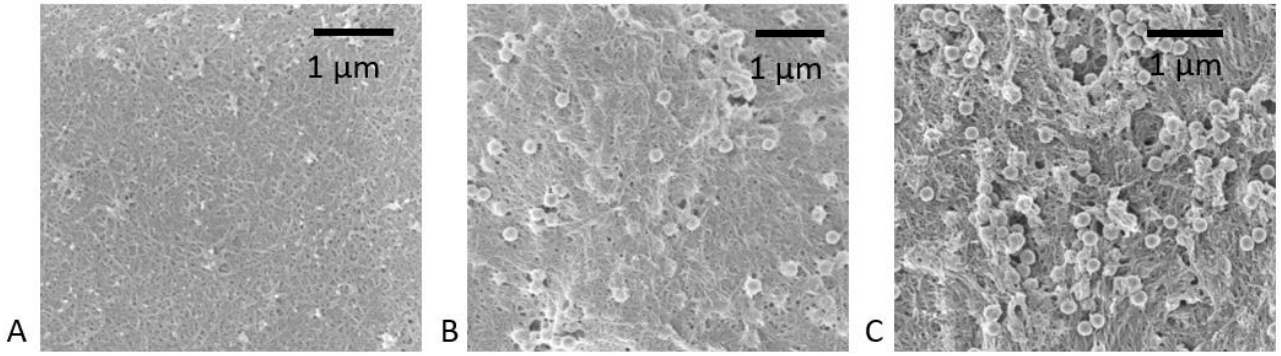

Figure II-13 : SEM images of (A) PA layer alone, (B) with 1.3 mol% or (C) 2.6 mol% SiNPs post gelation.

4. Biological activity

In the following text, all co-assemblies will be made within a PA matrix, unless specified, so that the @PA notation will be not mentioned for sake of simplicity.

4.1. Bioactivity of the single-peptide composite: the clustering effect

To compare the effect of an homogeneous distribution of RGDS with a clustered configuration, we cultured 3T3 fibroblasts on PA-RGDS and SiNP-RGDS (Figure II-14-A,B) at different RGDS concentrations.

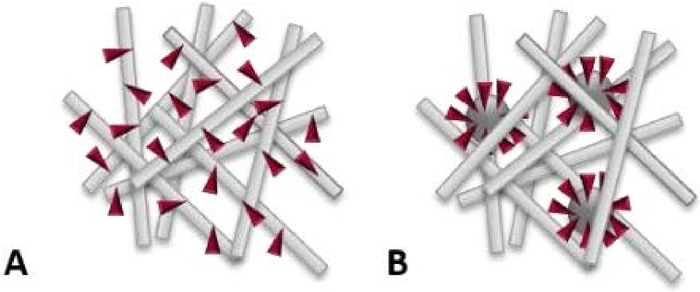

Figure II-14 : Schematic representation of RGDS (A) on PA fibers or (B) clustered on SiNP.

For PA only, confocal microscopy images showed a poor spreading of the cells after 4h30 of culture (Figure II-15-A,a). In contrast, a clear improvement of cell spreading was vizualized for PA-RGDS matrices when reaching 2.6 mol% RGDS. Below this value, the peptides did not appear to improve the spreading process (PA-RGDS concentrations of 0.6 and 1.3 mol%, Figure II-15-A,b-d)).

Very interestingly, the incorporation of SiNP-RGDS showed a positive effect with an improved cell spreading at a concentration as low as 0.6 mol% (Figure II-15-A,f). No further increase in cell area could be observed when increasing SiNP-RGDS concentration up to 2.6 mol% (Figure II-15-A,g-h). This is particularly interesting when considering that similar cell area thresholds are reached for PA-RGDS at 2.6 mol% and SiNP-RGDS at 0.6 mol%, indicating that more than four time less peptide epitopes are required when confined at the surface of SiNPs.

These observations were confirmed by quantitative determination of cell area (Figure II-15-B). The parameter of interest here is the impact of the particles as a display. Consequently, we choose the PA bearing the same function as a reference in the statistical calculation, here PA-RGDS-0.6 mol%. The presence of RGDS at low density (PA-RGDS-0.6 mol % and 1.3 mol% or SiNP-RGDS 0.2 mol%) seems even to inhibit the spreading in comparison with pure PA sample. The density of adhering cells was also determined and found to be significantly greater in presence of 0.6 mol% SiNP-RGDS than on PA-RGDS at 2.6 mol%, itself significantly larger than the PA alone (Figure II-15-C). It is worth noting that whereas a rather good correlation is observed in the impact of the layer composition on cell area and number of cells (Figure II-15-B,C), the significance of variations for the later parameter is lower compared to the former. This may be attributed to the low density of the seeded cell population (5,000/mL) that can impact on the statistical analysis of our data.

Finally, when grafting SiNPs with a scrambled peptide RGES that has *per se* no effect on cell adhesion, no significant improvement compared to the PA alone could be observed in either cell spreading or number (Figure II-15-A-i,j, B, C).

Taken together, these results show that clustering of RGDS peptide on the surface of SiNPs and their incorporation within a self-assembled PA matrix is an efficient approach to favor fibroblast adhesion, in particular when compared to the homogeneous dispersion of epitopes over the whole matrix.

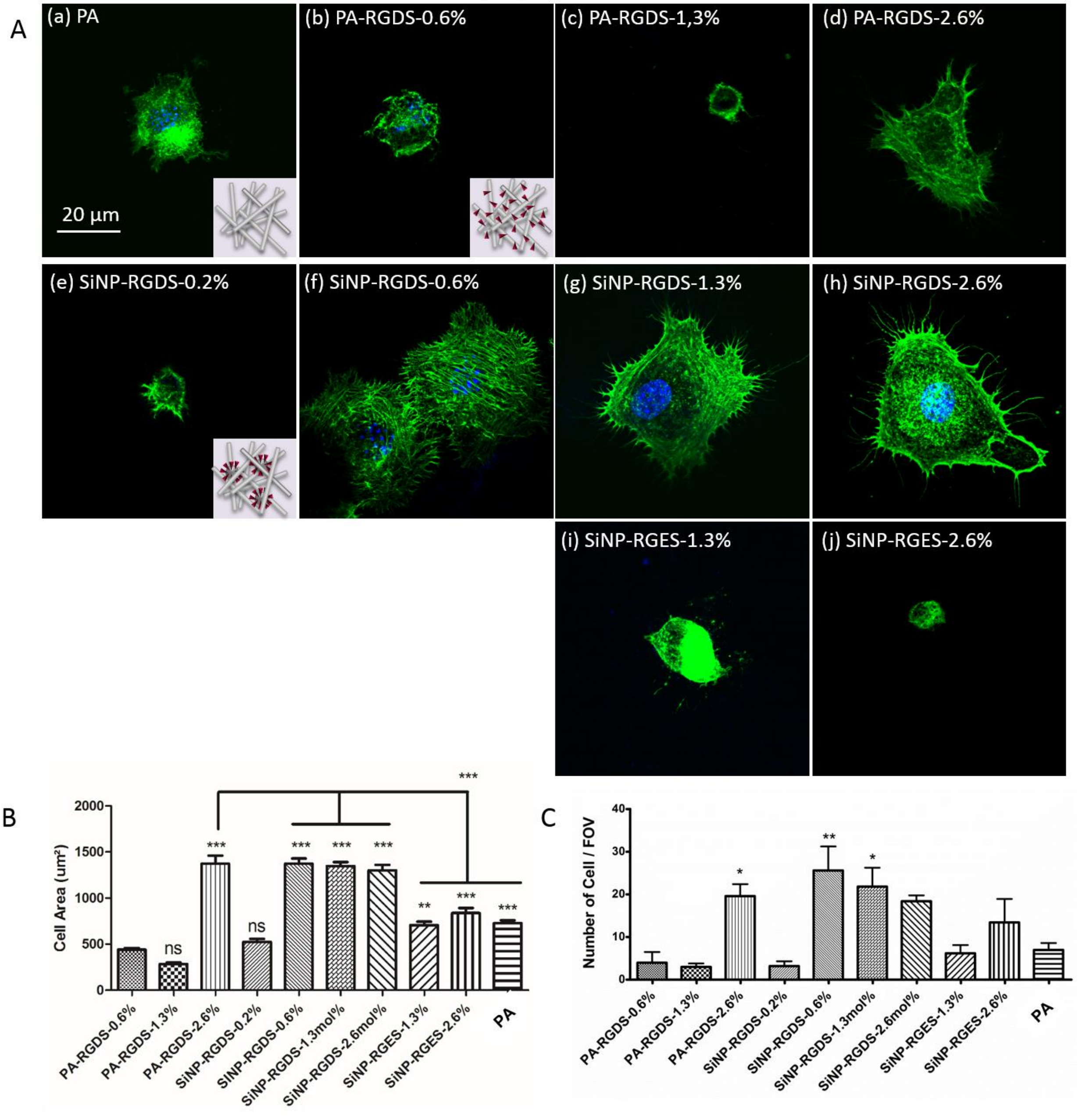

Figure II-15 : (A) Representative confocal images of 3T3 fibroblasts cultured on PA layers for 4h30 and stained for actin (phalloidin) and nucleus (DAPI) (a) on the PA alone, (b-d) on PA-RGDS at different peptide concentrations, (e-h) on the SiNP-RGDS at different peptide concentrations, and (i,j) on SiNP-RGES negative control at different peptide concentrations. (B,C) Cell morphologies on the different PA layers are compared by measuring the projected cell area and the number of cells by Field of View (FOV). In the plots, the column represents Mean with SEM. (* $p < 0.05$, ** $p < 0.001$, *** $p < 0.0001$; calculated against the base PA-RGDS-0.6 mol %, unless indicated, using Turkey's Multiple Comparison test; each condition from three independent experiments).

4.2. Bioactivity of the divalent-peptide composite: ligand inter-spacing in clustering

SiNP@PA composites offer a unique modularity to display multiple biological signals that can act synergistically. This is particularly interesting when working with the two integrin-binding sequences RGDS and PHSRN that operate in a spacing-dependent manner to promote cell adhesion and spreading (Figure II-16).[15,16] Indeed, when the fibronectin protein is in living systems, it folds in a specific conformation driven by non-covalent interactions. The distance between two domains of the protein is therefore fixed and corresponds to the optimal spacing for the two sequences to cooperatively display full bioactivity. Being able to position these peptides at the right distance on or within biomaterials is therefore a promising strategy to improve their interaction with cells. As a matter of fact, the conjugation of RGDS and PHSRN onto amphiphilic constructs,[21–25] oligopeptide backbones, [26–28] or DNA backbone[29–31] has been found to improve cell adhesion in comparison with the RGD sequence alone.

Figure II-16 : Schematic representation of (A) fibronectin protein with its interaction domains (adapted from [32]) and (B) fold with its specific conformation (adapted from [15]).

In our strategy, PA and SiNPs may both be conjugated with one (or two) peptide epitope(s) so that several different possibilities exist to display the RGDS and PHSRN motifs (Figure II-17): (i) two bioactive PAs can be co-assembled, bearing RGDS and PHSRN peptides respectively (PA-RGDS + PA-PHSRN, Figure II-17-A), (ii) SiNPs grafted with one peptide can be incorporated within a PA matrix containing the other peptide (SiNP-PHSRN@PA-RGDS or SiNP-RGDS@PA-PHSRN, Figure II-17-B,C), (iii) two populations of SiNPs grafted with one or the other peptide can be incorporated within a peptide-free PA matrix (SiNP-RGDS + SiNP-PHSRN, Figure II-17-D), (iv) divalent SiNPs grafted with both RGDS and PHSRN may also be mixed with the peptide-free PA (SiNP-RGDS-PHSRN, Figure II-17-E).

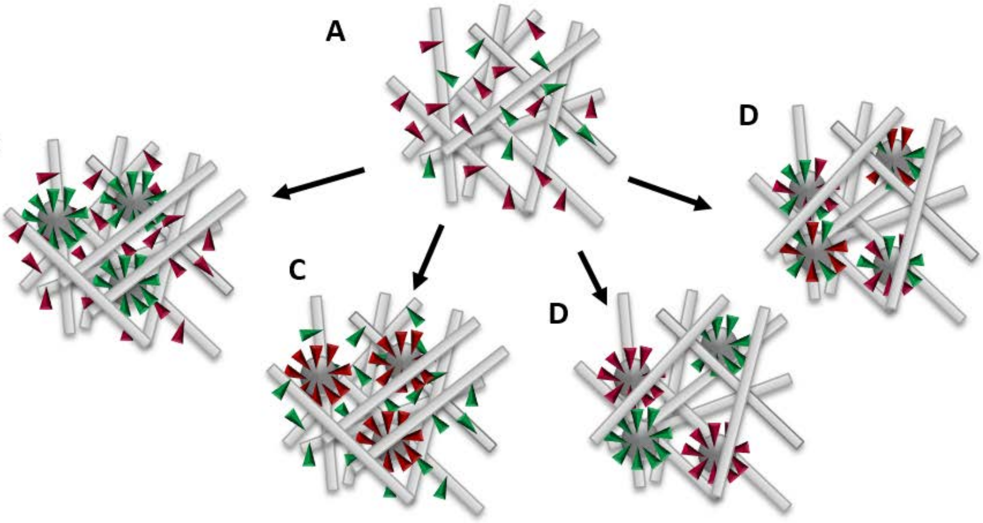

Figure II-17 : Schematic representation of (A-C) the effect of the 3D peptide clustering in biomaterials and of the clustering of the two synergistic peptide motifs (RGDS and PHSRN). (D,E) Dependence of the 3D clustering effect on ligand nanospacing.

Fibroblast adhesion and spreading on these composites were examined in a comparative manner, all divalent materials bearing a total peptide concentration of 2.6 mol%. Confocal imaging shows that mixed functional PA (PA-RGDS + PA-PHSRN) or SiNPs (SiNP-RGDS + SiNP-PHSRN @PA) induce poor spreading of the 3T3 fibroblasts, considering both cell spreading and number of cells (Figure II-18-A-a,b). Some improvements appear when one peptide is grafted on SiNPs and the second one conjugated to PA (PA-RGDS + SiNP-PHSRN or PA-PHSRN + SiNP-RGDS) (Figure II-18-A,c,d). This synergistic effect expected for the RGDS-PHSRN interaction is even exemplified when grafting both peptides simultaneously on the SiNP surface (SiNP-RGDS-PHSRN, Figure II-18-A,e). Importantly no such effect could be observed when using a scrambled peptide (RGES) grafted together with PHSRN on the particle surface (SiNP-RGES-PHSRN, Figure II-18-A,f).

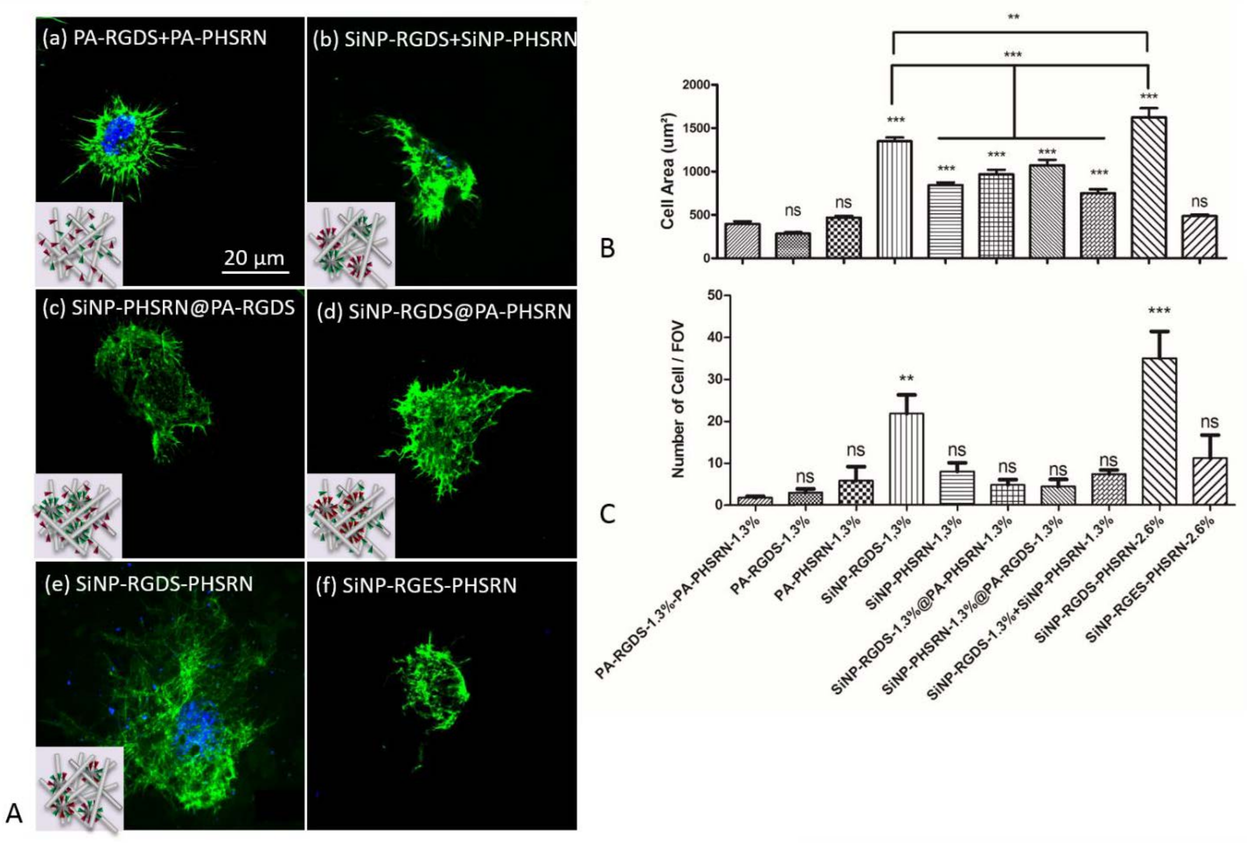

Figure II-18 : Representative confocal images of 3T3 fibroblasts cultured on PA layers for 4h30 and stained for actin (phalloidin) and nucleus (DAPI): (a) on PA-RGDS + PA-PHSRN, (b) on SiNP-RGDS + SiNP-PHSRN, (c) SiNP-PHSRN@PA-RGDS, (d) SiNP-RGDS@PA-PHSRN, (e) SiNP-RGDS-PHSRN and (f) SiNP-RGES-PHSRN. (B,C) Cell morphologies on the different PA layers are compared by measuring the projected cell area and the number of cells by Field of View (FOV). In the plots, the column represents Mean with SEM. (* $p < 0{,}001$, ** $p < 0.001$, *** $p < 0.0001$; calculated against the base PA-RGDS-1.3 mol % + PA-PHSRN-1.3 mol %, unless indicated, using Turkey's Multiple Comparison test; each condition from three independent experiments).

Quantitative analyses confirmed the positive effect of the PA layers containing bi-functional particles, that can be attributed to the close interaction between RGDS and PHSRN. The statistics are calculated with PA-RGDS-1.3 mol% + PA-PHSRN-1.3 mol% as a reference, to evaluate the impact of the particles. Interestingly PHSRN clusterized at the surface of SiNPs improves cell spreading in comparison to PA-RGDS-1.3 mol% (Figure II-18-B). Similarly, the ability of SiNP-RGDS + SiNP-PHSRN, SiNP-RGDS@PA-PHSRN and SiNP-PHSRN@PA-RGDS mixed systems to promote cell spreading is interesting in comparison with PA-RGDS-

1.3 mol% but significantly lower than SiNP-RGDS-1.3 mol%. The only condition increasing the spreading in comparison with SiNP-RGDS-1.3 mol% is SiNP-RGDS-PHSRN, evidencing a synergy between the two peptides.

In term of cell adhesion and proliferation the only systems that was significantly different from the reference were the SiNP-RGDS@PA matrix and SiNP-RGDS-PHSRN (Figure II-18-C). In contrast, the ability of SiNP-PHSRN, SiNP-RGDS + SiNP-PHSRN, SiNP-RGDS@PA-PHSRN and SiNP-PHSRN@PA-RGDS systems to promote cell adhesion and proliferation could not be confirmed.

Overall, the main results of this work can be summarized thanks to SEM observations of the 3T3 fibroblast morphologies. In the case of monofunctional PA-RGDS, no cell adhesion could be observed below a bioactive peptide concentration of 2.6 mol% (Figure II-19-A,B). No cell adhesion was observed with PA-PHSRN (Figure II-19-C,D). In contrast, a highly improved cell adhesion could be induced by the clustering of RGDS motifs onto the SiNP surface at RGDS concentrations of 1.3 mol% and below (down to 0.6 mol%, Figure II-19-E). This illustrates the efficiency of the 3D clustering of bioactive peptide. Previous works have shown that 70 nm is a threshold in the interspacing of RGD ligands within clusters.[33–40] A shorter spacing leads to a more significant cell spreading, while a larger one dramatically reduces cell adhesion and spreading.[41] In this regard, we show here that the use of SiNPs having a diameter of 200 nm appears particularly well-adapted to ensure the formation of effective peptide clusters with a statistic local interligand spacing below the threshold value.

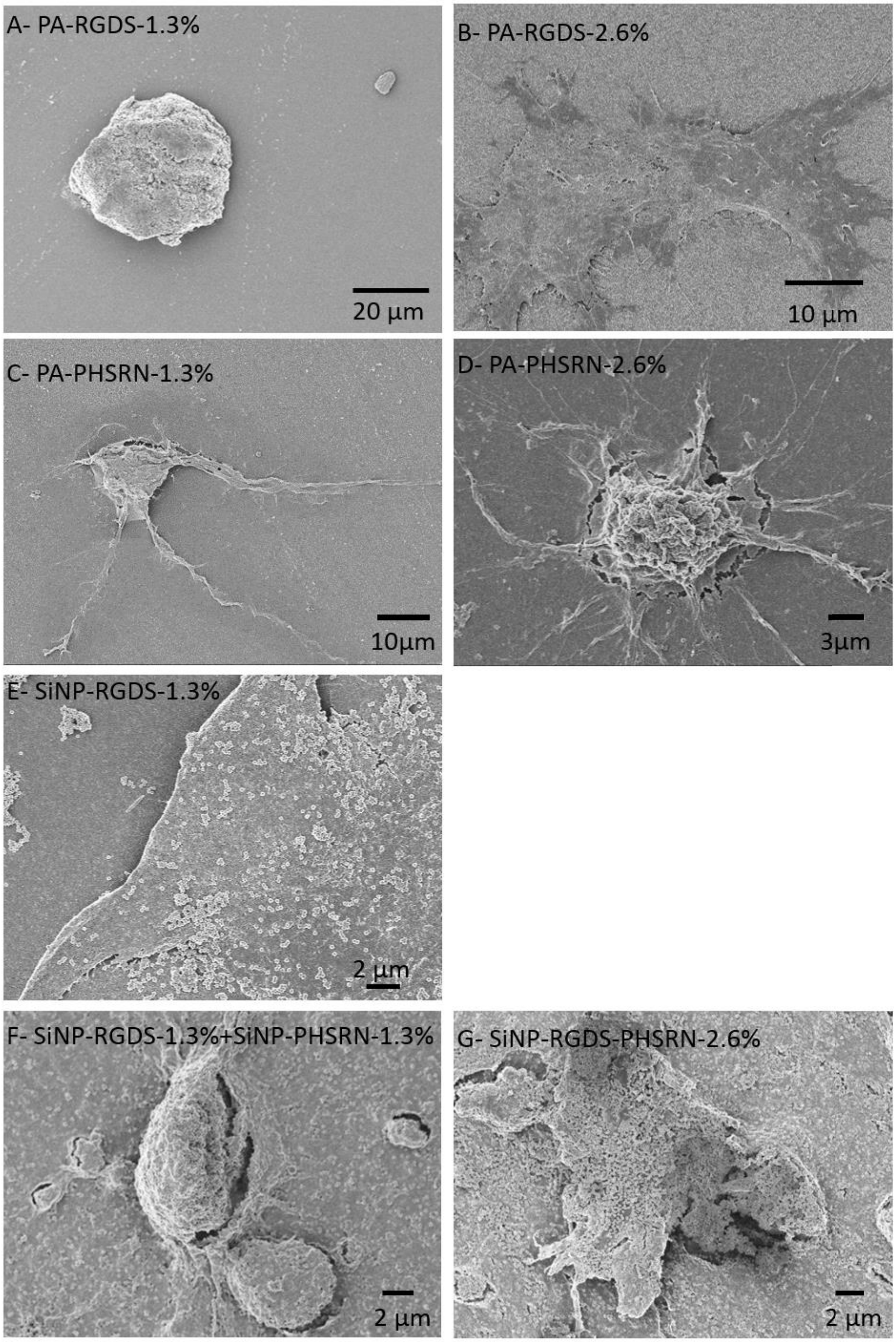

Figure II-19 : SEM of 3T3 fibroblasts cultured on PA layers for 4h30 on (A,B) PA-RGDS at 1.3 and 2.6 mol%, (C,D) PA-PHSRN at 1.3 and 2.6 mol%, (E) SiNP-RGDS- 1.3 mol%, (F) SiNP-RGDS + SiNP-PHSRN-1.3 mol% and (G) SiNP-PHSRN-RGDS-2.6 mol%.

The clustering of a monoligand is not efficient when working with synergistic peptide motifs that interact in a distance-dependent manner, RGDS-PHSRN. In this case, not only is the clustering important, but the proximity of the peptides within the cluster need to be controlled. The incorporation of particles into a 3D matrix is a particularly powerful mean to address this key issue, as it is a platform that can easily be chemically engineered to simultaneously graft multiple bioactive peptides. As a result, an improved cell adhesion is observed when incorporating divalent SiNP-RGDS-PHSRN into the PA matrix, while the mixture of SiNP-RGDS and SiNP-PHSRN does not have any beneficial effect (Figure II-19-F,G). By using precise tools, like DNA strands with a variable spacer region to tune the inter ligand distance, it has been shown that the ideal inter-distance between RGDS and PHSRN ligand for cell adhesion is 5.4 nm.[31] Here, we can assume that, at the surface of SiNP, the two peptides are statistically distributed. Based on the Cy3 grafting experiments, we estimated the density of peptides to 0.2 molecules per nm^2, i.e 1 peptide every 5 nm^2. This corresponds to a distance of ca. 5 nm between two peptides, thus in the good range to create a synergy between RGDS and PHSRN.

5. Conclusion

Because each component can be functionalized with multiple bioactive motifs, the composite approach offers a high modularity for the design of efficient biomaterials. In particular, we show that the presence of particles allows the clustering of bioactive motifs in 3D that allows in turn for a highly-significant improvement in cell adhesion and spreading. Most importantly, by grafting simultaneously the two integrin-binding sequences RGDS and PHSRN known to work in a distance-dependent manner, we show that the particle surface can successfully be used as a platform to control the clustering of multiple ligands and promote the synergistic interactions necessary for triggering a given cell behavior. This makes the silica nanoparticle - peptide amphiphile composites very promising candidates for tissue engineering and regenerative medicine, providing a unique way of tuning the scaffold bioactivity.

Although this composite approach may be easily extended to virtually any kind of particles, SiNPs have two important advantages. First their versatile surface chemistry offers the possibility to graft a wide range of biomolecules, from short peptides to large antibodies. Second, and more importantly for our strategy, their diameter can be tuned over a broad range of dimensions (from tens of nanometers to microns) that should allow addressing fundamental questions about the most efficient size of clusters, or unravelling the impact of ligand ordering after careful control of the functionalization pattern of the 3D SiNPs surface. While our results show that bi-functional SiNPs are interesting platforms to create synergies between two peptides, being able to go further and precisely control the clustering of two epitopes within patches distributed on the particle surface would be particularly interesting. In that context, the work that we performed to design such patchy particles will be described in the next chapter.

6. Experimental methods

6.1. PA and Peptide synthesis

PAs and peptides were synthesized using a standard fluorenylmethyloxycarbonyl (Fmoc) solid phase peptide synthesis (SPPS) on Rink Amide MBHA resin as described previously.[20] Amino acid couplings were performed either manually or on a CEM Liberty microwave-assisted peptide synthesizer. Rink Amide MBHA resin, Fmoc-protected amino acids and 2-(1H-benzotriazole-1-yl)-1,1,3,3-tetramethyluronium hexafluorophosphate (HBTU) were purchased from Novabiochem; Fmoc-NH-PEG$_4$-CH$_2$COOH was purchased from ChemPep Inc.; palmitic acid was purchased from Acros Organics; Fmoc-(4-amino)benzoic acid and Fmoc-(4-aminomethyl)benzoic acid were purchased from VWR and Chem-Impex International Inc., respectively. All other reagents and solvents were purchased from Sigma Aldrich and used as received. Fmoc deprotection was performed using 30% piperidine in N,N-dimethylformamide (DMF) and amino acid and palmitic acid couplings were performed with 4 molar equivalent (eq.) protected amino acid or palmitic acid, 3.95 eq. HBTU, and 6 eq. of N,N-diisopropylethylamine (DIEA) in DMF alone or in a solvent mixture of 1:1:1 DMF:dichloromethane (DCM):N-methyl-2-pyrrolidone (NMP). The coupling reaction for the PEGylated amino acid was performed similarly to other standard Fmoc-protected amino acids, using Fmoc-PEGylated amino acid (3 eq.), HBTU (2.95 eq.), and DIEA (4.5 eq.) in DMF. For the coupling of Fmoc-(4-amino)benzoic acid and Fmoc-(4-aminomethyl)benzoic acid, both were converted into acid chloride first (procedure described below) to increase the coupling yields. The coupling reaction was performed by using 4 eq. of Fmoc-(4-amino)-benzoyl chloride or Fmoc-(4-aminomethyl)benzoyl chloride and 6 eq. of DIEA in NMP. Synthesized PA and peptide molecules were cleaved from the resin using a mixture of 95% trifluoroacetic acid (TFA), 2.5% water, and 2.5% triisopropylsilane (TIPS). After removing TFA by rotary evaporation, the product was precipitated with cold diethyl ether, dried, and purified using preparative scale reverse phase high performance liquid chromatography on a Varian Prostar Model 210 system equipped with a Phenomenex Jupiter Proteo column (C12 stationary phase, 10 mm, 4 µm particle size and 90 Å pore size, 150 × 30 mm). A linear gradient of acetonitrile (2 to 100%) and water with 0.1% ammonium hydroxide (added to aid PA solubility) was used as the mobile phase for purification. Electrospray ionization mass spectrometry (Agilent 6510 Q-TOF LC/MS) was used to identify the pure fractions, which were then combined together and lyophilized after removing excess acetonitrile by rotary evaporation.

6.2. Synthesis of silica particles

Stöber silica particles were synthesized using 32 ml ultrapure water, 600 ml absolute ethanol (VWR, GPR RectaPur), 45 ml ammonium hydroxide solution (25%, Carlo Erba), and 21 ml tetraethyl orthosilicate (TEOS 98%, Aldrich). TEOS was added to the solution dropwise, and the sol was stirred overnight at room temperature (RT).[18] Ethanol and ammonia were removed by centrifugation (twice at 10 000 rpm for 5 min). Stöber particles were first functionalized with amine groups with (3-Aminopropyl)triethoxysilane (APTES, 99%, Aldrich). Typically, 0.77 g of silica particles were redispersed in a mixture of 76.6 ml ethanol and 1.7 ml ammonium hydroxide solution before addition of 0.75 ml APTES (4.2 mmol.g^{-1} silica). The mixture was stirred for 18 h at RT. Subsequently, the reaction mixture was heated to 80°C and the total volume was reduced to approximately two-thirds by distillation of ethanol and ammonia at ambient pressure. The mixture was left to cool down to RT and was subsequently washed three times with ethanol (by centrifugation at 12 000 rpm for 15 min) before drying under vacuum.

6.3. Dibenzocyclooctyne-N-hydroxysuccinimidyl ester grafting on SiNP-APTES

Stöber particles were redispersed in a phosphate buffer solution at pH 8.3 before addition of 94 µmol of Dibenzocyclooctyne-N-hydroxysuccinimidyl ester (DBCO-NHS, Aldrich) in Dimethysulfoxyde (DMSO, Aldrich) (3 mmol.g^{-1} silica). The mixture was stirred for 12 h at RT and subsequently washed three times with water (by centrifugation at 12 000 rpm for 15 min) before drying under vacuum.

6.4. Copper-free Click Chemistry Cy3-Azide

SiNP-DBCO or nude SiNPs were redispersed in water before addition of 1.2 µmol of Cy3-azide (Cy3-N3, 90%, Aldrich) in DMSO (4 mmol.g^{-1} silica). The mixture was stirred for 12 h at RT and subsequently washed as many times as necessary (at least 5 times) with water (by centrifugation at 12 000 rpm for 15 min). The absorbance was measured with a Uv-vis spectrophotometer and fluorescence intensity signal with a fluorescence spectrometer Cell Imager and Plate Reader Cytation3 BioTek.

6.5. Dynamic light scattering (DLS) and zeta-potential measurements

DLS was performed on a Brookhaven spectrometer equipped with a ζ potential analyzer (BI-ZetaPlus). The autocorrelation functions were recorded at a scattering angle $\theta = 90°$ and analyzed by the non-negatively constrained least squares technique (NNLS-Multiple Pass) for the determination of the particle diameter.

6.6. Peptide Amphiphile Preparation

The desired amount of PA powder was weighed out in an Eppendorf tube in order to make 100 μL of a 1 wt% PA stock solution in H_2O. The PA solution was subsequently annealed in 80°C PCR machine for 30 min and slowly cooled down for 1h30 to RT.

6.7. SiNP-PA composite

SiNP were redispersed in water and subsequently mixed with the PA at different ratios. The mixture was sonicated and then annealed in 80°C PCR machine for 30 min and slowly cooled down to RT for 1h30.

6.8. Rheology

Rheological measurements were performed on a Paar Physica MCR 300 oscillating plate rheometer equipped with a 25 mm diameter cone-plate geometry and a gap of 0.05 mm. PA solutions at a concentration of 0.5% (w/v) in water were pipetted (180 μL) onto the rheometer plate and gelled by exposure to 50 μL $CaCl_2$ solution (20 mM $CACl_2$, 150 mM NaCl). All measurements were done at 25°C, and the gels were allowed to equilibrate for 5 min at 0.1% strain prior to measurement. Data were collected at 0.1% strain over a frequency range of 1 to 100 s^{-1} and all measurements repeated 3 times.

6.9. Transmission Electron Microscopy (TEM)

PA samples were deposited and dried on 300 square mesh carbon-coated copper grids (Ted Pella, Redding, CA) and stained with 0.5% uranyl acetate (UA) solution. Images were obtained using a Hitachi HT-7700 Biological TEM (Hitachi High Technologies America, Schaumburg, IL) equipped with a LaB6 filament working at an accelerating voltage of 100 kV.

6.10. Preparation of PA layers

PA layers were prepared on sterile glass coverslips (12 mm diameter) or tissue culture plates following a previously described method. Briefly, the sample surface was first coated with 0.01% (w/v) poly-D-lysine (Aldrich) in milliQ water. 1% (w/v) PA solution in milliQ water was added onto the surface and the layer was gelled with 10 mM aqueous $CaCl_2$ solution.

6.11. Cell culture

NIH 3T3 mouse embryonic fibroblasts were maintained in growth medium containing Dulbecco's Modified Eagle's Medium (DMEM) with high glucose, supplemented with 10% fetal bovine serum (FBS) and 1% penicillin-streptomycin (P/S). The cells were grown in 75 mm^2 flasks (BD Falcon) and passaged every three days. All culture reagents were purchased from Gibco. For cell morphology experiments on PA layers, fibroblasts were seeded at a low density (5 k cells per well) in order to minimize cell–cell contacts, and incubated (at 37°C, 5% CO_2) under serum free condition (DMEM + 1% P/S) following a reported procedure.[20] The serum free media was used to eliminate any interference effects from serum adsorption to the nanofibers. Within the time-period of experiment (4h30), no adverse cellular responses were observed from serum deprivation or serum shock after a transfer from serum containing growth media.

6.12. Confocal microscopy

PA layers were stained by DAPI. Images of fluorescently stained samples were obtained using an inverted confocal laser scanning microscope (Nikon A1R).

6.13. Fluorescence staining

Cells were fixed with 4% paraformaldehyde in PBS and 1 mM $CaCl_2$ for 30 min at RT. For immunostaining, fixed samples were first permeabilized with 0.1% Triton X-100 in PBS (5 min, RT). Actin filaments were fluorescently labeled with AlexaFluor-488-conjugated phalloidin (Life Technologies; 1 : 200 dilution, 1 h at RT) for visualization. Cell nuclei were counterstained with DAPI (Life Technologies).

6.14. Image acquisition and analysis

Images of fluorescently stained samples were obtained using an inverted confocal laser scanning microscope (Nikon A1R) or TissueGnostics cell imaging and analysis system mounted to an upright microscope (Zeiss). Cell morphology was quantified from phalloidin stained fluorescent images acquired by a 20× objective from randomly selected regions on the coverslip. Acquired grayscale images were background subtracted and thresholded to convert into binary images using ImageJ software (NIH).

6.15. Statistical Analysis

Statistical analysis was performed using Graphpad Prism v.6 software. Analysis of variance (ANOVA) with the Turkey's Multiple Comparison test was used for all multiple group experiments. P values < 0.05 were deemed significant. Values in graphs are the mean and standard error of mean (SEM).

6.16. Scanning electron microscopy (SEM)

Cells on PA-coated glass coverslips were fixed with 2.5% glutaraldehyde in PBS (containing 1 mM $CaCl_2$) for 1 h at RT. Fixed samples were dehydrated by exposure to a graded series of water-ethanol mixtures. Once in 100% ethanol, samples were dried at the critical point of CO_2 using a critical point dryer (Tousimis Samdri-795) to preserve structural details. Dried samples were then coated with 14 nm of osmium using an osmium plasma coater (Filgen, OPC-60A), and imaged using a Hitachi S-4800 Field Emission Scanning Electron Microscope working at an accelerating voltage of 5 kV.

7. References

(1) Hendricks, M. P.; Sato, K.; Palmer, L. C.; Stupp, S. I. Supramolecular Assembly of Peptide Amphiphiles. Accounts of Chemical Research 2017, 50 (10), 2440–2448.

(2) Berndt, P.; Fields, G. B.; Tirrell, M. Synthetic Lipidation of Peptides and Amino Acids: Monolayer Structure and Properties. Journal of the American Chemical Society 1995, 117 (37), 9515–9522.

(3) Hartgerink, J. D.; Beniash, E.; Stupp, S. I. Self-Assembly and Mineralization of Peptide-Amphiphile Nanofibers. Science 2001, 294 (5547), 1684–1688.

(4) Stephanopoulos, N.; Ortony, J. H.; Stupp, S. I. Self-Assembly for the Synthesis of Functional Biomaterials. Acta Materialia 2013, 61 (3), 912–930.

(5) Velichko, Y. S.; Stupp, S. I.; de la Cruz, M. O. Molecular Simulation Study of Peptide Amphiphile Self-Assembly. The Journal of Physical Chemistry B 2008, 112 (8), 2326–2334.

(6) Silva, G. A.; Czeisler, C.; Niece, K. L.; Beniash, E.; Harrington, D. A.; Kessler, J. A.; Stupp, S. I. Selective Differentiation of Neural Progenitor Cells by High-Epitope Density Nanofibers. Science 2004, 303 (5662), 1352–1355.

(7) Guler, M. O.; Stupp, S. I. A Self-Assembled Nanofiber Catalyst for Ester Hydrolysis. Journal of the American Chemical Society 2007, 129 (40), 12082–12083.

(8) Freeman, R.; Boekhoven, J.; Dickerson, M. B.; Naik, R. R.; Stupp, S. I. Biopolymers and Supramolecular Polymers as Biomaterials for Biomedical Applications. MRS Bulletin 2015, 40 (12), 1089–1101.

(9) Zhang, S.; Greenfield, M. A.; Mata, A.; Palmer, L. C.; Bitton, R.; Mantei, J. R.; Aparicio, C.; de la Cruz, M. O.; Stupp, S. I. A Self-Assembly Pathway to Aligned Monodomain Gels. Nature Materials 2010, 9 (7), 594–601.

(10) Hartgerink, J. D.; Beniash, E.; Stupp, S. I. Peptide-Amphiphile Nanofibers: A Versatile Scaffold for the Preparation of Self-Assembling Materials. Proceedings of the National Academy of Sciences 2002, 99 (8), 5133–5138.

(11) Webber, M. J.; Tongers, J.; Newcomb, C. J.; Marquardt, K.-T.; Bauersachs, J.; Losordo, D. W.; Stupp, S. I. Supramolecular Nanostructures That Mimic VEGF as a Strategy for Ischemic Tissue Repair. Proc Natl Acad Sci U S A 2011, 108 (33), 13438–13443.

(12) Berns, E. J.; Álvarez, Z.; Goldberger, J. E.; Boekhoven, J.; Kessler, J. A.; Kuhn, H. G.; Stupp, S. I. A Tenascin-C Mimetic Peptide Amphiphile Nanofiber Gel Promotes Neurite Outgrowth and Cell Migration of Neurosphere-Derived Cells. Acta Biomaterialia 2016, 37, 50–58.

(13) Shah, R. N.; Shah, N. A.; Del Rosario Lim, M. M.; Hsieh, C.; Nuber, G.; Stupp, S. I. Supramolecular Design of Self-Assembling Nanofibers for Cartilage Regeneration. Proceedings of the National Academy of Sciences 2010, 107 (8), 3293–3298.

(14) Ruoslahti, E. RGD AND OTHER RECOGNITION SEQUENCES FOR INTEGRINS. Annual Review of Cell and Developmental Biology 1996, 12 (1), 697–715.

(15) Aota, S.-I.; Nomizu, M.; Yamada, K. M. The Short Amino Acid Sequence Pro-His-Ser-Arg-Asn in Human Fibronectin Enhances Cell-Adhesive Function. Journal of Biological Chemistry 1994, 269 (40), 24756–24761.

(16) Cavalcanti-Adam, E. A.; Volberg, T.; Micoulet, A.; Kessler, H.; Geiger, B.; Spatz, J. P. Cell Spreading and Focal Adhesion Dynamics Are Regulated by Spacing of Integrin Ligands. Biophysical Journal 2007, 92 (8), 2964–2974.

(17) Stöber, W.; Fink, A.; Bohn, E. Controlled Growth of Monodisperse Silica Spheres in the Micron Size Range. Journal of Colloid and Interface Science 1968, 26 (1), 62–69.

(18) Thomassen, L. C. J.; Aerts, A.; Rabolli, V.; Lison, D.; Gonzalez, L.; Kirsch-Volders, M.; Napierska, D.; Hoet, P. H.; Kirschhock, C. E. A.; Martens, J. A. Synthesis and Characterization of Stable Monodisperse Silica Nanoparticle Sols for in Vitro Cytotoxicity Testing. Langmuir 2010, 26 (1), 328–335.

(19) Quignard, S.; Hélary, C.; Boissière, M.; Fullana, J.-M.; Lagrée, P.-Y.; Coradin, T. Behaviour of Silica Nanoparticles in Dermis-like Cellularized Collagen Hydrogels. Biomater. Sci. 2014, 2 (4), 484–492.

(20) Sur, S.; Matson, J. B.; Webber, M. J.; Newcomb, C. J.; Stupp, S. I. Photodynamic Control of Bioactivity in a Nanofiber Matrix. ACS Nano 2012, 6 (12), 10776–10785.

(21) Dillow, A. K.; Ochsenhirt, S. E.; McCarthy, J. B.; Fields, G. B.; Tirrell, M. Adhesion of A5β1 Receptors to Biomimetic Substrates Constructed from Peptide Amphiphiles. Biomaterials 2001, 22 (12), 1493–1505.

(22) Mardilovich, A.; Craig, J. A.; McCammon, M. Q.; Garg, A.; Kokkoli, E. Design of a Novel Fibronectin-Mimetic Peptide−Amphiphile for Functionalized Biomaterials. Langmuir 2006, 22 (7), 3259–3264.

(23) Ochsenhirt, S.; Kokkoli, E.; Mccarthy, J.; Tirrell, M. Effect of RGD Secondary Structure and the Synergy Site PHSRN on Cell Adhesion, Spreading and Specific Integrin Engagement. Biomaterials 2006, 27 (20), 3863–3874.

(24) Benoit, D. S. W.; Anseth, K. S. The Effect on Osteoblast Function of Colocalized RGD and PHSRN Epitopes on PEG Surfaces. Biomaterials 2005, 26 (25), 5209–5220.

(25) Susuki, Y.; Hojo, K.; Okazaki, I.; Kamata, H.; Sasaki, M.; Maeda, M.; Nomizu, M.; Yamamoto, Y.; Nakagawa, S.; Mayumi, T. Preparation and Biological Activities of a Bivalent Poly (Ethylene Glycol) Hybrid Containing an Active Site and Its Synergistic Site of Fibronectin. Chemical and pharmaceutical bulletin 2002, 50 (9), 1229–1232.

(26) Chen, X.; Sevilla, P.; Aparicio, C. Surface Biofunctionalization by Covalent Co-Immobilization of Oligopeptides. Colloids and Surfaces B: Biointerfaces 2013, 107, 189–197.

(27) Kao, W. J.; Lee, D.; Schense, J. C.; Hubbell, J. A. Fibronectin Modulates Macrophage Adhesion and FBGC Formation: The Role of RGD, PHSRN, and PRRARV Domains. Journal of Biomedical Materials Research Part A 2001, 55 (1), 79–88.

(28) Kim, T.-I.; Jang, J.-H.; Lee, Y.-M.; Ryu, I.-C.; Chung, C.-P.; Han, S.-B.; Choi, S.-M.; Ku, Y. Design and Biological Activity of Synthetic Oligopeptides with Pro-His-Ser-Arg-Asn (PHSRN) and Arg-Gly-Asp (RGD) Motifs for Human Osteoblast-like Cell (MG-63) Adhesion. Biotechnology letters 2002, 24 (24), 2029–2033.

(29) Rinker, S.; Ke, Y.; Liu, Y.; Chhabra, R.; Yan, H. Self-Assembled DNA Nanostructures for Distance-Dependent Multivalent Ligand–protein Binding. Nature Nanotechnology 2008, 3 (7), 418–422.

(30) Diezmann, F.; Seitz, O. DNA-Guided Display of Proteins and Protein Ligands for the Interrogation of Biology. Chemical Society Reviews 2011, 40 (12), 5789–5801.

(31) Freeman, R.; Stephanopoulos, N.; Álvarez, Z.; Lewis, J. A.; Sur, S.; Serrano, C. M.; Boekhoven, J.; Lee, S. S.; Stupp, S. I. Instructing Cells with Programmable Peptide DNA Hybrids. Nature Communications 2017, 8, 1–11.

(32) Akiyama, S. K.; Olden, K.; Yamada, K. M. Fibronectin and Integrins in Invasion and Metastasis. Cancer and Metastasis Reviews 1995, 14 (3), 173–189.

(33) Wang, X.; Yan, C.; Ye, K.; He, Y.; Li, Z.; Ding, J. Effect of RGD Nanospacing on Differentiation of Stem Cells. Biomaterials 2013, 34 (12), 2865–2874.

(34) Schvartzman, M.; Palma, M.; Sable, J.; Abramson, J.; Hu, X.; Sheetz, M. P.; Wind, S. J. Nanolithographic Control of the Spatial Organization of Cellular Adhesion Receptors at the Single-Molecule Level. Nano Letters 2011, 11 (3), 1306–1312.

(35) Koo, L. Y.; Irvine, D. J.; Mayes, A. M.; Lauffenburger, D. A.; Griffith, L. G. Co-Regulation of Cell Adhesion by Nanoscale RGD Organization and Mechanical Stimulus. Journal of cell science 2002, 115 (7), 1423–1433.

(36) Huang, J.; Gräter, S. V.; Corbellini, F.; Rinck, S.; Bock, E.; Kemkemer, R.; Kessler, H.; Ding, J.; Spatz, J. P. Impact of Order and Disorder in RGD Nanopatterns on Cell Adhesion. Nano Letters 2009, 9 (3), 1111–1116.

(37) Huang, J.; Ding, J. Nanostructured Interfaces with RGD Arrays to Control Cell–matrix Interaction. Soft Matter 2010, 6 (15), 3395–3401.

(38) Graeter, S. V.; Huang, J.; Perschmann, N.; López-García, M.; Kessler, H.; Ding, J.; Spatz, J. P. Mimicking Cellular Environments by Nanostructured Soft Interfaces. Nano Letters 2007, 7 (5), 1413–1418.

(39) Arnold, M.; Hirschfeld-Warneken, V. C.; Lohmüller, T.; Heil, P.; Blümmel, J.; Cavalcanti-Adam, E. A.; López-García, M.; Walther, P.; Kessler, H.; Geiger, B.; et al. Induction of Cell Polarization and Migration by a Gradient of Nanoscale Variations in Adhesive Ligand Spacing. Nano Letters 2008, 8 (7), 2063–2069.

(40) Arnold, M.; Schwieder, M.; Blümmel, J.; Cavalcanti-Adam, E. A.; López-Garcia, M.; Kessler, H.; Geiger, B.; Spatz, J. P. Cell Interactions with Hierarchically Structured Nano-Patterned Adhesive Surfaces. Soft Matter 2009, 5 (1), 72–77.

(41) Arnold, M.; Cavalcanti-Adam, E. A.; Glass, R.; Blümmel, J.; Eck, W.; Kantlehner, M.; Kessler, H.; Spatz, J. P. Activation of Integrin Function by Nanopatterned Adhesive Interfaces. ChemPhysChem 2004, 5 (3), 383–388.

III. Nanostructuration of 3D surfaces: Clusterization on silica nanoparticles

Content

1. Introduction to Patchy Particles

Nanoparticles of different size, shape and chemistry can be incorporated within materials to tune their optical, magnetic, mechanical properties.[1,2] The functionality of the resulting composites can also be modulated by modifying the surface chemistry of the nanoparticles and by grafting functional ligands. This is particularly relevant in a biological context, because biomolecules such as nucleic acids,[3–5] peptides and proteins[6–8] can be conjugated at the surface of nanoparticles, favoring the interface with a biological environment. In addition to the chemical nature of the biological ligand, its spatial distribution is key to drive a given cell behavior.[9] In particular, the clustering of biomolecules is ubiquitous in biological systems and has to be reproduced in synthetic systems.[10–12] Patchy particles are patterned particles with at least one chemically-defined domain or *patch*.[13,14] Patchy particles have raised a large interest given their chemical nanostructuration making them prone to self-assemble into colloidal crystals. As such, they may serve as photonic bandgap structures with potential use for nano- and bio-photonic applications,[15,16] as well as for electronics[17] and targeted drug delivery.[18,19] Back to the single nano-object, the formation of a patch defines an inhomogeneous distribution of surface ligands, leading to the formation of clusters. Moreover, the delimitation of a functional domain leads to nanoparticles with multiple surface chemistries and functionalities, where a distinct chemistry is accessible all around or in between patches. These two features – clustering and bifunctionality – are of particular interest when dealing with the biofunctionalization of nanoparticles to be incorporated within biomaterials.

In the last decades many strategies have been employed to synthesize patchy particles, including Janus nanoparticles, by vapor deposition onto a nanoparticle monolayer (by glancing-angle vapor deposition[20] or lithography[21]), or in a liquid environment. In this last case, several possibilities have been tested, like template-assisted fabrication where only one patch is created,[22–24] or by Pickering emulsion.[25,26] Examples exist in the literature of direct self-assembly of particles through evaporation-driven colloidal assembly by Manoharan and coworkers.[27–29] Particle lithography can also be performed in a liquid environment.[21] Finally liquid streams in capillaries have also been used to create multiphasic particles.[30–32] Ravaine and co-workers proposed a method of seeded emulsion polymerization at the surface of silica nanoparticles (SiNPs) for the formation of polystyrene, gold or silica nodules.[33–35] Alternatively, molecular approaches have been developed to create localized patches using anisotropic particles that exhibit spatially-defined reactivities,[36–38] or based on the segregation of functional ligands during particles synthesis or at their surface.[39–41]

In this context, we have explored a new strategy involving amorphous spherical SiNPs and self-assembling alkoxysilanes to induce the formation of functional patches on their surface. Silane chemistry is very versatile and allows to design and synthesize virtually any precursor to be hydrolyzed and condensed *via* a sol-gel route,[39,40,42–46] including for their grafting at SiNP surfaces. The SiNPs then serve as a platform with multiple chemistries that could enable the display of bioactive peptides.

In order to control the nanostructuration of the SiNP surface and direct the formation of patches, we have designed and synthesized several precursors that are self-assembling alkoxysilanes. Those precursors meet several criteria. They bear a moiety that will favor self-assembly (in blue on the Figure III-1-A), a chemical group of interest for further bioconjugation (in red on the Figure III-1-A) and an alkoxysilane function (in yellow on the Figure III-1-A). A polycyclic aromatic group was selected to introduce self-assembling properties to the precursor. It can be removed in a following step by an acidic treatment to reveal the function of interest. The alkoxysilane should allow for grafting on the surface of the SiNPs by a sol-gel route. With this design, different contributions have to be taken into account in the self-assembly process and those molecules are expected not to have the same behavior in a polar or non-polar solvent, exposing only their polar (or apolar) moiety according to the chosen solvent.

Our strategy requires precursors to first self-assemble in solution before their transfer at the surface to create SiNP-1 (Figure III-1-B), while a following acidic treatment frees the function of interest on SiNP-2 (Figure III-1-B). The size and distribution of the patches may be tuned by modifying the size and shape of the self-assemblies in solution, playing with the concentration and solvent. A second molecule of interest may also be grafted in between patches, in two-steps or simultaneously, in order to create bi-functional patchy particles.

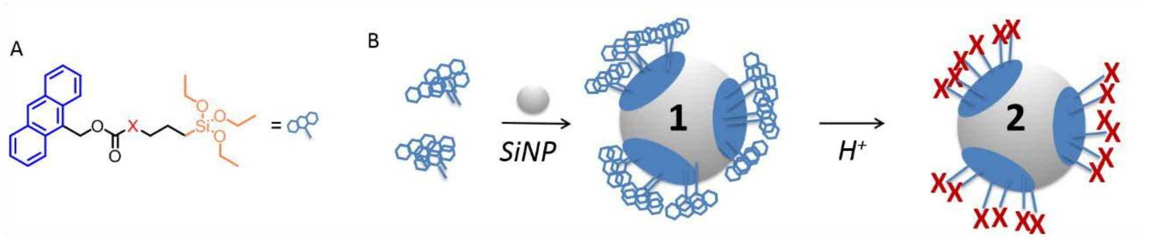

Figure III-1 : (A) Molecular structure of a typical synthesized alkoxysilane, (B) Schematic representation of the synthesis of patchy particles *via* the self-assembly of alkoxysilanes. Transfer of self-assemblies on SiNPs creates SiNP-1. Acidic hydrolysis can be used to reveal functions of interest on SiNP-2.

2. Synthesis of self-assembling silanes bearing an aromatic moiety

We synthesized thanks to the help of Nicolas Delsuc (Laboratory of Biomolecules, Ecole Normale Supérieure) a library of precursors based on the previously-described molecular design. All molecules contained a triethoxysilane and an aromatic moiety hiding a function of interest *via* a cleavable carbamate group (also named urethane linkage). The aromatic group could be a anthracene (Figure III-2-A,C) or a pyrene (Figure III-2-B,D). The function of interest was an amine group, colored in red, that can be used to further graft molecules at the surface of the SiNPs, such as a bioactive peptide by peptide conjugation. This amine was protected using an aromatic carbamate that can be hydrolyzed in acidic conditions, thus releasing the aromatic group and revealing the amine function. All these molecules present an amphiphilis character given the π-stacking and hydrophobic character of the aromatic group and hydrogen bond forming properties of the carbamate and alkoxysilane groups.

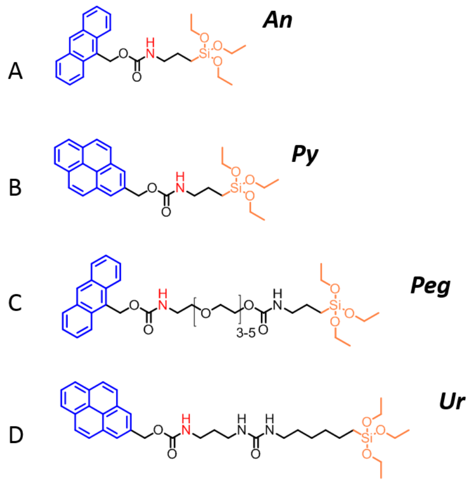

Figure III-2 : Molecular structure of the synthesized precursors (A) N-[3-(Triethoxysilyl)propyl]-anthracen-9-ylmethyl carbamate, (B) N-[3-(Triethoxysilyl)propyl]-pyren-9-ylmethyl carbamate, (C) N-[N-[3-(Triethoxysilyl)propyl]-(n-polyethyleneglycol-ethyl ether) carbamate]]-pyren-9-ylmethyl carbamate and (D) N-[N-[3-(Triethoxysilyl)propyl]-N'-propyl urea]]-pyren-9-ylmethyl carbamate.

For the next parts of this manuscript, the precursors will be designated as listed in Table III-1.

An	N-[3-(Triethoxysilyl)propyl]-antracen-9-ylmethyl Carbamate
Py	N-[3-(Triethoxysilyl)propyl]-pyren-9-ylmethyl Carbamate
Peg	N-[N-[3-(Triethoxysilyl)propyl]-(n-polyethyleneglycol-ethyl ether) Carbamate]]-pyren-9-ylmethyl Carbamate
Ur	N-[N-[3-(Triethoxysilyl)propyl]-N'-propyl urea]]-pyren-9-ylmethyl Carbamate.

Table III-1 : Nomenclature of synthesized precursors

2.1. Synthesis of the An precursor

The first organic precursor synthesized for this study was the N-[3-Triethoxysilyl)propyl]-anthracen-9-ylmethyl carbamate (Figure III-2-A), bearing an anthracene moiety as aromatic group.

During the synthesis of **An (**Scheme III-1**)**, the alcohol function of the anthracene derivative, 9-anthracenemethanol, reacts with the isocyanate to create a carbamate. This reaction proceeds in basic conditions using a non-nucleophilic base, here triethylamine.

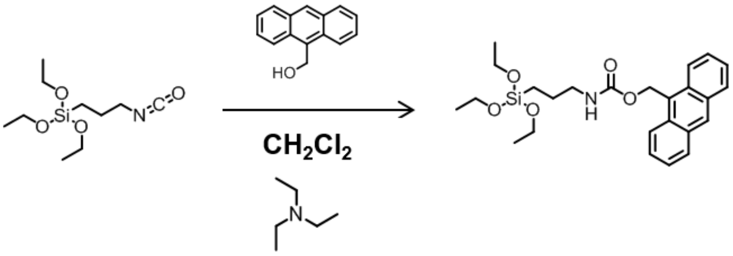

Scheme III-1 : Synthesis of *An*.

This reaction was performed several times, with a yield of approximately 87%. At the end of our first preparation, the main peak observed in Mass Spectrometry (MS, Figure III-3) matched with the expected mass of 478,2 Da. ^{1}H Nuclear Magnetic Resonance (NMR) analysis was also consistent with the molecular structure (Figure III-4). However, the product recovered after the second batch did not have the same aspect and solubility than the first one. We identified the presence of a small amount of an impurity in the first batch characterized by a m/z = 150 in Mass Spectrometry (Figure III-3) and a triplet peak at 1.2 ppm, a quartet at 3.5

ppm and singlet at 5.4 ppm in the ^{1}H NMR spectrum (Figure III-4). This impurity is most probably a triethylamine derivative but it has not been formally identified. The presence of this impurity leads to very different behaviors of the precursors in terms of appearance, solubility and self-assembly thus biasing the results. A purification by column chromatography on silica gel was required to remove this impurity in order to obtain reproducible results for the self-assembly behavior study.

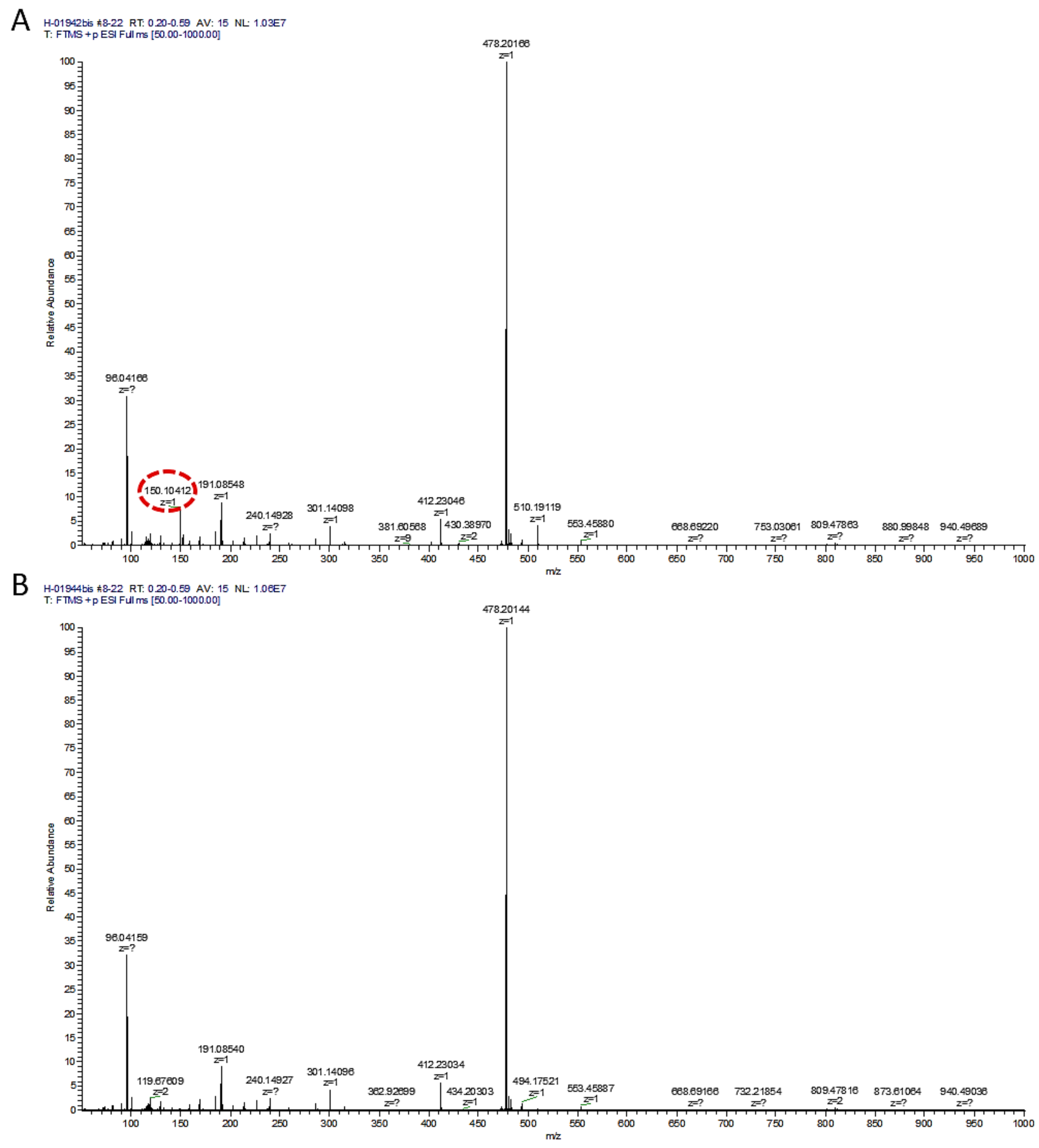

Figure III-3 : Mass Spectrometry spectra of two batches of the anthracene precursor showing an impurity in the first one (A) –p ESI in methanol.

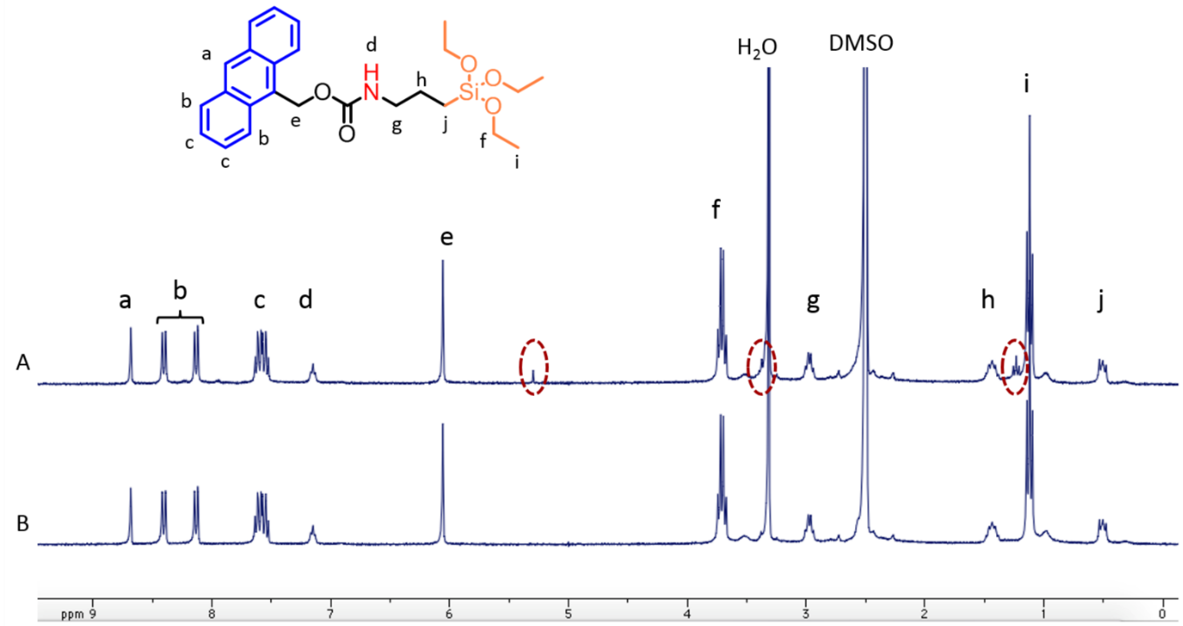

Figure III-4 : ^{1}H NMR spectra of two batches of the anthracene precursor showing an impurity in the first one (A).

2.2. Synthesis of the *Py* precursor

We chose to synthesize **Py** (Figure III-2-B) for the extended aromatic surface of the pyrene group and its fluorescence properties. Indeed, pyrene molecules are convenient probes to study the distance between molecules and, by extension, the distance between silanes within self-assembled structures, which should be really useful for our study.

The procedure to synthesize this molecule (Scheme III-2) was identical to **An**, but using 1-Pyrenemethanol instead of 1-Anthracenemethanol. The crude was also purified by silica-gel column chromatography. The synthesis was achieved with a yield of 65%, with no issue in reproducibility and no identified impurity.

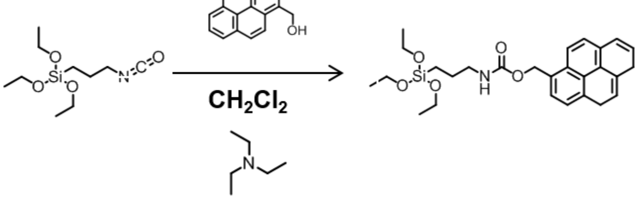

Scheme III-2 : Synthesis of precursor *Py*.

2.3. Design of new precursors by introducing a PEG or a Urea moiety

The two first precursors differ in their aromatic part, thus tuning their hydrophobicity. In order to increase the importance of the hydrophilic part, we have designed two other precursors derived from the **Py**: one by adding a Polyethylene glycol (PEG) linker and the other by incorporating a urea group. The PEG unit was introduced to increase the hydrophilicity of this part of the molecules and thus strengthening the amphiphilic character, whereas the urea function was incorporated to introduce more hydrogen bond donors and acceptors.[48–53] In both cases, we were hoping that the behavior of these precursors could differ and generate interesting self-assembled structures.

2.3.1. Synthesis of the *Peg* precursor

The synthesis of the Peg precursor (Figure III-2-C) starts from the commercially-available PEG functionalized triethoxysilane (Scheme III-3). The commercial PEG reagent contains 4 to 6 EG units. The final product would then be a mixture of silanes, which is not ideal for their intended use. However, this system was a good candidate to test this synthesis pathway and evaluate whether a PEG-containing product would exhibit interesting self-assembling properties.

In order to introduce the alkyl isocyanate group and create the first precursor **Peg-1** the procedure described in [54] was followed. Having an isocyanate on the PEG moiety would allow us to follow the same synthesis path as with the 9-anthracenemethanol. In this reaction, the tetrabutylammonium cyanate (Bu_4NOCN) is the source of isocyanate and 2,3-Dichloro-5,6-dicyano-p-benzoquinone (DDQ) and Triphenylphosphine (PPh_3) are used to generate a good leaving group and thus to favor the nucleophilic substitution.

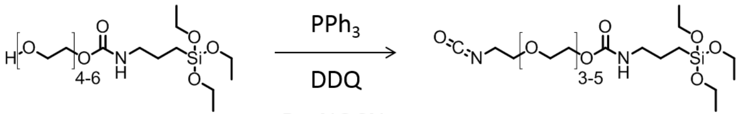

Scheme III-3 : First step of the synthesis of *Peg*.

In a first attempt, no product was obtained after purification. In a second attempt, the eluent of chromatography was modified, from cyclohexane: ethyl acetate to dichloromethane:

methanol with the hope to take down any product interacting too strongly with the silica column.

The recovered product was a yellow-brown oil. The PEG moiety could be identified on the ^{1}H NMR spectrum, with distinct chemical shifts compared to the initial reagent. The analysis by Infrared spectroscopy in an Attenuated Total Reflectance mode (IR-ATR) showed a vibration band at 2203 cm^{-1} signing for the presence of an isocyanate group (Figure III-5).

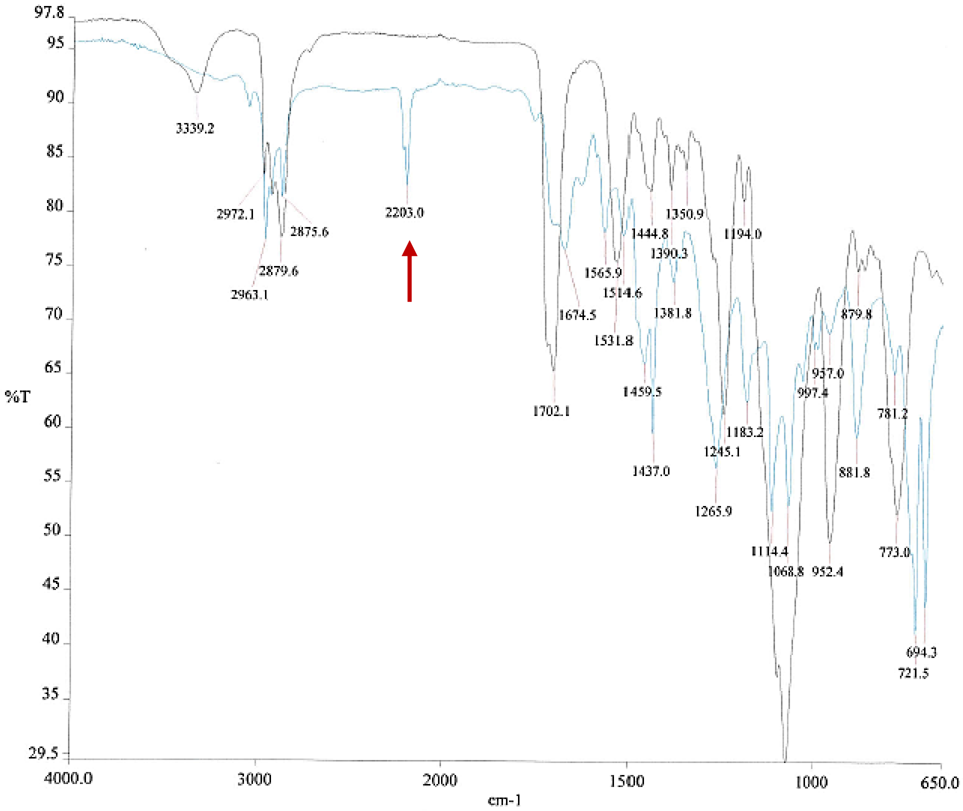

Figure III-5 : IR-ATR spectra of the PEG-silane molecule before (dark) and after (light blue) reaction with Bu_4NOCN.

The recovered molecule was then linked to the anthracene derivative following the protocol already described in paragraph 2-2 and depicted on Scheme III-4. However, we were not able to identify the targeted product **Peg** by NMR and IR-ATR. The isocyanate was probably not stable enough or maybe not even correctly synthesized. Indeed, the isocyanate moiety identified by IR-ATR may originate from DDQ still present in the product despite all purification steps.

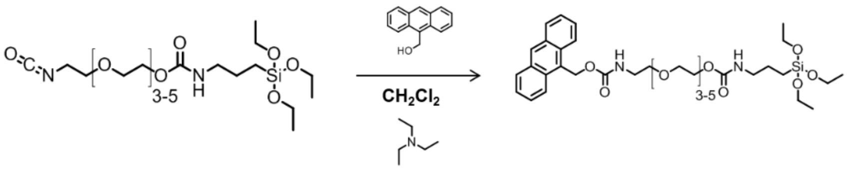

Scheme III-4 : Second step of the synthesis of *Peg.*

At this stage, we decided not to continue our attempts to obtain this precursor. It would certainly be interesting to reinvestigate this synthesis in the future, in particular starting from a pure PEGylated silane instead of a mixture.

2.3.2. Synthesis of the *Ur* precursor

To synthesize the **Ur** precursor (Figure III-2-D), the difunctional 1,6-Diisocyanatohexane was used to create **Ur-1** with a pyrene function at one side and the urea at the other. This bi-isocyanate reacted first with the alcohol function of the pyrene-methanol derivative (described on Scheme III-5). A large excess (5 equivalents) of diisocyanatohexane was used in order to avoid the symmetrical by-product resulting from the reaction of both isocyanates with pyrenemethanol. The excess of diisocyanatohexane was eliminated by washing the solid with cyclohexane.

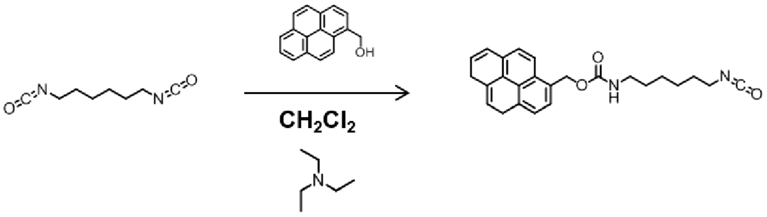

Scheme III-5 : First step of the synthesis of *Ur.*

In a the second step, the remaining isocyanate function was reacted with the amine of (3-Aminopropyl)triethoxysilane (APTES) as described on Scheme III-6 to generate the expected urea function. The crude product was then purified by silica-gel column chromatography to obtain the expected compound, as checked by ^{1}H NMR, with an overall yield of 31% over two steps.

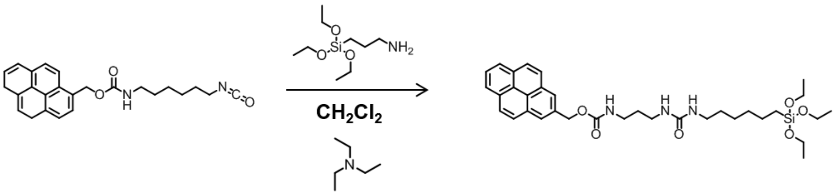

Scheme III-6 : Second step of the synthesis of *Ur*.

Altogether, among the four designed molecules, three of them were successfully synthesized with good reproducibility and obtained with excellent purities, as confirmed by NMR, being therefore suitable for further investigations of their self-assembling properties.

3. Self-assembly of the synthesized alkoxysilanes

The formation of functional domains, or patches, at the surface of SiNPs first requires to investigate the self-assembling behavior of **An**, **Py** and **Ur** in solution as a function of solvent and concentration. In terms of concentration, a broad range was first investigated, from few µM to 50 mM.

3.1. Self-assembling behavior of An

3.1.1. Fluorescence spectroscopy

Anthracene is a polycyclic aromatic hydrocarbon composed of three linearly-fused benzene rings. The presence of the anthracene moiety confers unique optical properties to **An**.[55,56] Its fluorescence signal evolves as a function of its concentration in ethanol and in toluene (Figure III-6-A and B respectively). At a concentration as low as 0.01 µM in toluene, the fluorescence emission of the anthracenic alkoxysilane (λ_{exc} = 365 nm) shows three bands at 390 nm, 413 nm and 437 nm and a shoulder centered at 465 nm, the band at 413 nm being the most intense one (Figure III-6-C). This emission spectrum is attributed to the monomer state of **An**. In both solvents, with increasing concentration, the overall fluorescence intensity increases and then decreases. Some changes in the relative intensities of the different peaks are also observed and, in particular, the band at 390 nm disappears around 10 mM.

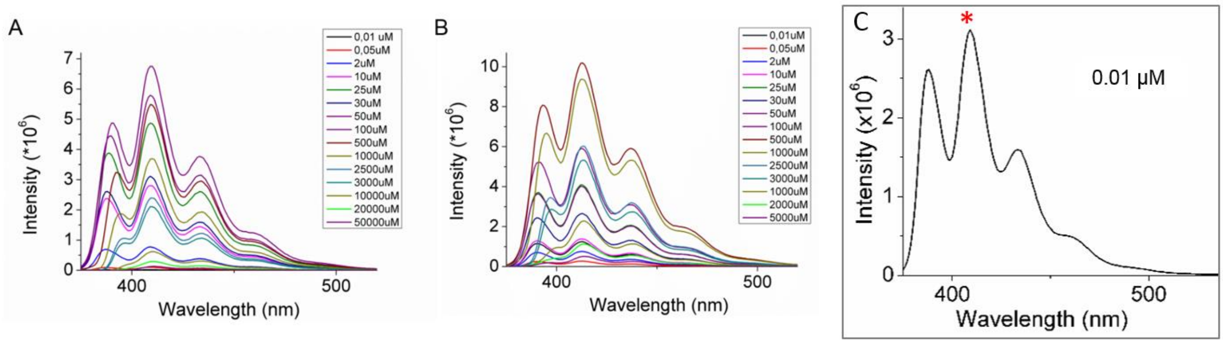

Figure III-6 : Fluorescence spectra of *An* (A) in ethanol and (B) in toluene; (C) Monomer signature at 0.01 µM in toluene.

We have followed more precisely the evolution of the emission properties of **An** with increasing concentration from 0.01 µM to 50 mM in ethanol and toluene by plotting the maximum intensity at 413 nm as a function of concentration (Figure III-7-A). Two regimes can be distinguished: at low concentration, the fluorescence intensity increases almost linearly before decreasing with increasing concentration (see the zoom-in region on Figure III-7-B). This transition occurs when reaching a concentration of 0.6 mM in toluene and between 0.05 and 0.1 mM in ethanol (on Figure III-7-B). The decrease in emission with increasing concentration can be attributed to a very efficient self-quenching of the anthracene fluorescence due to intermolecular interactions. As expected, this phenomenon is observed at lower concentrations in ethanol than in toluene, the latter being a better solvent for the anthracene rings that are therefore less likely to interact via π–stacking.

If we take a closer look at relevant concentrations of **An** within the investigated range, we observe that the emission spectra of the silane at 100 µM in toluene and in ethanol are of similar intensity and very similar to the monomer signature, with a slightly higher intensity of the peak at 390 nm in toluene (Figure III-7-C). At 10 mM however, the emission intensity decreases in both solvents, to a much higher extent in ethanol than in toluene (Figure III-7-D). This self-quenching can be associated with intermolecular interactions between anthracene rings and can therefore sign for the formation of supramolecular structures. This phenomenon is even more striking when reaching 50 mM (Figure III-7-E). Again this effect is more marked in ethanol, with the full disappearance of the monomer band at 390 nm, than in toluene. This indicates that more precursors are interacting one with another *via* their anthracene rings in this solvent and therefore suggests that larger self-assemblies are formed than in toluene.

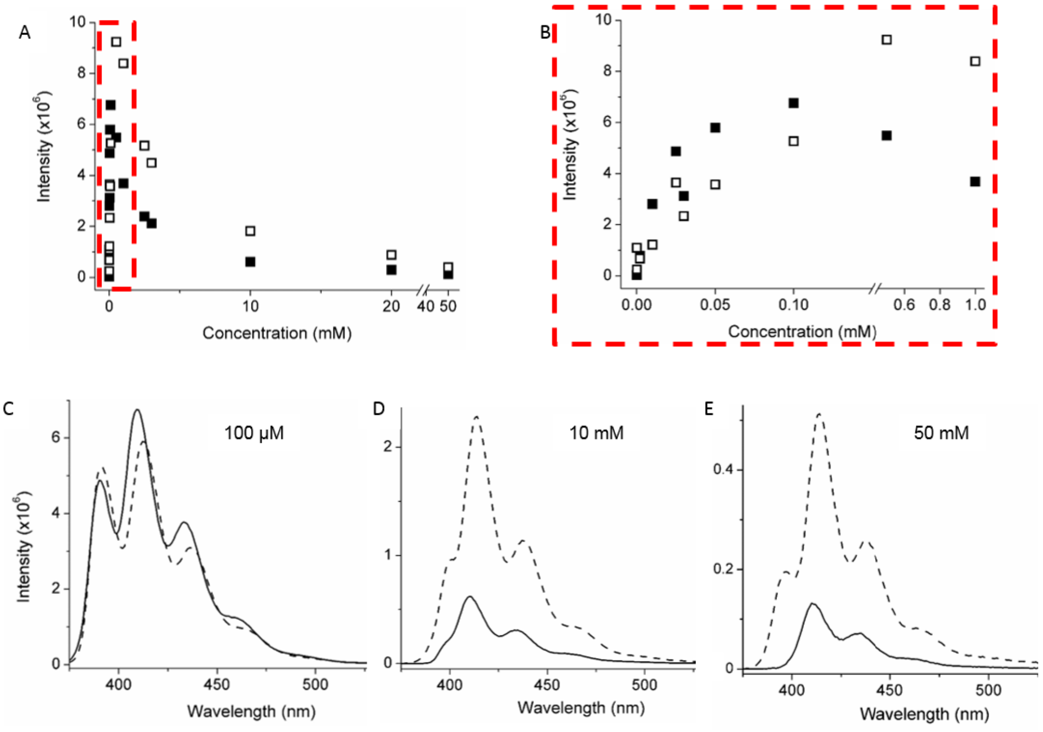

Figure III-7 : Fluorescence spectroscopy of *An*. (A,B) Fluorescence emission of *An* at λ_{em} 413 nm (λ_{exc} = 365 nm) in toluene (open squares) and ethanol (solid squares) as a function of concentration. (C-E) Fluorescence emission spectra of *An* in toluene (dashed lines) and in ethanol (solid lines) at 100 µM, 10 mM and 50 mM respectively.

Unlike some other aromatic hydrocarbons, no excimer emission has been reported for anthracene in solution in the absence of any spatial constraints, such as crystallization or covalent interactions between aromatic rings. Consequently, no apparition of red shifted bands in the optical spectra is expected in case of the formation of self-assemblies, in good agreement with our observations. However, in the excited state, anthracene molecules are able to form photo-dimers. This photo-reversible process depends on experimental conditions (concentration, solvent) and can be controlled.[57–62] The loss of intensity obtained in the case of **An** is probably a consequence of the formation of those photodimers.

3.1.2. Dynamic light scattering

Dynamic light scattering (DLS) has been used to further investigate the formation of supramolecular objects in both solvents with increasing concentration of **An**. In ethanol, no detectable objects could be detected at concentrations lower than 0.5 mM. From this value, well-defined monodisperse assemblies were measured with a hydrodynamic diameter of 425 nm (Figure III-8-A, solid circles). The assemblies then grow with increasing concentration until a hydrodynamic diameters of 1180 nm at 50 mM. In toluene, supramolecular structures could be detected from 2.5 mM, showing the appearance of two populations having hydrodynamic diameter of 20 and 440 nm. The proportion of the population is represented by the size of the circle on the graph. A red square indicates the smallest dot to facilitate the reading. As Rayleigh light scattering is related to the particle diameter to the power of 6, the population with the smallest diameter is difficult to observe with a size distribution by intensity. To better interpret the data coming from smallest size objects, the size distribution obtained by DLS has been corrected and given in terms of number (Figure III-8-B, open circles). This better shows that progressively, with increasing concentration, the importance of the population at 20 nm decreases until disappearance above 20 mM, while the larger one increases in number and in size stabilizing around 630 nm. For the rest of the investigation, two concentrations were selected: 10 and 50 mM, showing objects of 930 and 1180 nm in ethanol, and of 20 and 630 nm in toluene.

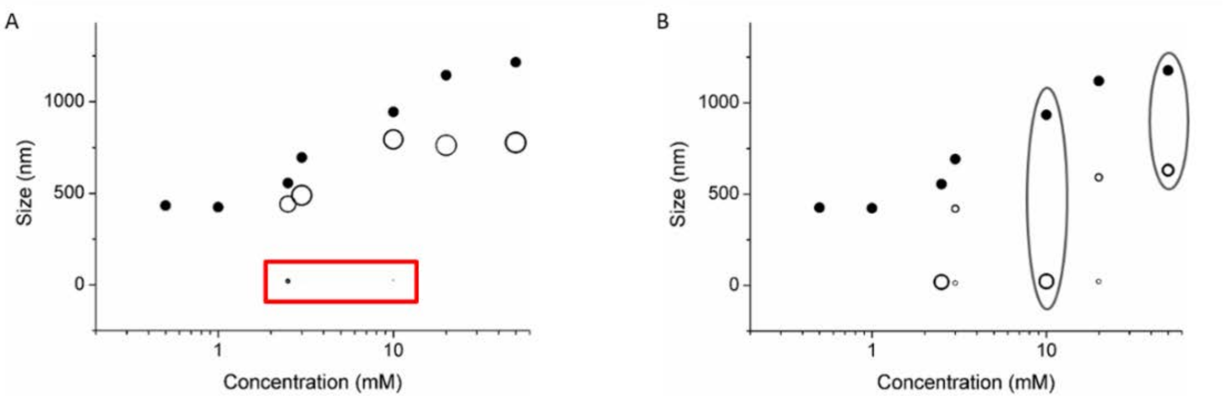

Figure III-8 : DLS of *An* in toluene (open circles) and in ethanol (solid circles) as a function of concentration plotted as intensity and number respectively.

The anthracene self-assembly was remarkably stable over time in ethanol, Figure III-9. For all concentrations from 1 mM to 50 mM, no major changes were recorded between T0 after dissolution by sonication (light blue curve), 40 min rest (darker blue curve) and overnight rest (black curve). Even after sonication (dotted black curve) and 40 min rest (grey curve) we could not induce any change. Therefore, the self-assemblies do not evolve with time and appear really resistant to external perturbations.

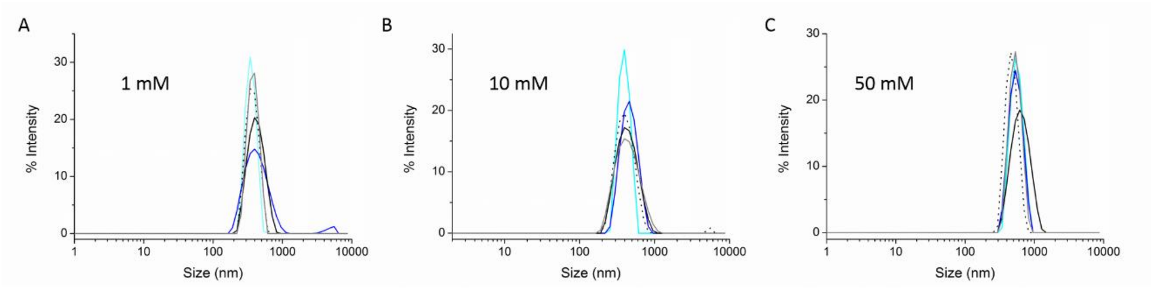

Figure III-9 : DLS study of the stability of the self-assembly of *An* in ethanol over time: T0 after dissolution by sonication (light blue curve), 40 min rest (darker blue curve), overnight resting (black curve), sonication again (dotted black curve) and 40 min rest (grey curve) at (A) 1 mM, (B) 10 mM and (C) 50 mM.

The stability over time was also studied in toluene. In this condition, at 5 mM and 10 mM, the self-assembled structures grew with time (from light blue curve at T0 to black curve after an overnight rest, Figure III-10). This suggests that self-assemblies need time to reach an equilibrium. Sonication (dotted black curve) helped to reduce their size. At 50 mM, the self-assembled systems seemed to be stable, maybe because they reached their equilibrium faster.

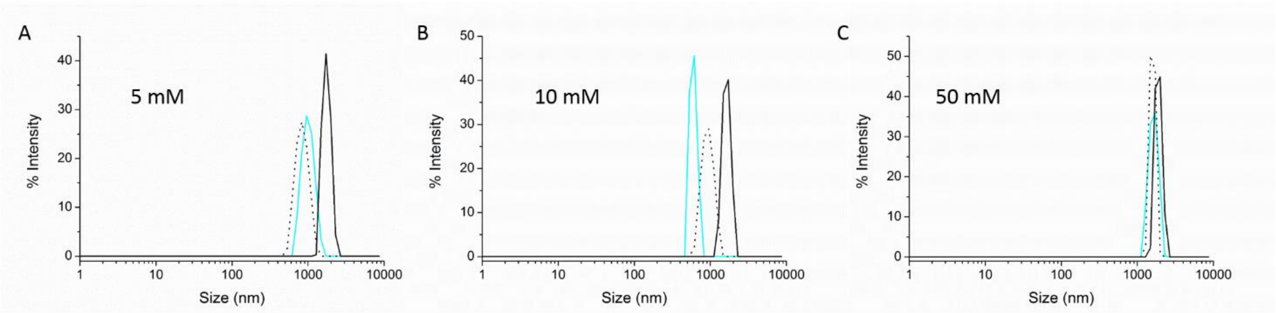

Figure III-10 : DLS study of the stability of the self-assembly of *An* in toluene over time: T0 after dissolution by sonication (light blue curve), overnight resting (black curve), and sonication again (dotted black curve) at (A) 5 mM, (B) 10 mM and (C) 50 mM.

We must notice that some variations in the size of the self-assembled objects at a given concentration were obtained from one set of experiments to the other (for instance when changing the precursor synthetic batch or the solvent bottle) but the here-reported evolutions were always the same.

3.1.3. CryoTEM of supramolecular structures

Cryo-TEM was then used to investigate the supramolecular objects in solution (Table III-2 and Figure III-11). Those images were obtained in collaboration with G. Mosser and P. Le Griel (LCMCP, Sorbonne Université) and G. Pehau-Arnaudet (Institut Pasteur). In toluene, at 10 mM the molecule self-assembled into nanospheres with a mean diameter of 75 nm (Figure III-11-A). At a concentration of 50 mM, nanospheres are still present, but ill-defined larger structures could be observed with a diameter of *ca*. 410 nm (Figure III-11-B-D) in agreement with the size increase measured by DLS. In ethanol, different assemblies could be observed under cryoTEM. At 10 mM, platelets were identified with a width of *ca*. 80 nm and a length of ca. 385 nm (Figure III-11-E). Larger objects were detected upon increasing concentration to 50 mM. Microneedles were observed with a width of 220 nm and a length in the range of few micrometers (3 µm in average over 34 microneedles, Figure III-11-F-H).

Solvent	**Concentration**	**Size (nm)**	**Std. dev. (nm)**	**Population**
Toluene	10 mM	73	34	53 nanospheres
	50 mM	410	203	17 assemblies
Ethanol	10 mM	83 (width)	27	11 platelets
		387 (length)	74	6 platelets
	50 mM	219 (width)	65	47 microneedles
		3300 (length)	1300	34 microneedles

Table III-2 : Cryo-TEM analysis of *An* self-assemblies.

The growth of nano- to micrometric objects results from molecular self-assembly based on different contributions including π-stacking of the anthracene group and the hydrogen bonding of the carbamate and alkoxysilane groups. This explains why different self-assembling behaviors are observed in a rather polar – ethanol- and in non-polar - toluene - solvent. In toluene the anthracene group interacts favorably with the molecules of solvent. This should favor the formation of micelle-type spherical structures, burying the alkoxysilane moiety of the molecule inside the spheres. At higher concentrations, the balance between different self-assembly driving forces leads to the apparition of a second population with indistinct contour. Extended packing of the anthracene rings by π-stacking probably creates larger structuration of the molecule. In ethanol, intermolecular interactions between anthracene groups occur at lower concentrations than in toluene because the solvatation of the anthracene rings is less efficient.

Indeed, the anthracene moiety exhibits a rigid planar molecular structure that makes possible molecular packing with maximum overlap in a preferred direction leading to highly anisotropic structures such as the microneedles (Figure III-12). The polar moieties (carbamate and triethoxysilane) may be in direct contact with the protic solvent, burying the hydrophobic moiety.

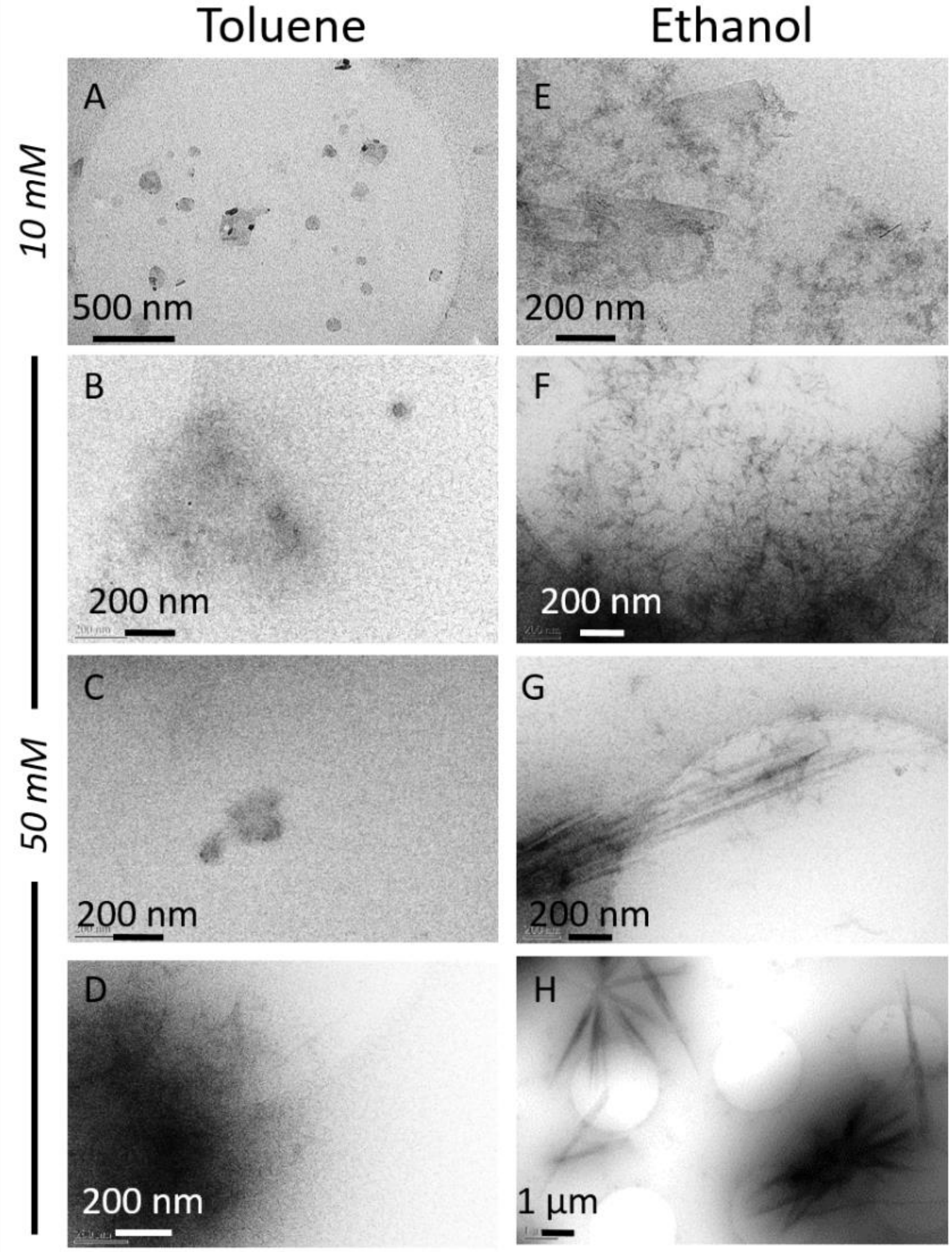

Figure III-11 : Cryo-TEM observations of *An* in toluene and ethanol at 10 mM and 50 mM.

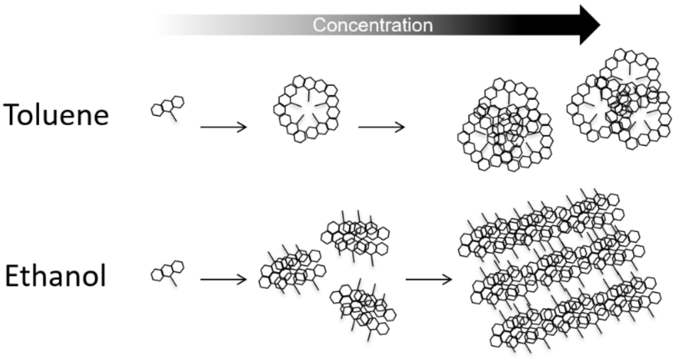

Figure III-12 : Hypothesis on self-assembly mechanism for *An*.

3.2. Self-assembly of *Py*

3.2.1. Fluorescence Analysis

When **Py** is solubilized in toluene or ethanol, its fluorescence spectrum (λ_{exc} = 365 nm) is evolving as a function of concentration (Figure III-13-A,B). Two distinct bands are visible at 393 nm and 413 nm, named respectively 1 and 2. When the concentration increases, a band at 474 nm, indicated by 3, appears. At low concentration, 0.05 µM in ethanol and toluene, we obtained a signal that we attributed to the monomer signature [63] (on Figure III-13-C) with two distinct bands 1 and 2. The concentration threshold for the appearance of band 3 is lower in ethanol than in toluene, around 1 mM.

We have followed more precisely the evolution of the emission properties of **Py** with increasing concentration from 0.01 µM to 50 mM in ethanol and toluene by plotting the maximum intensity at 393 nm, 413 nm and 474 nm as a function of concentration (Figure III-13-D-F). At 393 nm and 413 nm, two regimes can be distinguished: at low concentration, the fluorescence intensity increases almost linearly before decreasing with increasing concentration in toluene, while its stabilizes in ethanol. This transition occurs when reaching a concentration of between 3 mM and 10 mM in toluene and in ethanol. At 474 nm the intensity is constantly low at low concentration and started to rise around 1 mM in ethanol and 3 mM in toluene.

We compared the pyrene fluorescence spectra at three different concentrations in ethanol and toluene. At 100 µM, the concentration was low enough not to see band at 474 nm. Two bands were still visible in ethanol and toluene at 393 nm and 413 nm. However, the relative intensities were different, with the 413 nm band being relatively less intense than the 393 nm band in ethanol compared to the monomer signal. At 10 mM, the band at 474 nm started to be of significant intensity in ethanol but not visible yet in toluene. The 413 nm band was relatively less intense both in ethanol and in toluene. Finally, at 50 mM, the 413 nm band was present in both solvents but slightly more intense in ethanol.

Contrary to anthracene, when two pyrenes rings are close enough (approximately 10 Å) during excitation, a large red-shifted band appears at higher wavelengths. This is the excimer emission reported numerous times in the literature.[63–66] This band is here at 474 nm and is in our system a probe of close distance of pyrene molecules. Thus, it can be suggested that **Py** self-assembly starts at a lower concentration in ethanol than in toluene, similarly to what was observed for **An**, and for the same reasons.

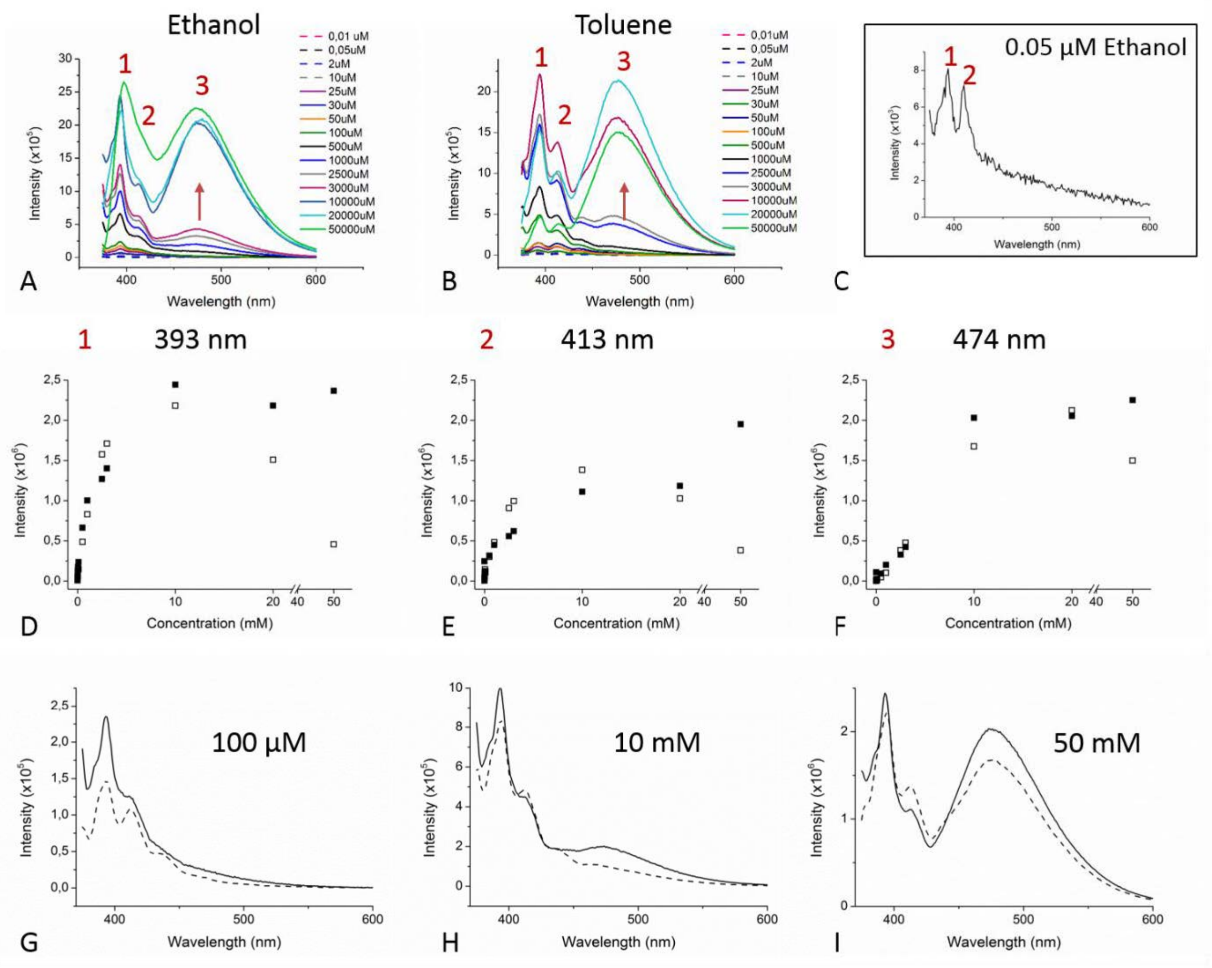

Figure III-13 : Fluorescence spectroscopy of *Py*. Evolution of the fluorescence signal of Py as a function of concentration in (A) ethanol or (B) toluene. (C) Monomer signal at 0.05 µM in ethanol. Fluorescence emission of *Py* at (D) λ_{em} 393 nm, (E) λ_{em} 413 nm and (F) λ_{em} 474 nm (λ_{exc} = 365 nm) in toluene (open squares) and ethanol (solid squares) as a function of concentration. (G-I) Fluorescence emission spectra of Py in toluene (dashed lines) and in ethanol (solid lines) at 100 µM, 10 mM and 50 mM respectively.

3.2.2. Dynamic light scattering

In toluene, it was not possible to obtain a reliable DLS measurement of the size of the pyrene precursor self-assemblies. This might indicate that these systems are highly dynamic and/or that they can adopt a large rang of size/morphology. In contrast, in ethanol, we could measure the size of the supramolecular structures for concentrations higher than 1 mM. On Figure III-14-A, we showed that these structures have an average hydrodynamic diameter of *ca.* 85 nm in the 1-10 mM concentration range that increased up to 150 nm for 20 mM and 50 mM.

Those structures were quite stable over time, as shown in Figure III-14-B. At 1 mM, their size only slightly evolves from T0 post sonication (light blue curve) to overnight resting (black curve) and after a new sonication step (dotted black curve). Yet some modifications of the size distribution were noticed.

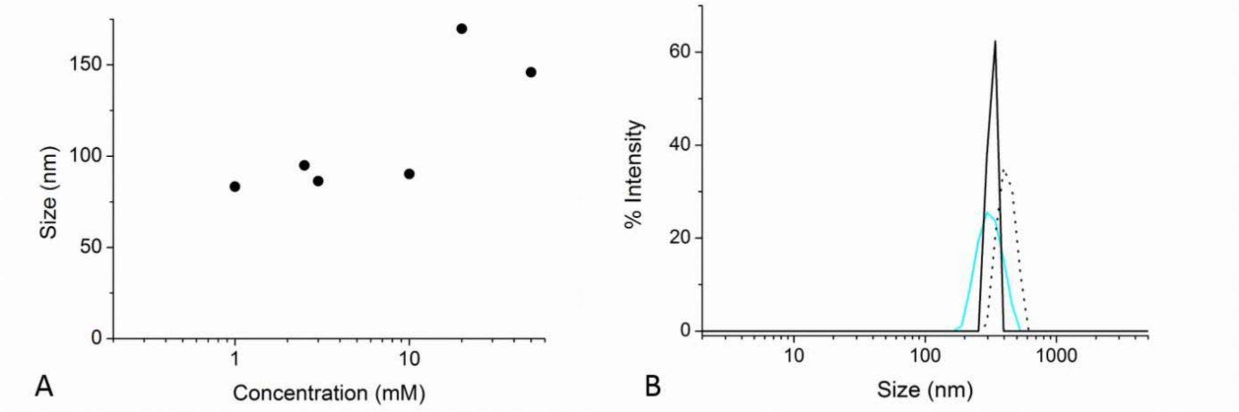

Figure III-14 : DLS of *Py*. (A) Evolution of the size as a function of concentration in ethanol plotted as intensity. (B) Stability over time of the size of the self-assemblies at 1 mM in ethanol: T0 after dissolution by sonication (light blue curve), overnight resting (black curve) and sonication again (dotted black curve).

3.2.3. Cryo-TEM and visualization of supramolecular structures

By Cryo-TEM we were able to observe directly the self-assembled structures in ethanol (Figure III-15). Those images were obtained in collaboration with G. Mosser and P. Le Griel (LCMCP, Sorbonne University) and G. Pehau-Arnaudet (Institut Pasteur).

We studied the **Py** precursor at 1 mM, the lower concentration where structures were reliably measured by DLS. We observed the presence of particles *ca.* 200 nm long and 100 nm large, stacked together. These dimensions are in the same order of magnitude, but larger, than the sizes measured by DLS.

Py was also observed at 10 mM in ethanol, i.e. in conditions where the excimer fluorescence peak was detected. Interestingly, we observed a different structure at this concentration. The precursors self-assemble in thin and long fibers up to several microns in length that are aligned and organized to form hair-like structures. Here the difference between Cryo-TEM imaging and DLS in terms of particle size is striking.

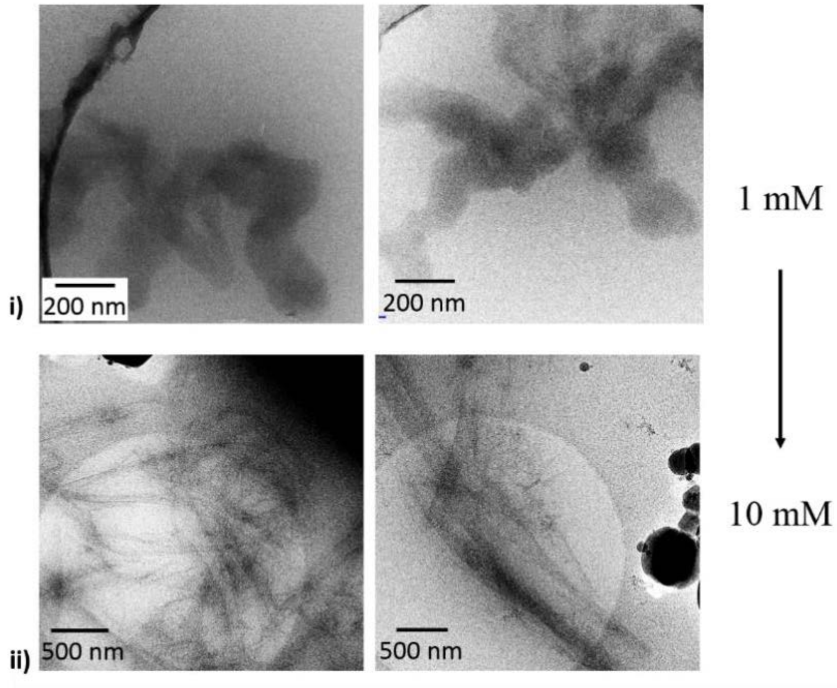

Figure III-15 : Cryo-TEM observations of *Py* at (i) 1 mM and (ii) 10mM in ethanol.

While this discrepancy is difficult to fully explain, it contributes to the overall picture of the **Py** self-assembly process as being highly dynamic so that the structure of the objects present in solution is highly sensitive to the precise experimental conditions. In that sense, the protocol used to prepare samples for cryo-TEM may have “frozen” the system in a specific configuration. As a matter of fact, since the ethanol medium is a poor solvent for the pyrene ring, it should allow for significant pyrene-pyrene interactions that confer some stability to the self-assembled structures. In contrast, in toluene, π-π interactions between aromatic rings are less favored so that the self-assemblies are less stable. In this context, while we decided not to investigate **Py** self-assembly in toluene by Cryo-TEM, mainly based on the un-conclusive results of the DLS study, we may have been able to also observe some “frozen” structures in these conditions.

3.3. Self-assembly of the *Ur* precursor

Attempts were made to dissolve precursor **Ur** in ethanol, toluene, water, and a 50%-50% ethanol-toluene mixture. Even at the lowest investigated concentration, we were unable to completely dissolve the precursor. If we look back at its structure (Fig III-2), it differs from **Py** by the presence of an additional propyl-urea motif on the linker chain. If we hypothesize that the urea introduces strong intermolecular interactions *via* hydrogen bonding, it could have been expected that water would allow for their dissociation. However, the other parts of the molecule, i.e. the alkoxysilane and pyrene moieties, are hydrophobic (let us remind that alkyl-triethoxysilanes are not miscible with water), which may prevent the access of water molecule to the urea linkages. It may be interesting to further test some apolar protic solvents that would be able to interact more significantly with all moieties of the **Ur** precursor.

3.4. Intermediary conclusion

Among the three precursors that we successfully synthesized, only two were fully studied in solution, in ethanol and toluene. Based on fluorescence, DLS and Cryo-TEM experiments, it is quite clear than **An** and **Py** can self-assemble in ethanol to form well-defined objects. Going from ethanol to toluene, higher silane concentrations were required to induce significant interactions between their aromatic moieties, due to the higher solvating efficiency of the latter towards these aromatic rings. While this allowed again to obtain stable systems for **An**, **Py** revealed to have a more complex behavior that will require further investigations.

4. Transfer of *An* self-assemblies to the SiNP surface to create Patchy SiNPs

The next step of our project was to study how these self-assembled systems could be transferred to the surface of the SiNPs to create functional patches. For the sake of clarity, only the results obtained with the precursor **An** will be presented in this chapter. The results for **Py** transfer are presented in the Appendix 1.

Our strategy is represented on Figure III-16. A solution of precursor is prepared in ethanol or toluene at a concentration where self-assembly was assessed in the previous study. SiNPs are then added to this solution so as to allow the transfer of the self-assembled system to their surface *via* the reaction of the silane moiety with silanol groups of the particle surface. The resulting SiNP-1 particles bearing aromatic groups are then treated in acidic conditions to hydrolyze the carbamate group of the precursor, revealing amines at the surface of SiNP-2.

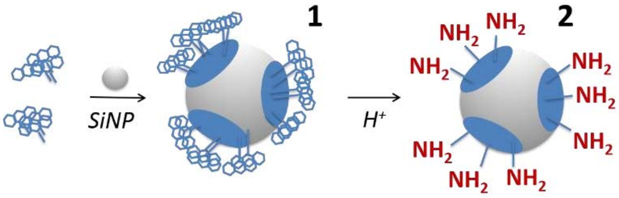

Figure III-16 : Schematic representation of the synthesis of patchy particle *via* self-assembly.

4.1. Comments on the grafting reaction conditions

The grafting of functional alkoxysilanes on the surface of SiNPs is a widely used chemical process. However, it is far from being as simple as the literature data would suggest. Although Si-O-Si bonds can be formed between alkoxysilane functions Si-OR and silanol Si-OH groups present on the particle surface, most favorable conditions consist in (i) the pre-hydrolysis of the alkoxysilane by addition of water (i.e. Si-OR -> Si-OH) and (ii) slightly basic conditions where part of the silanols are in the silanolate ($Si-O^-$) form. Unfortunately, these conditions, also favor the self-condensation of the alkoxysilane, a reaction that enters in competition with the grafting process. Therefore, the grafting procedure should be optimized as a function of the silane and solvent conditions.

In our work, we needed to achieve grafting in toluene and in ethanol. The first situation is quite favorable as, after hydrolysis, the silanes are very unlikely to be soluble in the toluene phase and are therefore prone to interact with the particle surface. Moreover, it has been shown that, unless a specific treatment is performed, SiNPs obtained by the sol-gel process are always hydrated to some extent, this water content allowing to induce the hydrolysis of the alkoxysilane close to the particle surface.

The case of ethanol is more complex. On the one hand, it can lead to the formation of $Si-O-C_2H_5$ groups at the surface of the particle, reducing its reactivity. On the other hand, as it is miscible with water, it can speed up the hydrolysis of the ethoxysilane function. Both conditions would in fact favor self-condensation over grafting. The best way to counter-balance this effect is to add ammonia solutions that allow to work in basic conditions (to favor condensation) in the presence of low amount of water (to slow down hydrolysis). These are in fact the conditions of the Stöber process used for SiNP preparation.

On this basis, transfer of the self-assembled systems to SiNPs has been performed either in pure toluene or in ethanol/ammonium hydroxide mixtures (see Experimental Section – paragraph 7 for full protocol).

4.2. Fluorescence spectroscopy

At 5 mM in both solvents (Figure III-17-A-plain lines), the fluorescence emission of the particles in contact with the anthracenic silane shows three bands at 390 nm, 413 nm and 437 and a shoulder centered at 465 nm, the band at 413 nm being the most intense one. This emission spectrum is the signature of the monomer **An**. Thus, the grafting reaction was successful. The silane density should be quite low as no clear sign of anthracene-anthracene interactions are evidenced, in contrast to what was observed in solution at this concentration. The anthracene is fixed in non-dynamic conformation with probable molecular inter-distance higher than in solution. In a second step, carbamate hydrolysis was induced in acidic conditions to cleave the anthracene moiety (Figure III-17-A-dot line). Consequently, the fluorescence signal was almost completely shut down. This indicates that **An** was well-hydrolyzed and the anthracene moieties efficiently released.

At 10 mM in ethanol (Figure III-17-B-blue plain line), the grafted particles also showed the monomer signature. In toluene, (Figure III-17-B-black plain line), the intensity of the 390 nm peak is lower compared to the monomer and an additional broad band is observed with a maximum at *ca*. 500 nm. This new band is highly reminiscent of the reported excimer band of the anthracene molecule. As pointed out earlier, this band appears only in very specific situations, when the molecules are constrained at a suitable distance and positioning, like in microscrystals.[57–62] Noticeably, this band was not observed for the silane in solution at the same concentration. Thus, it suggests that the organization of the **An** molecules on the SiNP surface differs from the one in solution. Additionally, the anthracene rings are less mobile. Noticeably, after reaction with **An** at 50 mM, similar fluorescence spectra were recorded in both solvents (Figure III-17-C- plain lines). Again the excimer band is present for the particles, whereas it was absent in solution at this concentration. This again signs for a different packing of the anthracene rings when **An** is grafted on the surface.

On the one hand, at 5 mM, the concentration of **An** after transfer appeared to be smaller than in solution. On the other hand, at 10 mM in toluene and 50 mM in the two solvents, some of the anthracene rings appear to be in closer/stronger interactions than in solution. The 10 mM situation is very interesting because the recorded signal depends on the solvent. This suggests that the organization of the grafted moieties is strongly related to the initial self-assembled structure in solution. An alternative possibility would be that the solvent itself influences the grafting reaction. However, the particle spectra recorded at 5 mM and 50 mM are very similar for the two solvents, suggesting that this influence should not be of major importance.

It is also interesting to notice that, at 50 mM, the 390 nm band is still visible for the particles while it had totally disappeared in solution. It has to be reminded that the fluorescence peaks of the anthracene monomer correspond to vibronic transitions, *i.e* that involve a change in both electronic and vibrational states. The band at 390 nm corresponds to the 0-0 transition, i.e. with no variation in the vibrational state. As such, it is the less sensitive to modifications in the environment of the anthracene ring. However, it corresponds to the transition at the highest energy and therefore closest to the absorption peaks of the molecule. Therefore the fluorescence intensity of this 390 nm band is expected to decrease as the anthracene concentration increases due to re-absorption processes.[67] This is exactly what we have observed in solution. However, the excimer emission band that we have observed here has its mirror equivalent in the absorption spectra, decreasing the intensity of the absorbance bands of the monomer. In other words, the formation of excimers can decrease the re-absorbance of the emitted light. This can explain why the particles still show a significant emission peak at 390 nm.

After hydrolysis, the typical emission bands of anthracene are no longer visible for 10 mM **An** in ethanol but we could notice a rather high background signal (Figure III-17-B). At 50 mM in ethanol, the monomer spectra at low intensity is recorded, suggesting that some anthracene rings remain at the surface of the particles (Figure III-17-C). In toluene, the monomer spectra can be recorded even at 10 mM and increases in intensity at 50 mM, again indicating that some aromatic moieties remain. It is interesting to note that there seems to be a correlation between the deprotection efficiency and the formation of excimers. This would make sense considering that densely packed aromatic rings could limit the accessibility of the carbamate function.

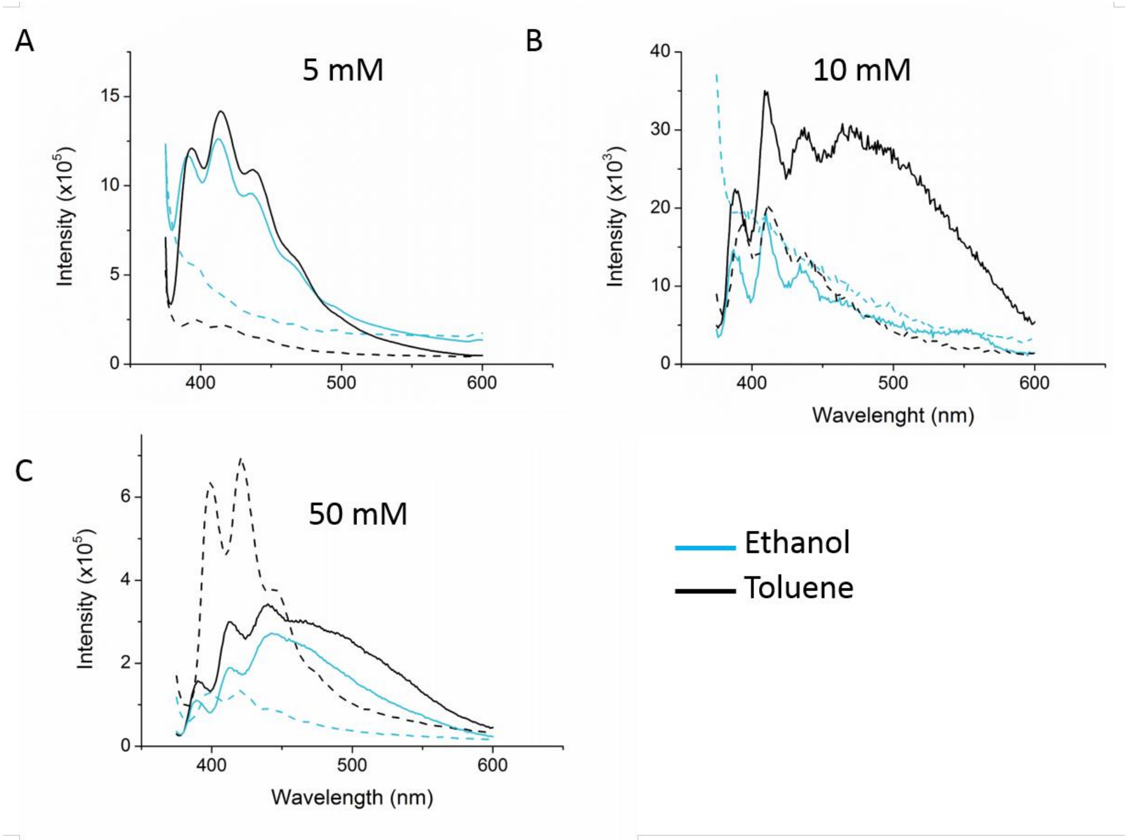

Figure III-17 : Fluorescence spectroscopy of *An*-modified SiNPs in ethanol (blue lines) and toluene (black lines) at (A) 5 mM, (B) 10 mM and (C) 50 mM before (solid lines) and after (dotted lines) acidic hydrolysis.

4.3. Zetametry study

In parallel, the grafting of **An** and removal of the anthracene moiety has been monitored by zeta potential measurements as a function of pH. Figure III-18-A shows the zeta potential values representative of non-functionalized SiNPs bearing silanol groups (in grey, pKa *ca*. 3) and of control particles homogeneously functionalized with amines by grafting APTES (in red, pKA ca. 10). When APTES is grafted on SiNP-OH, zeta potentials are modified at low pH (from ca. +2 mV to +40 mV at pH 2) and high pH (from -38 mV to +10 mV at pH 8). The silanol groups initially present on the particle surface has been involved in the grafting reaction to form (particle)Si-O-Si-NH_2 bonds, decreasing the density of negative charge at high pH compared to bare particles, whereas the amine groups provide positive charges in the acidic to slightly pH conditions.

After grafting of **An** at 5 mM, zeta potential values increase in both solvents when compared to the bare particles (Figure III-18-B-plain squares). As discussed before, this is attributed to the decrease of the density of surface silanols upon grafting, while the silane **An** itself, being neutral, do not contribute to the particle electrostatic charge. We can notice that this increase is moderate in ethanol and very significant in toluene, which would suggest a higher grafting efficiency in the latter solvent. After acid hydrolysis, a further increase in zeta potential value is observed for both solvents (Figure III-18-A-open squares), indicating that free amines are now available and contribute to the positive charge density at the particle surface. At low pH, the increase is more significant in toluene than in ethanol, which supports our previous assumption of a higher grafting efficiency in toluene.

The influence of initial silane concentration is shown on Figure III-18-C-D. If we consider that the zeta potential value after deprotection is a reliable indication of grafting density then, for toluene, we already have a significant amount of grafting at 5 mM (+13 mV at pH 2) that increases at 10 mM (+22 mV) and levels-off (+22 mV at 50 mM). In ethanol, the density of positive charges was lower (+2 mV) at 5 mM and 10 mM. At 50 mM it increased around +12 mV. These results are in rather good agreement with fluorescence spectroscopy studies: the grafting is higher in toluene and in a similar extent at 10 mM and 50 mM whereas in ethanol the concentration needs to reach 50 mM to observe the excimer band.

Additionally, we can notice a clear increase of zeta potential values between grafted and hydrolysed states in neutral to basic pH conditions when 5 mM and 50 mM concentrations in ethanol are compared, evidencing a much higher amount of grafted silanes at higher initial concentration. The fact that such a variation does not fully appear after deprotection can be related to our previous observation of uncomplete hydrolysis in these conditions. The toluene system evolves in a more complex manner, which may be related to the fact that excimers are formed at lower concentration, with possible related issues in terms of molecular crowding at the particle surface.

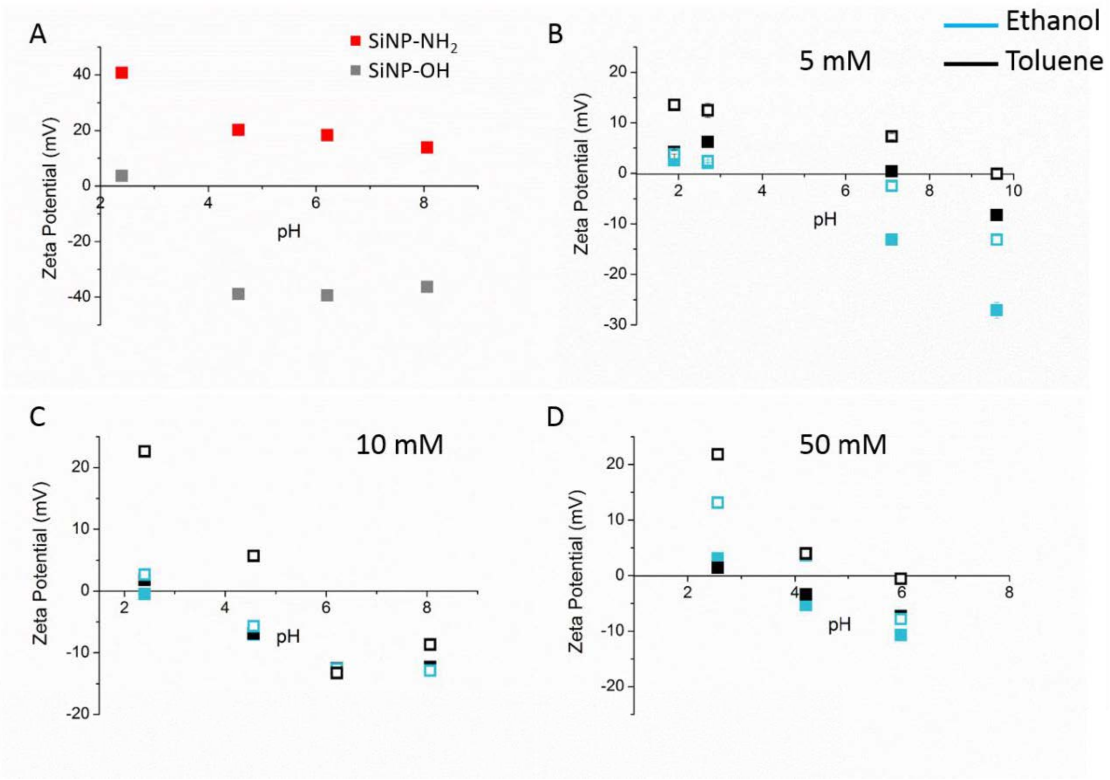

Figure III-18 : Zeta potential measurements of *An*-modified SiNPs in ethanol (blue squares) and toluene (black squares) at A) 5 mM, B) 10 mM and C) 50 mM before (solid squares) and after (open squares) acidic hydrolysis. D) Zeta potential of SiNP-OH and SiNP-NH$_2$as a function of pH.

4.4. Study of amine distribution on SiNPs surface by grafting of gold-nanoparticles and electron microscopy

The previous results indicate the successful grafting of **An** at the surface of the particles. However, information on the positioning of the functional groups is also required to demonstrate the clustering of **An** and the formation of functional domains. To this aim, we used carboxylate-modified gold nanoparticles (AuNPs 10 to 20 nm in diameter) as tags to be detected by electron microscopy. The AuNPs can be conjugated to the SiNP surface by a peptide coupling between the carboxylates of the AuNPs and the amines at the surface of SiNPs (Figure III-19). This should allow to specifically identify the presence and distribution of amine groups.

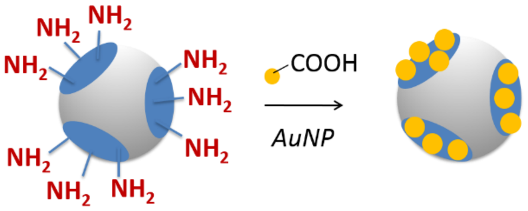

Figure III-19 : Schematic representation of the AuNPs grafting to visualized amines distribution on SiNP surface.

The specificity of the peptide coupling has first been tested by the conjugation of AuNPs at the surface of SiNPs homogeneously grafted with amines. Images obtained by scanning electron microscopy using a field emission gun (SEM-FEG) show the presence of AuNPs having a diameter of 10 to 20 nm homogeneously distributed over the surface of the SiNP (Figure III-20-A,B). In contrast, no AuNP could be grafted onto bare SiNPs bearing silanol groups (Figure III-20-C,D). In this view, the peptide coupling of AuNPs could be a powerful tool to identify the formation of clusters at the surface of SiNPs.

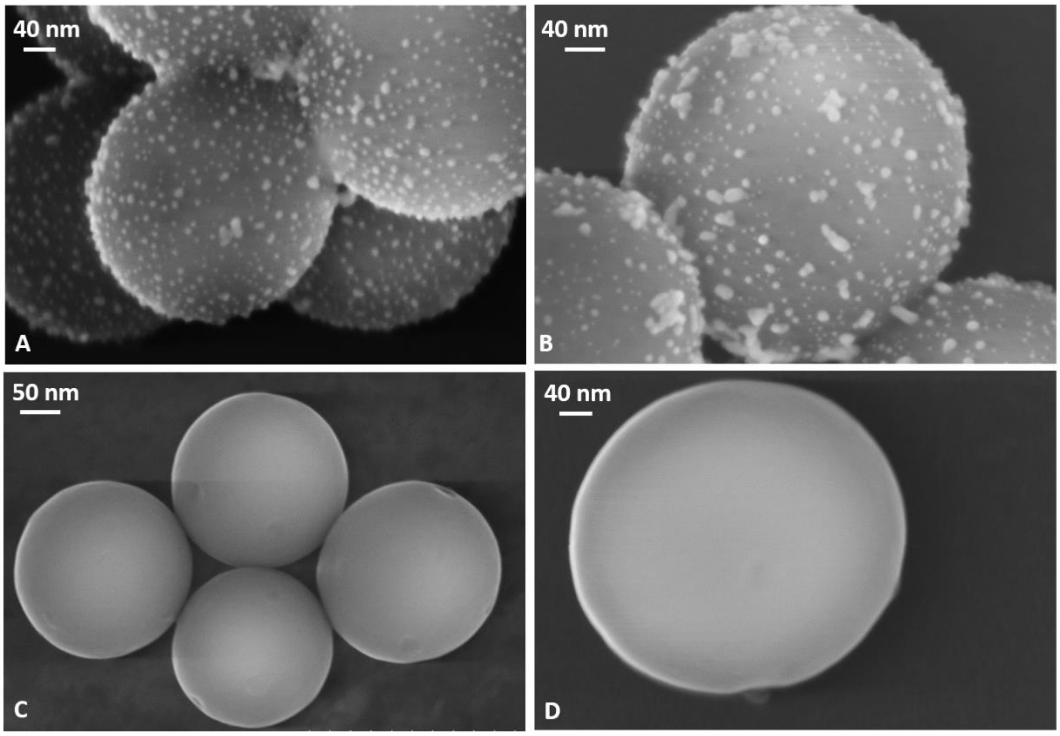

Figure III-20 : SEM-FEG images of A) positive control SiNP-NH_2 and B) negative control SiNP-OH after grafting of AuNPs.

In the following results carboxylate-modified AuNPs are from commercial source. We have synthesized our own particles and successfully grafted them on amines too. However, we faced a lack of reproducibility in the particle synthesis. We also attempted to replace AuNPs by iron oxides nanoparticles, in collaboration with Pr. Christine Ménager, (PHENIX, Sorbonne Université). Fe_2O_3 particles were ~10 nm diameter. We considered different possible organic molecules that would allow to conjugate Fe_2O_3 particles to amine-modified SiNPs and chose di-mercaptosuccinic acid (ADMS) molecules. We attempted to graft Fe_2O_3 many times with different protocols. We succeeded to have nice, convincing and reproducible positive controls on SiNP-NH_2, but nonspecific reactions between Fe_2O_3 particles and silica made difficult to have clean negative controls on SiNP-OH (cf. Appendix 2).

4.5. Characterization of the positioning of the functional groups on *An*-modified SiNPs by AuNP grafting

In the following, a concentration of 50 mM of **An** in ethanol and in toluene has been used for the grafting.

4.5.1. *An*-modified SiNPs in ethanol

After grafting **An** in ethanol at 50 mM, we could observe fiber-like objects surrounding the SiNPs in an inhomogeneous way (Figure III-21-A) Those structures were obtained in a reproducible manner and could match with the needle-shaped assemblies observed by Cryo-TEM in the same conditions. After the acidic treatment, on Figure III-21-B, the large fibers are no longer visible but some organic coating is still visible at the particle surface. After grafting with AuNPs, large patches of gold colloids were observed on the SiNPs surface, unevenly distributed and at a low density (Figure III-21-C,D). In this case, surface analysis of SEM-FEG images by Image J© indicates that approximately 10% of the surface was covered by AuNPs (Figure III-23).

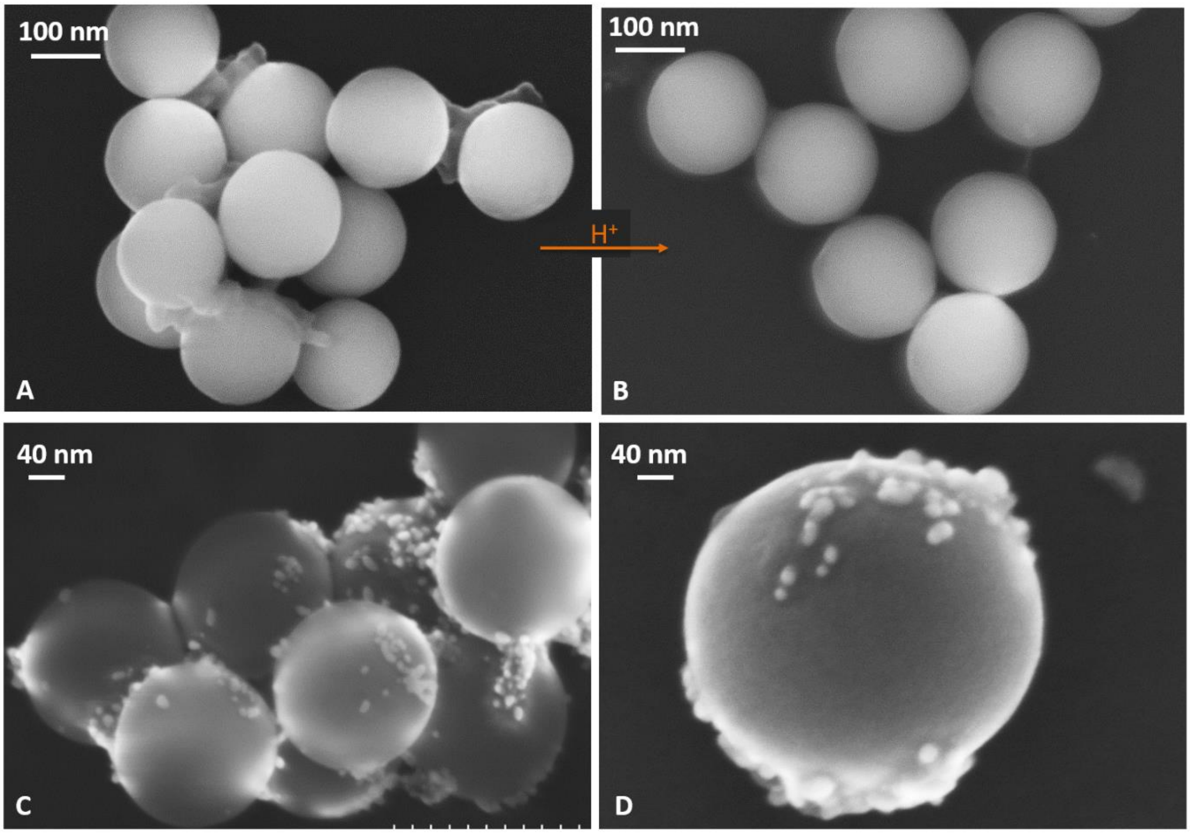

Figure III-21 : SEM-FEG images of SiNPs grafted in ethanol with *An* precursor at 50 mM A) before and B) after the acidic hydrolysis. C-D) Characterization of NH_2 positioning with AuNP-grafting.

4.5.2. *An*-modified SiNPs in toluene

When grafting was performed in toluene, an organic layer was visible on SiNP surface (Figure III-22-A). Its structure is less defined than in ethanol, similar to a sheet wrapping SiNPs. The layer is so thin that it is hard to identify its boundaries. However, there is a reasonable agreement between the sheet average dimensions and the size of micelles observed by cryo-TEM (ca. 400 nm) in toluene at 50 mM. This structure apparently fully disappeared after the acidic treatment - Figure III-22-B. Numerous small patches with a high density of AuNPs could then be observed (Figure III-22-C,D), covering approximately 30% of the surface (Figure III-23).

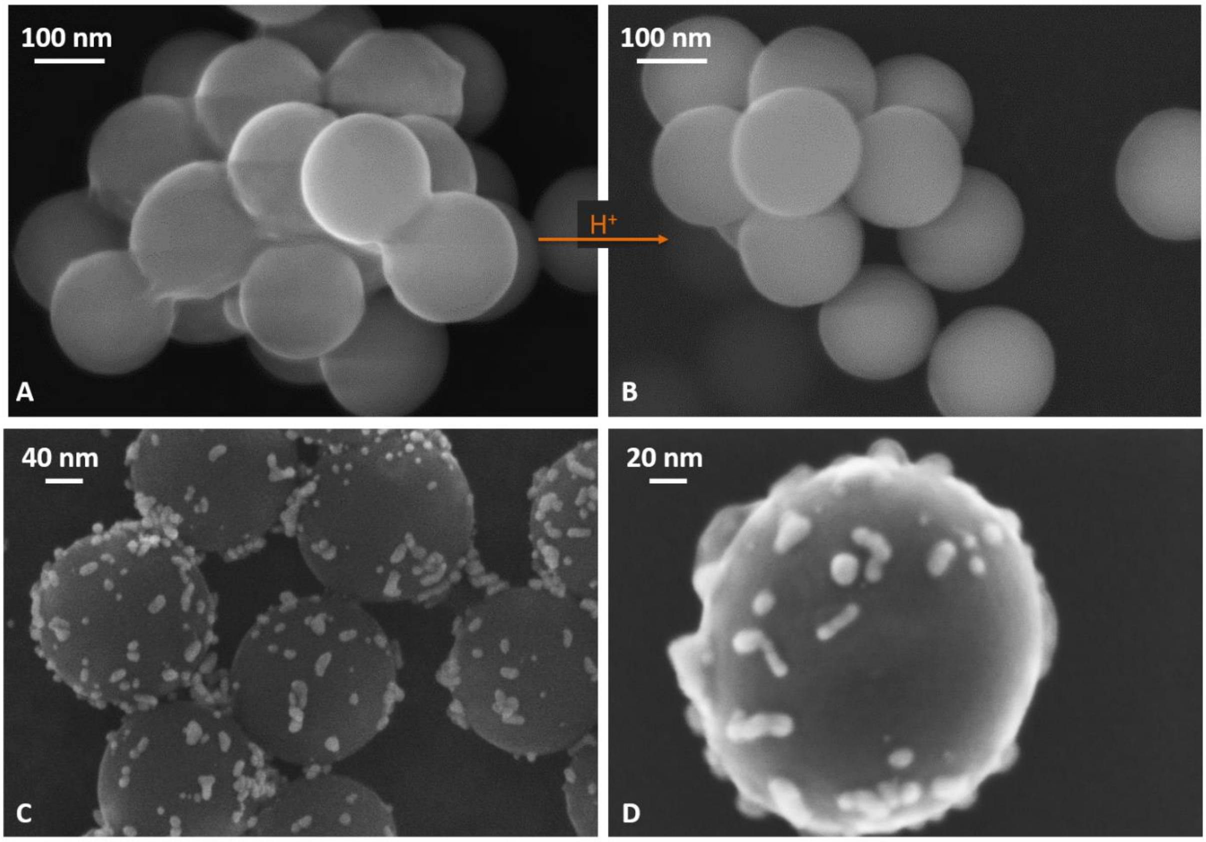

Figure III-22 : SEM-FEG images of SiNPs grafted in toluene with *An* precursor at 50 mM A) before and B) after the acidic hydrolysis. C-D) Characterization of NH_2 positioning with AuNP-grafting.

These results show that we can obtain different distributions of the AuNPs when comparing the APTES-functionalized surface and the surface obtained using the alkoxysilane **An** either in ethanol or in toluene. This shows first that we can deviate from a homogeneous distribution (as obtained with APTES) by designing self-assembling alkoxysilanes and hence induce the formation of clusters. One step further we can also control the pattern of clustering by playing with the solvent, going from numerous small clusters in toluene to larger ones in ethanol. This is in agreement with the self-assembling behavior observed in solution, where larger assemblies were detected and observed in ethanol compared to toluene.

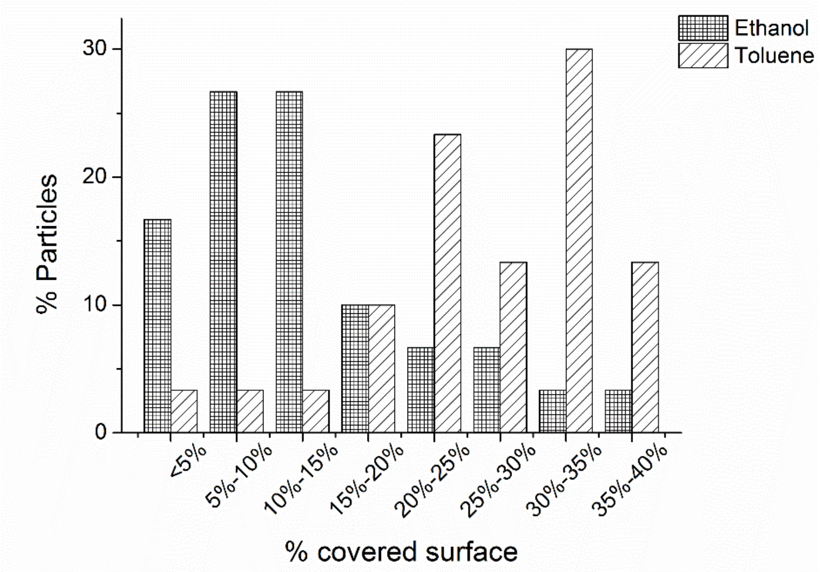

Figure III-23 : Quantification of the SiNP surface grafted with AuNPs for the *An* precursor grafting in ethanol and toluene at 50 mM by surface analysis with Image J©.

A closer look at the SEM images also shows that most of the AuNPs attached to the surface of patchy SiNPs have a large diameter (*ca*. 20 nm), while smallest particles with a diameter of 10 nm are mostly observed on SiNP-NH_2. This may result from a higher density of amine groups within clusters when compared to homogeneously-functionalized surface. In solution, APTES molecules are grafted as “monomers” so that the intermolecular distance between amine groups should be similar over the whole surface. In contrast, our observations suggest that when **An** molecules are initially self-assembled, their transfer to the surface preserves, at least to some extent, the anthracene-induced packing of the silane molecules. In the case of toluene, **An** would evolve directly from the compact micelle to the SiNP surface, leaving the fingerprint of the assembly. In ethanol, when the microneedles meet the particle surface, their rigid structure, fixed by strong π-π interactions between anthracene, would partially allow coating of the SiNPs surface, favoring the condensation reaction between the stabilized ethoxysilanes and silanols.

Very importantly, the small distance between two grafted alkoxysilanes, hence between two amines, obtained at 50 mM appears to allow the anchorage of the largest AuNPs, whereas more dispersed amine groups on SiNP-NH_2 surface may only efficiently bind the smallest gold colloids. This constitutes a direct demonstration that silane clusterization enhances the strength of interaction of the SiNPs surface with an external element.

Indeed, many questions remain about the transfer of the self-assembled systems from the solution to the particle surface. In toluene after reaching the threshold concentration of

10 mM the amount of amines (and therefore the grafting extent) is stable. This may be due to steric hindrance induced by the supramolecular structures already located on the particle surface. In contrast, in ethanol, we need to reach 50 mM to have a significant grafting. The needle-shape particles therefore seem to be the more suitable supramolecular structures to interact with SiNP surface, despite the fact that they are larger than platelets observed at lower concentration. Indeed, it has to be keep in mind that self-condensation of **An** can also occur, which is expected to be favored at high silane concentration. Hence, the overall grafting reaction results from a complex equilibrium between self-assembly in solution, self-condensation and condensation at the surface. As a matter of fact, our fluorescence studies have pointed out that the grafting reaction had a significant effect on the packing of anthracene rings. On the one hand, at low concentration, the silanes appear more distant on the surface than in solution. On the other hand, at high concentrations, we observed the formation of excimers only after grafting, signing for a smaller distance between aromatic rings than in solution. This result is maybe due to a loss of the dynamic character of the self-assembly in solution. **An** is constrained by covalent grafting in a specific distance allowing the formation of excimers.

To conclude, we have gathered strong evidences that our strategy involving the formation of self-assembled silanes and their transfer to the surface of SiNPs could successfully lead to patchy particles. We have also shown that by playing with the experimental conditions of grafting, it was possible to modify the size of these patches although the underlying mechanisms remain largely unclear. Finally, we could evidence the benefits of clustering on the grafting of gold colloids, providing an ultimate validation of our strategy for the purpose of creating domains with specific interactions towards a selected target.

5. Bifunctional patchy particles

The final step in this project was to confer bifunctionality to the SiNPs. Starting from SiNPs grafted with **An** in ethanol, we explored two different routes to introduce a second chemical functionality.

5.1. Two steps functionalization

The engineering of functional domains defines *per se* areas of different chemistries, in other words bifunctional particles. From the patchy particles described previously, another functionality can be achieved by a second step of grafting with a soluble alkoxysilane in between the patches (Figure III-24-A).

Amine groups obtained by the condensation of **An** into domains are relevant in a biological context for the grafting of bioactive peptides. In parallel, it has been previously shown in our group that sulfonate groups interact favorably with collagen *via* electrostatic interactions to control the growth of fibrils from the inorganic surface.[7] Along this line, we chose to graft the mercaptopropyltrimethoxysilane precursor (MPTMS, Figure III-24-A) on our patchy **An**-modified SiNPs. After oxidation by hydrogen peroxide (H_2O_2), the thiol functions are converted into sulfonates (SO_3^-) groups (Figure III-24-A-c). Finally, an acidic treatment allows to remove the anthracene moiety of **An**, to obtain bifunctional SO_3^- / NH_2 SiNPs (Figure III-24-A-d). These SiNPs were characterized by fluorescence spectroscopy and zeta potential.

First, the different steps to obtain bifunctional particles were followed by fluorescence spectroscopy. From the initial SiNPS grafted in ethanol in basic conditions with 50 mM **An**, the reaction with MPTMS in the same condition preserved the fluorescence spectra of the anthracene ring, although the excimer band appeared less intense (Figure III-24-B-a-b). After treatment with hydrogen peroxide, the fluorescence intensity strongly decreases until complete extinction after the acidic treatment and removal of the anthracene moiety of **An** (Figure III-24-B-c and d respectively). The fluorescence quenching in step (c) may be due to the oxidation of the aromatic cycle by hydrogen peroxide before the acidic treatment.

In parallel, the SiNP surface charge was monitored by zeta potential measurements after each step. While MPTMS grafting induced a slight decrease of zeta potential value (Figure III-24-C-a-b, pKa of thiols *ca.* 13), thiol oxidation by the addition of hydrogen peroxide very significantly lower it down to - 40 mV (Figure III-24-C-c). The fact that the zeta potential value remains very low even at pH 2 suggest that sulfonate groups were formed (pKa of alkyl sulfonic acids *ca.* 1, *cf.* Figure III-24-D). Finally, the acidic treatment hydrolyzes the carbamate and reveals the amine whose positive contribution at low pH compensate the negative contributions of SO_3^- groups, leading to an increase in the zeta potential values (Figure III-24-C-d). Thus, although the evolution between steps c and d indicates the loss of the anthracene by the acidic treatment, the fluorescence data suggest that these aromatic rings were oxidized by H_2O_2.

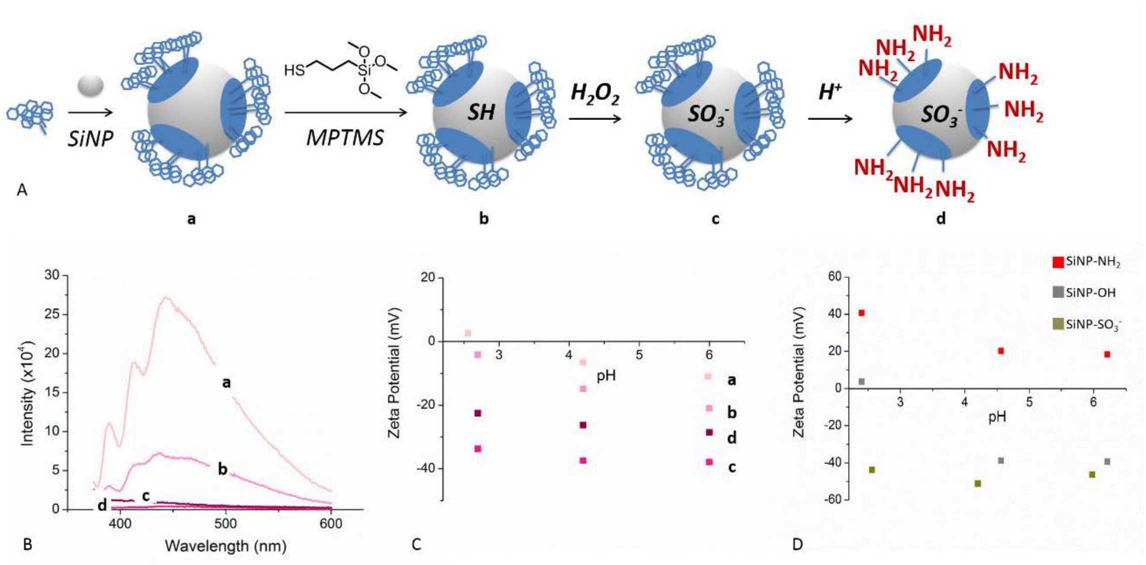

O

Figure III-24 : (A) Schematic representation of the grafting of a second alkoxysilanes (MPTMS) at the surface of patchy SiNP surface to get bifunctional patchy particles in two steps. (B) Fluorescence emission spectra of the SiNPs (b) before grafting, (c) after hydrogen peroxide treatment, and (d) acidic hydrolysis (50 mM in ethanol, λ_{exc} = 365 nm). (C,D) Zeta potential of SiNPs at each step of the functionalization path and of monofunctional SiNPs controls respectively.

5.2. One pot functionalization

Alternatively, bifunctionality may be reached in a one pot process. This relies on the use of self-assembling alkoxysilane **An** together with a soluble alkoxysilane. In this case, the self-segregation of alkoxysilanes is the driving force for the formation of two populations of domains having distinct chemistries: **An** forms clusters and the soluble alkoxysilane condense in between clusters at the surface of SiNPs (Figure III-25-A).

Again, fluorescence spectroscopy and zeta potential were used to follow the different steps to obtain bifunctional particles. The two precursors (**An** and MPTMS) were first mixed with SiNPs in ethanol in basic conditions (Figure III-25-Aa). At this stage, the fluorescence spectra shows the anthracene signature similar to that of particles grafted with **An** only (Figure III-25-B-b). After treatment with hydrogen peroxide, the fluorescence intensity largely decreases until complete extinction after the acidic treatment and removal of the anthracene moiety of **An,** as previously observed (Figure III-25-B-b and c respectively).

Zeta potential measurements after each step confirmed those results. The results are interstingly similar to the previous one obtained in two steps.

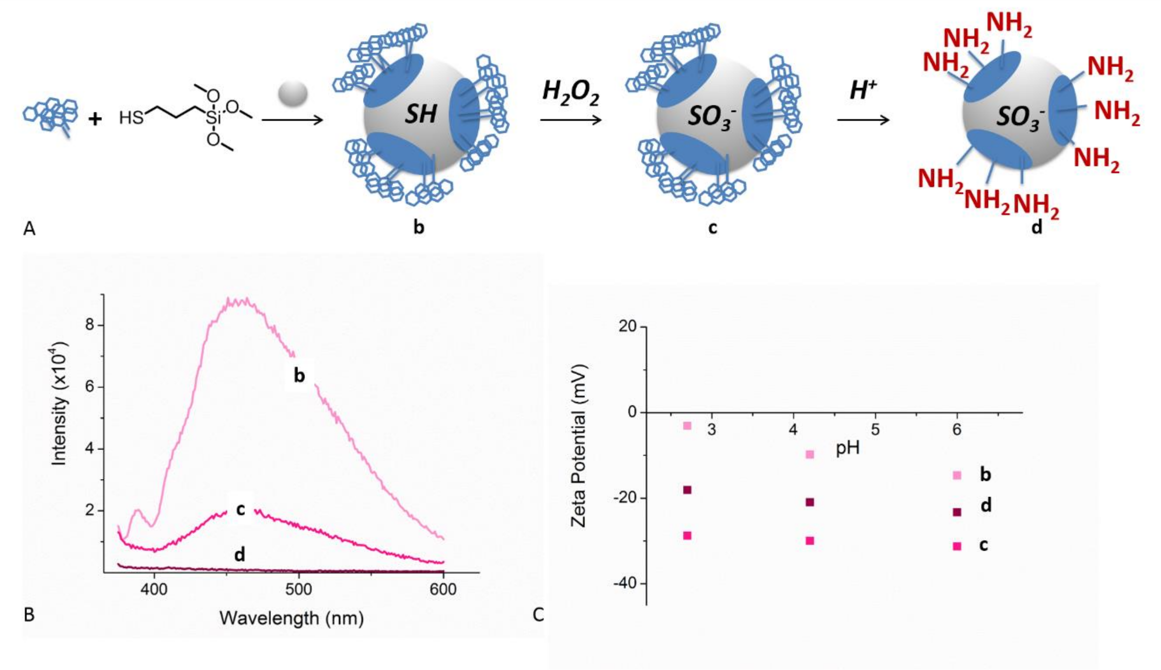

Figure III-25 : (A) Schematic representation of the segregation of two alkoxysilanes (*An* and MPTMS) and their transfer at the SiNP surface to get bifunctional patchy particles in one step. (B) Fluorescence emission spectra of the SiNPs (a) before grafting, (b) after hydrogen peroxide treatment, and (c) acidic hydrolysis (50 mM in ethanol, λ_{exc} = 365 nm). C) Zeta potential of SiNPs at each step of the functionalization path.

5.3. Characterization by adsorption of collagen fibrils

To characterize the presence of sulfonate groups on our bifunctional SiNPs, we use collagen I monomers solubilized in acetic acid. We followed the procedure already published by the group to fibrillate collagen from the surface of sulfonate-modified SiNPs.[7] Collagen did create stable hybrids with SiNP-SO$_3^-$ but not with bare SiNPs, with which only large aggregates were reported. After raising the pH by ammonia diffusion,[68] a stable collagen–NP-SiSO$_3^-$ suspension was obtained and TEM observations indicated the formation of large fibrils bridging nanoparticles. Type I collagen triple helices are known to undergo self-assembly under mild acidic to neutral conditions, forming fibrils ca. 100 nm in diameter and > 1 mm in length.[69,70] Those fibrils were then considered as evidences of the presence of sulfonate groups at the surface of the particles.

Associated with AuNPs linked on amines we would have an interesting way to characterize the bifunctional particles by electron microscopy. As a proof of concept, we used bifunctional patchy particles functionalized in two steps (Figure III-26). Numerous fibrils are seen that expand from the SiNP surface, evidencing the presence of sulfonate groups on the bifunctional particles. The co-existence of gold-particle and collagen fibrils on two steps-modified SiNPs (Figure III-26) is a nice proof of the bifunctionality of those patchy particles.

Whereas this result is highly encouraging, the same protocol needs to be reproduced on one-pot bifunctional SiNPs and on statistically distributed bifunctional particles obtained by mixing APTES and MPTMS.

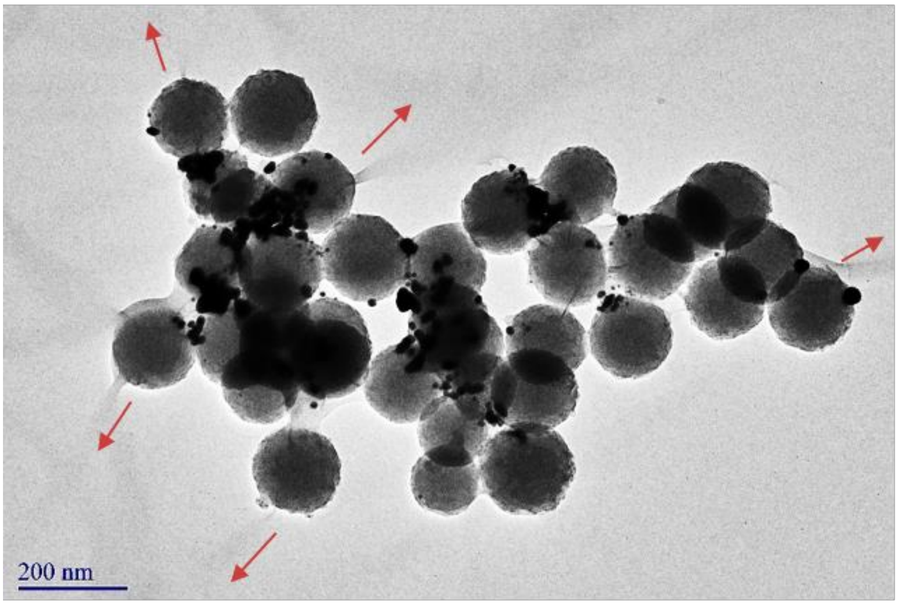

Figure III-26 : Collagen fibrils (highlighted by red arrows) triggered by neutralization of pH from two steps modified bifunctional patchy SiNPs with AuNP.

6. Conclusion and perspectives

In this chapter, we have shown that the design and synthesis of self-assembling alkoxysilanes allows to form functional clusters at the surface of amorphous spherical silica particles in solution. Different patterns are obtained depending on the solvent and concentration used and permit to tune the binding efficiency of the functional domains towards gold colloids. In addition, it is possible to obtain bifunctional patchy SiNPs. Altogether, our strategy appears particularly promising as a broad library of self-assembling alkoxysilanes may be further designed that would lead to patches of different sizes and density on the surface.

A major difficulty that we identified is to achieve a precise control of the supramolecular structure. The obtained self-assembled systems are not monodispersed, quite large in comparison with the size of SiNPs and not always very reproducible. During my PhD, another set of precursors bearing a trityl group has been synthesized and studied in our team by Julien Graffion (Figure III-27). In this molecular design, the trityl group is used to drive the formation of well-defined objects. Contrary to the anthracene or pyrene moiety, its non-planar structure (one sp3 carbon) should favor π-stacking interactions over a short-range, avoiding the formation of extended self-assembled structures. Antisolvent precipitation in an ethanol/water mixture was used to obtain supramolecular objects from **2**. Precipitation could be monitored by DLS in the range 60 to 95% water leading to well-defined objects with sizes from 210 nm to ca. 100 nm. Very interestingly, similar trends could be observed by precipitating precursor **3**, with a constant decrease in size from 60 to 80% water giving rise to well-defined objects with a mean hydrodynamic diameter above 200 nm at 60% water levelling around 90 nm from 80 to 95% water. Due to the similarity of the self-assembling behavior of both precursors, the counterpart molecule lacking the alkoxysilane group was prepared (**1**). Again, similar trends could be measured by DLS: hydrodynamic diameter above 200 nm at 60% levelling around 90 nm from 80 to 95% water. Playing with the tritylated molecule concentration at a given water content provided an additional way to tune the size of the resulting supramolecular structures. At 90% water, when increasing the alkoxysilane concentration from 100 to 400 µM, the hydrodynamic diameter of **2** varied from 95 to 125 nm, and from 80 to 100 nm for **3**. CryoTEM observations show the formation of well-defined spherical objects in solution. This work has been published in the European Journal of Inorganic Chemistry in 2017.[46] When attempting to transfer these self-assembled systems on the surface of SiNPs, it was possible in some conditions to observe silica particles decorated with a few smaller spherical objects, that disappeared after acidic treatment. This clearly suggests that our control of the patchy domains will depend on our ability to obtain well-defined self-assembled structures.

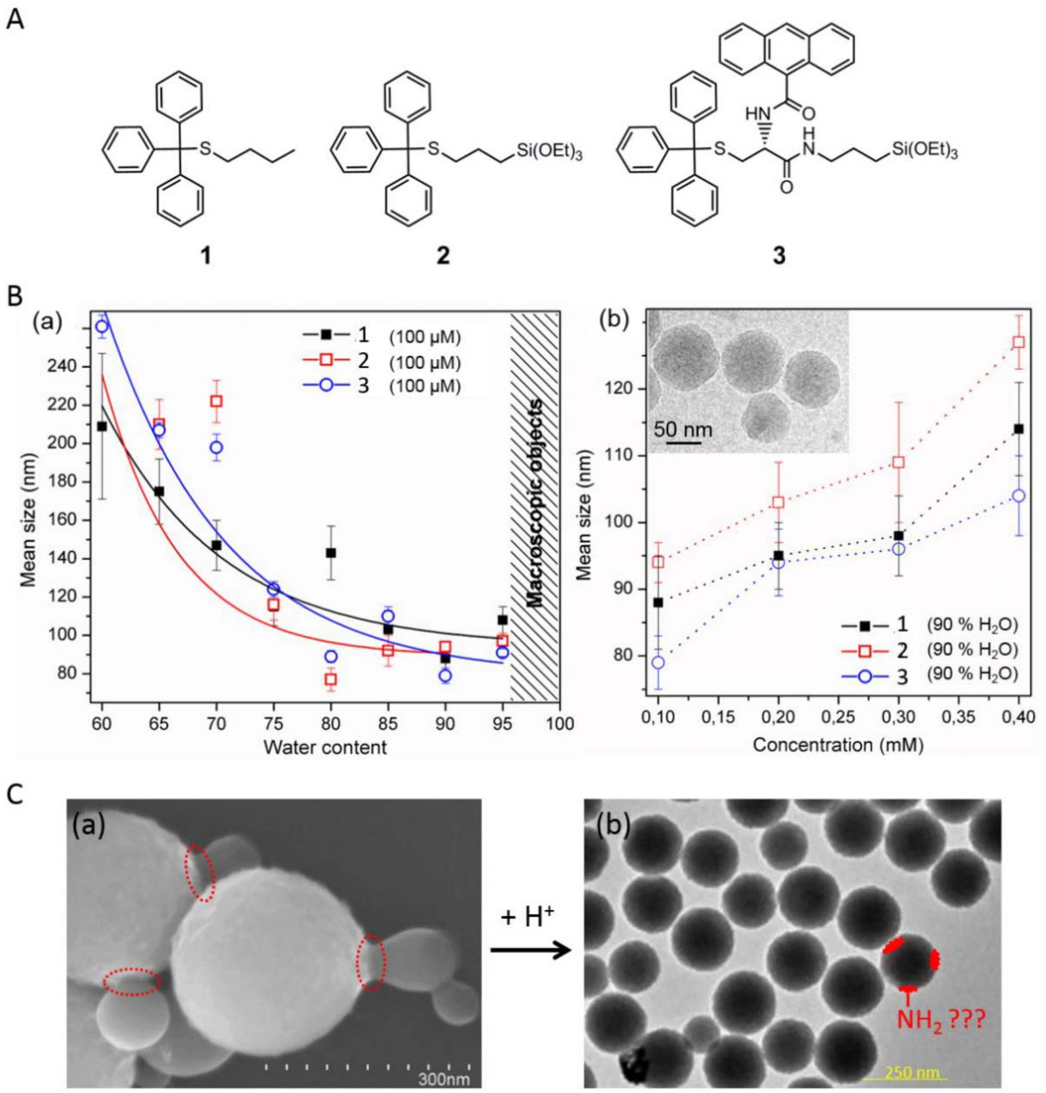

Figure III-27 : (A) Molecular structure of precursors 1, 2 and 3. (B) Characterization of the self-assembly by DLS and cryoTEM (inset) of 1, 2 and 3 as a function of (a) water content and (b) concentration. (C) Interactions between the assemblies and the SiNP surface. (a) SEM-FEG of the hybrid assemblies interacting with the SiNP surface, and (b) TEM of the SiNP after removal of the hybrid assemblies in acidic conditions.

The obtained particles may act as platforms for grafting peptides and proteins using different conjugation routes to become key components of biomaterials with tunable mechanical and functional properties and able to direct cellular fate. We have shown here that it is possible to achieve the co-existence of amine patches, that can allow further grafting of bioactive peptides, and sulfonate group, that interact with collagen, on the surface of silica nanoparticles. Therefore, here-developed bifunctional patchy particles represent ideal building blocks for the preparation of bioactive collagen-based composite materials for tissue engineering.

7. Experimental section

7.1. Synthesis of *N*-[3-(Triethoxysilyl)propyl]-anthracen-9-ylmethyl carbamate precursor (according to a procedure described in [47])

In a Schlenk tube, 6 mL of triethylamine was added under argon to a suspension of 9-Anthracenemethanol (2,5 g, 12 mmol – Sigma Aldrich, 97%) in 30 mL of dry dichloromethane. After addition of 3-(triethoxysilyl)propyl isocyanate (3.3 mL, 13.3 mmol – Sigma Aldrich, 95%), the reaction was homogenized and the reaction mixture was stirred at room temperature (RT) for 18 h. The solvent was then removed under vacuum with a rotary evaporator. To eliminate the excess of triethylamine, 25 mL of diethyl ether was placed in the Schlenk tube, was heat using a heat gun and then evaporated under vacuum with a rotary evaporator. The precursor was precipitated in cyclohexane, washed three times with cyclohexane and filtered. 5.5 g (93% yields) of the compounds were obtained. After chromatography on a silica gel column (eluent dichloromethane: methanol), 4.75 g (87% yield) of the compound were obtained. Analysis (by NMR and MS) were consistent with those obtained in [47].

7.2. Synthesis of N-[3-(Triethoxysilyl)propyl]-pyren-9-ylmethyl carbamate precursor

In a Schlenk tube, 4 mL of triethylamine was added under argon to a suspension of 9-pyreemethanol (2 g, 8.6 mmol – Sigma Aldrich, 97%) in 30 mL of dry dichloromethane. After addition of 3-(triethoxysilyl)propyl isocyanate (3 mL, 12.1 mmol – Sigma Aldrich, 95%), the reaction was homogenized and the reaction mixture was stirred at RT for 18 h. The solvent was then removed under vacuum with a rotary evaporator. To eliminate the excess of triethylamine, 25 mL of diethyl ether was placed in the Schlenk tube, heated with a heat gun and evaporated under vacuum with a rotary evaporator. The precursor was precipitated in cyclohexane, washed three times with cyclohexane and filtered. 2.7 g (5.6 mmol, 65% yields) of the compound were obtained after chromatography on a silica gel column (eluent dichloromethane: methanol).

^{1}H NMR (300 MHz, DMSO-*d*$_6$): δ (ppm) 8.39 – 8.05 (m, 9H), 7.31 (t, *J* = 5.7 Hz, 1H), 5.76 (s, 2H), 3.71 (q, *J* = 6.9 Hz, 6H), 3.00 (q, *J* = 6.7 Hz, 2H), 1.46 (p, *J* = 7.1 Hz, 2H), 1.12 (t, *J* = 7.0 Hz, 9H), 0.61 – 0.40 (m, 2H).

^{13}C NMR (75 MHz, DMSO): δ (ppm) 156.1, 130.8, 130.7, 130.6, 130.2, 128.6, 127.82, 127.5, 127.4, 127.3, 126.3, 125.5, 125.4, 124.6, 123.9, 123.8, 123.2, 63.50, 57.6, 43.0, 39.5, 23.0, 18.2, 7.1.

HR-MS (ESI+): m/z calculated for [$C_{27}H_{33}NO_5Si+Na^+$]: 502.2026, found 502.2011, error 0.4 ppm

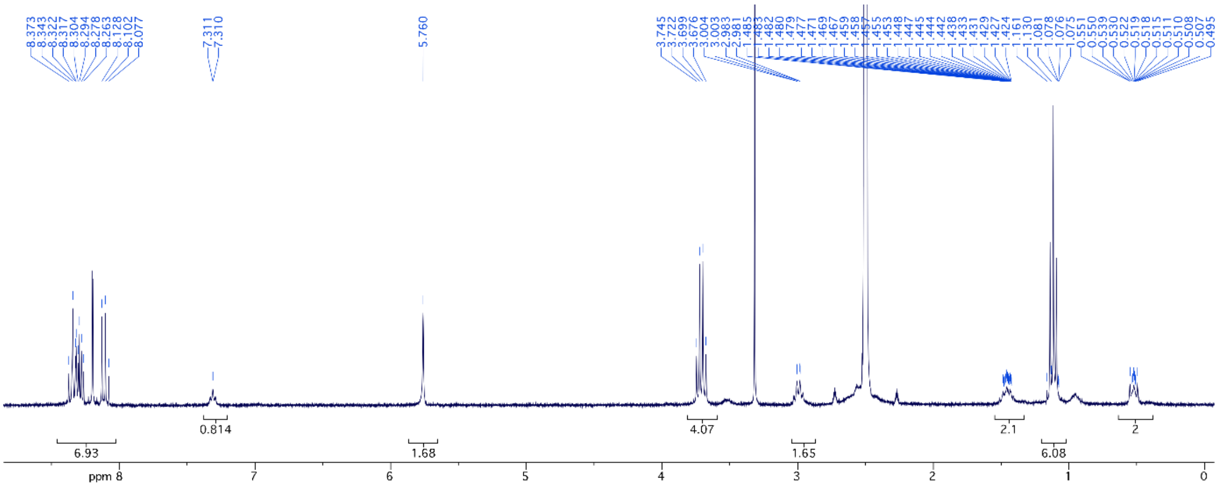

Figure III-28 : NMR ^1H of of N-[3-(Triethoxysilyl)propyl]-pyren-9-ylmethyl carbamate precursor.

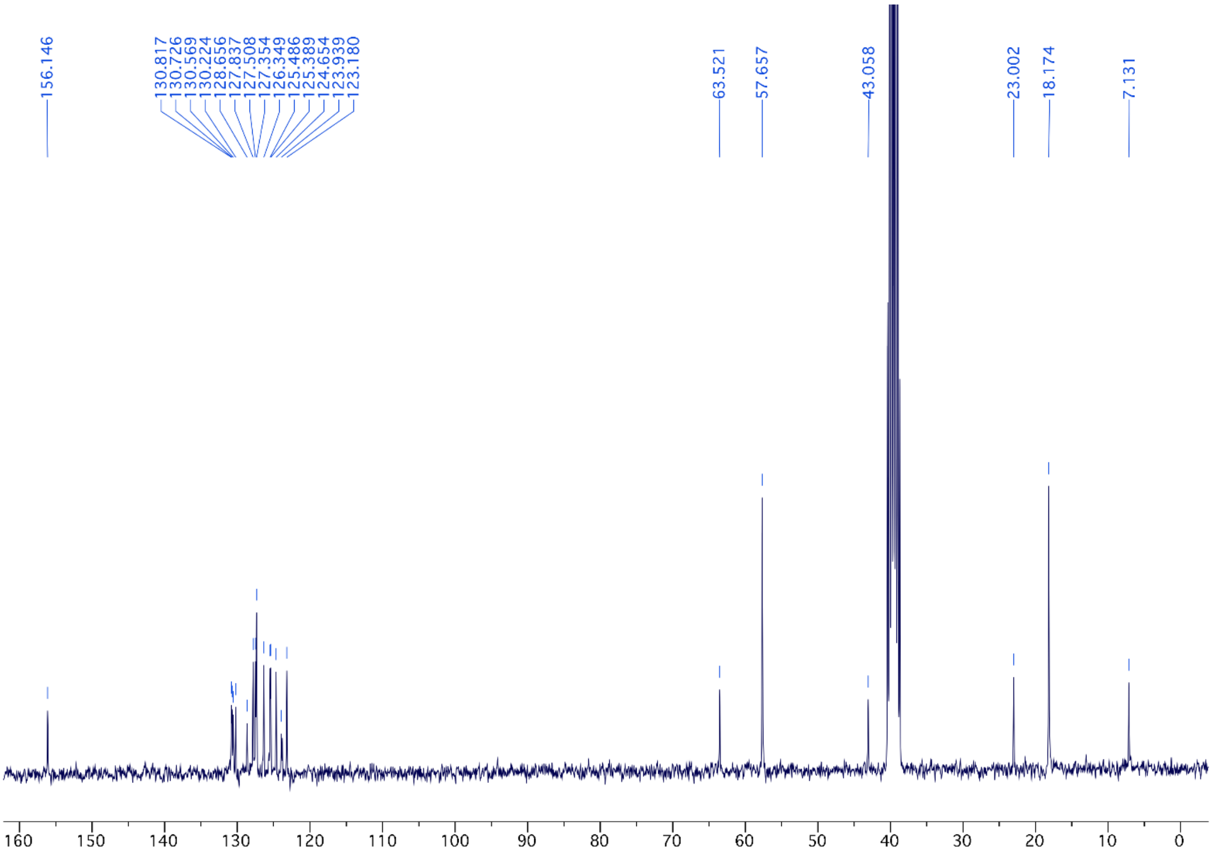

Figure III-29 : NMR ^{13}C of of N-[3-(Triethoxysilyl)propyl]-pyren-9-ylmethyl carbamate precursor.

7.3. Synthesis of N-[N-[3-(Triethoxysilyl)propyl]-(n-polyethyleneglycol-ethyl ether) Carbamate]]-anthracen-9-ylmethyl carbamate precursor

In a Schlenk tube, an equimolar mixture of 2,3-Dichloro-5,6-dicyano-p-benzoquinone (DDQ, 98%, Sigma Aldrich), triphenylphosphine (PPh_3, ReagentPlus®, 99%, Sigma Aldrich), tetrabutylammonium cyanate (Bu_4NOCN) and N-(triethoxysilylpropyl)-O-polyethylene oxide urethane (95%, Gelest) were mixed and stirred at RT for 4 h. Then the solvent was removed under vacuum with a rotary evaporator and the product purified by filtration by chromatography on a silica gel column (eluents cyclohexane: ethyl acetate, or dichloromethane: methanol).

In a Schlenk tube, 0.4 mL of triethylamine was added under argon to a suspension of 9-Anthracenemethanol (167 mg, 0.8 mmol – Sigma Aldrich, 97%) in 2 mL of dry dichloromethane. After addition of the PEG-isocyanate (0.4 g, 0.9 mmol), the reaction was homogenized and the mixture was stirred at RT for 18 h. The solvent was then removed under vacuum with a rotary evaporator. To eliminate the excess of triethylamine, 25 mL of diethyl ether was placed in the Schlenk tube, heated with a heat gun and evaporated under vacuum with a rotary evaporator. The precursor was precipitated in cyclohexane and washed three times with cyclohexane. The product was then extracted with methanol in a separating funnel. No product was obtained with satisfying purities.

7.4. Synthesis of Ur for N-[N-[3-(Triethoxysilyl)propyl]-N'-propyl urea]]-pyren-9-ylmethyl carbamate precursor

7.4.1. Pyrene-isocyanate *Py-1*

In a Schlenk tube, 2 mL of triethylamine was added under argon to a solution of 1-Pyrenemethanol (1 g, 1.3 mmol – Sigma Aldrich, 97%) in 10 mL of dichloromethane. After addition of 1,6-Diisocyanatohexane (3.46 mL, 6.5 mmol, 5 eq – Sigma Aldrich, 98%), the reaction mixture was stirred at RT for 1 h. The solvent was then removed under vacuum with a rotary evaporator. The precursor was washed by cyclohexane, and filtered. 1.32 g (75% yields) of the compound were obtained.

^{1}H NMR (300 MHz, Chloroform-*d*): δ (ppm) 8.64 – 7.72 (m, 9H), 5.83 (s, 2H), 4.76 (s, 1H), 3.37 – 3.06 (m, 4H), 1.44 (d, J = 46.8 Hz, 8H). The integration is not always matching, especially at 3.37 - 3.06 ppm. Reactive 1,6-Diisocyanatohexane is probably still present.

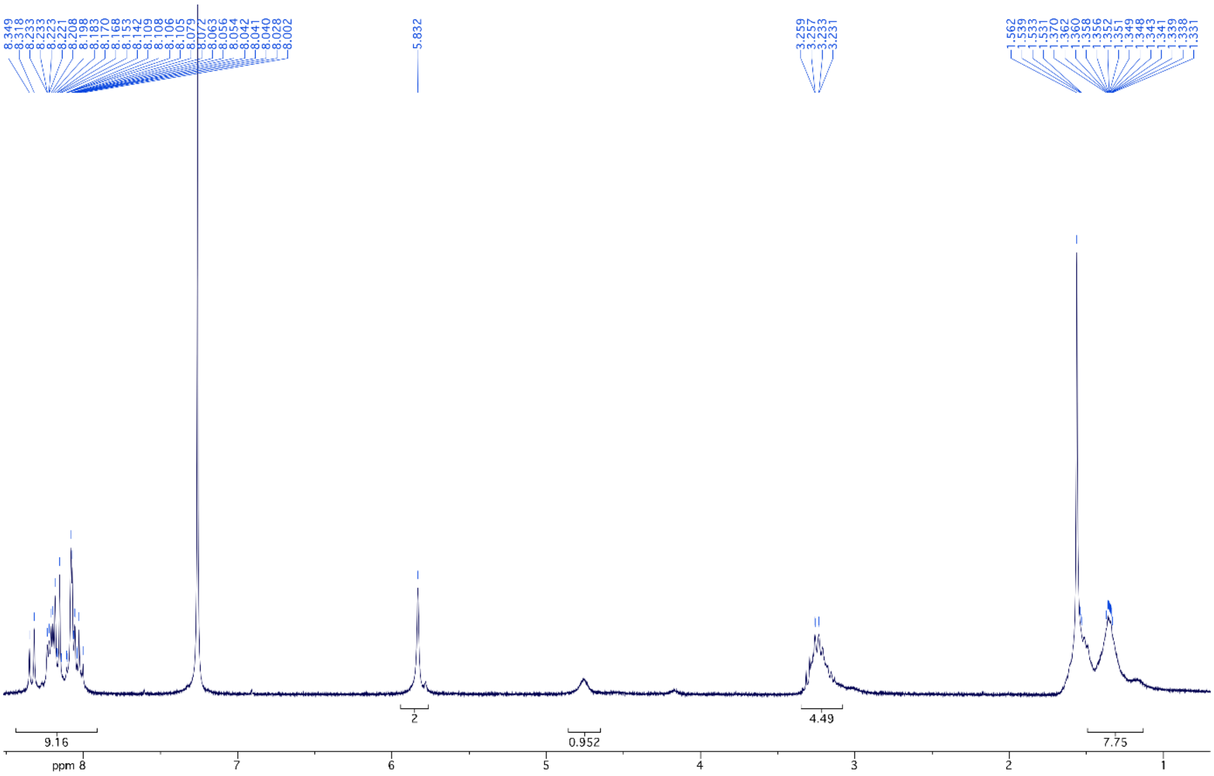

Figure III-30 : NMR ^{1}H of Pyrene-isocyanate.

7.4.2. Alkoxysilane *Py*

In a Schlenk tube, 4.3 mL of triethylamine was added under argon to a solution of 1-Pyreneisocyanate (1.32 g, 3.3 mmol) in 13 mL of dichloromethane. After addition of (3-Aminopropyl)triethoxysilane (0.92 mL, 3.95 mmol, 1.2 eq – Sigma Aldrich, 99%), there is precipitation of a product. The solvent was removed under vacuum with a rotary evaporator. The precursor was further washed by cyclohexane, filtered and purified by chromatography on a silica gel column (eluents dichloromethane: methanol). 0.850 g of the compound (41% yields) were obtained.

^{1}H NMR (300 MHz, DMSO-*d*$_6$): δ (ppm) 8.46 – 7.95 (m, 9H), 7.28 (s, 1H), 5.76 (s, 2H), 3.85 – 3.60 (m, 6H), 3.43 (m, 2H), 3.09 – 2.85 (m, 6H), 1.51 – 1.18 (m, 8H), 1.12 (t, *J* = 7.1 Hz, 9H), 0.50 (bs, 2H).

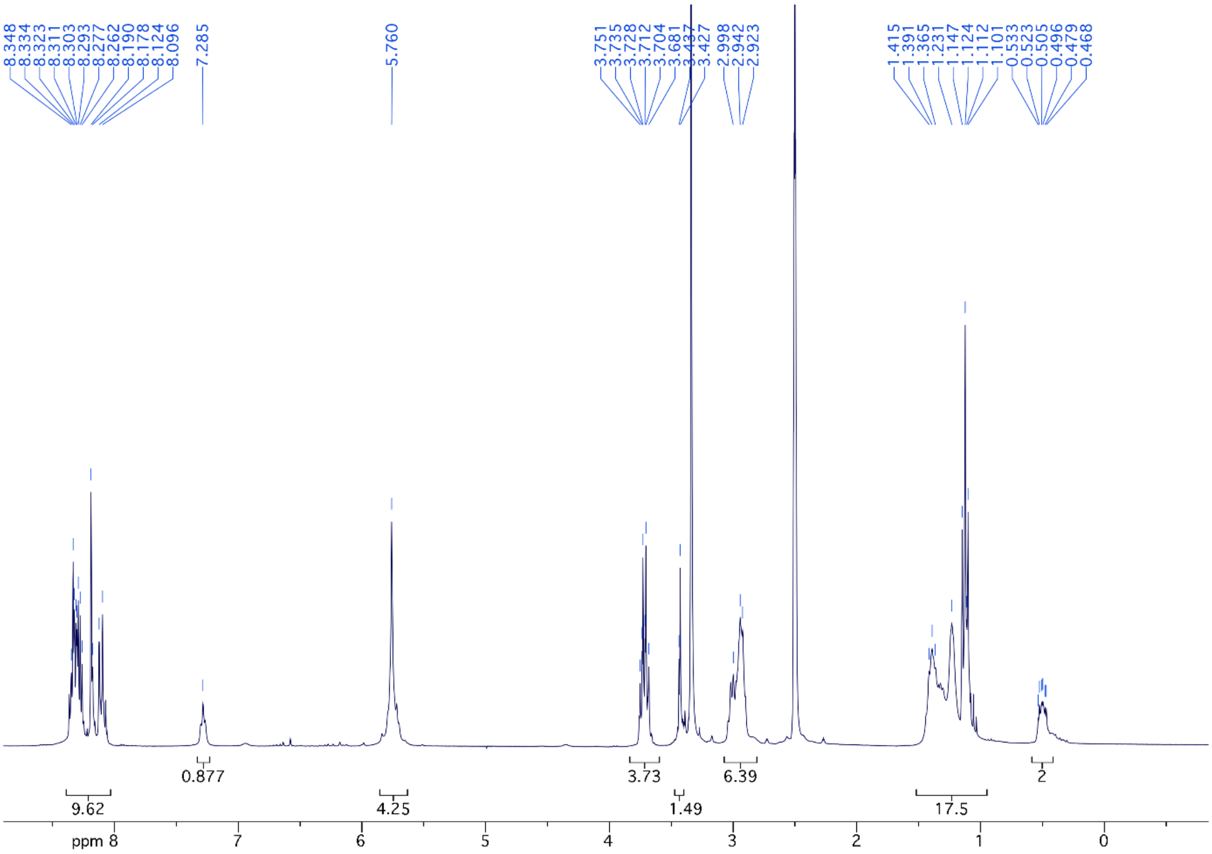

Figure III-31 : NMR ^{1}H of N-[N-[3-(Triethoxysilyl)propyl]-N'-propyl urea]]-pyren-9-ylmethyl Carbamate precursor.

7.5. Synthesis of silica particles (SiNPs)

In 32 mL ultrapure water, 600 mL absolute ethanol (VWR, GPR RectaPur) and 45 mL ammonium hydroxide solution (25%, Carlo Erba), 21 mL tetraethyl orthosilicate (TEOS 98%, Sigma Aldrich) was added dropwise. The solution was let under stirring overnight at RT.[71,72] SiNPs were washed with ethanol through an ultrasonic redispersion-centrifugation process (12 000 rpm for 15 min) and dried under vacuum.

7.6. Synthesis of carboxylate-modified gold nanoparticles (according to a procedure described in 73)

For a typical preparation of 5 nm diameter particles, 1.25 mmol of $HAuCl_4$ dissolved as a 10 mL % (w/v) aqueous solution was at first mixed with 0.63 mmol of mercaptosuccinic acid (Sigma Aldrich 97%) in 50 mL methanol to give a transparent solution in a 500 mL Erlenmeyer flask. A freshly prepared 0.2 M aqueous sodium borohydride solution (62.5 mL, Sigma Aldrich 98%) was then added at a rate of 5 mL per min under vigorous stirring. The solution turned dark-brown immediately but remained transparent until approximately 13 mL of the reductant was added. After further stirring for 1 h, the solvent was removed by decantation after centrifugation at 10000 rpm for 5 min. The precipitate was washed twice with a 20% (v/v) water/methanol solution through an ultrasonic redispersion-centrifugation process to remove impurities. This process was further repeated with methanol and ethanol and dried.

7.7. Patchy SiNPs

N-[3-Triethoxysilyl)propyl]-anthracen-9-ylmethyl precursor was solubilized and sonicated for 3 min in ethanol or toluene at the specific concentration. After a resting time of 1 h the solution was sonicated again for 1 min. The self-assembly was ready for characterization (DLS, fluorescence spectroscopy, CryoTEM) or for grafting on SiNPs.

Typically, 30 mg of SiNPs was dispersed in 4 mL of toluene or ethanol, with 165 µL of NH_4OH in the case of ethanol, in a Schlenk tube. N-[3-Triethoxysilyl)propyl]-anthracen-9-ylmethyl precursor was added all at once at 50 mM in 36 mL. After 18 h stirring at RT the reaction mixture was heated to 80°C for 20 min. The mixture was left to cool down to RT and was subsequently washed three times with ethanol through an ultrasonic redispersion-centrifugation process (12 000 rpm for 15 min) and dried under vacuum.

Bifunctionalization in two steps

For the bifunctional SiNPs synthesized in two steps in ethanol, SiNPs were dispersed in 30 mL ethanol with 685.5 µL NH_4OH and 294 µL 3-mercaptopropyltrimethoxysilane (MPTMS, 1.6 mmol). After 40 min stirring at RT the reaction mixture was heated to 80°C for 20 min. The mixture was left to cool down to RT and was subsequently washed three times with ethanol through an ultrasonic redispersion-centrifugation process (12 000 rpm for 15 min) and dried under vacuum.

Bifunctionalization in one pot

For the bifunctional SiNPs synthesized in one pot in ethanol, SiNPs were directly functionalized with a mixture containing N-[3-Triethoxysilyl)propyl]-anthracen-9-ylmethyl precursor and MPTMS.

Oxidation of thiol groups to sulfonates [74]

In a typical reaction, 3.6 g of thiol-modified particles were suspended in 1.5 mL hydrogen peroxide (H_2O_2 35%, Acros Organics) under stirring at RT for 48 hours. The powder was washed by centrifugation before addition of 1.5 mL sulfuric acid (H_2SO_4, Sigma Aldrich) and stirred for 2 hours at RT. SiNPs were washed with ethanol and water through an ultrasonic redispersion-centrifugation process at 12 000 rpm for 15 min and dried under vacuum.

Acidic treatment to free the amines

The carbamate was hydrolyzed by sonication during 20 min with 2.5 mL trifluoroacetic acid (Sigma Aldrich). NH_2-modified particles were washed with dichloromethane one time (VWR), with a mixture dichloromethane: N,N-diisopropylethylamine one time (90:10, DIEA, Sigma Aldrich) and dichloromethane once again. NH_2-modified particles were recovered through an ultrasonic redispersion-centrifugation process (12 000 rpm for 15 min) and dried under vacuum.

7.8. Peptide coupling between carboxylates on AuNPs and amines on SiNPs

2.5 mg SiNPs were dispersed in 1 mL dimethylformamid (DMF, VWR) and 10 µL DIEA with 11.5 mg AuNPs, 4,5 mg hydroxybenzotriazole (HOBT, 97%, Sigma Aldrich) and 8,3 mg 2-(1H-benzotriazol-1-yl)-1,1,3,3-tetramethyluronium hexafluorophosphate (HBTU, 98%, Sigma Aldrich). The mixture was sonicated for 3 h before being washed with methanol (VWR) through an ultrasonic redispersion-centrifugation process (12 000 rpm for 15 min) and dried under vacuum.

7.9. Control Sulfonate-functionalized SiNPs

Stöber particles were first functionalized with thiol groups by silylation with MPTMS (95%, Sigma Aldrich).[75] Typically, 4.12 g of silica particles were redispersed in a mixture of 410 mL ethanol and 9 mL ammonium hydroxide solution before addition of 4 mL MPTMS (5 $mmol.g^{-1}$ silica). The mixture was stirred for 40 min at RT. Then, the reaction mixture was heated to 80°C for 20 min. The mixture was left to cool down to RT and was subsequently washed three times with ethanol through an ultrasonic redispersion-centrifugation process (12 000 rpm for 15 min) and dried under vacuum. Finally, oxidation of thiol groups leads to sulfonic acid functionalized particles.[75] In a typical reaction, 3.6 g of thiol-modified particles were suspended in 180 mL hydrogen peroxide (H_2O_2 35%, Acros Organics) under stirring at RT for 48 hours. The powder was washed by centrifugation before addition of 150 mL sulfuric acid (H_2SO_4, Sigma Aldrich) and stirred for 2 hours at RT. SiNPs were washed with ethanol and water through an ultrasonic redispersion-centrifugation process (12 000 rpm for 15 min) and dried under vacuum.

7.10. Control Amine-functionalized SiNPs

Typically, 0.77 g of silica particles were dispersed in a mixture of 76.6 mL ethanol and 1.7 mL ammonium hydroxide solution before addition of 0.75 mL (3-Aminopropyl)triethoxysilane (4.2 $mmol.g^{-1}$ silica APTES 99%, Aldrich). The mixture was stirred for 18 h at RT. Then, the reaction mixture was heated to 80°C for 20 min. The mixture was left to cool down to RT and subsequently washed three times with ethanol through an ultrasonic redispersion-centrifugation process (12 000 rpm for 15 min) and dried under vacuum.

7.11. Fluorescence Spectroscopy

Fluorescence intensity emission measurements of N-[3-Triethoxysilyl)propyl]-anthracen-9-ylmethyl precursor in ethanol or toluene at the specific concentration were performed in a HORIBA Jobin-Yvon fluorimeter in a quartz Hellma Analytics high precision cell, with excitation wavelengths of 365 nm and slits of 1 and 5 nm.

7.12. Dynamic light scattering (DLS) and zeta-potential measurements

DLS and zeta-potential measurements were performed on a Malvern Zetasizer Nano spectrometer. The autocorrelation functions were recorded at a scattering angle $\Theta = 90°$ and analyzed by the non-negatively constrained least squares technique (NNLS-Multiple Pass) for the determination of the particle diameter. DLS were measured at RT at low concentration (*ca.* 5 $g.L^{-1}$) in water for SiNPs and at specific concentration in ethanol or toluene for N-[3-Triethoxysilyl)propyl]-anthracen-9-ylmethyl precursor. Zeta Potential measurements were proceeded at 5 $g.L^{-1}$ in DTS1060C cells at RT in KCl buffer (Concentration 100 mM) at different pHs adjusted by addition of NaOH and HCl.

7.13. Electron Microscopy

A drop of sample in aqueous solution was deposited on carbon-coated copper grids (300 mesh). After 3 minutes, the excess liquid was blotted with filter paper. TEM was performed at RT using a Tecnai spirit G2 electron microscope operating at 120 kV and the images were recorded on a Gatan Orius CCD camera. SEM-FEG measurements were proceeded by David Montero, Platform *Institut des Matériaux de Paris Centre.* The same grids were used than for TEM observations. SEM-FEG were performed at RT using Hitachi SU-70 operating at 15 kV.

7.14. Cryo-Transmission Electron Microscopy

A drop of sample in aqueous solution was deposited on plasma treated QUANTIFOIL grids before vitrification: the excess sample was removed by blotting with filter paper (Whatman #4) to obtain a thin film before plunging the grid in liquid nitrogen. CryoTEM was then performed using a FEI Technai Spirit G2 operating at 120 kV equipped with a Gatan cryo-holder operating at -180 °C. Images were recorded on a Gatan Orius CCD camera. At Pasteur institute, this is a Tecnai F20 at 200 kV TEM that was used.

7.15. Preparation of hybrid silica–collagen building blocks (according to a procedure described in 7)

3 mL of a 7.5 x 10^{-1} M sol of sulfonate-grafted Stöber silica particles were mixed with 24 mL of 0.422 mg mL^{-1} of collagen (in 17 mM acetic acid) in 73 ml acetic acid 0.5 M (pH = 2.5, Vf = 100 mL). Collagen fibrillogenesis was triggered upon increasing pH by ammonia diffusion for 3h30.

8. References

(1) Aimé, C.; Coradin, T. Nanocomposites from Biopolymer Hydrogels: Blueprints for White Biotechnology and Green Materials Chemistry. *Journal of Polymer Science Part B: Polymer Physics* **2012**, *50* (10), 669–680.

(2) Aimé, C.; Coradin, T. *Bionanocomposites: Integrating Biological Processes for Bio-Inspired Nanotechnologies.*, Wiley-VCH.; Hoboken USA, 2017.

(3) Mirkin, C. A.; Letsinger, R. L.; Mucic, R. C.; Storhoff, J. J. Mirkin, C. A.; Letsinger, R. L.; Mucic, R. C. Storhoff, J. J. Nature1996, 382, 607-609..Pdf. *Nature* **1996**, *382*, 607–609.

(4) Parak, W. J.; Pellegrino, T.; Micheel, C. M.; Gerion, D.; Williams, S. C.; Alivisatos, A. P. Conformation of Oligonucleotides Attached to Gold Nanocrystals Probed by Gel Electrophoresis. *Nano Letters* **2003**, *3* (1), 33–36.

(5) Wu, J.; Silvent, J.; Coradin, T.; Aimé, C. Biochemical Investigation of the Formation of Three-Dimensional Networks from DNA-Grafted Large Silica Particles. *Langmuir* **2012**, *28* (4), 2156–2165.

(6) Banerjee, I. A.; Yu, L.; Matsui, H. Location-Specific Biological Functionalization on Nanotubes: Attachment of Proteins at the Ends of Nanotubes Using Au Nanocrystal Masks. *Nano Letters* **2003**, *3* (3), 283–287.

(7) Aimé, C.; Mosser, G.; Pembouong, G.; Bouteiller, L.; Coradin, T. Controlling the Nano–bio Interface to Build Collagen–silica Self-Assembled Networks. *Nanoscale* **2012**, *4* (22), 7127–7134.

(8) Mout, R.; Ray, M.; Tay, T.; Sasaki, K.; Yesilbag Tonga, G.; Rotello, V. M. General Strategy for Direct Cytosolic Protein Delivery *via* Protein–Nanoparticle Co-Engineering. *ACS Nano* **2017**, *11* (6), 6416–6421.

(9) Banani, S. F.; Lee, H. O.; Hyman, A. A.; Rosen, M. K. Biomolecular Condensates: Organizers of Cellular Biochemistry. *Nature Reviews Molecular Cell Biology* **2017**, *18* (5), 285–298.

(10) Romero, S.; Quatela, A.; Bornschlögl, T.; Guadagnini, S.; Bassereau, P.; Tran Van Nhieu, G. Filopodium Retraction Is Controlled by Adhesion to Its Tip. *Journal of Cell Science* **2012**, *125* (22), 5587–5587.

(11) Steketee, M. B.; Moysidis, S. N.; Jin, X.-L.; Weinstein, J. E.; Pita-Thomas, W.; Raju, H. B.; Iqbal, S.; Goldberg, J. L. Nanoparticle-Mediated Signaling Endosome Localization Regulates Growth Cone Motility and Neurite Growth. *Proceedings of the National Academy of Sciences* **2011**, *108* (47), 19042–19047.

(12) Hoffmann, C.; Mazari, E.; Lallet, S.; Le Borgne, R.; Marchi, V.; Gosse, C.; Gueroui, Z. Spatiotemporal Control of Microtubule Nucleation and Assembly Using Magnetic Nanoparticles. *Nature Nanotechnology* **2013**, *8* (3), 199–205.

(13) Zhang, Z.; Glotzer, S. C. Self-Assembly of Patchy Particles. *Nano Letters* **2004**, *4* (8), 1407–1413.

(14) Glotzer, S. C.; Solomon, M. J. Anisotropy of Building Blocks and Their Assembly into Complex Structures. *Nature Materials* **2007**, *6* (8), 557–562.

(15) Liddell, C. ; Summers, C. .; Gokhale, A. . Stereological Estimation of the Morphology Distribution of ZnS Clusters for Photonic Crystal Applications. *Materials Characterization* **2003**, *50* (1), 69–79.

(16) Yang, S.-M.; Kim, S.-H.; Lim, J.-M.; Yi, G.-R. Synthesis and Assembly of Structured Colloidal Particles. *Journal of Materials Chemistry* **2008**, *18* (19), 2177–2190.

(17) Grätzel, M. Photoelectrochemical Cells. **2001**, *414*, 7.

(18) Champion, J. A.; Katare, Y. K.; Mitragotri, S. Making Polymeric Micro- and Nanoparticles of Complex Shapes. *Proceedings of the National Academy of Sciences* **2007**, *104* (29), 11901–11904.

(19) Langer, R.; Tirrell, D. A. Designing Materials for Biology and Medicine. *Nature* **2004**, *428* (6982), 487–492.

(20) Zhao, Y.-P.; Ye, D.-X.; Wang, G.-C.; Lu, T.-M. Novel Nano-Column and Nano-Flower Arrays by Glancing Angle Deposition. *Nano Letters* **2002**, *2* (4), 351–354.

(21) Snyder, C. E.; Yake, A. M.; Feick, J. D.; Velegol, D. Nanoscale Functionalization and Site-Specific Assembly of Colloids by Particle Lithography. *Langmuir* **2005**, *21* (11), 4813–4815.

(22) Cui, J.-Q.; Kretzschmar, I. Surface-Anisotropic Polystyrene Spheres by Electroless Deposition. *Langmuir* **2006**, *22* (20), 8281–8284.

(23) Hong, L.; Jiang, S.; Granick, S. Simple Method to Produce Janus Colloidal Particles in Large Quantity. *Langmuir* **2006**, *22* (23), 9495–9499.

(24) Perro, A.; Meunier, F.; Schmitt, V.; Ravaine, S. Production of Large Quantities of "Janus" Nanoparticles Using Wax-in-Water Emulsions. *Colloids and Surfaces A: Physicochemical and Engineering Aspects* **2009**, *332* (1), 57–62.

(25) Binks, B. P. Particles as Surfactants Ͳsimilarities and Differences. *Interface Science* **2002**, *7*, 21–41.

(26) Gu, H.; Yang, Z.; Gao, J.; Chang, C. K.; Xu, B. Heterodimers of Nanoparticles: Formation at a Liquid−Liquid Interface and Particle-Specific Surface Modification by Functional Molecules. *Journal of the American Chemical Society* **2005**, *127* (1), 34–35.

(27) Manoharan, V. N.; Elsesser, M. T.; Pine, D. J. Dense Packing and Symmetry in Small Clusters of Microspheres. *Science* **2003**, *301* (5632), 483–487.

(28) Cho, Y.-S.; Yi, G.-R.; Lim, J.-M.; Kim, S.-H.; Manoharan, V. N.; Pine, D. J.; Yang, S.-M. Self-Organization of Bidisperse Colloids in Water Droplets. *Journal of the American Chemical Society* **2005**, *127* (45), 15968–15975.

(29) Wang, Y.; Wang, Y.; Breed, D. R.; Manoharan, V. N.; Feng, L.; Hollingsworth, A. D.; Weck, M.; Pine, D. J. Colloids with Valence and Specific Directional Bonding. *Nature* **2012**, *491* (7422), 51–55.

(30) Roh, K.-H.; Martin, D. C.; Lahann, J. Biphasic Janus Particles with Nanoscale Anisotropy. *Nature Materials* **2005**, *4* (10), 759–763.

(31) Roh, K.-H.; Martin, D. C.; Lahann, J. Triphasic Nanocolloids. *Journal of the American Chemical Society* **2006**, *128* (21), 6796–6797.

(32) Xu, S.; Nie, Z.; Seo, M.; Lewis, P.; Kumacheva, E.; Stone, H. A.; Garstecki, P.; Weibel, D. B.; Gitlin, I.; Whitesides, G. M. Generation of Monodisperse Particles by Using Microfluidics: Control over Size, Shape, and Composition. *Angewandte Chemie International Edition* **2005**, *44* (5), 724–728.

(33) Désert, A.; Hubert, C.; Fu, Z.; Moulet, L.; Majimel, J.; Barboteau, P.; Thill, A.; Lansalot, M.; Bourgeat-Lami, E.; Duguet, E.; et al. Synthesis and Site-Specific Functionalization of Tetravalent, Hexavalent, and Dodecavalent Silica Particles. *Angewandte Chemie International Edition* **2013**, *52* (42), 11068–11072.

(34) Chomette, C.; Duguet, E.; Mornet, S.; Yammine, E.; Manoharan, V. N.; Schade, N. B.; Hubert, C.; Ravaine, S.; Perro, A.; Tréguer-Delapierre, M. Templated Growth of Gold Satellites on Dimpled Silica Cores. *Faraday Discussions* **2016**, *191*, 105–116.

(35) Désert, A.; Chaduc, I.; Fouilloux, S.; Taveau, J.-C.; Lambert, O.; Lansalot, M.; Bourgeat-Lami, E.; Thill, A.; Spalla, O.; Ravaine, S.; et al. High-Yield Preparation of Polystyrene/Silica Clusters of Controlled Morphology. *Polymer Chemistry* **2012**, *3* (5), 1130–1132.

(36) Salant, A.; Amitay-Sadovsky, E.; Banin, U. Directed Self-Assembly of Gold-Tipped CdSe Nanorods. *Journal of the American Chemical Society* **2006**, *128* (31), 10006–10007.

(37) Carbone, L.; Jakab, A.; Khalavka, Y.; Sönnichsen, C. Light-Controlled One-Sided Growth of Large Plasmonic Gold Domains on Quantum Rods Observed on the Single Particle Level. *Nano Letters* **2009**, *9* (11), 3710–3714.

(38) Hamon, C.; Martini, C.; Even-Hernandez, P.; Boichard, B.; Voisin, H.; Largeau, L.; Gosse, C.; Coradin, T.; Aimé, C.; Marchi, V. An Aqueous One-Pot Route to Gold/Quantum Rod Heterostructured Nanoparticles Functionalized with DNA. *Chemical Communications* **2015**, *51* (89), 16119–16122.

(39) Moreau, J. J. E.; Vellutini, L.; Wong Chi Man, M.; Bied, C.; Dieudonné, P.; Bantignies, J.-L.; Sauvajol, J.-L. Lamellar Bridged Silsesquioxanes: Self-Assembly through a Combination of Hydrogen Bonding and Hydrophobic Interactions. *Chemistry - A European Journal* **2005**, *11* (5), 1527–1537.

(40) Ramin, M. A.; Le Bourdon, G.; Daugey, N.; Bennetau, B.; Vellutini, L.; Buffeteau, T. PM-IRRAS Investigation of Self-Assembled Monolayers Grafted onto SiO_2/Au Substrates. *Langmuir* **2011**, *27* (10), 6076–6084.

(41) DeVries, G. A.; Brunnbauer, M.; Hu, Y.; Jackson, A. M.; Long, B.; Neltner, B. T.; Uzun, O.; Wunsch, B. H.; Stellacci, F. Divalent Metal Nanoparticles. *Science* **2007**, *315* (5810), 358–361.

(42) Moreau, J. J. E.; Vellutini, L.; Chi Man, M. W.; Bied, C.; Bantignies, J.-L.; Dieudonné, P.; Sauvajol, J.-L. Self-Organized Hybrid Silica with Long-Range Ordered Lamellar Structure. *Journal of the American Chemical Society* **2001**, *123* (32), 7957–7958.

(43) Moreau, J. J. E.; Vellutini, L.; Wong Chi Man, M.; Bied, C. New Hybrid Organic−Inorganic Solids with Helical Morphology via H-Bond Mediated Sol−Gel Hydrolysis of Silyl Derivatives of Chiral (*R* , *R*)- or (*S* , *S*)-Diureidocyclohexane. *Journal of the American Chemical Society* **2001**, *123* (7), 1509–1510.

(44) Moreau, J. J. E.; Vellutini, L.; Wong Chi Man, M.; Bied, C. Shape-Controlled Bridged Silsesquioxanes: Hollow Tubes and Spheres. *Chemistry - A European Journal* **2003**, *9* (7), 1594–1599.

(45) Shimojima, A.; Liu, Z.; Ohsuna, T.; Terasaki, O.; Kuroda, K. Self-Assembly of Designed Oligomeric Siloxanes with Alkyl Chains into Silica-Based Hybrid Mesostructures. *Journal of the American Chemical Society* **2005**, *127* (40), 14108–14116.

(46) Graffion, J.; Dems, D.; Demirelli, M.; Coradin, T.; Delsuc, N.; Aimé, C. An All-in-One Molecule for the One-Step Synthesis of Functional Hybrid Silica Particles with Tunable Sizes: An All-in-One Molecule for the One-Step Synthesis of Functional Hybrid Silica Particles with Tunable Sizes. *European Journal of Inorganic Chemistry* **2017**, *2017* (43), 5047–5051.

(47) Gil, R.; Guillerez, M.-G.; Poulin, J.-C.; Schulz, E. Charge-Transfer Complex Study by Chemical Force Spectroscopy: A Dynamic Force Spectroscopic Approach. *Langmuir* **2007**, *23* (2), 542–548.

(48) Song, H.; Yang, G.; Huang, P.; Kong, D.; Wang, W. Self-Assembled PEG–poly(L - Valine) Hydrogels as Promising 3D Cell Culture Scaffolds. *Journal of Materials Chemistry B* **2017**, *5* (9), 1724–1733.

(49) Lee, B. K.; Lee, H. Y.; Kim, P.; Suh, K. Y.; Seo, J. H.; Cha, H. J.; Kawai, T. Stepwise Self-Assembly of a Protein Nanoarray from a Nanoimprinted Poly(Ethylene Glycol) Hydrogel. *Small* **2008**, *4* (3), 342–348.

(50) Thakur, G.; Prashanthi, K.; Thundat, T. Directed Self-Assembly of Proteins into Discrete Radial Patterns. *Scientific Reports* **2013**, *3* (1).

(51) Shimizu, L. S.; Smith, M. D.; Hughes, A. D.; Shimizu, L. S. Self-Assembly of a Bis-Urea Macrocycle into a Columnar Nanotube. *Chemical Communications* **2001**, No. 17, 1592–1593.

(52) Yabuuchi, K.; Marfo-Owusu, E.; Kato, T. A New Urea Gelator: Incorporation of Intra- and Intermolecular Hydrogen Bonding for Stable 1D Self-Assembly. *Organic & Biomolecular Chemistry* **2003**, *1* (19), 3464.

(53) Dawn, S.; Dewal, M. B.; Sobransingh, D.; Paderes, M. C.; Wibowo, A. C.; Smith, M. D.; Krause, J. A.; Pellechia, P. J.; Shimizu, L. S. Self-Assembled Phenylethynylene Bis-Urea Macrocycles Facilitate the Selective Photodimerization of Coumarin. *Journal of the American Chemical Society* **2011**, *133* (18), 7025–7032.

(54) Akhlaghinia, B. A New and Convenient Method of Generating Alkyl Isocyanates from Alcohols, Thiols and Trimethylsilyl Ethers Using Triphenylphosphine/ 2,3-Dichloro-5,6-Dicyanobenzoquinone/Bu4NOCN. *Synthesis* **2005**, No. 12, 1955–1958.

(55) Wu, J. H.; Xu, T. Z.; Ang, S. G.; Xu, Q.-H.; Xu, G. Q. Radially Oriented Anthracene Nanowire Arrays: Preparation, Growth Mechanism, and Optical Fluorescence. *Nanoscale* **2011**, *3* (4), 1855–1860.

(56) Liu, H.; Li, Y.; Xiao, S.; Gan, H.; Jiu, T.; Li, H.; Jiang, L.; Zhu, D.; Yu, D.; Xiang, B.; et al. Synthesis of Organic One-Dimensional Nanomaterials by Solid-Phase Reaction. *Journal of the American Chemical Society* **2003**, *125* (36), 10794–10795.

(57) Seko, T.; Ogura, K.; Kawakami, Y.; Sugino, H.; Toyotama, H.; Tanaka, J. Excimer Emission of Anthracene, Perylene, Coronene and Pyrene Microcrystals Dispersed in Water. *Chemical Physics Letters* **1998**, *291* (3–4), 438–444.

(58) Kalinowski, J.; Giro, G.; Cocchi, M.; Fattori, V.; Zamboni, R. The Nature of Emitting States in Electroluminescence of Polymeric Films Doped with Anthracene and Anthracene-Based Supramolecules. *Chemical Physics* **2002**, *277* (3), 387–396.

(59) Manna, B.; Ghosh, R.; Palit, D. K. Exciton Dynamics in Anthracene Nanoaggregates. *The Journal of Physical Chemistry C* **2015**, *119* (19), 10641–10652.

(60) Ferguson, J.; Castellan, A.; Desvergne, J.-P.; Bouas-Laurent, H. Excimer Intermediate in the Unsymmetrical Photodimerization of the Anthracene Ring System. *Chemical Physics Letters* **1981**, *78* (3), 446–450.

(61) Bouas-Laurent, H.; Desvergne, J.-P.; Castellan, A.; Lapouyade, R. Photodimerization of Anthracenes in Fluid Solution: Structural Aspects. *Chemical Society Reviews* **2000**, *29* (1), 43–55.

(62) Birks, J. B.; Aladekomo, J. B. THE PHOTO-DIMERIZATION AND EXCIMER FLUORESCENCE OF 9-METHYL ANTHRACENE. *Photochemistry and Photobiology* **1963**, *2* (4), 415–418.

(63) Bains, G. K.; Kim, S. H.; Sorin, E. J.; Narayanaswami, V. The Extent of Pyrene Excimer Fluorescence Emission Is a Reflector of Distance and Flexibility: Analysis of the Segment Linking the LDL Receptor-Binding and Tetramerization Domains of Apolipoprotein E3. *Biochemistry* **2012**, *51* (31), 6207–6219.

(64) Birks, J. B.; Christophorou, L. G. Excimer Fluorescence Spectra of Pyrene Derivatives. *Spectrochimica Acta* **1963**, *19* (2), 401–410.

(65) Lehrer, S. S. Pyrene Excimer Fluorescence as a Probe of Protein Conformational Change. In *Proteins: Structure, Function, and Engineering.*; Subcellular Biochemistry; Biswas B.B., Roy S., 1995; Vol. 24.

(66) Birks, J. B. *Photophysics of Aromatic Molecules.*, Wiley-Interscience.; 1970.

(67) del Valle, J. C.; Turek, A. M.; Tarkalanov, N. D.; Saltiel, J. Distortion of the Fluorescence Spectrum of Anthracene with Increasing Laser Pulse Excitation Energy. *The Journal of Physical Chemistry A* **2002**, *106* (20), 5101–5104.

(68) Giraud-Guille, M.-M.; Besseau, L.; Martin, R. Liquid Crystalline Assemblies of Collagen in Bone and in Vitro Systems. *Journal of Biomechanics* **2003**, *36* (10), 1571–1579.

(69) Birk, D. E.; Bruckner, P. Collagen Suprastructures. In *Collagen: Primer in Structure, Processing and Assembly*; Brinckmann, J., Notbohm, H., Müller, P. K., Eds.; Springer Berlin Heidelberg: Berlin, Heidelberg, 2005; pp 185–205.

(70) Köster, S.; Evans, H. M.; Wong, J. Y.; Pfohl, T. An In Situ Study of Collagen Self-Assembly Processes. *Biomacromolecules* **2008**, *9* (1), 199–207.

(71) Stöber, W.; Fink, A.; Bohn, E. Controlled Growth of Monodisperse Silica Spheres in the Micron Size Range. *Journal of Colloid and Interface Science* **1968**, *26* (1), 62–69.

(72) Thomassen, L. C. J.; Aerts, A.; Rabolli, V.; Lison, D.; Gonzalez, L.; Kirsch-Volders, M.; Napierska, D.; Hoet, P. H.; Kirschhock, C. E. A.; Martens, J. A. Synthesis and Characterization of Stable Monodisperse Silica Nanoparticle Sols for *in Vitro* Cytotoxicity Testing. *Langmuir* **2010**, *26* (1), 328–335.

(73) Chen, S.; Kimura, K. Synthesis and Characterization of Carboxylate-Modified Gold Nanoparticle Powders Dispersible in Water. *Langmuir* **1999**, *15* (4), 1075–1082.

(74) Maria Claesson, E.; Philipse, A. P. Thiol-Functionalized Silica Colloids, Grains, and Membranes for Irreversible Adsorption of Metal(Oxide) Nanoparticles. *Colloids and Surfaces A: Physicochemical and Engineering Aspects* **2007**, *297* (1–3), 46–54.

(75) Marschall, R.; Bannat, I.; Caro, J.; Wark, M. Proton Conductivity of Sulfonic Acid Functionalised Mesoporous Materials. *Microporous and Mesoporous Materials* **2007**, *99* (1–2), 190–196.

IV. Biomaterials engineering for neural type cells differentiation

Content

1. Peripheral nerve regeneration

1.1. Biological mechanism

Peripheral nerves (PN) comprise all nerves in the body except for the brain and spinal cord. It is a network of 43 pairs of motor and sensory nerves that connect the brain and spinal cord (the central nervous system) to the entire human body. These nerves control the functions of sensation, movement and motor coordination. Injuries in the Peripheral Nervous System (PNS) are mostly caused by trauma like traffic accidents, bone fractures and joint dislocations. Nerves are usually damaged by elongation, laceration or compression. More than half of nerve injuries affect the lower limbs and it is estimated that 2.8% of trauma patients are due to peripheral nerve injury.[1] Damages in PN can also result from complications of anesthesia and neuropathic or metabolic disorders. These injuries often lead to partial or complete loss of sensory, motor or autonomic functions that can seriously compromise the life quality of the patients.[2–4]

The PNS has a great potential for self-regeneration that the central nervous system (CNS) has not. This is mainly due to the differences in response to injury of the respective glial cells.[5] The glial cells are all non-neuronal cells, providing support and protection to the neurons. The glia of the PNS, Schwann cells, convert to a regenerative phenotype thereby promoting the formation of a basal lamina and providing abundant cues to trigger neuronal regenerative response.[6] In the immediate time post injury, the nerve cell adapts its functioning. The priority is not anymore the nervous influx, but the synthesis of the structural element necessary to restore the architecture, metabolism and function of the damaged tissue.[7] All the genomic regulation gets modified too, in particular the synthesis of proteins, like the ones expressed at the surface of Schwann cells.[8]

The process of regeneration is named Wallerian degeneration, first studied by Augustus Volney Waller in 1850 (Figure IV-1).[9] Following injury, Schwann cells split and detach, retracting their sheaths from the axons.[10] They start proliferating and help the recruited macrophages to clear the cellular and myelin debris over 3 to 6 weeks. At the same time, the loss of contact with the axons stimulate the proliferation of Schwann cells and fibroblasts. Those cells align themselves to create the bands of Bünger, also named tubes of regeneration. Those bands express stimulating factors to create a favorable environment for nerve regrowth towards the target organ. In particular, they produce neurotrophic growth factors to attract neurites. In a next step, a growth cone emerges from severed axons, in a budding structure and containing filopodia that react in function of their environment. They will retract when they meet an unfavorable signal, and look for a more favorable one toward which they can orient and extend. This is a growth mediated by chemoattraction and chemorepulsion and the Band of Bünger becomes a chemotactic guide. The elongation of axons in the direction of the synaptic target has a rate of about 2–5 mm per day, therefore severe damage can take month to heal.[11]

Figure IV-1 : Schematic representation of Wallerian degeneration, adapted from [3].

Several factors can prevent the regeneration after a traumatic injury: axons regrow but may not properly connect to their targets. In addition, inflammation and scarring processes can inhibit neuronal regeneration. Overall, the success of nerve self-repair depends crucially on the length of the gap. Nerve cells have been found to be able to easily bridge gaps of less than 6 mm.[12]

1.2. Nerve repair

For larger gaps than 6 mm, when the nerve is not able to self-regenerate, surgical repair (grafts) is currently the gold standard with all the associated concerns already exposed (Chapter I).[13–20] Bioengineering approaches have the advantages not to have any compatibility issue and avoid a second injury. The material is used to connect the damage nerves at the site of injury, providing a direct framework for nerve regeneration with minimum surgery work. This scaffold must simulate the environment needed for cell growth and consequently has to fit specific identified requirements (*cf.* Chapter I). An ideal scaffold needs to feature a combination of optimal material size, architecture, and surface properties to allow the formation of a new extracellular matrix in which blood vessels, fibroblasts and Schwann cells can colonize and collectively create favorable circumstances for nerve regeneration to occur.[19] The biomaterial is ideally longitudinally oriented to mimic highly ordered and aligned bundles of axons from PNS and provide guidance for neurite regrowth.[21]

2. Engineering a bionanocomposite

This exposed state of the art underlined the necessity for orientational order and functionalization with bioactive epitopes, both controlled at the nanoscale in order to promote PN regeneration. In this field, very few nanohybrid organic-inorganic matrices were developed so far. In particular, the use of inorganic particles has been restricted to the design of colloidal systems for drug delivery.

2.1. Extrusion of collagen-SiNP threads

The structuration of the biomaterial has a great importance to promote PN regeneration, in particular in terms of alignment. To help the neurites to grow in the specific direction toward their synaptic target, the material has to drive the orientational growth.

For this reason, in this study, the bionanocomposite will be extruded to produce hybrid collagen-based threads, thanks to the help of Lise Picaut (PhD student, LCMCP & INSP, Sorbonne University) (Figure IV-2). Soluble collagen is mixed in acid conditions (pH 2.5) with the SiNPs of interest. Extrusion is performed in a buffered solution (pH 7.5) triggering collagen fibrillogenesis through pH increase.

The buffered solution was selected according to a previous study of our group. Eight extrusion buffers of different ionic strengths from 150 mM to 1.65 M were tested and the extrusion and ageing of the collagen threads were monitored to obtain the most suitable characteristics: preservation of the diameter of the extruded thread, no shrinking or swelling recorded at this ionic strength.[22] Through the analysis, the Phosphate Buffered Saline (PBS) 5X was selected.

Numerous parameters have to be taken account in this study and some fixed in the following experiment. The diameter of the blunt needle is chosen at 390 μm and the extrusion speed at 400 $\mu m.s^{-1}$.

Figure IV-2 : (A) Scheme of the experimental set-up of extrusion adapted from [22]. (B) Picture of an extruded thread in the solution bath at the needle exit. The black rectangle is the needle exit. Scale bare: 200 µm.

We will focus on the collagen concentration, the collagen-SiNP ratio and the SiNP surface chemistry that will be varied in this study. After extrusion, the threads will be characterized by optical microscopy to follow up their diameter evolution. A maturation of ten days was necessary to obtain a stable material.

2.2. PC12, a cellular model

PN regeneration studies are usually performed with cells from dorsal root ganglion (DRG), a cluster of neurons in the dorsal root of a spinal nerve. However, the isolation and culture of DRG neurons is time consuming and highly technical, and requires specific equipment and authorization.

We chose for this project to proceed with a cell line named PC12 graciously given by Flore Renaud-Païtra (Laboratoire de Génétique et Biologie Cellulaire, Université Versailles Saint-Quentin-en-Yvelines). It is a cell line derived from a pheochromocytoma (or tumor) of the rat located in the kidney. PC12 cells have an embryonic origin from the neural crest. PC12 cells resemble the phenotype of sympathetic ganglion neurons upon differentiation with growth factors and present the great advantage to be subcultured indefinitely.[23] It gives a good idea of the response of neuronal cells to a biomaterial in a first step. Promising candidates for *in vivo* experiment should then be tested with DRG cells.

Two different growth factors can trigger survival and differentiation of PC12 cells after adhesion to the collagen thread: nerve growth factors (NGF), or fibroblast growth factors (FGF) in presence of heparin.[24–26] Differentiation usually occurs in 3 to 4 days after growth factor addition.

Cell experiments were conducted thanks to the help of C. Hélary (LCMCP). In a preliminary study, we analyzed the cells behavior over time. We plated the PC12 cells on the different collagen-based threads at 30 mg.mL^{-1}. The differentiation of PC12 cells is usually described in the literature with growth factor, either with NGF or FGF, but we decided to also analyze the influence of the scaffold in absence of growth factor and we have compared the cell adhesion and differentiation on the different threads with and without FGF (Figure IV-3). The differentiation of the PC12 in nerve cells can be characterized by the number of extensions per cell, named neurites, and the length of those neurites. The orientation of the neurites is indicated by yellow arrows on the Figure IV-3 and seems to have a good alignment with threads direction. As expected, samples treated with FGF seem to have more and longer neurites (Figure IV-3-B).

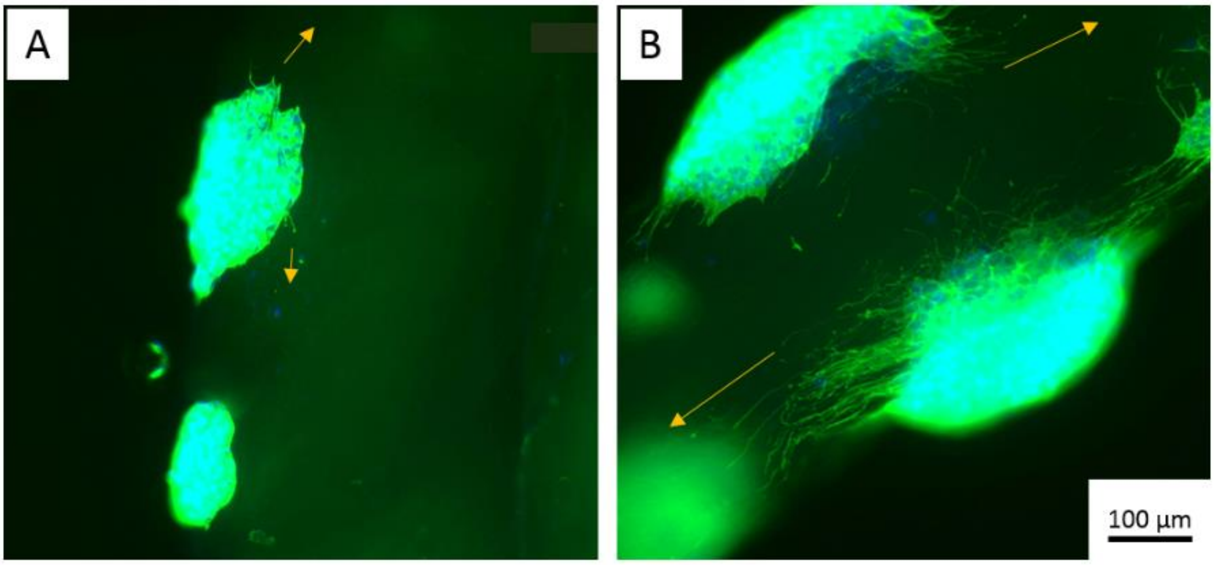

Figure IV-3 : Representative fluorescence microscopy images of PC12 cultured for 10 days and stained for actin (phalloidin) and nucleus (DAPI) on collagen threads (A) without or (B) with FGF.

One thread of each condition (SiNPs of different surface chemistry, different concentrations, ± FGF) was fixed at day 3, 5, 7 and 10. Cell viability of PC12 cells was compared on Figure IV-4. The number of cells varies strongly over time and as a function of the condition. It is in constant increase for the control glass without FGF, or for collagen thread with collagen with FGF. It stabilized quickly for SiNP-IKVAV-10x, or SiNP-SO$_3^-$-10x. No specific tendency is visible here, however the cell viability seems to mostly be stabilized between 5 to 10 days.

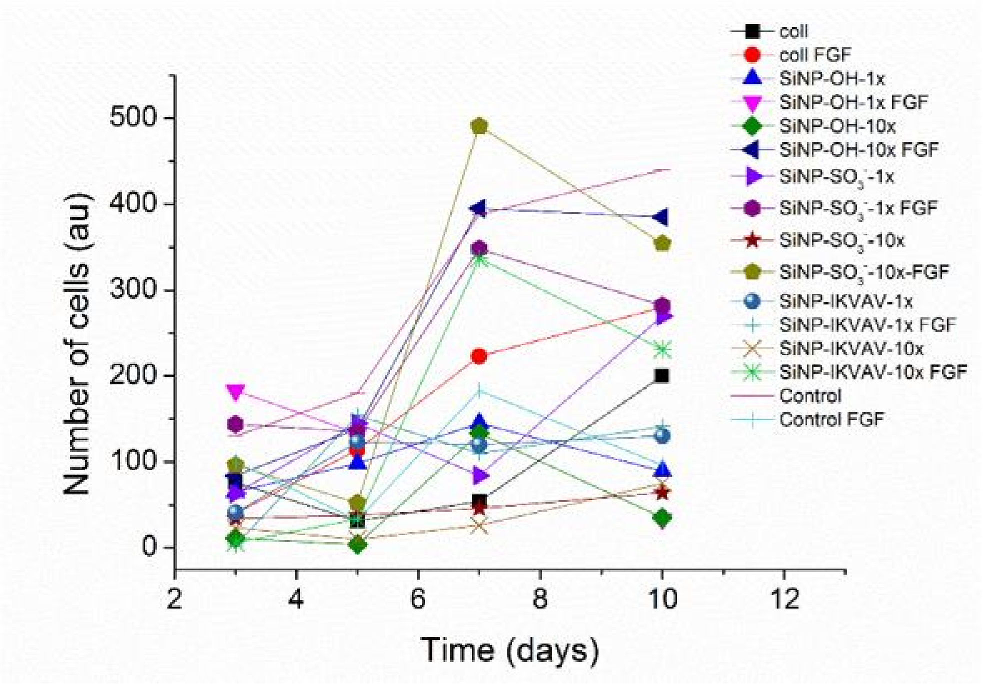

Figure IV-4 : Number of cells as a function of the time.

In order to analyze more precisely the PC12 behavior on the different scaffolds, we determined with this preliminary study that 10 days could be an interesting time length.

3. Bionanocomposites of the study

3.1. Collagen-SiNP threads

In this project, we propose a bottom-up approach using silica nanoparticles (SiNP) integrated within a collagen matrix. SiNPs are functionalized to control (1) the collagen structure (fibrillogenesis) and (2) the bioactivity of the material (peptide epitope). (1) Indeed, the first chemical group that we grafted at the surface of SiNPs is sulfonate. Collagen triple helices in acetic acid interacts electrostatically with sulfonate groups.[27] Type I collagen triple helices are known to undergo self-assembly under mild acidic to neutral conditions, forming fibrils *ca*. 100 nm in diameter and > 1 mm in length.[28,29] The presence of SiNP-SO_3^- has been shown to modify the self-assembly of collagen by tuning its local concentration and consequently has a structuring effect on the biomaterial. (2) SiNPs are also used as a platform to present neuro active laminin epitope IKVAV to the cells. This previously described cell-binding peptide is expected to promote neurite extension.[30]

Groups (1) and (2) can also be combined at the surface of a single SiNP. They can be statistically distributed at the surface of SiNPs, or organized into functional clusters or patches. Those patches have been already described in chapter III. The clusters can allow the growth of well-calibrated collagen fibrils forming the scaffold structure, and the simultaneous incorporation of neuro-active biomolecules. In particular, from a functional point of view, and as previously described, the clustering of functional peptide epitopes should strengthen neuron differentiation, as compared to an identical concentration of functional molecules dispersed in a matrix. This should ultimately lead to the elaboration of hybrid biomaterials for axon regeneration.

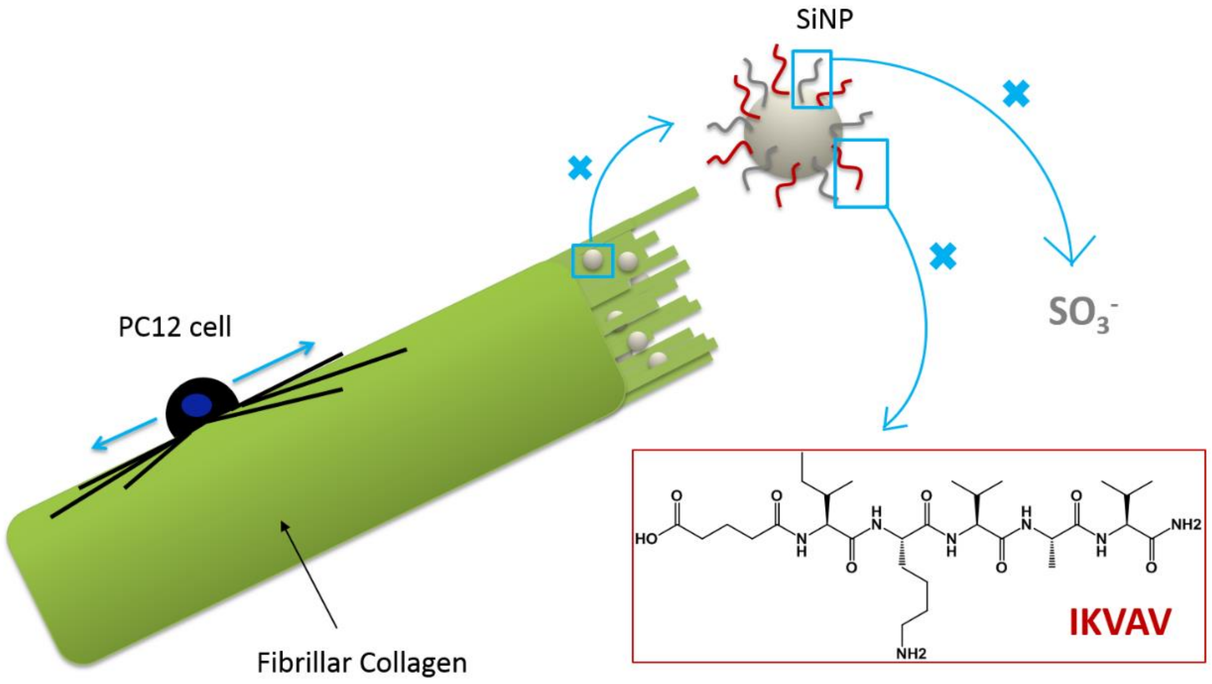

Figure IV-5 : Schematic representation of a composite thread made of fibrillar collagen and functionalized SiNPs used as a scaffold for PC12 cell culture. SiNPs can be modified with sulfonate groups (SO_3^-) and / or IKVAV peptides.

3.2. Fluorescent SiNPs

Fluorescent SiNPs have been synthesized in two steps. First, a fluorophore was incorporated within the SiNPs during their preparation. Then a silica shell was deposited to control the surface chemistry and the presence of silanols. This core-shell structure results in SiNPs with a more irregular surface compared to Stöber nanoparticles, as evidenced by Transmission Electron Microscopy (TEM, Figure IV-6-A), and to a non-homogenous distribution of the size of the SiNPs. Two populations were observed with a majority of small particles (diameter of 107 ± 9 nm *vs* 178 ± 15 nm for the larger particles).

SiNP-SO_3^-: From the bare SiNPs (SiNP-OH), sulfonate modified particles (SiNP-SO_3^-) were obtained by post-functionalization with akoxysilane mercaptopropyltrimethoxysilane (MPTMS). SiNPs display thiol groups that are oxidized in sulfonate groups (Figure IV-6-C). While SiNP-OH show neutral zeta potential at low pH and negative zeta potential from pH 4 (silanols pKA *ca.* 3.5), the presence of sulfonate groups is confirmed at low pH (below 3) were the zeta potential of SiNP-SO_3^- reached – 48 mV. This is attributed to the low pKa of alkyl sulfonic acids (*ca.* 1).

SiNP-IKVAV: Other mono-functionalized SiNPs were synthesized displaying the IKVAV peptide (*cf.* Figure IV-5). SiNPs are first modified with aminopropyltriethoxysilane (APTES) to graft amines. Then, by peptide coupling between the terminal carboxylic acid of IKVAV and the amines on SiNPs, IKVAV is grafted on the surface of the particles. IKVAV has two positive charges with the terminal NH_2 and on the lysine (K, pKa *ca.* 10). Zeta potential of SiNP-IKVAV is highly positive on the pH scale investigated, 49 mV, consistent with an effective grafting of IKVAV.

Patchy SiNPs: Patchy SiNPs, already described chapter III, are SiNPs exhibiting patches of amines, surrounded with sulfonates. By peptide coupling, we grafted IKVAV peptides on the amines. Zeta Potential measurement of those patchy SiNPs is constant for all the investigated pH *ca.* -23 mV. The zeta potential is in between the negative value of SiNP-SO_3^- (-48 mV) and the positive value of SiNP-IKVAV (49 mV). This indicated that both groups are grafted on the particle. The resulting negative value indicates that sulfonate groups may be present to a larger extent at the surface of SiNPs with respect to IKVAV.

SiNP-Stat: The relevance in using patchy particles will be assessed by comparing bifunctional SiNPs exhibiting functional groups statistically distributed over the particle surface. Both soluble alkoxysilanes, MPTMS and APTES are mixed before grafting. IKVAV is then grafted on amines from APTES. Once again, zeta potential is constant for all the investigated pH *ca.* -10 mV. The zeta potential is comprised between the negative value of SiNP-SO_3^- and the positive value of SiNP-IKVAV. This indicates that both groups are grafted on the particle. The resulting negative value indicates that sulfonate groups may be present to a larger extent at the surface of SiNPs with respect to IKVAV.

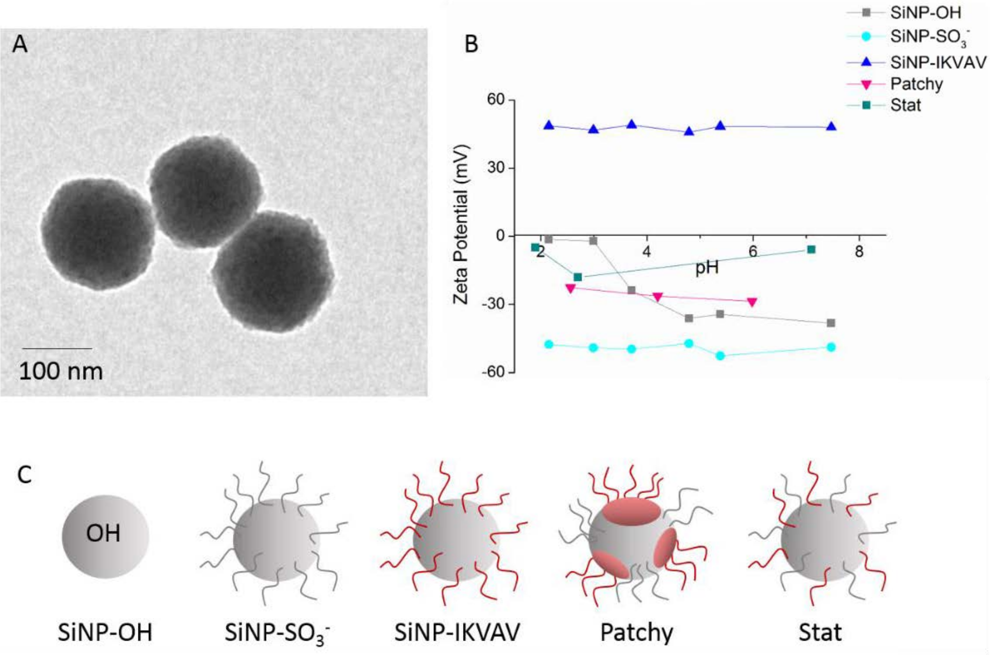

Figure IV-6 : A) TEM of SiNP-OH. B) Zeta potential measurements of SiNP as a function of pH. C) Schematic representation of the different surface chemistries of the SiNPs.

All of those characterized SiNPs were dispersed in acetic acid (500 mM) and mixed with collagen at a final particle concentration of 0.5 mg.mL^{-1} (1x), 5 mg. mL^{-1} (10x) and 50 mg.mL^{-1} (100x). The composite materials were extruded to get threads that will be characterized and evaluated as scaffold for PC12 adhesion and differentiation.

The conditions treated and reported in this chapter are listed in Table IV-1.

Collagen	*SiNP-OH*			*SiNP-IKVAV*			*SiNP-SO_3^-*			*SiNP-Mix*			*SiNP-Stat*			*SiNP-patch*		
mg.mL^{-1}	**1x**	**10x**	**100x**	**1x**	**10x**	**100x**	**1x**	**10x**	**100x**	**1x**	**10x**	**100x**	**1x**	**10x**	**100x**	**1x**	**10x**	**100x**
30	×	×	×	×	×	×	×	×	×									
15	×	×	×	×	×	×	×	×	×		×	×			×		×	

Table IV-1: Investigated conditions in bionanocomposites in terms of collagen concentration and SiNP surface chemistries and concentrations.

4. PC12 differentiation on collagen-SiNP threads

Structures of the threads have been systematically investigated using polarized light microscopy in order to analyze the impact of the incorporation of SiNPs on collagen alignment depending on SiNP surface chemistry. Additionally, localization and distribution of fluorescent particles was studied by fluorescence microscopy. Finally, PC12 adhesion and differentiation have been monitored for all conditions.

4.1. Collagen-based threads at 30 mg.mL^{-1}

4.1.1. Observation by optical microscopy

Collagen-based threads at a concentration of 30 mg.mL^{-1} were observed by optical microscopy (Figure IV-7-A-G-1). Collagen thread are *ca.* 400 µm in diameter for all conditions. Then we used polarized light microscopy (PLM) to investigate the alignment and orientation of collagen fibers in the threads. PLM is used to probe the anisotropic organization of birefringent materials, which have a refractive index that depends on the polarization light. The colors indicate fibers alignment and their orientation with respect to the thread (Figure IV-7-A-G-2). Finally, because we incorporated fluorescently labeled SiNPs, particles can be identified within the threads by fluorescence microscopy (Figure IV-7-A-G-3). Despite the low resolution, this provides information about the overall distribution and aggregation state of the particles within the threads.

Figure IV-7-A shows that pure collagen threads are homogeneous and smooth by optical microscopy. The fibrils are mostly aligned, as indicated by the birefringence observed. However, local extinctions are observed that can be attributed to areas that are not aligned with the whole structure. In addition, no fluorescence is observed by fluorescence microscopy, which is consistent with the absence of fluorescent SiNPs (Figure IV-7-A1-A3).

The SiNP-OH collagen thread is also smooth at a particle concentration 1x (Figure IV-7-B1) with a birefringence qualitatively similar to the pure collagen sample (Figure IV-7-B2). By fluorescence microscopy SiNP-OH are visible with a homogeneous distribution over the thread volume but with the formation of small clusters. When the concentration is increased to 10x, the thread is still smooth (Figure IV-7-C1). By PLM, more birefringence extinction is observed inside the thread (Figure IV-7-C2). This shows that the increase in SiNP-OH concentration affects the alignment of collagen fibrils. By fluorescence microscopy, SiNP-OH are again visible with a homogeneous distribution but with the formation of larger clusters (Figure IV-7-C3).

In presence of SiNP-IKVAV-1x, the thread is twisted and large area of birefringence extinction are observed under PLM (Figure IV-7-D1-2). By fluorescence microscopy, we observe micrometer size spherical objects that may correspond to bubbles that have been trapped in the highly viscous collagen solution. In parallel, the background fluorescence is very homogeneous, suggesting a good dispersion of the particles (Figure IV-7-D3). When the concentration is increased by ten, the thread become smoother (Figure IV-7-E1). The alignment seems to be improved as it shows a homogenous structure by PLM (Figure IV-7-E2). By fluorescence microscopy, we again observe a continuous fluorescent signal inside the thread, and only a few aggregates are visible. This is surprising that the SiNP are less disturbing the structure of the thread at a higher concentration. It might be because some interactions exist between the peptide IKVAV and the collagen, such as hydrogen bonding.

SiNP-SO_3^- collagen thread at the concentration 1x is smooth according to optical microscopy (Figure IV-7-F1). The birefringence observed by PLM shows that the particles do not disturb the alignment of collagen (Figure IV-7-F2). Besides bubbles, aggregates of fluorescent SiNPs are visible by fluorescence microscopy (Figure IV-7-F3). When the concentration increases to 10x, the structure of the thread is more impacted, twisted and we observed irregularities at its surface (Figure IV-7-G1). By PLM, the thread is not homogenously birefringent, demonstrating defect of alignment (Figure IV-7-G2). SiNP-SO_3^-, visible by fluorescence, are not homogeneously distributed, but aggregated (Figure IV-7-G3). Many bubble-like objects are also observed.

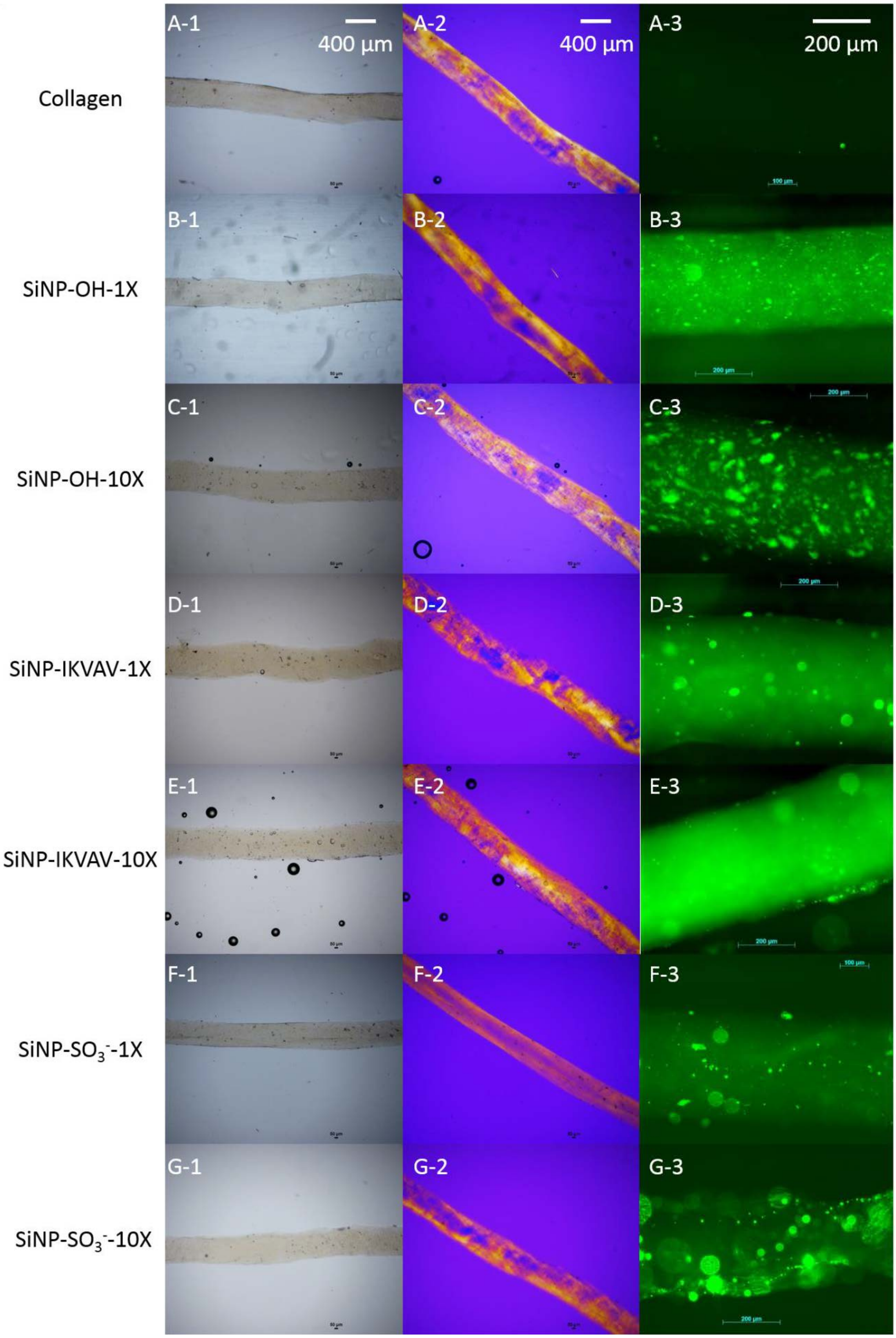

Figure IV-7 : Collagen threads at 30 mg.mL^{-1} ± SiNPs observed by (1) optical microscopy, (2) PLM and 3) fluorescence microscopy.

4.1.2. PC12 cells on 30 mg.mL^{-1} threads at the SiNP concentration of 1x

The PC12 cell study has been performed on the 30 mg.mL^{-1}-1x on a triplicate of threads twice. Cells were cultured for 10 days without (Figure IV-8A-D-1) and with (Figure IV-8A-D-2) FGF.

Without FGF, the cell viability of each sample were directly compared with the pure collagen one. No significant differences were analyzed between the different threads (Figure IV-8A-1). This means that no difference in adhesion, proliferation or cytotoxicity is induced by the different scaffolds. The number of neurites per cell is around 1 neurite per 10 cells, which is quite low. No significant differences are observed between the threads. However, the neurites are significantly longer for SiNP-SO$_3^-$ and SiNP-IKVAV: *ca.* 45 µm whereas neurites are *ca.* 35 µm long on collagen threads and SiNP-OH threads. The percentage of aligned neurites with the thread is also statistically higher for SiNP-IKVAV sample: *ca.* 90%, against *ca.* 65% for pure collagen and SiNP-OH conditions.

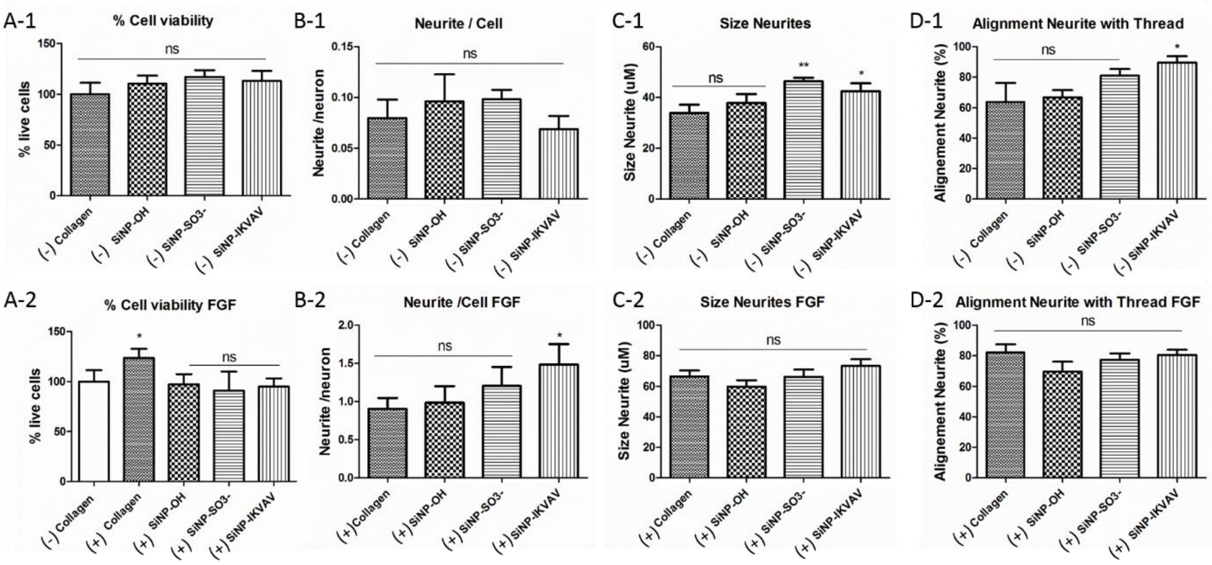

Figure IV-8 : PC12 cells after 10 days of culture on collagen -SiNP threads at 30 mg.mL^{-1}-1x. A) Cell viability compared to pure collagen (–) FGF. B) Number of neurites per cell, C) neurite size and D) alignment with the thread orientation (1) without or (2) with FGF. The column represents Mean with standard error of mean (SEM). (* $p < 0.05$, ** $p < 0.001$; calculated against the pure collagen threads, using one-tailed Wilcoxon-Mann-Whitney non parametric test; each condition from two independent triplicates.

When growth factor FGF was added, the number of cells on pure collagen increased by *ca.* 25% in comparison with the pure collagen without FGF (Figure IV-8A-2). However, on the threads with particles, the cell viability is the same than for pure collagen (-) FGF. It is possible that the increase of number of cells triggered by FGF is prevented by the presence of SiNPs, or compensated by a hypothetic cell death or lack of adhesion cause by the presence of particles. Thought, the cell viability is around 100% of the collagen (-) FGF, so there is no concern about cell viability or adhesion on the threads at 30 mg.mL^{-1}.

The number of neurites per cell is this time around 1 neurite per cell for pure collagen thread, which is ten times higher than pure collagen thread without FGF. As expected the growth factor did trigger the formation of cell extensions and consequently the differentiation of PC12 cells. The number of neurites is once again higher for SiNP-SO_3^- and SiNP-IKVAV threads: *ca.* 1.5 neurites per cell in comparison with *ca.* 1 neurite for collagen and SiNP-OH samples. The difference is statistically significant only for the SiNP-IKVAV threads in comparison with pure collagen threads. The size of the neurites is *ca.* 66 µm for all the conditions and no significant differences were observed. The length of the PC12 neurites is consequently larger in presence of FGF than without FGF. The percentage of aligned neurites along the threads is around 80% for all the conditions.

After 10 days of culture on collagen-SiNP threads at 30 mg/mL^{-1}-1x, PC12 appear mostly sensitive to the presence of the IKVAV-bearing nanoparticles. In order to increase the impact of the functionalized SiNPs on cell behavior, we increased their concentration by a factor of ten, keeping the collagen concentration constant (30 mg.mL^{-1}).

4.1.3. PC12 cells on 30 mg.mL^{-1} threads at the SiNP concentration of 10x

Cells were cultured for 10 days without and with FGF(Figure IV-9-A-D-1-2). The experiment has been realized twice in triplicate of threads.

The number of cells on each sample has been compared with the one on pure collagen (100%) without any FGF (Figure IV-9-A-1). A significant increase in cell viability is recorded for SiNP-SO_3^- sample, whereas no difference is observed with SiNP-OH or SiNP-IKVAV threads. The number of neurites per cell is *ca.* 0.8 neurite for 10 cells and no difference is observed between the different scaffolds. The size of the neurites is around 30 µm and their alignment with the threads is around 70% for all the samples.

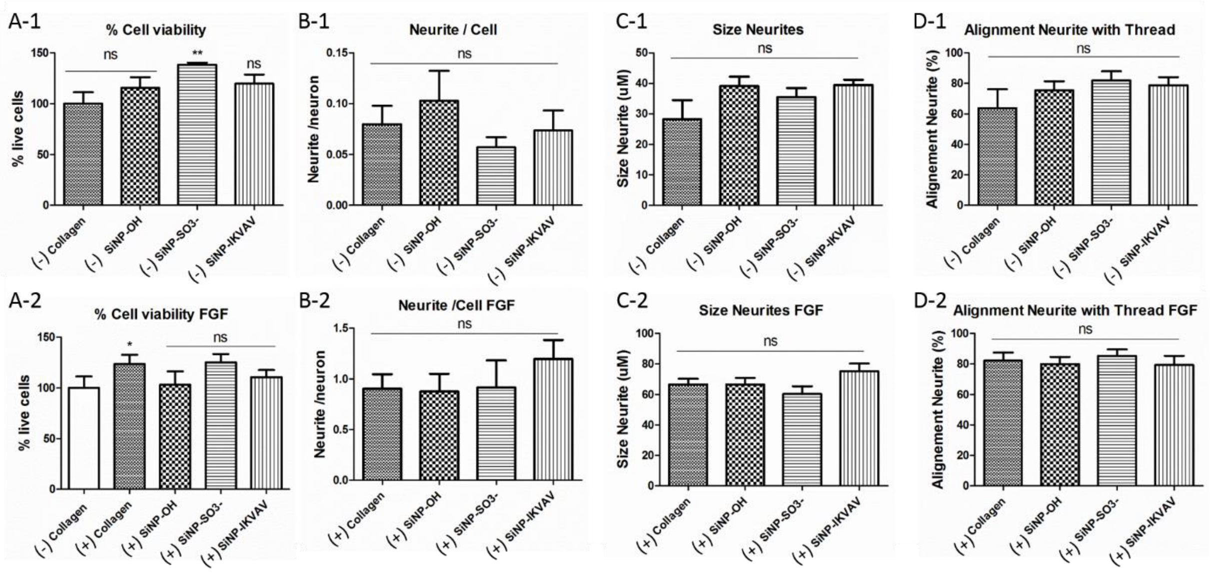

Figure IV-9 : PC12 cells after 10 days of culture on collagen -SiNP threads at 30 mg.mL^{-1}-10x. A) Cell viability compared with pure collagen (–) FGF. B) Number of neurites per cell, C) neurite size and D) alignment with the thread orientation (1) without or (2) with FGF. The column represents Mean with standard error of mean (SEM). (* $p < 0.05$, **$p < 0.001$; calculated against the pure collagen threads, using one-tailed Wilcoxon-Mann-Whitney non parametric test; each condition from two independent triplicates.

When FGF is added in the cell culture medium, the number of cells increases in pure collagen thread again, in comparison with the pure collagen (-) FGF control (Figure IV-9-A-2). The cell viability decreases to the same level than the pure collagen (-) FGF sample when SiNPs are present. No significant difference between the conditions is observed in terms of number of neurites per cell, *ca.* 1 neurite per cell. The size of the neurites is also similar for all threads, *ca.* 70 µm. Around 80% of the neurites are aligned with the threads whatever the surface chemistry of the particles.

Therefore, surprisingly, the increase in SiNPs did not enhance the effect observed previously at a concentration of 1x. The only significant effect in the experiment at 30 mg.mL^{-1}-10x is a higher number of PC12 cells for SiNP-SO_3^- collagen thread without FGF.

Altogether, for 30 mg.mL^{-1} threads, significant variations compared to the FGF-free collagen control were obtained only for SiNP-IKVAV 1x (neurite size and alignment without FGF, number of neurite per cell with FGF) and for SiNP-SO_3^- 1x (neurite size) and 10x (viability). We can note that all these variations are positive (*i.e.* higher viability, better alignment…). Whereas correlation with the thread structure is difficult at this stage, we nevertheless may point out that the SiNP-IKVAV containing threads showed the better particle dispersion state, as determined by fluorescence imaging.

In order to find a way to enhance the effect of the functionalized particles on PC12 differentiation, we then decreased the concentration of collagen inside the thread from 30 mg.mL^{-1} to 15 mg.mL^{-1} while keeping the concentration of SiNPs identical to the first set of experiments at 1x and 10x and adding the concentration 100x.

4.2. Collagen-based threads at 15 mg.mL^{-1}

4.2.1. Observation by optical microscopy

The pure collagen thread at 15 mg.mL^{-1} is smoother than the one at 30 mg.mL^{-1} according to the observation by optical microscopy (Figure IV-10-A1). The thread is homogeneously birefringent, and by consequent collagen fibrils are aligned (Figure IV-10-A2). As no fluorescent particle were embedded in this sample, no fluorescence is observed (Figure IV-10-A3).

The SiNP-OH thread at 1x is similar to the pure collagen thread, showing a smooth surface by optical microscopy and a homogeneous birefringence signal by PLM (Figure IV-10-B1-B2). Irregularities start to be visible at 10x by optical microscopy (Figure IV-10-C1) and local extinctions are observed in the birefringence, signing for area where collagen fibrils are not aligned (Figure IV-10-C2). At 100x, darks spots, probably indicative of large SiNP aggregates, appear on optical microscopy images (Figure IV-10-D1). The birefringence again decreases with more extinction zones (Figure IV-10-D2). At this concentration, SiNP-OH disturb the fibril alignment. Fluorescence microscopy reveals fluorescent areas where SiNP-OH are very significantly aggregated (Figure IV-10-D3).

The SiNP-IKVAV thread observed by optical microscopy reveals irregularities at the surface at the concentration of SiNP of 1x, that are less visible at 10x and even less at 100x (Figure IV-10-E1, F1, G1). Some extinction areas are visible in the birefringence by PLM for the SiNP-IKVAV thread at 1x (Figure IV-10-E2). However, the birefringence is homogeneous in SiNP-IKVAV threads at 10x and 100x (Figure IV-10-F2, G2). Fluorescence signal measured on SiNP-IKVAV thread at 100x is homogenous, without visible aggregates (Figure IV-10-G3).

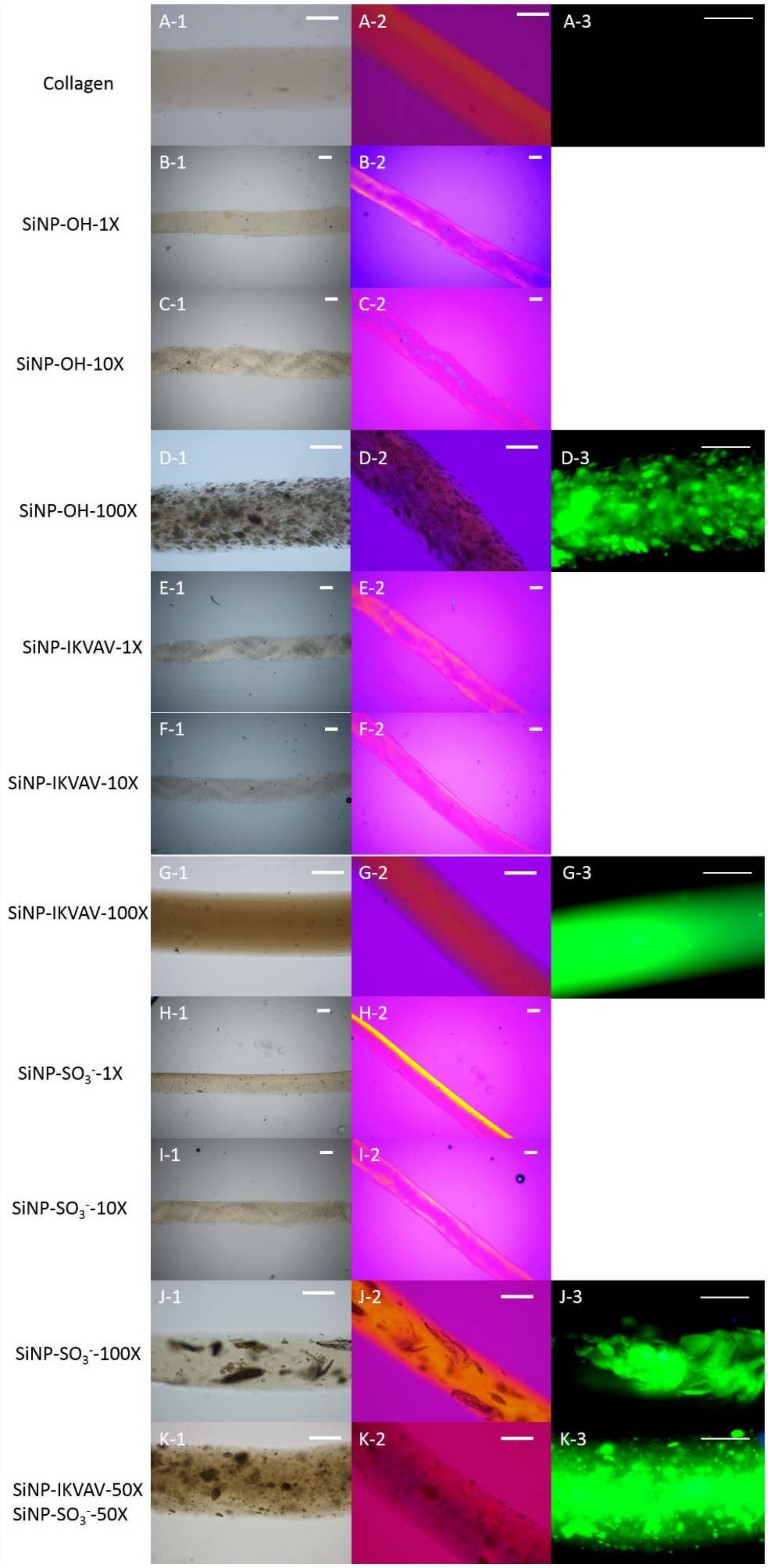

Figure IV-10 : Collagen threads at15 mg.mL^{-1} ± SiNPs observed by (1) optical microscopy, (2) PLM and 3) fluorescence microscopy. Scale bars 200 µm.

The SiNP-SO_3^- thread observed by optical microscopy shows a smooth surface, similar to pure collagen thread (Figure IV-10-H1). Birefringence monitored by PLM is not homogeneous, being more intense on one side of the thread (Figure IV-10-H2). When the concentration increases to 10x, irregularities start to be visible by optical microscopy (Figure IV-10-I1). Birefringence is hardly observed by PLM, which shows that collagen fibrils alignment is disturbed by SiNP-SO_3^- at the concentration 10x (Figure IV-10-I2). At the concentration of 100x, the thread is twisted and not homogenous by optical microscopy observations (Figure IV-10-J1). However, some birefringence is observed by PLM (Figure IV-10-J2). Fluorescence microscopy show that the signal is not homogenous in the thread, indicating that SiNP-SO_3^- are probably highly aggregated (Figure IV-10-J3).

The two groups of interest in this study are SO_3^- groups and IKVAV peptides respectively for a structural and a bioactive role. We were able to see that for collagen-based thread at 30 mg. mL^{-1}, SO_3^- and IKVAV-bearing particles have an impact on cell behavior at low concentration. It was therefore interesting to check what was would happen when the two types of particles were simultaneously present within the threads. For this, SiNP-SO_3^- and SiNP-IKVAV were mixed together and embedded in collagen at a final particle concentration of 100x (50x SiNP-SO_3^- + 50x SiNP-IKVAV). The thread showed structural defects by optical microscopy (Figure IV-10-K1). We did not observe a clear birefringence by PLM (Figure IV-10-K2). The fluorescence signal appeared more homogenous than for the SiNP-SO_3^- sample at 100 x but aggregates were clearly visible (Figure IV-10-K3). The characteristics of this thread are therefore intermediate between homogeneous SiNP-IKVAV threads and highly disordered SiNP-SO_3^- threads.

4.2.2. PC12 cells on 15 mg.mL^{-1} threads at the SiNP concentration of 1x

After 10 days of PC12 culture without and with FGF, the cell survival and morphology were analyzed (Figure IV-11-A-D-1-2). The experiment has been performed twice on triplicate of threads.

The number of cells on each sample has been compared with the one on pure collagen sample (100%) in absence of FGF (Figure IV-11-A-1). A significant increase in the number of living cells is measured for SiNP- SO_3^- threads, whereas no significant difference is observed for SiNP-OH or SiNP-IKVAV threads. The number of neurites per cell is *ca.* 1 neurite for 10 cells and there is no significant difference between the different scaffolds. The different threads do not influence the neurite size (around 40 µm for all conditions). Around 70% of the neurites are aligned with the thread for all conditions, except in presence of SiNP-IKVAV, where 85% of the neurites are aligned.

After addition of FGF in the cell culture medium, the cell viability is the same for all conditions, around 100% compare to the pure collagen sample in absence of FGF (Figure IV-9-A-2). There is *ca.* 1 neurite per cell and the neurites are *ca.* 65 µm long for all the different threads. 85% of neurites are aligned with respect to the threads for all scaffolds.

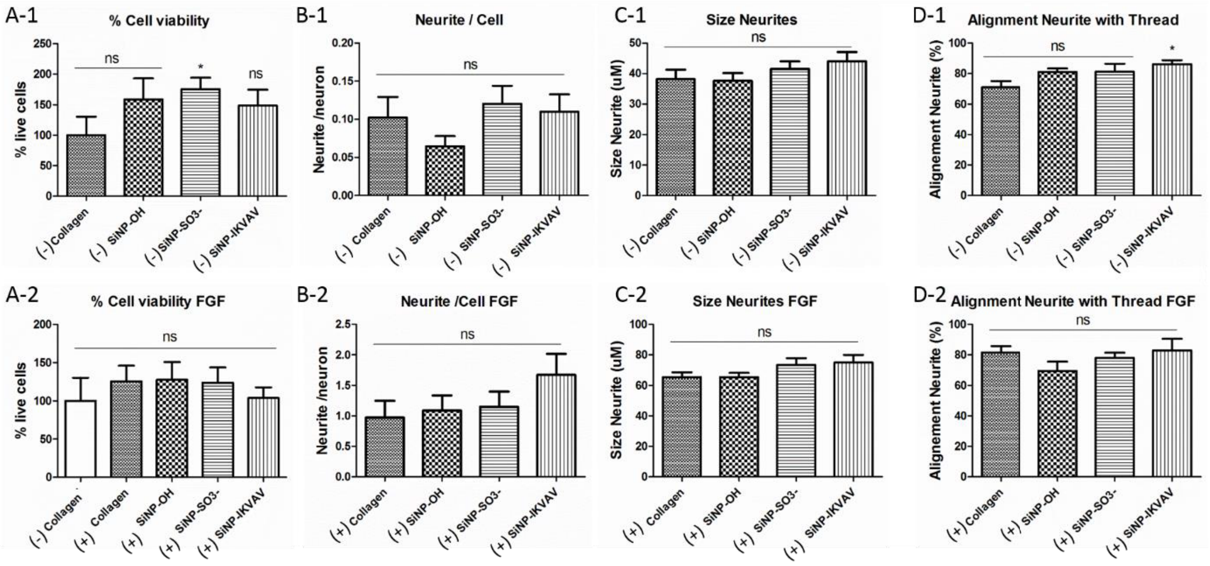

Figure IV-11 : PC12 cells after 10 days of culture on collagen -SiNP threads at 15 mg.mL^{-1}-1x. A) Cell viability compared with pure collagen (–) FGF. B) Number of neurites per cell, C) neurite size and D) alignment with the thread orientation (1) without or (2) with FGF. The column represents Mean with standard error of mean (SEM). (* $p < 0.05$, ** $p< 0.001$; calculated against the pure collagen threads, using one-tailed Wilcoxon-Mann-Whitney non parametric test; each condition from two independent triplicates.

In these conditions, we could again observe the benefit of SINP-IKVAV on cell alignment in the absence of FGF, as well as an increase in cell viability in presence of SiNP-SO$_3^-$. Thus, while keeping the collagen concentration constant to 15 mg.mL^{-1}, we increased the concentration of SiNPs by a factor of ten (10x) with the hope of enhancing their influence on cell behavior.

4.2.3. PC12 cells on 15 mg.mL^{-1} threads at the SiNP concentration of 10x

The analysis of PC12 cell survival and morphology after 10 days of PC12 culture is reported Figure IV-12. The experiment has been realized in triplicate of threads and repeated once. In this experiment, two additional samples, containing either a mixture of SiNP-SO_3^- and SiNP-IKVAV, designated as "Mix SO_3^--IKVAV", or particles with patches of IKVAV surrounded with sulfonate groups, termed "patchy", were prepared and tested.

In absence of FGF the cell viability is the same for all conditions, close to the 100% established for the pure collagen sample, except in presence of patchy particles where the cell viability is *ca.* 190% (Figure IV-12-A-1). The number of neurites per cell is around 1 neurite per 10 cells for all conditions, except in presence of the mix IKVAV-SO_3^-, where the number of neurites is statistically higher: 2 neurites per 10 cells (Figure IV-12-B-1). However, the size of those neurites is *ca.* 40 µm for all conditions (Figure IV-12-C-1). There is no specific influence of SiNP addition and surface chemistry on the neurite growth. 85% of neurites alignment with respect to the threads is observed, with a significantly better alignment when only SiNP-SO_3^- particles are present (Figure IV-12-D-1).

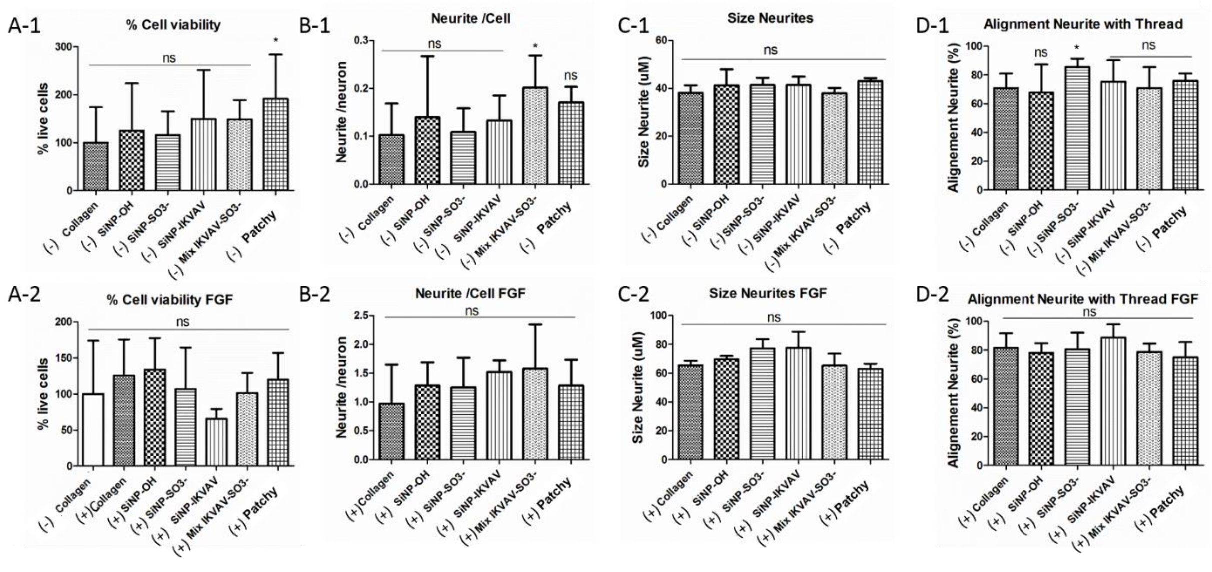

Figure IV-12 : PC12 cells after 10 days of culture on collagen -SiNP threads at 15 mg.mL^{-1}-10x. A) Cell viability compared with pure collagen (–) FGF. B) Number of neurites per cell, C) neurite size and D) alignment with the thread orientation (1) without or (2) with FGF. The column represents Mean with standard error of mean (SEM). (* $p < 0.05$, ** $p< 0.001$; calculated against the pure collagen threads, using one-tailed Wilcoxon-Mann-Whitney non parametric test; each condition from two independent triplicates.

After addition of FGF in the cell culture medium, the cell viability is not significantly impacted and is around 100% of the pure collagen sample (Figure IV-12-A-2). No statistical difference is observed between the different samples in terms of number of neurites per cell, *ca.* 1 (Figure IV-12-B-2). Neurites are *ca.* 65 µm long and aligned with respect to the thread at 80% for all scaffolds (Figure IV-12-C,D-2).

4.2.4. PC12 cells on 15 mg.mL^{-1} threads at the SiNP concentration of 100x

This last set of experiments has been performed with a higher particle concentration (100 x). A new condition using nanoparticles where SO_3^- and IKVAV groups are statistically distributed on the surface, called "stat-SiNP" has also been studied, offering an ideal control to assess the potential effect of the clusterization. However, this is a costly experiment in terms of SiNPs, and not enough stats SiNPs and patchy SiNPs were synthesized. The sample stat-SiNP was therefore tested on a triplicate of threads instead of a six replicated for now. In the case of patchy particles, a new experiment is ongoing.

In absence of FGF, cell viability is significantly impacted by stat-SiNP, that decrease the percentage of living cell to 26% in comparison to pure collagen (Figure IV-13-A-1). There is no effect in presence of other SiNPs on cell viability in this condition.

The number of neurite per cell is *ca.* 5 neurites for 100 cells for all collagen-based threads except a non-significant increase to 9 neurites per 100 cells for the mix SO_3^--IKVAV sample (Figure IV-13-B-1). The size of those neurites is *ca.* 35 µm and they are aligned with the threads at *ca.* 78% for all conditions (Figure IV-13-C-1, D-1).

In parallel, after addition of FGF in the cell culture medium, the cell viability strongly decreased in presence of SiNPs at a concentration of 100x whatever their surface functionalization with a statistical difference for the conditions: SiNP-IKVAV, mix SO_3^--IKVAV and stat SiNPs containing threads. In presence of stat-SiNPs, only 17% of cell viability is measured in comparison to pure collagen sample.

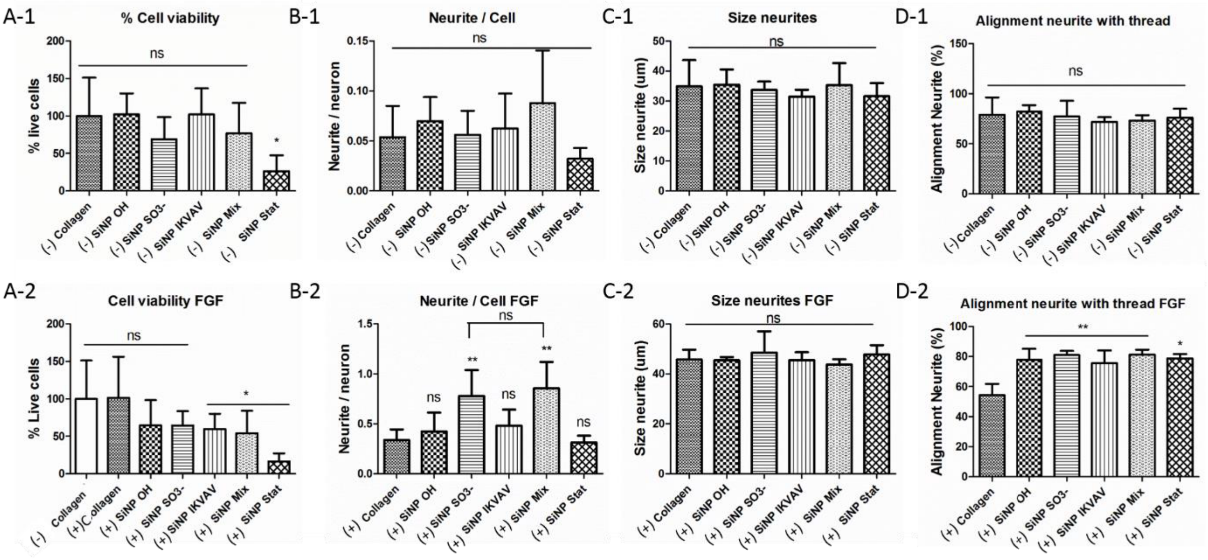

Figure IV-13 : PC12 cells after 10 days of culture on collagen -SiNP threads at 15 mg.mL^{-1}-100x *analyzed thanks to the help of N. Debons (LCMCP)*. A) Cell viability compared with pure collagen (–) FGF. B) Number of neurites per cell, C) neurite size and D) alignment with the thread orientation (1) without or (2) with FGF. The column represents Mean with standard error of mean (SEM). (* $p < 0.05$, ** $p < 0.001$; calculated against the pure collagen threads, using one-tailed Wilcoxon-Mann-Whitney non parametric test; each condition run on six different samples except for SiNP-stat thread where three different experiments were tested.

In terms of number of neurites per cell, *ca.* 3 neurites per 10 cells are observed for pure collagen, SiNP-OH, SiNP-IKVAV or SiNP-stat conditions (Figure IV-13-B-2). A significant increase is however observed for SiNP-SO_3^- and Mix of SiNP-SO_3^- and SiNP-IKVAV containing threads: *ca.* 9 neurites per 10 cells. The size of the neurites is *ca.* 45 µm for all conditions (Figure IV-13-C-2). Surprisingly, the alignment of the neurite drops to 54% for the pure collagen sample instead of 77% for the other conditions (Figure IV-13-D-2). However, similar pure collagen threads at 15 mg.mL^{-1} had already been tested in previous experiments and never showed such a behavior so that no conclusion can be drawn without complementary experiments.

Overall, at such high concentration, many of the investigated systems have a detrimental effect on PC12 cell viability, especially in the presence of FGF. The only clear benefit is observed for SiNP-SO_3^- and particle mixture with FGF where the number of neurites per cell significantly increases. Again, simple correlation with structural data is complex and we can notice that, despite presenting the more homogeneous structure, the SiNP-IKVAV-100 x thread do not exhibit specific beneficial interactions with cells.

5. Discussion

5.1. Collagen-based threads for PC12 cell culture

In this attempt to engineer a biomaterial for neural type cell differentiation, the strategy has been to prepare collagen-silica nanoparticle composite threads by progressively increasing the ratio between SiNPs with different surface chemistries and collagen to enhance a possible beneficial effect of the scaffolds on cell behavior.

PC12 cells behaviour has been followed with four parameters: cell viability, number of neurites per cell, size (length) of neurites and neurite alignment along the thread main axis. However, among all investigated combinations, very few of them showed significant variations compared to the control (Table IV-2).

Collagen	*SiNP-OH*			*SiNP-IKVAV*			*SiNP-SO_3^-*			*SiNP-Mix*			*SiNP-Stat*			*SiNP-patch*		
$mg.mL^{-1}$	**1x**	**10x**	**100x**	**1x**	**10x**	**100x**	**1x**	**10x**	**100x**	**1x**	**10x**	**100x**	**1x**	**10x**	**100x**	**1x**	**10x**	**100x**
30	×	×	×	**X**	×	×	×	×	×									
15	×	×	×	×	×	×	×	×	**X**		×	**X**			×		×	

Table IV-2 : Bionanocomposites that triggered cell differentiation (+FGF) indicated with red cross.

It has to be reminded that, in the absence of FGF, PC12 cell differentiation is not expected and the number of neurites per cells should be small (< 0.1). This is what we observed here indicating that none of the materials is able to induce differentiation *per se*. In such conditions, the other two related parameters (neurite size and neurite alignment) cannot be considered really significant. In contrast, cell viability can provide fruitful information on the cytotoxicity of the threads for undifferentiated PC12 cells, as well as their ability to adhere and proliferate on these materials. In this context, except for Stat-100x in 15 $mg.mL^{-1}$, no significant loss of viability was found in FGF-free conditions. This indicates that none of the other composites are cytotoxic and that they allow cell adhesion and proliferation to at least a similar extent than pure collagen. In fact, in a few cases, an increase in viability could be measured that may reflect an improvement of the mechanical properties of the thread upon nanoparticle incorporation but this would need to be studied in more details.

In presence of FGF, however, cell differentiation should be triggered. In this case, the cell viability data are more difficult to analyze as they concern both un-differentiated and differentiated cells. Again we observed a very significant decrease in cell viability for Stat-100x in 15 mg.mL^{-1} but, in these conditions, all nanocomposite threads appeared to impact negatively on cell survival, although to various extents. Cell differentiation is defined by an increase in number of neurites per cells. Differentiation is enhanced in comparison with the pure collagen sample (in presence of FGF) for IKVAV-1x in collagen 30 mg/mL^{-1} and, at collagen 15 mg.mL-1, for SiNP-SO_3^- 100 x and Mix-100 X. However, no increase in neurite size and alignment was found in the presence of FGF compared to the control.

Taken together, and except for the specific cases mentioned above that will be discussed afterwards, collagen-silica nanoparticles are therefore promising substrates for the growth and differentiation of PC12 cells upon FGF addition. The alignment of the neurites with respect to the thread is satisfying and interesting to help cells to properly differentiate as observed during the development or regeneration of the PN system, where glial cells and oriented ECM guide neurons to migrate along the desired direction.[31] As a matter of fact, it has been shown that neurite orientation can be controlled by the topographic features of micropatterned surfaces.[32–34] Thus, the fact that neurite alignment is almost independent on the collagen concentration and on particle chemistry and concentration may in fact indicate that this process is driven by the alignment of the collagen fibers at the surface of the threads due to the extrusion process.[22]

5.2. Impact of SiNP surface chemistry on PC12 cells

As pointed out above, the most significant results of this study were obtained with 15 mg.mL^{-1} collagen-based threads containing 100x SiNPs. Indeed, these are the conditions with the highest SINP:collagen ratio and therefore where the influence of the particles was expected to be the strongest.

We observed that SiNP-SO_3^- and a mixture of SiNP-SO_3^- and SiNP-IKVAV led to a higher number of neurites per cell compared to the control, indicating an enhancement of PC12 cell differentiation. Interestingly, no such result is obtained with SiNP-IKVAV at 100x. The surface chemistry of SiNPs is the key parameter here and we can suggest that the sulfonate groups are responsible for triggering differentiation.

Sulfonate groups interact with collagen by electrostatic interactions. The local concentration of collagen is higher around the particles before extrusion and when the pH is raised and the fibrillation occurs, SiNP-SO_3^- act as nucleation center for fibril growth.[27] SiNP-SO_3^- can therefore have a structural role in this system. The modulation in cell behavior would therefore be due to a modification in collagen thread architecture.

It has been shown that mechanical stiffness of the native ECM and of artificial scaffolds that support cells has a major role in cellular functions.[35,36] It can be explained using mechanotransduction mechanisms involving integrins, focal adhesions (FAs), and actin−myosin associations.[31,37,38] In the literature, it was shown that mechanical properties modulate the neuronal type cell differentiation, but tendencies vary according to cell type and materials.[39,40,41,42,22]

For PC12, decreasing substrate rigidity led to increased number of neurites, but only for gels with elastic moduli over 200 kPa.[43] According to work already performed in the group, at 30 mg.mL^{-1} pure collagen threads exhibit a young modulus *ca.* 180-200 kPa. Measurements should be performed on SiNP-containing threads. However, the increase in neurite number might be due mechanical properties at the scale of the cell. Indeed, growth cone-mediated neuronal elongation is viewed as a results of multiple cytoskeletal dynamics like polymerization of actin and tubulin subunits at the tip of the axon.[44] They are able to sense and generate local stiffness.

Moreover, what could be really important in this model is the migration over a gradient of stiffness named durotaxis. Sundararaghavan and co-workers developed a microfluidic system to study the response of cells to controlled gradients of mechanical stiffness in 3D collagen gels by using the genipin natural crosslinker.[45] They show than the neurites were growing significantly longer down the gradient of stiffness than up the gradient and that in control gel without any gradient no change in cell behavior were observed. Even if it is difficult to isolate here the stiffness from other parameters, such as porosity and degradation rate inside 3D gels, this is an interesting model.

What the optical characterization of these 15 mg.mL^{-1}/SiNP-SO_3^-100x materials has shown is that the silica particles form very large aggregates dispersed within the thread, which would suggest some kind of phase separation with large particles-rich and large collagen-rich area (Figure IV-10-J1). The comparison can be made with SiNP-OH-100x (Figure IV-10-D1) where the particles form smaller aggregates that are evenly dispersed in the thread. In the SiNP-SO_3^- system, the distance between two silica-rich domains is 100 µm or larger, *i.e.* larger than the cells but the organization of the collagen network should differ from the surface of the aggregates to the collagen-rich phase (Figure IV-14-A). This can create a mechanical gradient that cell extensions can detect when sensing their surroundings. On the contrary, for SiNP-OH system, the material heterogeneity and therefore gradient may be at a lower scale than the cells and therefore will be sensed as a homogeny surface of mixed silica/collagen composition (Figure IV-14-B). This would be even more true if nanoparticles are very well-dispersed in the collagen matrix, as suggested by imaging SiNP-SO_3^- systems at lower SiNP concentrations.

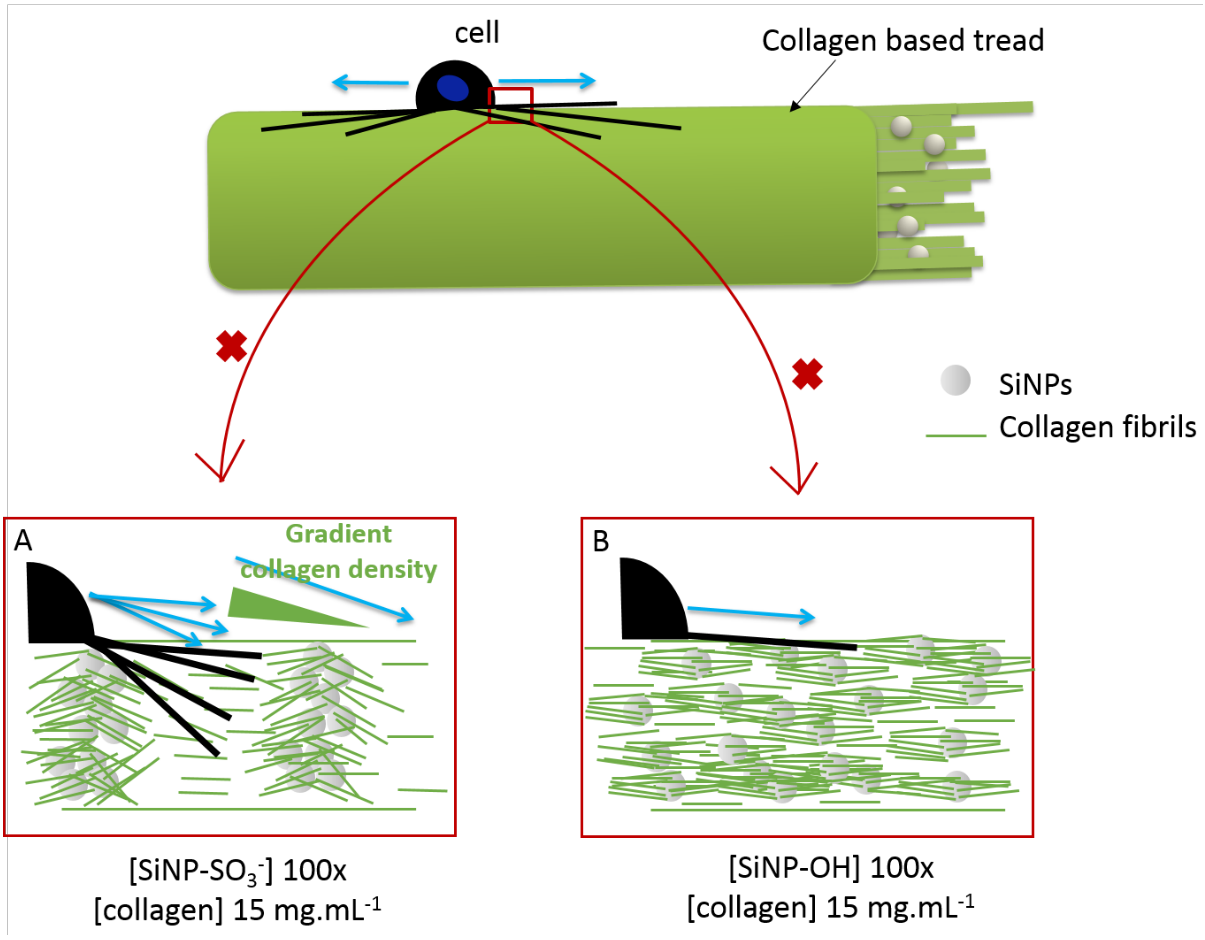

Figure IV-14 : Schematic representation of thread with PC12 cell. SiNPs at concentration 100x embedded in collagen at concentration 30 mg.mL^{-1}. Zoom on modulation of collagen architecture by interaction with (A) SiNP-SO_3^- and (B) SiNP- OH.

5.3. Impact of SO_3^- and IKVAV in collagen-based threads on PC12 cells

The other key result of this study concerns the various responses obtained for threads incorporating both SO_3^- and IKVAV either as a mixture of SiNP-SO_3^- and SiNP-IKVAV, clustered in domains on patchy SiNPs or statistically distributed at the surface of Stat-SiNP.

As already exposed, the mixture of the two kinds of particles induce an increase of the number of neurites per cell at concentration of 100x (50x SiNP-SO_3^- + 50x SiNP-IKVAV) embedded in collagen at 15mg.mL^{-1}. The result is similar to the one obtained with a concentration of 100x in SiNP-SO_3^-, while the sample that contained SiNP-IKVAV at the concentration of 100x did not have an influence on cell differentiation. These results highlight the fact than SiNP-IKVAV does not have influence on cell differentiation in our conditions. It can also be noticed that, referring again to the optical image of the mix thread (Figure IV-10-1), it seems that the way silica particle aggregates and interact with collagen to form gradients is intermediate between SiNP-OH and SiNP-SO_3^-.

This effect on cell differentiation is not observed for Stat-SiNP containing sample at 100x (in collagen at 15 mg.mL^{-1}). Moreover, their presence very significantly decreases cell viability. We unfortunately could not perform imaging studies of these materials so far. However, we can suggest that the statistical distribution of the chemical groups on the surface impair the electrostatic interaction of SO_3^- groups with collagen due to the close positive charge of IKVAV. This again strengthen our hypothesis that the differentiation induced by the presence of SO_3^- groups by themselves or in the mixture of SiNP-SO_3^- and SiNP-IKVAV is related to the interactions between the particles and the collagen that modulate the thread architecture.

It would have been really interesting to compare these results to ones obtained by introducing patchy SiNPs at the concentration of 100x in collagen at 15 mg.mL^{-1}. Technical difficulties prevented us to investigate this condition until now. These patchy particles were only tested at the concentration of 10x, embedded in collagen at 15 mg.mL^{-1}, in which they show an increase in viability in FGF-free conditions but no effect whatsoever in the presence of FGF. However, in these conditions, the mix system had not effect on PC12 differentiation and we have no common conditions for patchy and Stat systems.

Finally, we should emphasize that, even when incorporated in high concentrations, SiNP-IKVAV do not clearly influence cell behavior. It is possible that the peptide is not accessible enough for the cells either because these particles are buried inside the thread or because IKVAV is too close to the SiNP surface despite the spacer we introduced. Another possibility is that the collagen is itself rich enough in bioactive epitopes so that SiNP-IKVAV do not bring a significant added-value in biochemical signal for cell adhesion or differentiation.

6. Conclusion and perspectives

In this study, composite materials made of collagen and SiNPs were processed as threads to promote neural type cell differentiation. It was demonstrated that the functionalization and the concentration of SiNPs influence their dispersion in the thread and hence the collagen architecture, ultimately impacting PC12 behavior. We have suggested that this is the reason why particles bearing sulfonate groups, i.e. the most likely to interact with collagen, are the ones that, in best cases, can induce cell differentiation and in the worst case, decrease cell viability. When cells were able to differentiate and produce neurites, threads could guide and orient them. Neurites were aligned with respect to the threads, an interesting achievement for PN regeneration applications.

However, one major parameter to take into account towards PN regeneration is the growth factor FGF that we added in cell culture medium. It would be of great interest to incorporate it inside the system and slowly deliver it to the cells. Other solutions can be considered, such as mimicking FGF peptide and display it to the cells *via* conjugation on SiNP, as already shown on 2D surface.[46] Interestingly, FGF is not added alone in cell culture medium, but with heparin sulfate, a polysaccharide that form a complex *via* its sulfonate chemical function with FGF allowing for its activation. We may therefore try to electrostatically bind the protein FGF to the sulfonate groups on SiNP-SO_3^- and incorporate directly FGF *via* the particle inside the system. Going further, it would be interesting to study the influence of the threads on glial cells that can form myelin to support and protect neuronal development and axon pathfinding[31] and are also sensitive to chemical signalization and mechanical properties.[47,48]

To conclude, our approach appears particularly promising to prepare versatile scaffolds as guides for neuron-like cells. However, our data suggest that our way of control is based on the modulation of the scaffold architecture. In contrast, we could not get any evidence that bioactive epitopes located at the surface of incorporated nanoparticles were in contact with the seeded cells. One solution would be to prepare thinner threads or bionanocomposites and to organize them as 3D porous scaffolds to improve the particle accessibility to the cells. This is the aim of our preliminary work devoted to the engineering of self-supported collagen-based membranes by electrospinning that will be described in the next chapter.

7. Experimental methods

7.1. Collagen extraction and purification

Type I collagen was extracted from young Wistar rat tails as previously described.[22,49] Using young rats is preferable because intermolecular cross-linking in collagen fibrils increases with age, reducing its solubility. The tendons were excised in a sterile flow hood and washed with phosphate-buffered saline (137 mM NaCl, 2.68 mM KCl, 8.07 mM Na_2HPO_4, and 1.47 mM NaH_2PO_4) to remove cells and traces of blood. The tissues were then soaked in a 4 M NaCl solution to lyse remaining cells and precipitate some of the high molecular weight proteins. After the tendons were rinsed again with phosphate-buffered saline, they were solubilized in 500 mM acetic acid. The solution was clarified by centrifugation at 41,000×g for 2 h. Proteins other than type I collagen were selectively precipitated in 300 mM NaCl and removed by centrifugation at 41,000×g for 3 h. Collagen was retrieved from the supernatant by precipitation in 600 mM NaCl and centrifugation at 3000×g for 45 min. The pellets were solubilized in 500 mM acetic acid and thoroughly dialyzed against the same solvent to completely remove NaCl. The solutions were kept at 4°C and centrifuged at 41,000×g for 4 h before use. Sample purity was assessed by SDS-PAGE electrophoresis. Collagen concentration was determined from the acidic solution by titrating the amount of hydroxyproline.

7.2. Synthesis of fluorescent core shell silica particles

7.2.1. Synthesis of a fluorescent alkoxysilane precursor

To synthesize the fluorescent precursor, 50 µL of Alexa 488 at 1 ml. mL^{-1} is conjugated to 1.2 µL of Aminopropyltriethoxysilane (APTES, 99%, Aldrich) in 149 µL of dimethy sulfoxide (DMSO, Sigma-Aldrich) and let under stirring for 5 h.

7.2.2. Synthesis of the fluorescent core

Stöber silica particles were synthesized using 100 ml absolute ethanol (VWR, GPR RectaPur), 5.5 ml ammonium hydroxide solution (NH_4OH, 25%, Carlo Erba), 4 ml tetraethyl orthosilicate (TEOS 98%, Sigma Aldrich) and 200 µL of Alexa-APTES. TEOS and Alexa-APTES were added to the solution dropwise, and the sol was stirred overnight at RT. Ethanol and ammonia were removed by centrifugation (twice at 10 000 rpm for 5 min) before drying under vacuum.

7.2.3. Synthesis of the silica shell

Those fluorescent particles were dispersed in 300 mL absolute ethanol with 2.4 mL of ultra-pure water. 6 mL of TEOS and 3 mL of NH_4OH were added dropwise and the mixture was kept under stirring for 12 h. SiNPs were washed with ethanol through an ultrasonic redispersion-centrifugation process (12 000 rpm for 15 min) and dried under vacuum.

7.3. Sulfonate-functionalized SiNPs

Cf. previous chapters.

7.4. Amine-functionalized SiNP

Cf. previous chapters

7.5. Stat –SiNPs

Stöber particles were functionalized with amine groups and thiol groups by mixing APTES and MPTMS. Typically, 0.77 g of silica particles were redispersed in a mixture of 76.6 ml ethanol and 1.7 mL ammonium hydroxide solution before addition of 0.375 mL APTES (1.2 mmol g^{-1} silica) and 0.96 ml MPTMOS (1.2 mmol g^{-1} silica). The mixture was stirred for 18 h at RT. Subsequently, the reaction mixture was heated to 80°C for 20 min. The mixture was left to cool down to RT and was subsequently washed three times with ethanol (by centrifugation at 12 000 rpm for 15 min).

Finally, oxidation of thiol groups leads to sulfonic acid functionalized particles.[50] In a typical reaction, 3.6 g of thiol-modified particles were suspended in 180 mL hydrogen peroxide (H_2O_2 35%, Acros Organics) under stirring at RT for 48 hours. The powder was washed by centrifugation before addition of 150 mL sulfuric acid (H_2SO_4, Sigma Aldrich) and stirred for 2 hours at RT. SiNPs were washed with ethanol and water through an ultrasonic redispersion-centrifugation process (12 000 rpm for 15 min) and dried under vacuum.

7.6. Patchy SiNPs

N-[3-Triethoxysilyl)propyl]-anthracen-9-ylmethyl precursor was solubilized and sonicated for 3 min in ethanol at the concentration of 50 mM. After a resting time of 1 h the solution was sonicated again for 1 min. The self-assembly was ready grafting on SiNPs.

Typically, 30 mg of SiNP was dispersed in 4 mL of ethanol, with 165 µL of NH_4OH in a Schlenk tube. N-[3-Triethoxysilyl)propyl]-anthracen-9-ylmethyl precursor was added all at once at 50 mM in 36 mL. After 18 h stirring at RT the reaction mixture was heated to 80°C for 20 min. The mixture was left to cool down to RT and was subsequently washed three times with ethanol through an ultrasonic redispersion-centrifugation process (12 000 rpm for 15 min) and dried under vacuum.

Bifunctionalization in two steps

For the bifunctional SiNPs synthesized in two steps in ethanol, SiNPs were dispersed in 30 mL ethanol with 685.5 µL NH_4OH and 294 µL 3-mercaptopropyltrimethoxysilane (MPTMS, 1.6 mmol). After 40 min stirring at RT the reaction mixture was heated to 80°C for 20 min. The mixture was left to cool down to RT and was subsequently washed three times with ethanol through an ultrasonic redispersion-centrifugation process (12 000 rpm for 15 min) and dried under vacuum.

Oxidation of thiol groups to sulfonates [51]

In a typical reaction, 3.6 g of thiol-modified particles were suspended in 1.5 ml hydrogen peroxide (H_2O_2 35%, Acros Organics) under stirring at RT for 48 hours. The powder was washed by centrifugation before addition of 1.5 mL sulfuric acid (H_2SO_4, Sigma Aldrich) and stirred for 2 hours at RT. SiNPs were washed with ethanol and water through an ultrasonic redispersion-centrifugation process at 12 000 rpm for 15 min and dried under vacuum.

Acidic treatment to free the amines

The carbamate was hydrolyzed by sonication during 20 min with 2.5 mL trifluoroacetic acid (Sigma Aldrich). NH_2-modified particles were washed with dichloromethane once (VWR), with a mixture dichloromethane: N,N-Diisopropylethylamine one time (90:10, DIEA, Sigma Aldrich) and dichloromethane once again. NH_2-modified particles were recovered through an ultrasonic redispersion-centrifugation process (12 000 rpm for 15 min) and dried under vacuum.

7.7. Peptide coupling between amines on SiNPs and IKVAV peptides

The IKVAV-NH_2 peptide was graciously synthesized and purified by Nicolas Delsuc, Laboratory of Biomolecules, Ecole Normale Supérieure. It contains a terminal carboxylic acid to be conjugated to amine-modified particles. A tert-Butyloxycarbonyl protective group (BOC group) is coupled with the final amine of the lysine to avoid eventual byproducts.

Peptide coupling was performed between carboxylate acid on IKVAV and amine groups at the surface of SiNPs. 13 mg of SiNPs were dispersed in 13 µL dimethylformamid (DMF, VWR) and 0.24 µL DIEA with 0.5 mg IKVAV, 0.1 mg hydroxybenzotriazole (HOBT, 97%, Sigma Aldrich) and 0.25 mg 2-(1H-benzotriazol-1-yl)-1,1,3,3-tetramethyluronium hexafluorophosphate (HBTU, 98%, Sigma Aldrich). The mixture was stirred for 40 min and subsequently washed with DMSO, dichloromethane and methanol (VWR) through an ultrasonic redispersion-centrifugation process (12 000 rpm for 15 min) and dried under vacuum.

To deprotect the amine from the BOC group, an acidic treatment with trifluoroacetic acid (Sigma Aldrich) is performed under sonication for 20 min. SiNP-IKVAV were washed three times with ethanol through an ultrasonic redispersion-centrifugation process (12 000 rpm for 15 min) and dried under vacuum.

7.8. Zeta-potential measurements

Zeta-potential measurements were performed on a Malvern Zetasizer Nano spectrometer. They were performed at a concentration of particle of 5 g.L^{-1} in DTS1060C cells in KCl buffer (Concentration 100 mM) at different pHs adjusted with NaOH and HCl at RT.

7.9. Transmission Electron Microscopy

A drop of sample in aqueous solution was deposited on carbon-coated copper grids (300 mesh). After 3 minutes, the excess liquid was blotted with filter paper. TEM was performed at RT using a Tecnai spirit G2 electron microscope operating at 120 kV and the images were recorded on a Gatan Orius CCD camera.

7.10. Preparation of the composite materials

7.10.1. Collagen – SiNP mixture

Collagen solutions in acetic acid were concentrated using centrifugal filtration units (Vivaspin®, Sartorius, with a 100kD cutoff) spun at 3000xg, 10°C, until reaching the desired final concentrations (15 or 30 mg.mL^{-1}). SiNPs were weighted and diluted in acetic acid 500 mM at the desired concentration. Both solutions were mechanically mixed together. Final solution was then placed in 1 mL syringes and degassed by centrifugation at 3000xg for 30 min at 10°C.

7.10.2. Extrusion of the composite materials

The 1mL syringe, filled with the composite solution in 500 mM acetic acid, was mounted with a 23-gauge (inner diameter of 390 µm) blunt stainless-steel needle, and loaded vertically. A motorized stage was used to bring down a rod in contact with the syringe piston and to impose its speed. The extruded fluid velocity was about 25 µm.s^{-1}. The collecting cuvette was filled with the fibrillogenesis buffer PBS 5x (pH 7.4). At the blunt needle exit, extruded threads, plunging into the fibrillogenesis buffer, were observed and followed by an optical through-hole mounting. Prior to their use, the threads were kept and left for maturation in fibrillogenesis buffer at RT for 2 weeks under gentle agitation to prevent them to stick together.

7.11. Characterization of the threads by microscopy analysis

Threads were put in a homemade thin glass-chamber filled with fibrillogenesis buffer PBS 5x to prevent dehydration during observation. Polarized light microscopy was performed using a transmission Nikon Eclipse E600 Pol, equipped with crossed polarizers and a Nikon DXM 1200CCD camera. Fluorescence microscopy was performed using a fluorescence microscope Axio Imager D.1, Zeiss.

7.12. Cell culture

PC12 cells were cultured in Dulbecco's modified Eagle's medium (DMEM) supplemented with 10% fetal calf serum, 5% horse serum, 100 µg.ml^{-1} penicillin, 100 µg.ml^{-1} streptomycin and 1% Glutamax at 37°C in a humidified atmosphere of 5% CO_2 as previously described.[24,25] Recombinant FGF1 (50 ng/ml, R&D Systems, 232-FA) was added to the culture medium when indicated in presence of heparin (10 µg.ml^{-1}). The cells were grown in 75 mm² flasks (BD Falcon) and passaged every three days. All culture reagents were purchased from Gibco unless specified.

7.13. Cell experiments

Threads were immersed in cell culture medium for 3 h and washed 3 times. The threads were deposited in a 6 well plate. PC12 cells were seeded at a low density (50 k cells per well) in order to minimize cell–cell contacts. Cells were incubated on the threads at 37°C and 5% CO_2 for 48 h. Then the cell culture medium was changed, and FGF was added to the culture medium when indicated, in the presence of heparin (10 µg.ml^{-1}). Cell culture medium was then changed every 3 days, with addition of FGF (in presence of heparin) when indicated.

7.14. Alamar blue for cell viability assay

Alamar blue was used to assess the viability of cells. Aliquots of 20 µL of stock alamar blue solution (5 mg·mL^{-1}) were added to each well containing 200 µL of medium (10% final solution) and incubated with the cells for 3 h. Following incubation, the medium was removed and dilute five times. The absorbance was read on a UV-visible spectrophotometer at 550 and 690 nm. A subtraction analysis of the dual wavelength was performed (D_{550} to D_{690}) to increase accuracy of the measurement.

7.15. Fluorescence staining

Cells were fixed with 4% paraformaldehyde in PBS and 1 mM $CaCl_2$ for 30 min at RT. For immunostaining, fixed samples were first permeabilized with 0.1% Triton X-100 in PBS (5 min, RT). Actin filaments were fluorescently labeled with AlexaFluor-488-conjugated phalloidin (Life Technologies; 1:200 dilutions, 1 h at RT) for visualization. Cell nuclei were counterstained with DAPI (Life Technologies).

7.16. Image acquisition and analysis

Images of fluorescently stained samples were obtained using a fluorescence microscope (Axio Imager D.1, Zeiss). Cell morphology was quantified from phalloidin stained fluorescent images acquired by a 10× objective from randomly selected regions on the coverslip (at least 400 cells analyzed on each thread). Acquired images were analyzed using ImageJ software.

7.17. Statistical analysis

Statistical analysis was performed using Graphpad Prism v.6 software. Analysis were performed using a Mann-Whitney non parametric test; each condition on three triplicates from two independent experiments, except when specified. Values in graphs are the mean and standard error of mean (SEM).

8. References

(1) Noble, J.; Munro, C. A.; Prasad, V. S. S. V.; Midha, R. Analysis of Upper and Lower Extremity Peripheral Nerve Injuries in a Population of Patients with Multiple Injuries. *J Trauma 45* **1998**, *1*, 116–122.

(2) Gao, M.; Guo, J.; K. Leung, G. K.; Wu, W. Use of Self-Assembly Nanofibre Biomaterials for Neural Repair After Injury. In *Advances in Nanofibers*; Maguire, R., Ed.; InTech, 2013.

(3) Belanger, K.; Dinis, T. M.; Taourirt, S.; Vidal, G.; Kaplan, D. L.; Egles, C. Recent Strategies in Tissue Engineering for Guided Peripheral Nerve Regeneration. *Macromol. Biosci.* **2016**, *16* (4), 472–481.

(4) Rosberg, H.-E.; Carlsson, K. S.; Dahlin, L. B. Prospective Study of Patients with Injuries to the Hand and Forearm: Costs, Function, and General Health. *Scand. J. Plast. Reconstr. Surg. Hand Surg.* **2005**, *39* (6), 360–369.

(5) Chen, Z.-L.; Yu, W.-M.; Strickland, S. Peripheral Regeneration. *Annu. Rev. Neurosci.* **2007**, *30* (1), 209–233.

(6) Geuna, S.; Raimondo, S.; Ronchi, G.; Di Scipio, F.; Tos, P.; Czaja, K.; Fornaro, M. Chapter 3 Histology of the Peripheral Nerve and Changes Occurring During Nerve Regeneration. In *International Review of Neurobiology*; Elsevier, 2009; Vol. 87, pp 27–46.

(7) Stoll, G.; Müller, H. W. Nerve Injury, Axonal Degeneration and Neural Regeneration: Basic Insights. *Brain Pathol.* **1999**, *9*, 313–325.

(8) Martini, R. Expression and Functional Roles of Neural Cell Surface Molecules and Extracellular Matrix Components during Development and Regeneration of Peripheral Nerves. *J. Neurocytol.* **1994**, *23*, 1–28.

(9) Holland, T. J. Utilizing the Reaction of Degeneration Test for Individuals with Focal Paralysis. *J. Brachial Plex. Peripher. Nerve Inj.* **2012**, *7* (1), 6.

(10) Faroni, A.; Mobasseri, S. A.; Kingham, P. J.; Reid, A. J. Peripheral Nerve Regeneration: Experimental Strategies and Future Perspectives. *Adv. Drug Deliv. Rev.* **2015**, *82–83*, 160–167.

(11) Schmidt, C. E.; Leach, J. B. Neural Tissue Engineering: Strategies for Repair and Regeneration. *Annu. Rev. Biomed. Eng.* **2003**, *5* (1), 293–347.

(12) Haile, Y.; Haastert, K.; Cesnulevicius, K.; Stummeyer, K.; Timmer, M.; Berski, S.; Dräger, G.; Gerardy-Schahn, R.; Grothe, C. Culturing of Glial and Neuronal Cells on Polysialic Acid. *Biomaterials* **2007**, *28* (6), 1163–1173.

(13) Wu, J.; Chiu, D. T. W. Painful Neuromas: A Review of Treatment Modalities. *Ann Plas Surg* **1999**, *43*, 661–667.

(14) Marinescu, S.-A.; Zărnescu, O.; Mihai, I.-R.; Giuglea, C.; Sinescu, R. D. An Animal Model of Peripheral Nerve Regeneration after the Application of a Collagen-Polyvinyl Alcohol Scaffold and Mesenchymal Stem Cells. *Rom J Morphol Embryol* **2014**, *55* (3), 891–903.

(15) Mackinnon, S. E.; Hudson, A. R. Clinical Application of Peripheral Nerve Transplantation. *Plast Reconstr Surg* **1992**, *90* (4), 695–699.

(16) Pereira, J. H.; Palande, D. D.; Subramanian, A.; Narayanakumar, T. S.; Curtis, J.; Turk, J. L. Denatured Autologous Muscle Graft in Leprosy. *The Lancet* **1991**, *338* (8777), 1239–1240.

(17) Brandt, J.; Dahlin, L. B.; Lundborg, G. Autologous Tendons Used as Grafts for Bridging Peripheral Nerve Defects. *J. Hand Surg.* **1999**, *24* (3), 284–290.

(18) Tang, J.-B.; Shi, D.; Zhou, H. Vein Conduits for Repair of Nerves with a Prolonged Gap or in Unfavorable Conditions: An Analysis of Three Failed Cases. *Microsurgery* **1995**, *16* (3), 133–137.

(19) Konofaos, P.; Ver Halen, J. Nerve Repair by Means of Tubulization: Past, Present, Future. *J. Reconstr. Microsurg.* **2013**, *29* (03), 149–164.

(20) Liao, I.-C.; Wan, H.; Qi, S.; Cui, C.; Patel, P.; Sun, W.; Xu, H. Preclinical Evaluations of Acellular Biological Conduits for Peripheral Nerve Regeneration. *J. Tissue Eng.* **2013**, *4*, 2041731413481036.

(21) Bellamkonda, R. Peripheral Nerve Regeneration: An Opinion on Channels, Scaffolds and Anisotropy☆. *Biomaterials* **2006**, 3515–3518.

(22) Picaut, L. Synthèse d'un Tendon Artificiel, Université Pierre et Marie Curie: Paris, 2017.

(23) Westerink, R. H. S.; Ewing, A. G. The PC12 Cell as Model for Neurosecretion: PC12 Cells as Model for Neurosecretion. *Acta Physiol.* **2007**, *192* (2), 273–285.

(24) Rodriguez-Enfedaque, A.; Bouleau, S.; Laurent, M.; Courtois, Y.; Mignotte, B.; Vayssière, J.-L.; Renaud, F. FGF1 Nuclear Translocation Is Required for Both Its Neurotrophic Activity and Its P53-Dependent Apoptosis Protection. *Biochim. Biophys. Acta BBA - Mol. Cell Res.* **2009**, *1793* (11), 1719–1727.

(25) Bouleau, S.; Pârvu-Ferecatu, I.; Rodriguez-Enfedaque, A.; Rincheval, V.; Grimal, H.; Mignotte, B.; Vayssiere, J.-L.; Renaud, F. Fibroblast Growth Factor 1 Inhibits P53-Dependent Apoptosis in PC12 Cells. *Apoptosis* **2007**, *12* (8), 1377–1387.

(26) Drubin, D. G.; Feinstein, S. C.; Shooter, E. M.; Kirschner, M. W. Nerve Growth Factor-Induced Neurite Outgrowth in PC12 Cells Involves the Coordinate Induction of Microtubule Assembly and Assembly-Promoting Factors. *J. Cell Biol.* **1985**, *101* (5), 1799–1807.

(27) Aimé, C.; Mosser, G.; Pembouong, G.; Bouteiller, L.; Coradin, T. Controlling the Nano–bio Interface to Build Collagen–silica Self-Assembled Networks. *Nanoscale* **2012**, *4* (22), 7127–7134.

(28) Birk, D. E.; Bruckner, P. Collagen Suprastructures. In *Collagen: Primer in Structure, Processing and Assembly*; Brinckmann, J., Notbohm, H., Müller, P. K., Eds.; Springer Berlin Heidelberg: Berlin, Heidelberg, 2005; pp 185–205.

(29) Köster, S.; Evans, H. M.; Wong, J. Y.; Pfohl, T. An In Situ Study of Collagen Self-Assembly Processes. *Biomacromolecules* **2008**, *9* (1), 199–207.

(30) Jucker, M.; Kleinman, H. K.; Ingram, D. K. Fetal Rat Septal Cells Adhere to and Extend Processes on Basement Membrane, Laminin, and a Synthetic Peptide from the Laminin A Chain Sequence. *J. Neurosci. Res.* **1991**, *28* (4), 507–517.

(31) Hoffman-Kim, D.; Mitchel, J. A.; Bellamkonda, R. V. Topography, Cell Response, and Nerve Regeneration. *Annu. Rev. Biomed. Eng.* **2010**, *12* (1), 203–231.

(32) Foley, J. D.; Grunwald, E. W.; Nealey, P. F.; Murphy, C. J. Cooperative Modulation of Neuritogenesis by PC12 Cells by Topography and Nerve Growth Factor. *Biomaterials* **2005**, *26* (17), 3639–3644.

(33) Yao, X.; Peng, R.; Ding, J. Cell-Material Interactions Revealed Via Material Techniques of Surface Patterning. *Adv. Mater.* **2013**, *25* (37), 5257–5286.

(34) Mahoney, M. J.; Chen, R. R.; Tan, J.; Mark Saltzman, W. The Influence of Microchannels on Neurite Growth and Architecture. *Biomaterials* **2005**, *26* (7), 771–778.

(35) Arora, P. D.; Narani, N.; McCulloch, C. A. The Compliance of Collagen Gels Regulates Transforming Growth Factor-β Induction of α-Smooth Muscle Actin in Fibroblasts. *Am. J. Pathol.* **1999**, *154* (3), 871–882.

(36) Balgude, A. .; Yu, X.; Szymanski, A.; Bellamkonda, R. V. Agarose Gel Sti!Ness Determines Rate of DRG Neurite Extension in 3D Cultures. *Biomaterials* **2001**, *22*, 1077–1084.

(37) Chen, C. S. Mechanotransduction − a Field Pulling Together? *J. Cell Sci.* **2008**, *121* (20), 3285–3292.

(38) Geiger, B.; Spatz, J. P.; Bershadsky, A. D. Environmental Sensing through Focal Adhesions. *Nat. Rev. Mol. Cell Biol.* **2009**, *10* (1), 21–33.

(39) Koch, D.; Rosoff, W. J.; Jiang, J.; Geller, H. M.; Urbach, J. S. Strength in the Periphery: Growth Cone Biomechanics and Substrate Rigidity Response in Peripheral and Central Nervous System Neurons. *Biophys. J.* **2012**, *102* (3), 452–460.

(40) Flanagan, L. A.; Ju, Y.-E.; Marg, B.; Osterfield, M.; Janmey, P. A. Neurite Branching on Deformable Substrates. *Neuroreport* **2002**, *13* (18), 2411–2417.

(41) Leach, J. B.; Brown, X. Q.; Jacot, J. G.; DiMilla, P. A.; Wong, J. Y. Neurite Outgrowth and Branching of PC12 Cells on Very Soft Substrates Sharply Decreases below a Threshold of Substrate Rigidity. *J. Neural Eng.* **2007**, *4* (2), 26–34.

(42) Sur, S.; Newcomb, C. J.; Webber, M. J.; Stupp, S. I. Tuning Supramolecular Mechanics to Guide Neuron Development. *Biomaterials* **2013**, *34* (20), 4749–4757.

(43) Gunn, J. W.; Turner, S. D.; Mann, B. K. Adhesive and Mechanical Properties of Hydrogels Influence Neurite Extension. *J. Biomed. Mater. Res.* **2005**, *72A* (1), 91–97.

(44) Suter, D. M.; Miller, K. E. The Emerging Role of Forces in Axonal Elongation. *Prog. Neurobiol.* **2011**, *94* (2), 91–101.

(45) Sundararaghavan, H. G.; Monteiro, G. A.; Firestein, B. L.; Shreiber, D. I. Neurite Growth in 3D Collagen Gels with Gradients of Mechanical Properties. *Biotechnol. Bioeng.* **2009**, *102* (2), 632–643.

(46) Freeman, R.; Stephanopoulos, N.; Álvarez, Z.; Lewis, J. A.; Sur, S.; Serrano, C. M.; Boekhoven, J.; Lee, S. S.; Stupp, S. I. Instructing Cells with Programmable Peptide DNA Hybrids. *Nat. Commun.* **2017**, *8*, 1–11.

(47) Cai, L.; Zhang, L.; Dong, J.; Wang, S. Photocured Biodegradable Polymer Substrates of Varying Stiffness and Microgroove Dimensions for Promoting Nerve Cell Guidance and Differentiation. *Langmuir* **2012**, *28* (34), 12557–12568.

(48) Evans, E. B.; Brady, S. W.; Tripathi, A.; Hoffman-Kim, D. Schwann Cell Durotaxis Can Be Guided by Physiologically Relevant Stiffness Gradients. *Biomater. Res.* **2018**, *22* (14), 1–13.

(49) Gobeaux, F.; Mosser, G.; Anglo, A.; Panine, P.; Davidson, P.; Giraud-Guille, M.-M.; Belamie, E. Fibrillogenesis in Dense Collagen Solutions: A Physicochemical Study. *J. Mol. Biol.* **2008**, *376* (5), 1509–1522.

(50) Marschall, R.; Bannat, I.; Caro, J.; Wark, M. Proton Conductivity of Sulfonic Acid Functionalised Mesoporous Materials. *Microporous Mesoporous Mater.* **2007**, *99* (1–2), 190–196.

(51) Maria Claesson, E.; Philipse, A. P. Thiol-Functionalized Silica Colloids, Grains, and Membranes for Irreversible Adsorption of Metal(Oxide) Nanoparticles. *Colloids Surf. Physicochem. Eng. Asp.* **2007**, *297* (1–3), 46–54.

V. Self-supported collagen-based matrices by electrospinning

Content

1. Electrospinning

1.1. Process

Electrospinning (ES) is a broadly used technology for fibrous scaffold engineering. ES is a process that consists in extruding a polymer solution upon the application of a voltage between a needle and a grounded collector, leading to charge accumulation at the surface of the liquid.[1,2] The conical shape formed by the liquid at the tip of the capillary is named Taylor cone. At a sufficiently high voltage, the surface tension is overcome, leading to the formation of a liquid jet ejected from the tip of the Taylor cone. After solvent evaporation and elongation, the polymer forms a fiber of a diameter from tens nm to microns, which dries and is collected on the target, resulting in a fibers web, with tunable porosity, fiber diameter and orientation.[3–7]

Figure V-1 : ES process adapted from [8].

With a small diameter and high surface, electrospun fibers present an extremely high surface-to-volume ratio. This tunable porosity, size, shape and composition gives a modularity to conform to a broad variety of properties and functionalities. ES has been successfully applied in various fields, such as engineering (optical, electronics, defense and security protective clothing, filtration and environment), nanocatalysis, and healthcare (biomedicine, pharmaceutics, tissue engineering and biotechnology).[9–12]

ES material can be structured and shaped in various ways to fit a given application. For example, the collector can be on a fixed support or on a rotating mandrel. This rotating mandrel is indeed a well-known method to speed up the fibers drying and prevent the fibers coalescence. In addition, it can result in fibers alignment at high rotation speed.[13–15]

ES is an ideal tool to create artificial entangled scaffolds that can mimic the native extracellular matrix (ECM) for tissue engineering. Many synthetic and biological polymers have been successfully electrospun,[4,5,16,17] such as polylactic acid,[13] polyurethanes,[18] silk fibroin,[19–23] hyaluronic acid,[24] cellulose,[25] or chitosan/collagen.[26]

1.2. Electrospinning of collagen

An important aspect when processing collagen is to ensure the preservation of its native state as a triple helix and prevent denaturation. Conflicting results about collagen ES in the literature concern the conditions of collagen solubilization to improve electrospinnability: use of additional polymers,[27,28] fluorinated solvents[29] or cross-linkers.[30,31] Moreover, using high electrical field (10-20 kV) during ES may be detrimental to collagen structure.[39,40]

First, the choice of solvent to successfully electrospin the collagen will be discussed. In the literature fluoroalcohols like 1,1,1,3,3,3-hexafluoro-2-propanol (HFIP)[32–34] and 2,2,2-trifluoroethanol (TFE)[35] are widely used because of their great ES abilities. According to Zeugolis and coworkers, fluoroalcohols can cause collagen denaturation resulting in the formation of gelatin. Collagen maintains a triple helix structure because of a myriad of weak interactions, including hydrophobic interactions and hydrogen bonding. It is proposed by Bürk and co-workers,[29] that small molecules such as fluoroalcohols act directly *via* hydrophobic and hydrophilic interactions to separate the triple helices, hence destabilizing the tertiary structure of proteins by breaking most of the weak intramolecular interactions. This affects the rheology of the solution properties and increases the spinnability of the polymer solution.[29,36] Altogether, it is important to preserve intramolecular interactions within the collagen triple helix in solution before ES but spinnability is improved if intermolecular interactions between triple helices are weaken.

Several solvents may fulfill these requirements such as acids, water or buffer. Salts in buffer increase the ionic strength and can interact with the triple helix and replace the water network, enhancing its stability.[37] The other possibility is to introduce a component miscible in aqueous solution but bearing a hydrophobic moiety able to isolate the triple helices. Indeed, non-polar groups would enhance the solubility of nonpolar species, preventing their aggregation.[38] Ideal candidates are short-chain aliphatic alcohols because of their miscibility with water combined with a non-polar moiety. Ethanol has been used with phosphate buffered saline (PBS) for ES but it resulted in fibers with a wide range of diameters together with the presence of collagen beads .[27] At low salt concentration, collagen fibers around 200-500 nm were obtained. Increasing the salt concentration decreased the diameter of the fibers and the standard deviation because the higher the ionic strength the higher the collagen is soluble.[30] Ethanol was also used mixed with acetic acid (0.5 M) in a ratio of 1:1 but the ES processing was possible only by using polyethylene glycol (PEO) as additional support polymer. Electrospun nanofiber meshes with the fiber diameter ranging between 50 to 100 nm could be obtained.[29] In fluorinated solvent, the diameter of the fibers varies depending on the collagen concentration of the starting solution, evolving from 150 to 200 nm.

The second objective of this study is to engineer a self-supported membrane. Some studies report the use of crosslinkers to improve membrane stability.[29,30] However, crosslinkers induce a chemical modification of collagen and do not preserve the supramolecular structure. Based on the expertise of the team, we know that water-stable collagen materials can be obtained from solutions without cross-linking if the fibrillogenesis of the triple helices is induced. However, this requires that the protein has not been denatured during the course of the ES process.

In this context, the present work aimed at preparing water-stable collagen-based membranes by electrospinning that would be suitable for applications in tissue engineering. Specific emphasize has been made on obtaining homogeneous fibrous scaffolds, preserving the triple helix structure of this protein, achieving collagen fibrillation and evaluating their influence on fibroblast cells. This work has been performed at the LCMCP in collaboration with Christel Laberty-Robert and Natacha Krins.

2. A self-supported membrane

The implementation of ES involves parameters that can be varied independently including voltage, solution feeding rate, and environment including temperature and humidity. Moreover, the intrinsic characteristics of the solution must meet precise requirements: low surface tension and high conductivity,[30] appropriate viscosity to form a stable jet that does not break before drying,[41] while ensuring sufficient flowability [42] and drying before reaching the collector. [29] Therefore, in a first step, we have investigated the best parameters to obtain a self-supported membrane.

2.1. Parameters of the ES set-up

Based on previous works performed in the laboratory for other polymers than collagen, the speed of extrusion was varied in the range from 0.001 to 0.02 mL.min^{-1}, the distance between the needle and the collector from 7 to 17 cm and the voltage from 9 to18 kV.

The size, shape and surface chemistry of the collector is also an important parameter. The collector must be a conducting material, but should not interact strongly with collagen to be able to detach the membrane after ES. We considered as conducting material aluminum, copper and gold. We tried to cover them with an additional coating to help the peeling off: polytetrafluoroethylene (PTFE) layers or wax paper. Finally, we selected a copper tape alone to collect the ES collagen.

2.2. Parameters of the biopolymer solution

To tune the fluidity of the solution, we considered two options. The first one is to act on the starting concentration of the polymer. The second one is to modify the intermolecular interactions, hence the solvent.

2.2.1. Influence of the starting solution

Different collagen concentrations were tested to reach a polymer concentration high enough to create a stable jet without precluding extrusion. We investigated the concentration range of 1 to 15 mg.mL^{-1}. At 15 mg.mL^{-1} the polymer solution was gel-like and too viscous to be electrospun. On the contrary, stable jets were obtained for concentration 1-2 mg.mL^{-1}. We used 1.7 mg. mL^{-1} in the following.

In order to modify the intermolecular interactions, we decided to vary the fibrillation state of collagen. We can control and reproduce collagen fibrillation *in vitro* by increasing the pH, which is a good alternative to enzymatic control.[43] From an acetic acid solution we increased the pH with ammonia vapor to trigger the self-assembly of the soluble molecules of collagen into fibrils. However, we attempted to stop the self-assembly process in an “pre-fibrillated” state by raising the pH up to 4 only. Different methods were tested such as dialysis with water, or dilution with an aqueous NaOH solution to create small building blocks or nuclei of the fibrillation (Figure V-2). However, even in these conditions, collagen solutions were found to be too viscous, which led us to conclude that the collagen molecules have to remain in a monomeric form for ES.

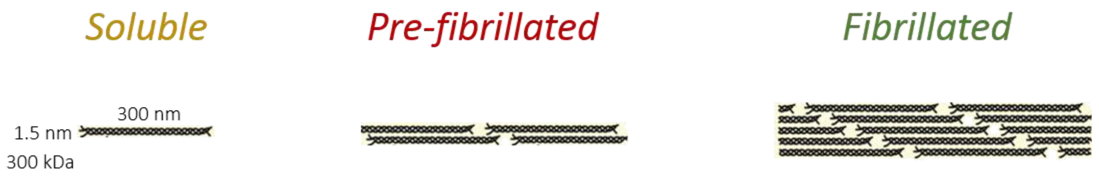

Figure V-2 : Three states of collagen : soluble triple helices (acidic media), pre-fibrillated state to create small building blocks (pH 4) and fibrillated collagen (pH *ca.* 7).

2.2.2. Influence of the solvent

After extraction and purification, collagen is routinely dissolved in acetic acid (AA) 500 mM. In these acidic conditions, collagen remains soluble as triple helix. We started then the ES process with collagen in AA 500mM. We did not succeed to create fibers, probably because the viscoelastic properties of the solution were not adapted to the process but also because AA does not evaporate fast enough before reaching the collector. Hence, only drops were observed.

To increase the evaporation rate, we mixed AA (10 mM) with hydrochloric acid (HCl) (0.3 mM), and also used pure HCl. In both cases the jet was not stable enough and we also produced drops. Acids are poor ES solvents for two raisons: their evaporation rate is slow and they interact strongly with collagen molecules leading to the deposition of ill-defined mats of fibers melted together with a loss of porosity.

To introduce a hydrophobic moiety both miscible with water and easy to evaporate, we added EtOH to AA and to HCl. Interestingly, a stable jet was obtained with the HCl-EtOH mixture. Several ratios between EtOH and HCl were tested. At 50% in EtOH no fiber elongation occured, instead only beads were observed from electrospray (Figure V-3-A,B). When the EtOH content increases to 75%, fibers start to form (Figure V-3-C-D). However, fiber elongation remains limited, ending with the formation of large beads. Further increase in EtOH content did not allow to improve fiber elongation. At more than 75% of EtOH, the collagen molecules aggregate and form a gel that is not compatible with the ES process. The 75 % EtOH-HCl condition therefore seemed the most appropriate but we wished to avoid the presence of beads. Those beads were already described in the literature and result from instabilities in the jet formation that are related to unfavorable viscosity, net charge density carried and surface tension of the solution.[44–46]

We first decreased the collagen concentration from 4 mg.mL^{-1} to 2 mg.mL^{-1} (Figure V-3-E-F). The fibers get longer and elongated, but large beads remained. Then, to improve electrospinnability at a fixed EtOH content, we raised the molarity of HCl from 3 mM to 30 mM in order to increase the net charge density and decrease the surface tension. Fibers got stretched out and elongated (Figure V-3-G,H). Increasing further the molarity of HCl up to 300 mM did not affect fiber morphology.

All the tested and selected parameters for collagen ES are gathered in Table V-1. By screening these parameters, various typologies of materials were obtained and observed by SEM, allowing to find the best compromise between the ideal surface tension, conductivity, viscosity, and drying to obtain a well-defined homogeneous network of electrospun collagen fibers. According to our results, the best initial solution consists of collagen at a concentration of 1.7 mg.mL^{-1} in 25% HCl 30 mM and 75% EtOH. The extrusion is performed at 0.005 mL.min^{-1} rate at a distance of 9 cm from the collector. The collector it-self is a copper rectangle tape (2.5 x 1.5 cm) on the middle of a fixed Teflon support.

Parameters	Range tested	Selected
Extrusion speed	0.02-0.001 mL.min^{-1}	0.005 mL.min^{-1}
Dist. Needle-collect	7 -17 cm	9 cm
Voltage	9 -18 kV	to be adjusted
Collector Coating	aluminum - copper - gold PTFE - wax paper	copper
Concentration	1 - 15 mg.mL^{-1}	1.7 mg.mL^{-1}
Solvent	AA 500 mM, HCl 3 mM, HCl 30 mM with or without EtOH	HCL 30 mM
Ethanol amount	50% - 90%	75%

Table V-1 : ES parameters

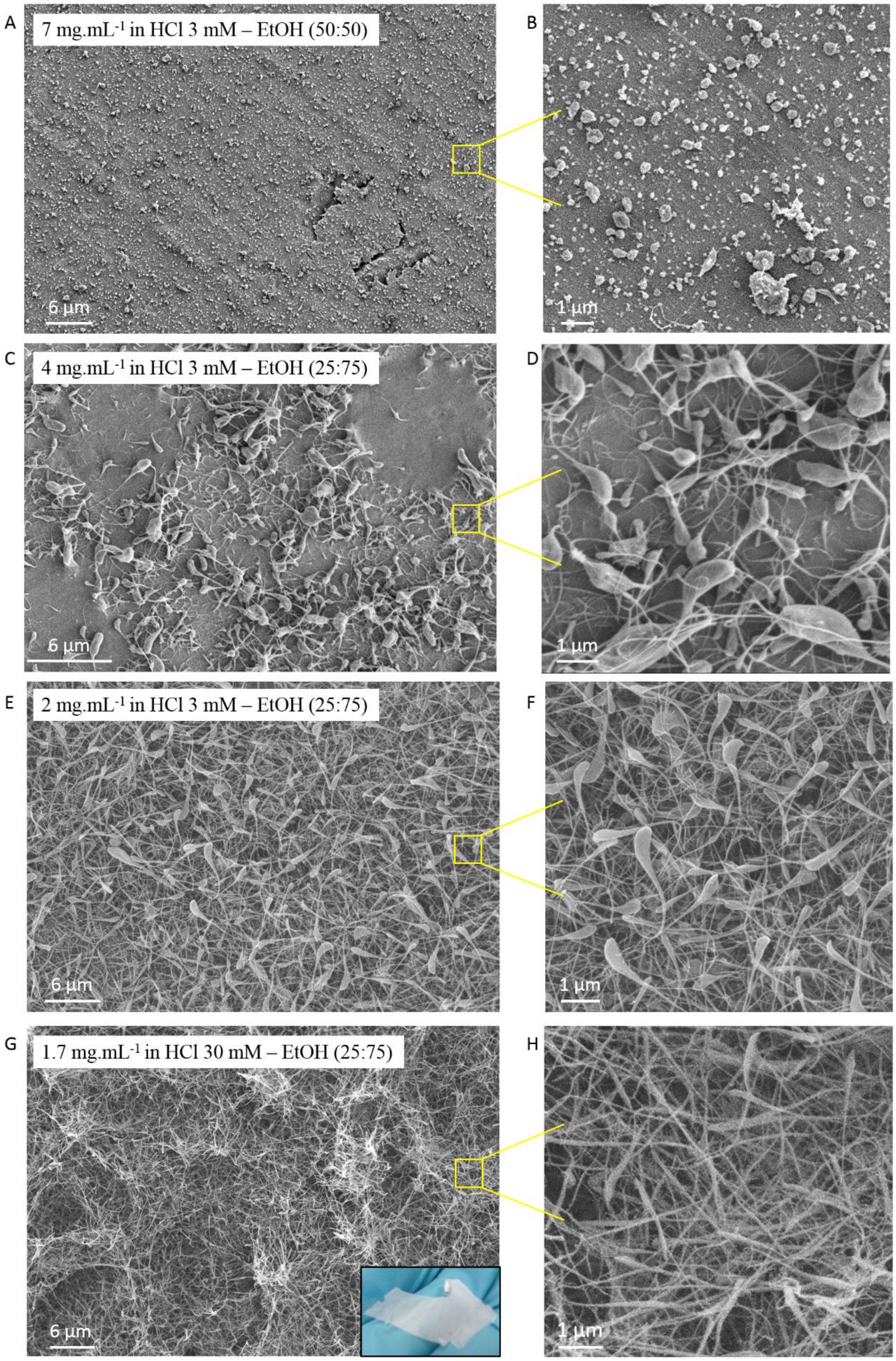

Figure V-3 : SEM photos of electrospun collagen (A-H) with the tested conditions. Insert: image of self-supported ES membrane.

After ES for at least 4 h accumulation we obtained a self-supported membrane (Figure V-3-insert). The longer the accumulation last, the thicker is the membrane and the easier it is to peel it off the copper support. Typically, the ES membranes have a thickness of 40 µm. Thicker membranes could not be obtained with this set up, since the growing collagen membrane turns the collector into an insulating material. The recovered membranes are opaque because of strong light scattering by the fibrous network. Fibers create a homogeneous mattress. Their diameter is 58 ± 10 nm, i.e. with quite low size polydispersity, in agreement with the results already reported in the literature.[27,29]

Our first objective consisting in obtaining a self-supported, homogeneous fibrillar scaffold has therefore been achieved. In a second step, we investigated whether the ES has preserved the ternary structure of the protein or induced denaturation.

3. Investigating the native structure of collagen by circular dichroism (CD)

3.1. Principle

Collagen structure may be subjected to damages due to the ES process, in particular because of the high electrical field (10-20 kV)[39,40] and the high EtOH content. The polymer is subjected to very high shear forces and strain rates (in the order of 100 s^{-1}) acting during the ES process, which could induce conformational changes and modify the native folding of collagen.[39,40]

In type I collagen, the presence of numerous glycine amino acids along the chains allows the three left-handed helices to associate to form a right-handed triple helix that is stabilized by hydrogen bonds. The triple helix has a length of 300 nm and a diameter of approximately 1.5 nm.

Circular dichroism (CD) is a very powerful method for rapidly characterizing the secondary structure and folding of proteins. This phenomenon was discovered by Jean-Baptiste Biot, Augustin Fresnel and Aimé Cotton in the first half of the 19th century.[49] CD is described as the difference of absorption of left-handed and right-handed circularly polarized light by chiral molecules. Plane polarized light is split into the left handed and right handed components by passage through a modulator subjected to an alternating electric field. The CD spectrum is obtained when the dichroism is measured as a function of wavelength in a spectropolarimeter. When left handed and right handed lights are absorbed to different extents, the resulting radiation is said to possess elliptical polarization.[50]

3.2. CD results

In this study, Synchrotron-radiation circular dichroism (SRCD) has been used to investigate the spectral signature of electrospun collagen. These experiments have been performed at Soleil synchrotron with the collaboration of Frank Wien as beam scientist. Unlike conventional CD, the high light flux produced at Soleil enables accurate observations of electronic transitions down to wavelengths as low as 170 nm, thereby providing spectra with higher information content and better signal-to-noise ratios compared to common laboratory equipment.

In a first step, an ES membrane was solubilized in hydrochloric acid 3 mM to get access to the molecular state of collagen. We can then directly compare this electrospun collagen to the initial one obtained after extraction and purification (Figure V-4-A). The corresponding spectrum (Figure V-4-A-plain line) shows a large negative band at 198 nm and a small positive one at 223 nm, which correspond to the spectral signature of the collagen triple helix, hence of native collagen. Indeed it is the same signature as the initial collagen molecules in HCl 3 mM (Figure V-4-A-dotted line).

In addition, collagen thermal denaturation has then been monitored by increasing temperature from 20°C to 71°C in steps of 3°C, inducing a breaking of the weak bonds like hydrogen bonds and a loss of the characteristic triple helix structure of the collagen. As expected, the intensity of both bands decreases with increasing temperature (Figure V-4-B-from dark blue to dark red). At the end of the denaturation process a single negative band is observed of lower molar ellipticity and slightly red-shifted compared to the spectral signature of pure collagen at 20°C. This is characteristic of random conformation of the α-chains and corresponds to the gelatin signature.

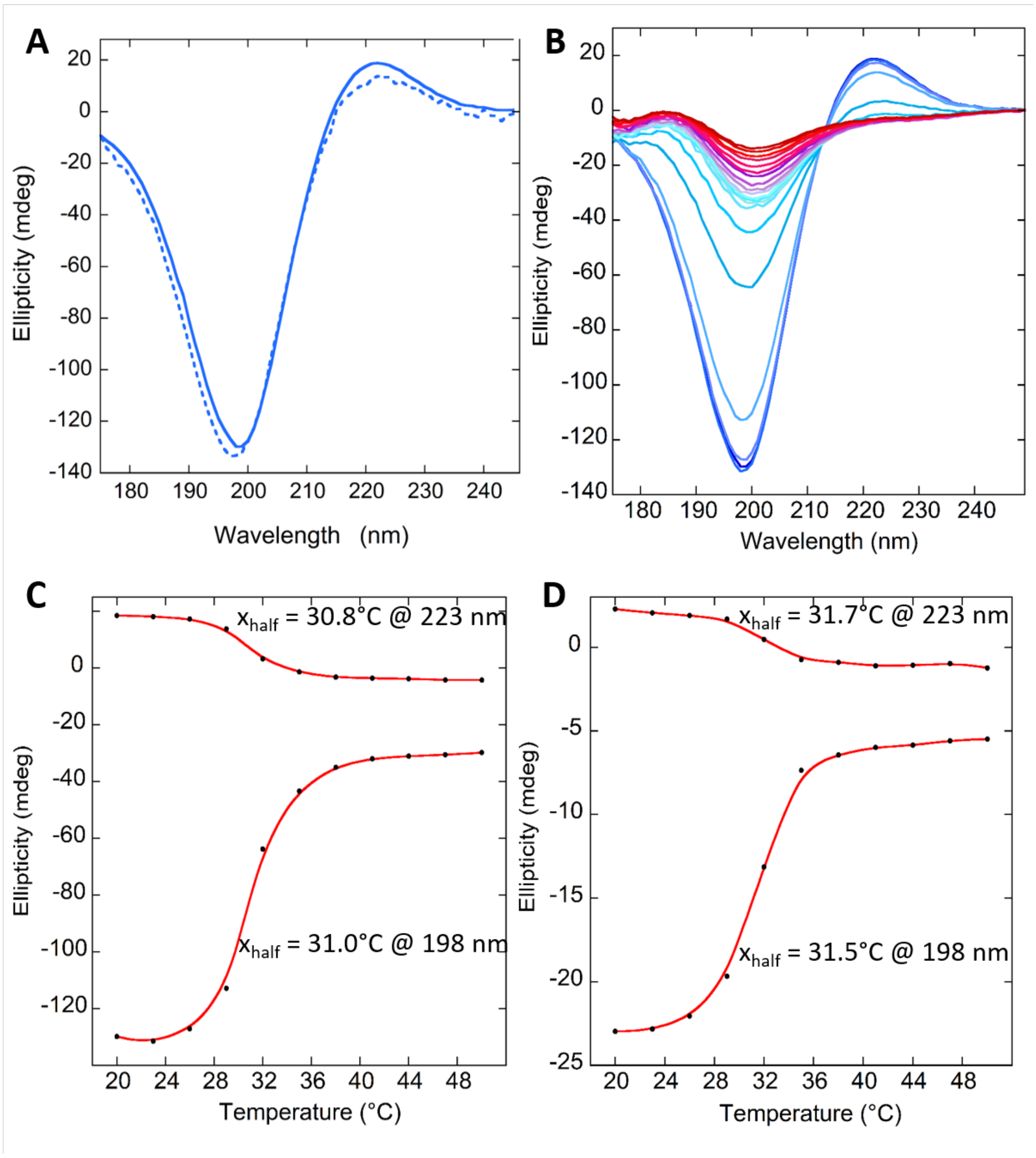

Figure V-4 : SRCD of collagen. (A) SRCD spectra of ES collagen (plain line) and native collagen at 2 mg.mL^{-1} (dotted line) in HCl 3 mM at 20°C. (B) SRCD spectra of thermal unfolding of ES collagen at temperatures ranging from 20 to 71°C in steps of 3°C. (C-D) Evolution of the ellipticity as a function of temperature: melting temperature at 198 and 223 nm for ES and native collagen respectively.

From this experiment, the melting temperature can be determined by plotting the ellipticity at 198 nm and 223 nm as a function of temperature. After ES, collagen melting temperature was found to be around 31°C (31°C at 198 nm and 30.8°C at 223 nm, Figure V-4-C), in agreement with previously reported values for native collagen.[29] The same experiments were performed from native collagen in HCl at 3 mM as obtained after extraction and purification and before ES. In this case, similar melting temperatures could be measured

(31.5 and 31.7°C at 198 and 223 nm respectively, Figure V-4-D). This demonstrates that the collagen was not denatured by the ES process and kept all the characteristics of its native structure.

Based on these encouraging results, we went a step further into the design of an ES membrane that could be useful for biological applications. A first requisite is to achieve the rehydration of the collagen network while preserving its structure. As pointed out earlier, this requires either a cross-linking reaction or the induction of collagen fibrillogenesis by a pH increase, the later having the benefits of better preserving the physical, chemical and biological properties of the protein.

4. Characterizing the collagen structure within the membrane

4.1. Stabilization of the membrane

During ES, the solvent HCl/EtOH evaporates and a dry matrix of collagen fibers is created (Figure V-5-B-C). At this point, the membrane is not stable enough to be hydrated.[47,48] To increase the pH we choose to expose the electrospun membrane to NH_3 vapors (Figure V-5-D). After this treatment, the membrane could be immersed into cell culture medium (details in experimental methods) for further biological evaluations (Figure V-5-E).

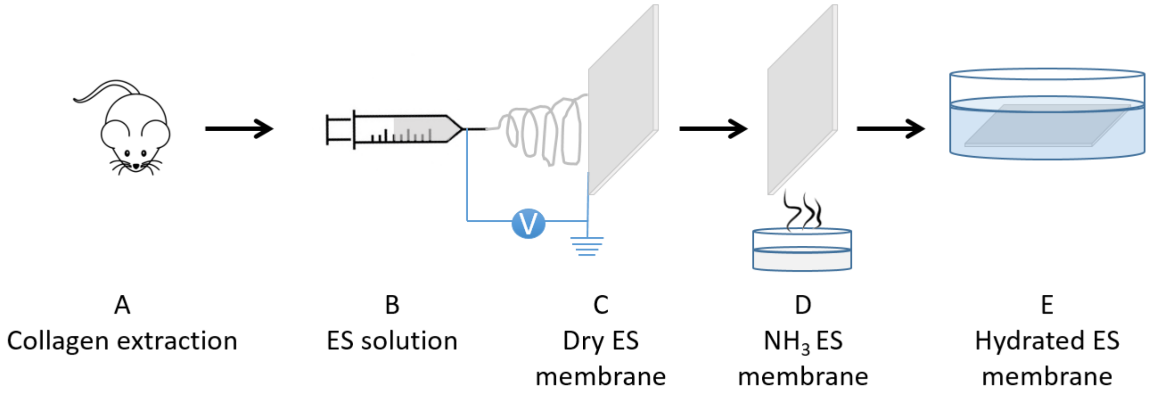

Figure V-5 : Process from A) collagen extraction, B) preparation of the ES solution, C) ES of a dry matrix, D) Stabilzation by NH_3 vapor exposure and E) membrane hydration.

4.2. Multi-photon microscopy based on second-harmonic generation (SHG)

4.2.1. SHG principle

SHG microscopy is a powerful technique to image tissue structure.[51] SHG is a coherent non-linear process that consist in two photons with the same frequency interacting with a material in a focal volume. The photons are combined to generate a new photon with twice the energy of the initial photons (or twice the frequency).[52,53] This signal intensity is then proportional to the square of the density of the molecules generating the harmonic response. This technique is highly specific for non-centrosymmetric media.[54–58]

The SHG process is due to the interaction of an electromagnetic wave with a molecular bond or a molecule. At this molecular scale, the wave induces an oscillation of the electrons in the matter. If molecules are excited with a radiation of frequency ω there are two possibilities. If it is a symmetrical molecule, the frequency of the excitation radiations is equal to that of the scattered radiation: this is the Rayleigh scattering (Figure V-6-A).

Figure V-6 : Schematic representation of the excitation of molecules with a radiation of frequency ω while exciting A) a symmetrical molecule, B) a non-centrosymmetric molecule, C) two parallel non-centrosymmetric molecules and D) two antiparallel non-centrosymmetric molecules (Adapted from [59,60]).

If the molecule is non-centrosymmetric, there is still the Rayleigh scattering but also generation of harmonic scattering (double frequency radiation: 2ω) at high excitation intensity (Figure V-6-B). In this case, if the radiation crosses the path of two molecules we have constructive interferences of the radiations at the double frequency 2ω if the two non-centrosymmetric molecules are parallel (Figure V-6-C). In the contrary, for two non-centrosymmetric antiparallel molecules, the radiation is in phase opposition and there is destructive interference with zero scattering intensity (Figure V-6-D). As a result, the SHG signal is dependent on the number of parallel non-centrosymmetric molecules and of their 3D organization in the focal volume.

SHG radiation is coherently amplified in highly anisotropic fibrillar collagen because of the tight alignment of peptide bonds along the collagen triple helix and within fibrils (Figure V-7).[61] At the molecular level, the SHG signal of collagen comes from the peptide bond, which gives the non-centrosymmetric character to collagen. This is the principal harmonophore in the tissue. Accordingly, type I fibrillar collagen exhibits strong endogenous SHG signals without the addition of exogenous labels resulting in highly contrasted images.[62] On the contrary, type IV non-fibrillar collagen, which is organized as a loose centrosymmetrical network in basal membranes, does not exhibit any SHG signal because of destructive interferences.[58,63] SHG microscopy is therefore considered as a sensitive structural probe of the macromolecular organization of collagen, and it has emerged as the gold standard technique for 3D characterization of collagen-rich biomimetic tissues.

Figure V-7 : Scheme of the hierarchical organization of collagen. The SHG signal from the peptide bond, harmonophore of collagen, depends of the 3D organization of the collagen fibrils. Adapted from[64].

4.2.2. Polarization-resolved SHG (P-SHG) principle

The Polarization-resolved SHG (P-SHG) allows to assess the three-dimensional mean orientation of collagen in the membrane. P-SHG consists in exciting the sample with a linearly polarized beam, which ɵ angle is constantly varied from 0° to 360° with a 10° step. A polarimetric diagram can be obtained indicating the intensity of SHG for each polarization. Each color codes for the orientation of the collagen triple helices in the focal volume for each polarization.

Figure V-8 : P-SHG principle. A) Excitation with a linear polarization with different angle Ɵ. B) Intensity diagram, adapted from [64].

4.2.3. SHG characterization of the ES membrane

We performed the SHG measurements in collaboration with Marie-Claire Schanne-Klein, at the Laboratory for Optics and Bioscience at the Ecole Polytechnique. The electrospun matrics were characterized by SHG microscopy at the different stages of preparation: A-dry membrane, B- after stabilization by NH_3 vapor and C- after immersion in cell culture medium (Figure V-9).

The dry ES membrane presents a very high SHG signal (Figure V-9-A1). This is indicative of the native state of collagen with a non-centrosymmetric packing of the triple helices. At this stage, it remains difficult to know whether collagen is fibrillated or not, as SHG is also observed in crystal liquid phases.[62] In addition, the grainy-like profile with a myriad of dots indicates the presence of small structures that may be highly entangled, in agreement with the previous SEM images (see below).

Polarized SHG was performed in order to get quantitative information on the orientational order of collagen distribution within the focal volume. The dry membrane presents a high P-SHG signal and we can observe a colored map made of numerous dots (Figure V-9-A2). Each color coding for a direction, this multicolored cartography of dots shows that the highly packed structures of native collagen are randomly distributed with respect to one another. This supports our previous assumption that the matrix is made of highly entangled structures of small diameters. Figure V-10 schematically represents such a fibrillar network as observed by SHG (Figure V-10-A). While imaging the network with P-SHG, each fiber is coded with a unique color given that all molecules within a fiber are oriented in the same direction (Figure V-10-B). However, if the diameter of the fibers is small relatively to the focal volume, many fibers are simultaneously observed in one pixel. At their intersection point, molecules in the focal volume are not all oriented in the same direction anymore, which leads to a local strong decrease in SHG intensity (Figure V-10-C). Furthermore, if the network is highly entangled, SHG decrease is widespread throughout the focal volume leading to a grainy-like pattern.

We then studied the NH_3-treated membranes (Figure V-9-B1-B2). The images were similar to that of dry membranes, exhibiting a grainy-like pattern but the network appeared more compact and, on the P-SHG map, the individual colored domains looked smaller.

Thanks to NH_3 vapor exposure, stable hydrated membranes could be obtained and major modifications of their structure were observed by SHG (Figure V-9-C1). Large micrometer-long structures reminiscent of collagen fibers could be visualized that appear well-aligned and generate a strong SHG signal. Very interestingly, each fiber is encoded by a unique color in P-SHG observations, indicating that collagen molecules are all oriented in the same direction within a given fiber. The large size of the collagen assemblies should prevent the observation of multiple fibers within the focal volume, hence precluding significant local decrease in SHG intensity.

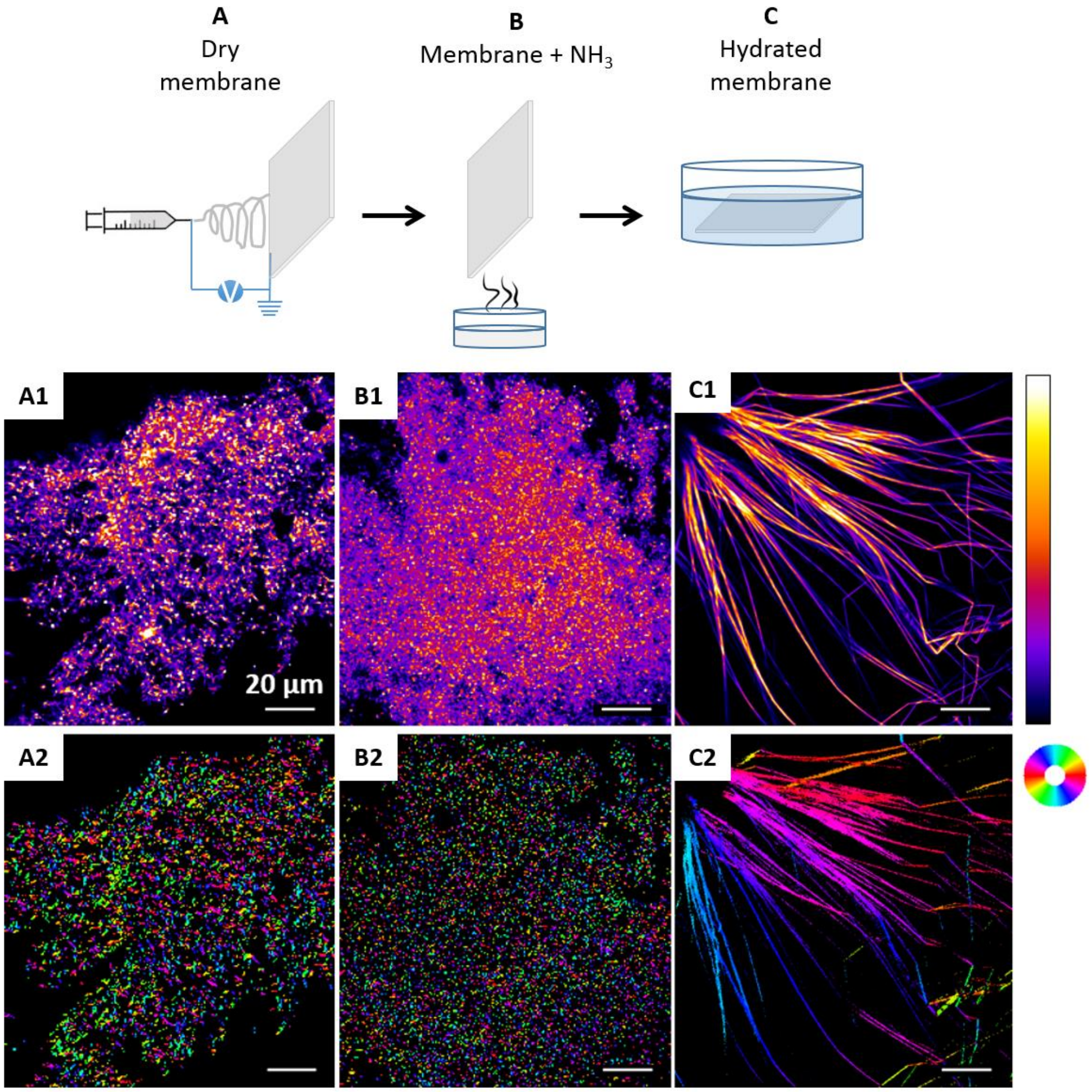

Figure V-9 : Schematic representation and SHG images of the different steps of the protocol: A) dry membrane, B) membrane post NH$_3$ treatment and C) hydrated membrane by (1) analyses of the SHG intensity in the plan or (2) by circular polarization.

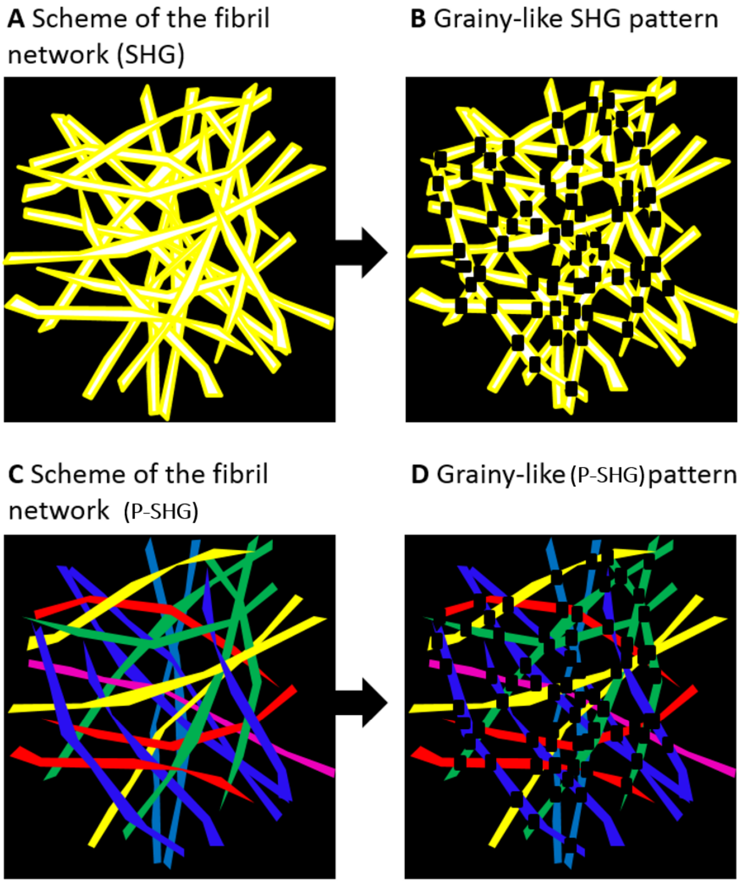

Figure V-10 : Scheme of (A,C) the network (for SHG and P-SHG) and of (C,D) the SHG and P-SHG observations showing local strong decreases in P-SHG intensities at the intersection of collagen fibers.

4.3. CryoSEM-FEG observations

4.3.1. Investigation of the ES membrane

To characterize the membrane at a lower scale we studied them by cryoSEM-FEG. Observing the sample after freezing in liquid nitrogen (-120°C) allows to preserve the hydrated state of the sample without any chemical modification, getting rid of any drying artefact that would induce changes in the collagen structure (e.g. collapse or shrinkage of the structure).

On Figure V-11-A1, A2 and A3, we can see cryoSEM-FEG images of the dry membrane, NH_3 membrane and hydrated membrane. As expected, a fibrous structure is visible for the dry membrane that is similar to that observed using conventional SEM. After the ammonia vapor treatment, fibers start to merge, but we can still distinguish the mesh and the global structure of the network, which is similar in size and entanglement. Very interestingly, after hydration in the culture medium, the typical banding pattern of fibrillated collagen within living tissues, with a periodicity of 67 nm (the D-band), is clearly visible. This again confirms the native state of collagen within ES membranes and ascertains the possibility to recover the self-assembling processes and hierarchical organization of collagen. To our knowledge, this is the very first time that such organization could be obtained and characterized after ES processing of pure collagen solutions. Those cryoSEM-FEG images are consistent with the SHG measurements. They confirmed that the NH_3-treatment had a minor influence on collagen organization, while fibrillation was indeed completed after immersion in culture medium.

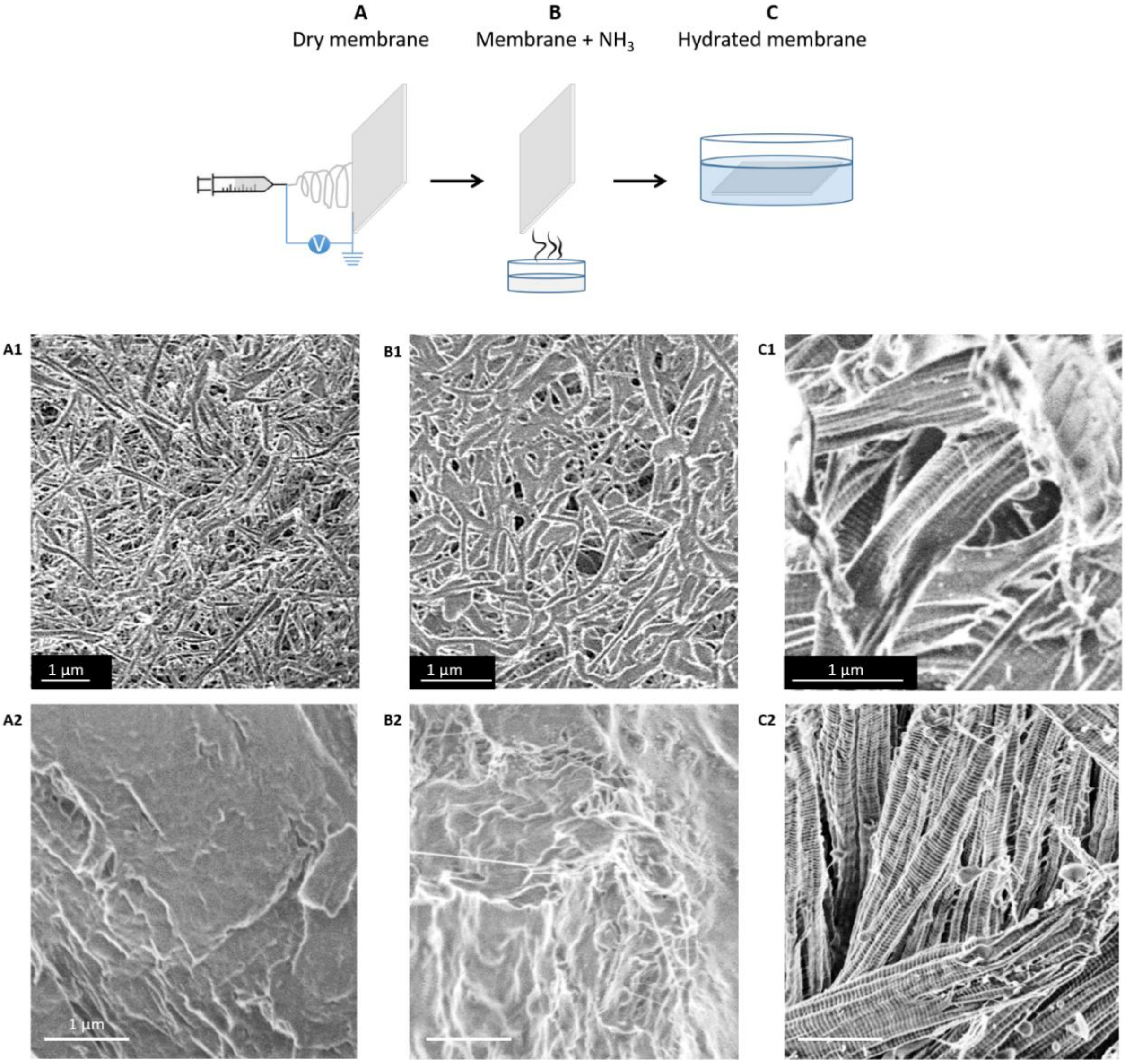

Figure V-11 : Schematic representation and cryoSEM-FEG images of the different steps of the protocol: A) dry membrane, B) stabilized membrane post NH_3 exposure and C) hydrated membrane for the (1) electrospun matrix and the (2) casted membrane.

4.3.2. Investigation of a casted membrane

To compare the structure and properties of ES membranes with more common forms of collagen materials, we prepared casted membranes simply by pouring a collagen solution into a silicon mold and letting the solvent to evaporate in ambient conditions.

The casted membranes were obtained with the same solvent and the same concentration than the ES membrane (HCl 30 mM -EtOH, 25-75% 1.7 mg.mL-1). However, it has to keep in mind that the final amount of collagen within the two types of membrane is not necessarily the same since it is hard to control the amount of collagen effectively deposited on the ES collector. The casted membranes were then treated following the same protocols as ES ones (NH_3 vapor exposure for 20 min and hydration in cell medium for the same duration). We analyzed the casted membrane by cryoSEM-FEG at each step, as we did for the electrospun matrix (Figure V-11-A2, B2, C2). This time no fiber is visible on the dry membrane and the NH_3-treated membrane. The surface is smooth and homogeneous. This casted membrane is very dense and does not exhibit any fiber, porosity and 3D entanglement. However, when the membrane is hydrated in cell culture medium, collagen molecules self-assembled into fibrils. The typical banding pattern of fibrillated collagen within living tissues is again visible. We can notice that collagen fibrils seem in higher density and with a better alignment with respect of each other than in the ES membrane but this should be further confirmed. In this context, we have initiated oriented linear dichroism (OLD) studies on the SRCD beamline at Soleil. This could provide information about the organization of the triple helices with respect to each other within the solid membrane. Some preliminary data have already been obtained on the casted membranes that are presented in the Appendix -3 and new runs are already planned at Soleil at the end of September 2018.

At this stage, the outcome of this initial morphological comparison between electrospun and casted membranes after fibrillation may appear rather disappointing as it is not clear to what extent the initial fibrous organization of the ES structure is preserved within the final hydrated scaffold. However, since our final objective is to design scaffolds for tissue engineering the most relevant validation of our approach must be based on the cell response to the various materials.

5. Cell adhesion on the different matrices

In a preliminary study, thanks to the help of C. Hélary (LCMCP), we investigated the adhesion and spreading of Normal Human Dermal Fibroblast cells (NHDF) on the ES and casted membranes. NHDFs were simultaneously cultured for 24 h on a triplicate of both matrices. This experiment was reproduced twice.

In the first set of experiments, cells were presenting a surface area of around 4200 µm² on ES scaffold *versus ca*. 3000 µm² on the casted membrane (Figure V-12-A-D) indicating a better cell spreading on the ES membrane. However, in a second experiment, the opposite tendency was observed: a surface area of *ca.* 2000 µm² on the ES scaffold, and 3500 µm² on the casted membrane. In this second experiment, the number of cells after 24 h on the two membranes was not statistically different (Figure V-12-E).

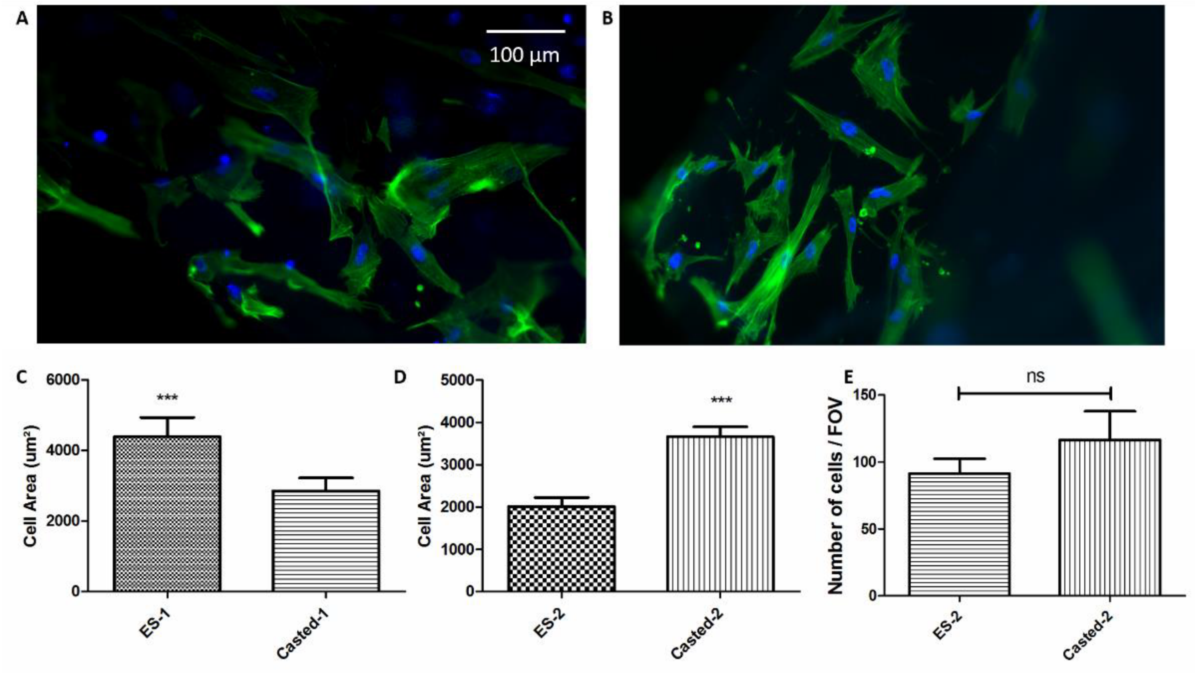

Figure V-12 : Representative fluorescence microscopy images of NHDF cells cultured for 24 h and stained for actin (phalloidin) and nucleus (DAPI) A) on ES or B) casted membranes. Cell morphologies on the different PA layers are compared by measuring the projected cell area on C) experience 1 and D) experience 2 and E) the number of cells by Field of View (FOV). The column represents Mean with SEM. Statistical test using Mann-Whitney non parametric test; each condition from three independent experiments.

No clear conclusion can be drawn from those experiments. Fibroblasts do not seem to attach and spread more on ES or casted membrane (Figure V-12-C-D). We noticed that, when the two sets of experiments are compared, the measured cell area for casted membranes are quite consistent whereas those obtained for ES scaffolds vary by a factor of two. As pointed out earlier, it is difficult to control the final amount of collagen that reaches the collector. Thus even if the initial concentration is the same, the casted membranes may be denser in collagen or thicker, modifying the mechanical properties, which can impact cell behavior independently of the membrane structure by itself. Moreover, it makes it difficult to prepare a relevant control casted membrane, i.e. that contains the same collagen amount.

6. Conclusion and perspectives

Electrospinning is an interesting process to create scaffolds for tissue engineering. In this field, the challenge is to design materials which are easy to process, non-cytotoxic and that combine the mechanical and cellular functions of a tissue. ES creates a variety of fibrous scaffolds with tunable porosity, fiber diameter and orientation. Applying this technique to collagen, the most abundant protein in human ECMs, is ideal to mimic the entangled fibrillar structure of our tissues.

The first objective was to find the best conditions to electrospin collagen to create long and homogeneous fibers, while preserving the native state of the protein. SRCD, SHG and cryo-SEM-FEG show that we have successfully (1) ES collagen to obtain a self-supported membrane; (2) preserved its native state; (3) stabilized the membrane in a hydrated state and (4) reproduced fibrillation as observed in living tissues.

Neither cryo-SEM-FEG imaging nor preliminary cell experiments allowed to evidence a clear difference between hydrated ES matrices and casted collagen membranes. However, the modularity of the ES process will allow to tune the porosity, fiber size, and to control the alignment of the network, in a much easier way than following a casting approach. Of particular interest is the creation of aligned fibers (see Chapter IV). The most popular option is to use a collector placed on a rotating mandrel.[13–15] Our first attempts were not successful but they were performed with a horizontal set up while using a vertical syringe could help by decreasing the effect of gravity. As a further step, the possibility to incorporate the silica nanoparticles earlier described within the ES membranes will have to be studied. ES is a major asset to produce a homogeneous bionanocomposite, not accessible by the casted-method.

7. Experimental methods

7.1. Electrospinning process

Collagen self-supported membranes were obtained by ES. A collagen solution was prepared at a concentration of 1.7 mg.mL^{-1} in HCl 30 mM and EtOH (25:75, v:v). Extrusion was realized at 0.005 mL.min^{-1} in an isolated box flushed with dry air, from a 5 mL syringe with a blunt needle. The grounded collector is a copper rectangle tape of *ca*. 2.5 cm by 1.5 cm large on the center of a fixed Teflon support placed at 9 cm from the tip of the needle. A high voltage of *ca.* 12-16 kV was applied by a voltage regulated DC power supply (Electrospinz, LTD) to generate the polymer jet. Voltage was adjusted to have a stable jet. Collecting lasts 4 h and the matrices were allowed to dry out at RT overnight.

7.2. Collagen casted membranes

Collagen casted membranes were obtained by pouring collagen solution at 1.7 mg.mL^{-1} in HCl 30 mM and EtOH (25:75, v:v) in a silicon mold and then evaporating the solvent.

7.3. Stabilization and hydration of the membrane

To get the stabilized membranes for hydration, membranes were detached from the support and exposed to NH_3 vapor for 20 min in a desiccator. The membranes were then immersed into cell culture medium. The medium was changed three times a day for 10 days to remove ammonium.

7.4. Scanning electron microscopy (SEM)

ES membranes were fixed on a carbon tape and coated with 10 nm of gold using a gold plasma coater. Imaging was performed using a Hitachi S-3400N SEM operating at 10 kV.

7.5. CryoSEM-FEG

The cryoSEM-FEG observations were performed at the platform “Institut de Biologie Paris-Seine” (IBPS) by V. Bazin, A. Canette, G. Frebourg and M. Trichet. The samples were placed between two holders, a tissue tech for the dry and stabilized membrane to help them to stick to the holders. The samples were frozen in liquid nitrogen at −195°C, and then transferred to the preparation chamber. No coating was applied on the samples. Cryo-fractionation was performed in the preparation chamber at −180°C. Cryo-fractionation allows observation of the internal organization of the membranes. Then, SEM observations were performed at −120°C at low voltage (0.790 kV) using a secondary electron (SE) detector (GeminiSEM 500, Zeiss,VCT100, Leica). A subblimation step at −90°C was applied for 15 min in the SEM chamber to remove the ice layer formed on the surface of the sample.

7.6. Second Harmonic Generation (SHG) Microscopy

SHG was carried out at the Ecole Polytechnique in the Laboratory for Optics and Biosciences by Marie-Claire Schanne-Klein, with a laser scanning microscope. The excitation is provided by a femto-second titanium-sapphire laser (Mai-Tai, Spectra-Physics) set at 860 nm. A circular polarization was used to image all the structures independently from their orientation in the focal plane or a linear polarization was used for P-SHG. The collagen membrane imaging was performed using a 25 x objective lens with lateral resolution of 0.4 µm and an axial resolution of 1.7 µm.

– Forward SHG: transmission (1 Semrock 680SP + 1 Semrock 720SP + 1 Semrock 427/10)

– Backward SHG: epidetection (1 Semrock 680SP + 1 Semrock 720SP + 1 Semrock 427/10)

The polarization was changed from 0° to 360° with a 10° step. Fine plane by plane images sampling was performed every micron over the first 50 µm from the membrane surface and then, every 10 µm until reaching the membrane center. Three areas were observed in order to check for the sample structure homogeneity.

7.7. Circular Dichroism Spectroscopy

Synchrotron-radiation circular dichroism (SRDC) spectroscopy was carry out at Soleil synchrotron on DISCO beamline with the collaboration of Frank Wien as beam scientist. The membrane was placed between quartz supports for SRCD measurements (0.5 mm path length). ES membranes were dissolved in chlorhydric acid HCl (3 mM). Spectra were recorded from 170 to 250 nm. Collagen denaturation has then been monitored by increasing temperature from 10°C to 71°C by step of 3°C.

7.8. Cell culture

Normal Human Dermal Fibroblasts (NHDF) were maintained in growth medium containing Dulbecco's Modified Eagle's Medium (DMEM), supplemented with 10% fetal bovine serum (FBS) 1% glutamax, 1% fungizone and 1% penicillin-streptomycin (P/S). The cells were grown in 75 mm² flasks (BD Falcon) and passaged every three days. All culture reagents were purchased from Gibco. For cell morphology experiments on membranes, fibroblasts were seeded at a low density (50 k cells per well) in order to minimize cell–cell contacts, but for the cell number by FOV they were seeded at 200 K cells per well. Cells were incubated at 37°C and 5% CO_2 for 24 h on the membranes fixed to silicon support by needles.

7.9. Fluorescence staining

Cells were fixed with 4% paraformaldehyde in PBS and 1 mM $CaCl_2$ for 30 min at RT. For immunostaining, fixed samples were first permeabilized with 0.1% Triton X-100 in PBS (5 min, RT). Actin filaments were fluorescently labeled with AlexaFluor-488-conjugated phalloidin (Life

Technologies; 1:200 dilutions, 1 h at RT) for visualization. Cell nuclei were counterstained with DAPI (Life Technologies).

7.10. Image acquisition and analysis

Images of fluorescently labeled samples were obtained using a fluorescence microscope (Axio Imager D.1, Zeiss). Cell morphology was quantified from phalloidin stained fluorescent images acquired by a 10× objective from randomly selected regions on the coverslip. Acquired grayscale images were background subtracted and thresholded to convert into binary images using ImageJ software.

7.11. Statistical Analysis

Statistical analysis was performed using Graphpad Prism v.6 software. Analysis were performed using a Mann-Whitney non parametric test; each condition was tested from three independent experiments. Values in graphs are the mean and standard error of mean (SEM).

8. References

(1) Huang, Z.-M.; Zhang, Y.-Z.; Kotaki, M.; Ramakrishna, S. A Review on Polymer Nanofibers by Electrospinning and Their Applications in Nanocomposites. *Composites Science and Technology* **2003**, *63* (15), 2223–2253.

(2) Teo, W. E.; Ramakrishna, S. A Review on Electrospinning Design and Nanofibre Assemblies. *Nanotechnology* **2006**, *17* (14), 89–106.

(3) Deitzel, J. .; Kleinmeyer, J.; Harris, D.; Beck Tan, N. . The Effect of Processing Variables on the Morphology of Electrospun Nanofibers and Textiles. *Polymer* **2001**, *42* (1), 261–272.

(4) McKee, M. G. Phospholipid Nonwoven Electrospun Membranes. *Science* **2006**, *311* (5759), 353–355.

(5) Haghi, A. K.; Akbari, M. Trends in Electrospinning of Natural Nanofibers. *physica status solidi (a)* **2007**, *204* (6), 1830–1834.

(6) Maneeratana, V.; Bass, J. D.; Azaïs, T.; Patissier, A.; Vallé, K.; Maréchal, M.; Gebel, G.; Laberty-Robert, C.; Sanchez, C. Fractal Inorganic−Organic Interfaces in Hybrid Membranes for Efficient Proton Transport. *Advanced Functional Materials* **2013**, *23* (22), 2872–2880.

(7) Dos Santos, L.; Rose, S.; Sel, O.; Maréchal, M.; Perrot, H.; Laberty-Robert, C. Electrospinning a Versatile Tool for Designing Hybrid Proton Conductive Membrane. *Journal of Membrane Science* **2016**, *513*, 12–19.

(8) Bhardwaj, N.; Kundu, S. C. Electrospinning: A Fascinating Fiber Fabrication Technique. *Biotechnology Advances* **2010**, *28* (3), 325–347.

(9) Luu, Y. K.; Kim, K.; Hsiao, B. S.; Chu, B.; Hadjiargyrou, M. Development of a Nanostructured DNA Delivery Scaffold via Electrospinning of PLGA and PLA–PEG Block Copolymers. *Journal of Controlled Release* **2003**, *89* (2), 341–353.

(10) Subbiah, T.; Bhat, G. S.; Tock, R. W.; Parameswaran, S.; Ramkumar, S. S. Electrospinning of Nanofibers. *Journal of Applied Polymer Science* **2005**, *96* (2), 557–569.

(11) Ramakrishna, S.; Fujihara, K.; Teo, W.-E.; Yong, T.; Ma, Z.; Ramaseshan, R. Electrospun Nanofibers: Solving Global Issues. *Materials Today* **2006**, *9* (3), 40–50.

(12) Welle, A.; Kröger, M.; Döring, M.; Niederer, K.; Pindel, E.; Chronakis, I. S. Electrospun Aliphatic Polycarbonates as Tailored Tissue Scaffold Materials. *Biomaterials* **2007**, *28* (13), 2211–2219.

(13) Yang, F.; Murugan, R.; Wang, S.; Ramakrishna, S. Electrospinning of Nano/micro Scale Poly(l-Lactic Acid) Aligned Fibers and Their Potential in Neural Tissue Engineering. *Biomaterials* **2005**, *26* (15), 2603–2610.

(14) Xia, H.; Xia, Y. An in Vitro Study of Non-Aligned or Aligned Electrospun Poly(methyl Methacrylate) Nanofibers as Primary Rat Astrocytes-Loading Scaffold. *Materials Science and Engineering: C* **2018**, *91*, 228–235.

(15) Jalili, R.; Morshed, M.; Ravandi, S. A. H. Fundamental Parameters Affecting Electrospinning of PAN Nanofibers as Uniaxially Aligned Fibers. *Journal of Applied Polymer Science* **2006**, *101* (6), 4350–4357.

(16) Liang, D.; Hsiao, B. S.; Chu, B. Functional Electrospun Nanofibrous Scaffolds for Biomedical Applications. *Advanced Drug Delivery Reviews* **2007**, *59* (14), 1392–1412.

(17) Wang, X.; Ding, B.; Li, B. Biomimetic Electrospun Nanofibrous Structures for Tissue Engineering. *Materials Today* **2013**, *16* (6), 229–241.

(18) Stankus, J. J.; Guan, J.; Wagner, W. R. Fabrication of Biodegradable Elastomeric Scaffolds with Sub-Micron Morphologies. *Journal of Biomedical Materials Research* **2004**, *70A* (4), 603–614.

(19) Ohgo, K.; Zhao, C.; Kobayashi, M.; Asakura, T. Preparation of Non-Woven Nanofibers of Bombyx Mori Silk, Samia Cynthia Ricini Silk and Recombinant Hybrid Silk with Electrospinning Method. *Polymer* **2003**, *44* (3), 841–846.

(20) Min, B.-M.; Jeong, L.; Nam, Y. S.; Kim, J.-M.; Kim, J. Y.; Park, W. H. Formation of Silk Fibroin Matrices with Different Texture and Its Cellular Response to Normal Human Keratinocytes. *International Journal of Biological Macromolecules* **2004**, *34* (5), 223–230.

(21) Min, B.-M.; Lee, G.; Kim, S. H.; Nam, Y. S.; Lee, T. S.; Park, W. H. Electrospinning of Silk Fibroin Nanofibers and Its Effect on the Adhesion and Spreading of Normal Human Keratinocytes and Fibroblasts in Vitro. *Biomaterials* **2004**, *25* (7-8), 1289–1297.

(22) Zarkoob, S.; Eby, R. .; Reneker, D. H.; Hudson, S. D.; Ertley, D.; Adams, W. W. Structure and Morphology of Electrospun Silk Nanofibers. *Polymer* **2004**, *45* (11), 3973–3977.

(23) Alessandrino, A.; Marelli, B.; Arosio, C.; Fare, S.; Tanzi, M. C.; Freddi, G. Electrospun Silk Fibroin Mats for Tissue Engineering. *Engineering in Life Sciences* **2008**, *8* (3), 219–225.

(24) Um, I. C.; Fang, D.; Hsiao, B. S.; Okamoto, A.; Chu, B. Electro-Spinning and Electro-Blowing of Hyaluronic Acid. *Biomacromolecules* **2004**, *5* (4), 1428–1436.

(25) Ma, Z.; Kotaki, M.; Ramakrishna, S. Electrospun Cellulose Nanofiber as Affinity Membrane. *Journal of Membrane Science* **2005**, *265* (1-2), 115–123.

(26) Chen, Z.; Mo, X.; Qing, F. Electrospinning of Collagen–chitosan Complex. *Materials Letters* **2007**, *61* (16), 3490–3494.

(27) Buttafoco, L.; Kolkman, N. G.; Engbers-Buijtenhuijs, P.; Poot, A. A.; Dijkstra, P. J.; Vermes, I.; Feijen, J. Electrospinning of Collagen and Elastin for Tissue Engineering Applications. *Biomaterials* **2006**, *27* (5), 724–734.

(28) Schoen, B.; Avrahami, R.; Baruch, L.; Efraim, Y.; Goldfracht, I.; Elul, O.; Davidov, T.; Gepstein, L.; Zussman, E.; Machluf, M. Electrospun Extracellular Matrix: Paving the Way to Tailor-Made Natural Scaffolds for Cardiac Tissue Regeneration. *Advanced Functional Materials* **2017**, *27* (34), 1700427, 1-9.

(29) Bürck, J.; Heissler, S.; Geckle, U.; Ardakani, M. F.; Schneider, R.; Ulrich, A. S.; Kazanci, M. Resemblance of Electrospun Collagen Nanofibers to Their Native Structure. *Langmuir* **2013**, *29* (5), 1562–1572.

(30) Dong, B.; Arnoult, O.; Smith, M. E.; Wnek, G. E. Electrospinning of Collagen Nanofiber Scaffolds from Benign Solvents. *Macromolecular Rapid Communications* **2009**, *30* (7), 539–542.

(31) Kitsara, M.; Joanne, P.; Boitard, S. E.; Ben Dhiab, I.; Poinard, B.; Menasché, P.; Gagnieu, C.; Forest, P.; Agbulut, O.; Chen, Y. Fabrication of Cardiac Patch by Using Electrospun Collagen Fibers. *Microelectronic Engineering* **2015**, *144*, 46–50.

(32) Matthews, J. A.; Wnek, G. E.; Simpson, D. G.; Bowlin, G. L. Electrospinning of Collagen Nanofibers. *Biomacromolecules* **2002**, *3* (2), 232–238.

(33) Li, M.; Mondrinos, M. J.; Gandhi, M. R.; Ko, F. K.; Weiss, A. S.; Lelkes, P. I. Electrospun Protein Fibers as Matrices for Tissue Engineering. *Biomaterials* **2005**, *26* (30), 5999–6008.

(34) Kwon, I. K.; Matsuda, T. Co-Electrospun Nanofiber Fabrics of Poly(L-lactide-co-E-caprolactone) with Type I Collagen or Heparin. *Biomacromolecules* **2005**, *6* (4), 2096–2105.

(35) Zhang, Y. Z.; Venugopal, J.; Huang, Z.-M.; Lim, C. T.; Ramakrishna, S. Characterization of the Surface Biocompatibility of the Electrospun PCL-Collagen Nanofibers Using Fibroblasts. *Biomacromolecules* **2005**, *6* (5), 2583–2589.

(36) Dror, Y.; Ziv, T.; Makarov, V.; Wolf, H.; Admon, A.; Zussman, E. Nanofibers Made of Globular Proteins. *Biomacromolecules* **2008**, *9* (10), 2749–2754.

(37) Bensusan, H. B.; Hoyt, B. L. The Effect of Various Parameters on the Rate of Formation of Fibers from Collagen Solutions [1]. *Journal of the American Chemical Society* **1958**, *80* (3), 719–724.

(38) Usha, R.; Maheshwari, R.; Dhathathreyan, A.; Ramasami, T. Structural Influence of Mono and Polyhydric Alcohols on the Stabilization of Collagen. *Colloids and Surfaces B: Biointerfaces* **2006**, *48* (2), 101–105.

(39) Zeugolis, D. I.; Khew, S. T.; Yew, E. S. Y.; Ekaputra, A. K.; Tong, Y. W.; Yung, L.-Y. L.; Hutmacher, D. W.; Sheppard, C.; Raghunath, M. Electro-Spinning of Pure Collagen

Nano-Fibres – Just an Expensive Way to Make Gelatin? *Biomaterials* **2008**, *29* (15), 2293–2305.

(40) Greenfeld, I.; Arinstein, A.; Fezzaa, K.; Rafailovich, M. H.; Zussman, E. Polymer Dynamics in Semidilute Solution during Electrospinning: A Simple Model and Experimental Observations. *Physical Review E* **2011**, *84* (4) 041806-1-9.

(41) Choktaweesap, N.; Arayanarakul, K.; Aht-Ong, D.; Meechaisue, C.; Supaphol, P. Electrospun Gelatin Fibers: Effect of Solvent System on Morphology and Fiber Diameters. *Polymer journal* **2007**, *39* (6), 622–631.

(42) Wan, Y.-Q.; He, J.-H.; Yu, J.-Y.; Wu, Y. Electrospinning of High-Molecule PEO Solution. *Journal of Applied Polymer Science* **2007**, *103* (6), 3840–3843.

(43) Besseau, L.; Giraud-Guille, M.-M. Stabilization of Fluid Cholesteric Phases of Collagen to Ordered Gelated Matrices. *Journal of Molecular Biology* **1995**, *251* (2), 197–202.

(44) Fong, H.; Chun, I.; Reneker, D. . Beaded Nanofibers Formed during Electrospinning. *Polymer* **1999**, *40* (16), 4585–4592.

(45) Magarvey, R. H.; Outhouse, L. E. Note on the Break-up of a Charged Liquid Jet. *Journal of Fluid Mechanics* **1962**, *13* (01), 151-157.

(46) Vollrath, F.; Edmonds, D. T. Modulation of the Mechanical Properties of Spider Silk by Coating with Water. *Nature* **1989**, *340*, 305–307.

(47) Jackson, D. S.; Fessler, J. . Isolation and Properties of a Collagen Soluble in Salt Solution at Neutral pH. *Nature* **1955**, *179*, 69–70.

(48) Gross, J.; Kirk, D. The Heat Precipitation of Collagen from Neutral Salt Solutions: Some Rate-Regulating Factors. *J Biol Chem* **1958**, *233* (2), 355–360.

(49) Lopes, J. L. S.; Miles, A. J.; Whitmore, L.; Wallace, B. A. Distinct Circular Dichroism Spectroscopic Signatures of Polyproline II and Unordered Secondary Structures: Applications in Secondary Structure Analyses: Polyproline II and Disordered CD Spectra. *Protein Science* **2014**, *23* (12), 1765–1772.

(50) Greenfield, N. J. Using Circular Dichroism Spectra to Estimate Protein Secondary Structure. *Nature Protocols* **2007**, *1* (6), 2876–2890.

(51) Pavone, F. S.; Campagnola, P. J. *Second Harmonic Generation Imaging*; CRC Press, 2013.

(52) Boyd, R. W. *Nonlinear Optics - Second Edition*; Academic press; Elsevier Science, 2003.

(53) Ustione, A.; Piston, D. W. A Simple Introduction to Multiphoton Microscopy: a simple introduction to Multiphoton Microsocpy. *Journal of Microscopy* **2011**, *243* (3), 221–226.

(54) Campagnola, P. J.; Millard, A. C.; Terasaki, M.; Hoppe, P. E.; Malone, C. J.; Mohler, W. A. Three-Dimensional High-Resolution Second-Harmonic Generation Imaging of Endogenous Structural Proteins in Biological Tissues. *Biophysical Journal* **2002**, 16, 493–508.

(55) Freund, I.; Deutsch, M. Second-Harmonic Microscopy of Biological Tissue. *Optics Letters* **1986**, *11* (2), 94-96.

(56) Zoumi, A.; Yeh, A.; Tromberg, B. J. Imaging Cells and Extracellular Matrix in Vivo by Using Second-Harmonic Generation and Two-Photon Excited Fluorescence. *Proceedings of the National Academy of Sciences* **2002**, *99* (17), 11014–11019.

(57) Zipfel, W. R.; Williams, R. M.; Christie, R.; Nikitin, A. Y.; Hyman, B. T.; Webb, W. W. Live Tissue Intrinsic Emission Microscopy Using Multiphoton-Excited Native Fluorescence and Second Harmonic Generation. *Proceedings of the National Academy of Sciences* **2003**, *100* (12), 7075–7080.

(58) Strupler, M.; Pena, A.-M.; Hernest, M.; Tharaux, P.-L.; Martin, J.-L.; Beaurepaire, E.; Schanne-Klein, M.-C. Second Harmonic Imaging and Scoring of Collagen in Fibrotic Tissues. *Optics Express* **2007**, *15* (7), 4054-4065.

(59) Strupler, M. Imagerie Du Collagène Par Microscopie Multiphotonique, Ecole Polytechnique: Palaiseau, 2008.

(60) Picaut, L. Synthèse D'un Tendon Artificiel, Université Pierre et Marie Curie: Paris, 2017.

(61) Deniset-Besseau, A.; Duboisset, J.; Benichou, E.; Hache, F.; Brevet, P.-F.; Schanne-Klein, M.-C. Measurement of the Second-Order Hyperpolarizability of the Collagen Triple Helix and Determination of Its Physical Origin. *The Journal of Physical Chemistry B* **2009**, *113* (40), 13437–13445.

(62) Deniset-Besseau, A.; De Sa Peixoto, P.; Mosser, G.; Schanne-Klein, M.-C. Nonlinear Optical Imaging of Lyotropic Cholesteric Liquid Crystals. *Optics Express* **2010**, *18* (2), 1113-1121.

(63) Pena, A.-M.; Boulesteix, T.; Dartigalongue, T.; Schanne-Klein, M.-C. Chiroptical Effects in the Second Harmonic Signal of Collagens I and IV. *Journal of the American Chemical Society* **2005**, *127* (29), 10314–10322.

(64) Teulon, C. Imagerie Quantitative Du Collagène Par Microscopie Par Génération de Second Harmonique Résolue En Polarisation, Ecole Polytechnique: Palaiseau, 2016.

Conclusion

Summary

The main objective of this project was to design tunable biomaterials for tissue engineering. The composite approach provides numerous advantages to enhance cell adhesion and control bioactivity by complying with both structural and functional requirements. The host matrix, made from a natural macromolecule (collagen), or from synthetic supramolecular polymers (self-assembled peptide amphiphiles), provides a suitable structural environment to the cells and can also exhibit intrinsic biochemical cues to influence cell behavior. In addition, functionalized silica nanoparticles (SiNPs) could be used as platforms either to further tune the architecture of the scaffold or display additional bioactive ligands.

The combination of peptide amphiphiles with SiNPs led to composite biomaterials with high modularity. In particular, we compared two types of display for the selected biomimetic epitope RGDS: homogeneous dispersion within peptide amphiphiles fibers or clusterization at the surface of SiNPs. The 3D clustering of the bioactive epitope within the matrix improved significantly cell adhesion and spreading. We were also able to graft simultaneously two integrin-binding sequences, RGD and PHSRN, known to work in a distance-dependent manner. We have shown that the modularity of the bionanocomposites allows to find the ideal molecular organization to create a synergy between the two peptide motifs.

The next step was to achieve the control of the spatial organization of several functions on the surface of a single nanoparticle. With this purpose, we have developed an original and challenging strategy based on the synthesis of self-assembling alkoxysilane precursors that could form pre-organized domains to be transferred at the SiNP surface. These domains then become functional patches. By playing with the self-assembly parameters (molecular design, solvent, concentration…) different patterns could be obtained. However, we evidenced the importance of (i) obtaining well-defined self-assembled systems to achieve controlled patches and (ii) finding suitable strategies to visualize these patches. Finally, reaching bifunctionality allowed to create interesting platforms that should be able to interact simultaneously with cells and with the polymer.

Overall, I have synthesized a whole library of mono- and bifunctional particles that were incorporated in collagen-based threads. These bionanocomposites were evaluated in a model of peripheral nerve regeneration with neural type cells. It was demonstrated that the functionalization and the concentration of SiNPs influence their dispersion in the thread and the collagen architecture. PC12 cells behavior was finally more impacted in presence of sulfonate-modified particles, which are the ones more likely to interact will collagen. Consequently, the most effective parameter to control cell adhesion and differentiation in our system was the architecture of the scaffold. All the neurites produced by differentiated PC12 cells were aligned with respect to the thread, which serves as effective guide for peripheral nerve regeneration.

In the collagen-based threads, no evidence of the effect of the bioactive epitopes grafted at the surface of SiNPs could be observed. Thus, we proceeded with the development of thinner 3D porous scaffolds (40 µm *vs* 400 µm) by electrospinning to improve the particle accessibility for the cells. By mimicking the entangled fibrillar structure of ECM, with tunable porosity and fiber diameter or orientation, electrospinning is a powerful technique in tissue engineering. However, applying this technique to collagen without altering its native state has remained challenging. We were able to engineer a self-supported collagen-based membrane by electrospinning and characterized it by synchrotron-radiation circular dichroism, multi-photon microscopy based on second harmonic generation and cryo-scanning electron microscopy. The collagen membrane could be stabilized and its integrity preserved in absence of cross-linkers.

Altogether, interesting tools to elaborate biomaterials with tunable structures and multiple functionalities have been developed during this thesis, opening many new projects and perspectives to engineer tissue-like structures.

Perspectives

1. Engineering SiNP building blocks

SiNPs were exploited in this study because they offer the great advantages of having a versatile surface chemistry to graft a great range of molecules at their surface. Playing with the nature of the displayed molecules and with the size of the cluster can be interesting to find the most efficient set-up to trigger cell fate. A broad library of self-assembling alkoxysilanes may be further designed that would lead to patches of different sizes and density on the surface with a more precise control of the supramolecular structure.

2. Collagen-SiNP bionanocomposites by electrospinning

The self-supported collagen membrane is an interesting scaffold for tissue engineering. However, we did not yet take advantage of all the possibilities that offers the modularity of ES process. The porosity, fiber size, and alignment of the network can be tuned in a much easier way than following a casting approach.

Additionally, electrospinning is an ideal tool to create collagen-SiNPs bionanocomposites for tissue engineering. Functionalized SiNPs add signals in the material to enhance the impact on cell behavior, similarly as what we achieved with peptide amphiphiles and extruded collagen threads. By creating self-supported membranes instead of thick 3D materials, ES can provide the advantage of increasing the accessibility of the cells to SiNPs and, therefore, to functional groups at their surface. SiNPs can also interact with the collagen and modulate the collagen architecture, which has been shown to have a significant impact on cell behavior. Those particles could be an interesting tool to adapt the scaffold to regenerate different kinds of tissue. Again the formation of a composite membrane with SiNPs homogeneously distributed within the scaffold could not be achieved by casting. By combining all our SiNP surfaces functionalization with the processing of collagen, we could efficiently widen the panel of possibilities to get materials with tunable structures and functions.

3. Incorporating growth factor within bionanocomposites to trigger cell differentiation

The architecture of the material and the display of bioactive epitopes are crucial to engineer an effective biomaterial for tissue engineering. However, one major parameter to take into account for effective cell differentiation is the presence of specific growth factors. Being in a free soluble form in native tissues, we have here added them in the cell culture medium for our peripheral nerve regeneration model. An interesting evolution would be to incorporate directly the growth factor in the biomaterial. Particles are interesting tools for drug delivery or display. Growth factor could be adsorbed or encapsulated to SiNPs in order to have a sustained delivery to the cell, or displayed to the cells *via* a chemical conjugation.

Appendix

Content

I. Patchy particles by grafting *Py* precursor

As reported in chapter III, **Py**'s self-assemblies were studied in ethanol and toluene from 0.01 µM to 50 mM. This precursor self-assemblies in stable structures measurable by DLS at the threshold concentration of 1 mM. In toluene self-assembly is less defined and is more difficult to fully characterize. In fluorescence spectroscopy, a large emission band appears at high wavelengths when two pyrenes rings are close enough (approximately 10 Å) during excitation. This is the excimer emission reported many times in literature.[63–66] This band is here centered at 474 nm and is in our system a probe of distance in between pyrene molecules.

1. Fluorescence spectroscopy and Zeta Potential on SiNPs

We studied how these self-assembled systems could be transferred to the surface of the SiNPs to create functional patches (Figure I-1). The resulting SiNP-1 particles bearing aromatic groups are then treated in acidic conditions to hydrolyze the carbamate group of the precursor, revealing amines at the surface of SiNP-2.

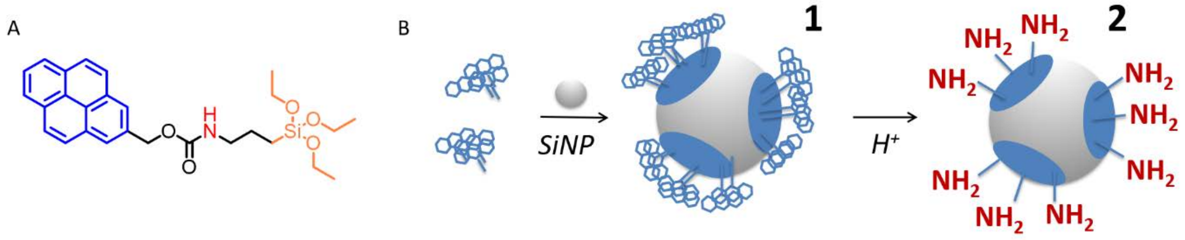

Figure I-1 : (A) Molecular structure of *Py* precursor. (B) Schematic representation of the synthesis of patchy particles *via* the self-assembly of Py. Transfer of self-assemblies on SiNPs creates SiNP-1. Acidic hydrolysis reveal amines on SiNP-2.

1.1. Fluorescence spectroscopy

Four concentrations were tested, from 0.5 mM to 50 mM, the ideal concentration for the **An** precursor. By fluorescence spectroscopy, on Figure I-2, pyrene signature was detected on **Py**-modified SiNP in toluene even at low concentration (0.5 mM). In toluene, two bands are detectable at 393 nm and 475 nm, respectively the monomer band and the excimer band. They are visible at all concentrations. The intensity of the excimer band increases progressively with the concentration indicating packing of the aromatic moieties that increases with increasing **Py** concentration. When the concentration is increasing, the amount of successfully grafted **Py** increase too in toluene. However, in the ethanol case, the fluorescence intensity on SiNP is less significant. From 0.5 mM to 10 mM, only the monomer band at 393 nm is visible. The excimer band at 475 nm appears only at 50 mM but with a considerably lower intensity than in toluene. The **Py** precursor seems not to be significantly grafted in ethanol.

After the acidic treatment, at 0.5 mM in toluene the signal was shut down (dotted line). The pyrene moiety was efficiently released after the acidic hydrolysis of the carbamate. At 1 mM, 10 mM and at 50 mM (even if the intensity is lower), an excimer band is still visible but blue-shifted around 457 nm (instead of 475 nm) translating a decrease in pyrene packing[53–56] not successfully deprotected from pyrene. In ethanol the weak signal that we detected is not visible anymore. The few pyrene precursors molecules grafted were well-de-protected by the acidic treatment.

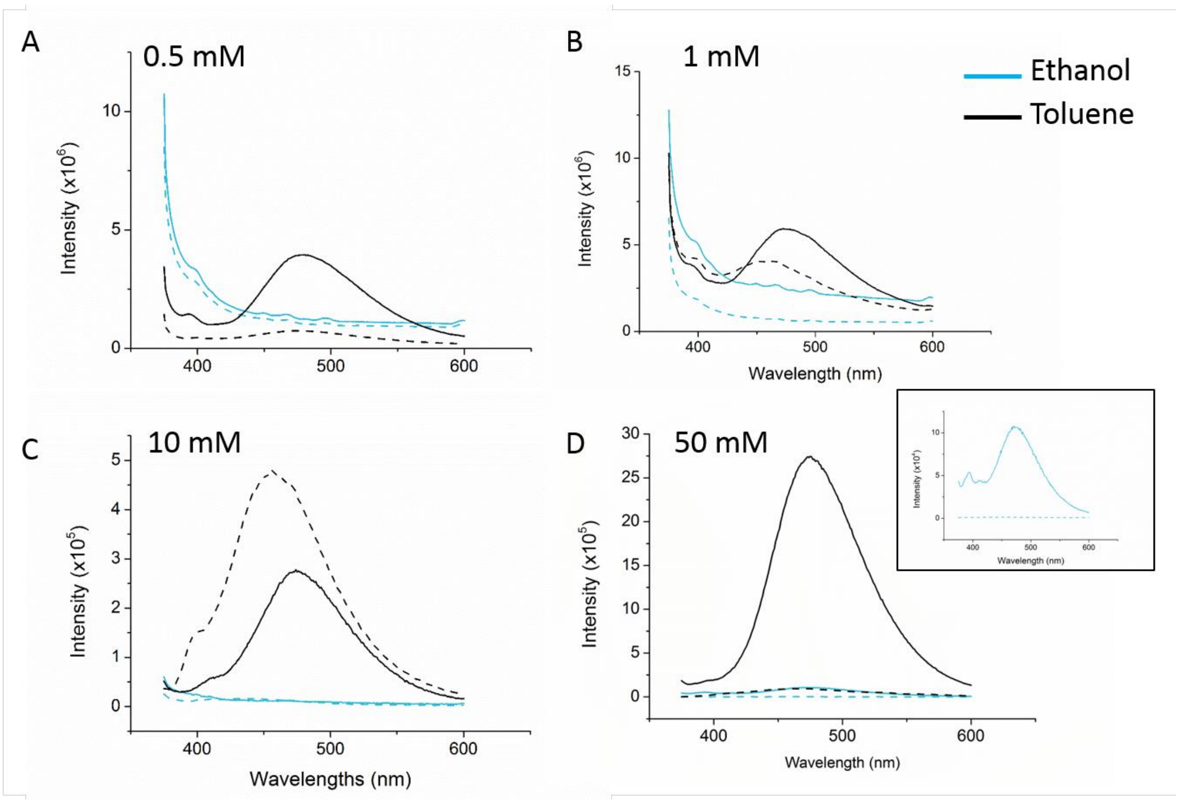

Figure I-2 : Fluorescence spectroscopy of *Py*-modified SiNPs in ethanol (blue lines) and toluene (black lines) at A) 0.5 mM, B) 1 mM, C) 10 mM and D) 50 mM before (solid lines) and after (dotted lines) acidic hydrolysis.

1.2. Zeta potential

The grafting of **Py** and removal of the anthracene moiety has also been monitored by zeta potential measurements as a function of pH. Figure I-3-A shows the zeta potential values representative of non-functionalized SiNPs bearing silanol groups (SiNP-OH, in grey, pKa *ca.* 3) and homogeneous **Py** functionalized SiNPs bearing amines (SiNP-NH_2, in red, pKA ca. 10). After grafting of **Py**, zeta potential values from bear SiNPs increases both in ethanol and toluene (Figure I-3-B-D plain squares). This is attributed to the replacement of exposed silanols by pyrene groups after condensation of **Py** at the SiNP surface. Further removal of the pyrene moiety by acidic treatment for the hydrolysis of the carbamate successfully revealed amine groups at the surface of SiNP. This is confirmed by a further increase in zeta potential, switching to positive values at low pH, highlighting the presence of positive charges in both solvents (Figure I-3-B-D-open squares). The amines revealed by the acidic treatment contribute positively so the amount of positive charges in acidic pH. We can see that we have more positive charges on SiNP modified in toluene than in ethanol, i.e. a more important number of amine groups. **Py** was grafted in higher extent in toluene than in ethanol. Zeta potential measurements are coherent with the fluorescence measurements. In toluene we reached the highest amount of positive charges at 0.5 mM : ~17 mV at pH 2. Increasing the concentration did not have a noticeable influence (~17 mV at pH 2 for 1 mM and 50 mM and ~22mV for 10 mM). In ethanol, the amount of charges was quite low (~2 mV) at 0.5, 1 and 10 mM. At 50 mM it finally increased around 8 mV.

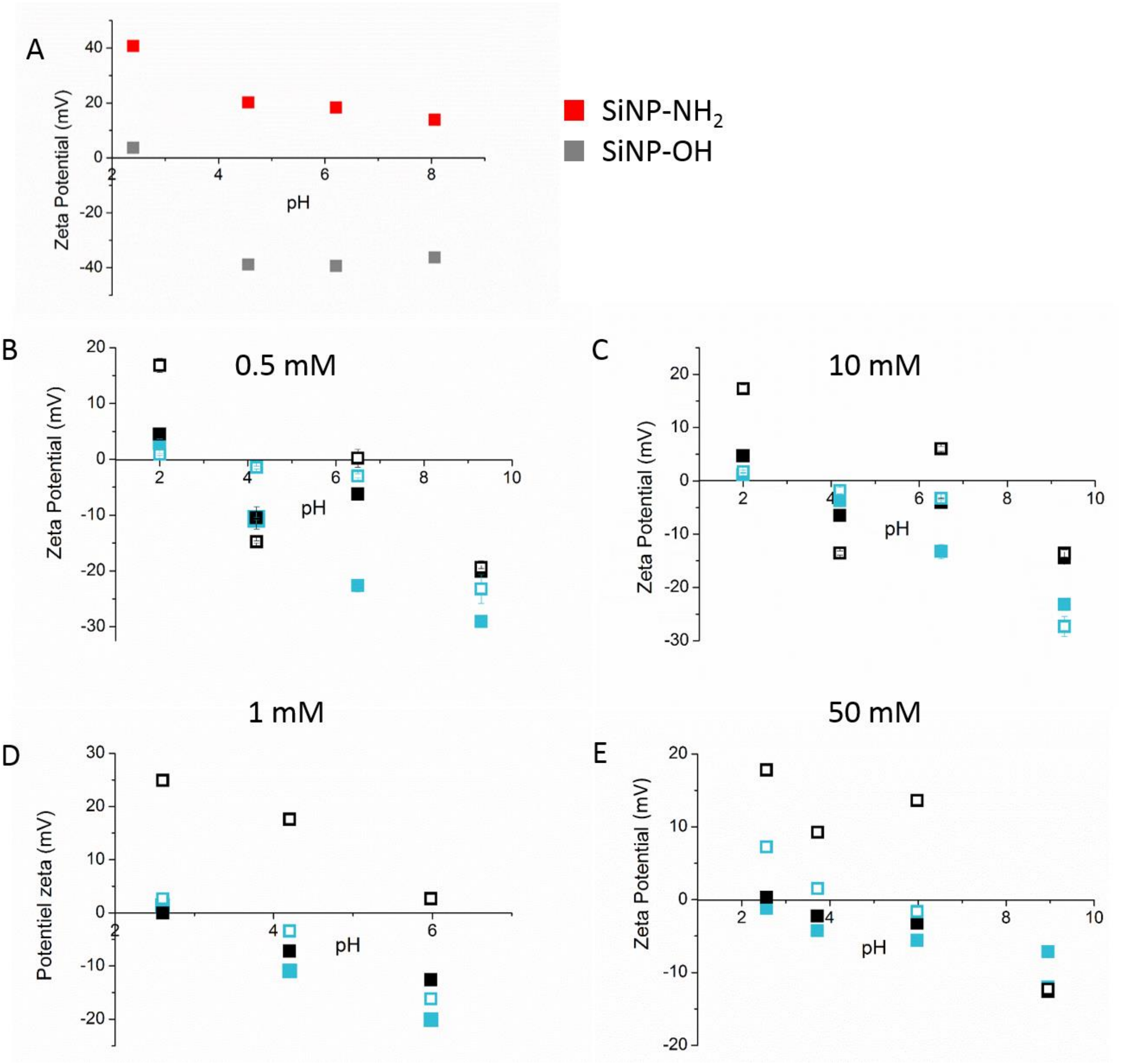

Figure I-3 : A) Zeta potential of SiNP-OH and SiNP-NH2 as a function of pH. Zeta potential measurements of *Py*-modified SiNPs in ethanol (blue squares) and toluene (black squares) at B) 0.5 mM, C) 1 mM, D) 10 mM and E) 50 mM before (solid squares) and after (open squares) acidic hydrolysis.

It seems then that modifying the concentration in toluene do not change the grafting. It might be because the self-assembly is maybe not really impacted by the concentration in toluene. Maybe the precursor **Py** do not self-assemble in toluene and the grafting is similar to an APTES grafting, homogeneous (but with a lower density). This would be in accord with the DLS results of **Py** in toluene where no major structures were highlights (Cf. Chapter III). At the opposite in ethanol we need to reach a very high concentration (50 mM) to have an impact. We need the biggest self-assembly structures at high concentration, to modify the total equilibrium in favor of grafting at the particle surface.

2. Amine distribution on *Py*-modified SiNPs surface by grafting of Gold-Nanoparticles and electron microscopy

2.1. SiNP functionalized in ethanol

Right after the **Py** grafting in ethanol at 1 mM, on Figure I-4-A, SEM observations show fibers around SiNPS. The fibers had a lace-effect structure interacting with the particle by covalent bonding. After acidic treatment the fibers were mostly removed (Figure I-4-B). The carbamate hydrolysis released the pyrene moiety, disrupting the self-assembly structure. Only the covalent grafting on SiNP remained, one again like a finger print of the self-assembly.

To visualize amines and understand the distribution or functionalization pattern at the particle surface we use again carboxylate-modified AuNPs (Figure I-4-C,D). No AuNP were visible on the particle surface after their grafting. This result is consistent with zeta potential measurements. No amine was revealed by the acidic treatment. One hypothesis could be that the sol-gel chemistry would occur preferentially between two pyrene precursor molecules instead of between the particles and the precursor, leading to unmodified particles.

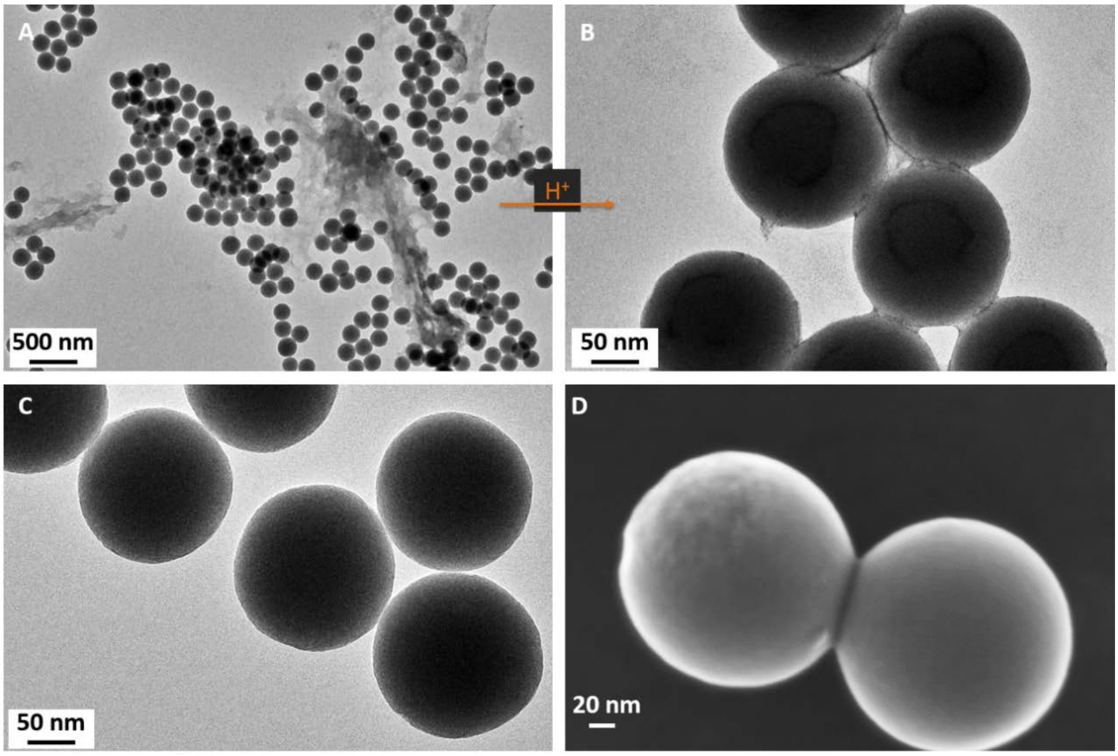

Figure I-4 : SiNPs grafted in ethanol with *Py* precursor at 1 mM A) before and B) after the acidic hydrolysis. C-D) Characterization of NH_2 positioning with AuNP-grafting.

2.2. SiNP functionalized in toluene

The **Py** precursor self-assembly in toluene was completely different. On Figure I-5-A, organic matter was present between particles, and did not resist the acidic treatment (Figure I-5-B). AuNPs were present on se the surface of SiNPs after conjugation but quite homogeneously distributed (Figure I-5-C,D). **Py** do not self-assemble in toluene, this is a good solvent for the precursor. Molecule-molecule interactions and solvent-molecule interaction are similar. It confirms DLS measurement of **Py** in toluene, and the fact that the particles are similarly modified whatever the concentration according to zeta potential measurement and ethanol. The grafting does not depend on any self-assembled structure, and **Py** cover the whole SiNP surface.

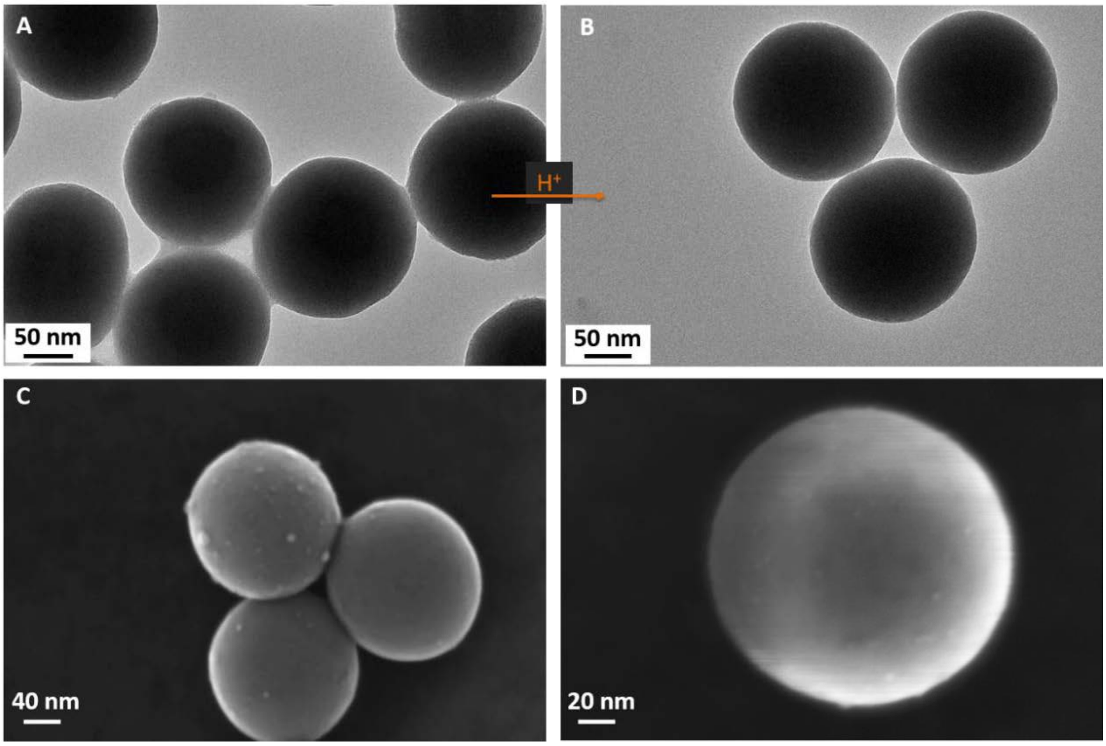

Figure I-5 : SiNPs grafted in toluene with *Py* precursor at 1 mM A) before and B) after the acidic hydrolysis. C-D) Characterization of NH_2 positioning with AuNP-grafting.

To conclude this part, we did not find the best experimental conditions to create patchy SiNPs *via* the grafting of the precursor **Py**. Self-assembly structures were too big and stable in ethanol to be transferred at the particle surface, and at the opposite too monomeric to create cluster in toluene.

II. Conjugation of di-mercaptosuccinic- acid modified Fe_2O_3 particles

This work was performed in collaboration with Pr. Christine Ménager (PHENIX, Sorbonne Université). Di-mercaptosuccinic-acid modified Fe_2O_3 (~10 nm diameter) were successfully grafted on SiNPs homogeneously modified with amine groups (through APTES grafting). The conjugation of Fe_2O_3 particles was found to be highly reproducible (Figure II-1-A). However, we were not able to have clean negative controls on SiNP-OH because of nonspecific reactions between Fe_2O_3 particles and the Stöber SiNPs (Figure II-1-B).

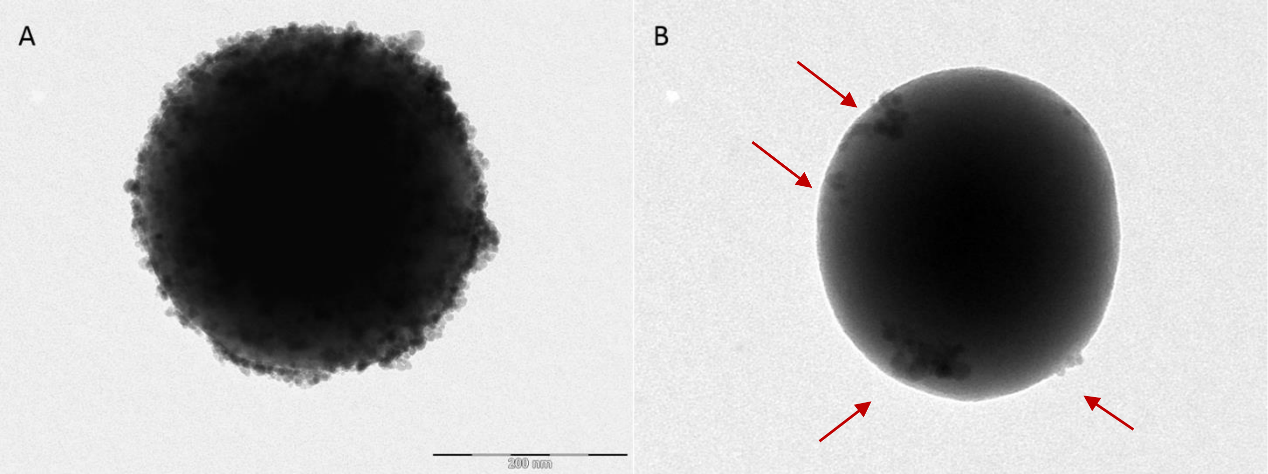

Figure II-1 : : TEM images of the conjugation of di-mercaptosuccinic- acid modified Fe_2O_3 particles at the surface of (A) SiNPs homogeneously grafted with amines and (B) un-modified SiNPs.

III. Synchrotron-radiation Oriented Linear Dichroism

The synchrotron radiation at Soleil can help us investigate the structural organization of collagen triple helices within self-supported membranes thanks to oriented linear dichroism (OLD). Indeed, while conventional CD reveals secondary structures, OLD addresses protein alignment within macroscopically oriented samples.[1] During our previous sessions at Soleil, we have investigated the possibility to run OLD on the different membranes: dry and hydrated electrospun and casted membranes. By varying the membrane orientations, we obtained different spectral signatures with variations of the absorption maxima. For example, concerning the casted membrane, the spectrum obtained with a positive maximum of absorption at 220 nm varies constantly with sample orientation (Figure III-1). The opposite spectrum is obtained with a maximum negative absorption band at 220 nm, when the sample is oriented at 180° from its original position. Then the spectrum with positive maximum at 220 nm is recovered when 360° from the initial position is reached. This shows that collagen molecules are highly oriented in the sample.

This orientation could be clearly evidenced in the casted membrane. However, this was much more difficult to obtain with the ES membrane due to a low signal-to-noise ratio, probably because the membranes are less transparent.

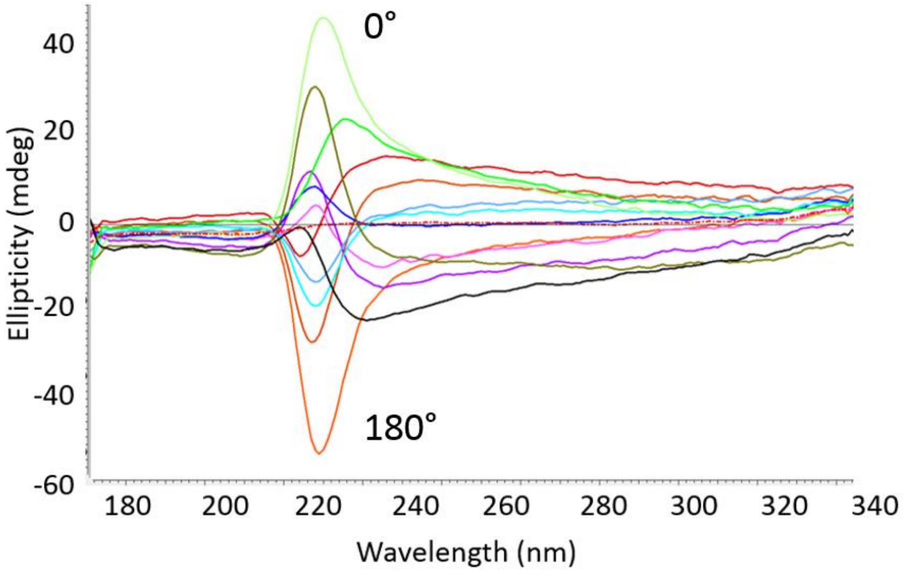

Figure III-1 : Oriented linear dichroism (steps of 30° over 360 ° of a casted membrane.

We would like to clarify the origin of these orientation-dependent variations of absorption despite light scattering problems in the solid membranes. Indeed, the optical transparency of the membranes (different in the case of ES- and casted-membranes) may impact their respective spectral signature. To this aim, mechanical pressure will be applied on the ES membrane to decrease porosity and suppress interfaces between collagen and air that are responsible for scattering. New measurements will be realized at Soleil in September 2018.

This could prove for the first time that we can get information on the molecular ordering of collagen within solid membranes.

(1) Bürck, J.; Heissler, S.; Geckle, U.; Ardakani, M. F.; Schneider, R.; Ulrich, A. S.; Kazanci, M. Resemblance of Electrospun Collagen Nanofibers to Their Native Structure. *Langmuir* **2013**, *29* (5), 1562–1572.

List of abbreviations

AA	Acetic Acid
AuNP	Gold-nanoparticles
CD	Circular Dichroism
CNS	Central nervous system
DAPI	4’,6-diamidino-2-phenylindole dihydrochloride
DLS	Dynamic light scattering
DNA	Deoxyribonucleic acid
ECM	Extracellular matrix
ES	Electrospinning
EtOH	Ethanol
FTIR	Fourier transform infrared spectroscopy
GF	Growth factor
HCl	Hydrochloric acid
NHDF	Normal human dermal fibroblast
OLD	Oriented linear dichroism
PA	Peptide amphiphile
PG	Proteoglycan
PN	Peripheral nerves
PNS	Peripheral nervous system
P-SHG	Polarized – Multi-photon microscopy based on second-harmonic generation
RT	Room temperature
SEM	Scanning electron microscopy
SEM-FEG	Scanning electron microscopy with a field-emission gun
SHG	Multi-photon microscopy based on second-harmonic generation
SiNP	Silica nanoparticles
SRCD	Synchrotron-radiation circular dichroism
TEM	Transmission electron microscopy
3D / 2D	Three dimensions / two dimensions